UNIVERSITAT DE BARCELONA

DEPARTAMENT D'ESTRUCTURA I CONSTITUENTS DE LA MATERIA

Muon Strategies for the High Level Trigger of the LHCb Experiment

Antonio Pérez-Calero Yzquierdo

UNIVERSITAT DE BARCELONA

Muon Strategies for the High Level Trigger of the LHCb Experiment

Memoria de la tesis presentada por

Antonio Pérez-Calero Yzquierdo

para optar al grado de Doctor en Física

Director de tesis: Dr. Hugo Ruiz Pérez

Programa de Doctorado: Física
Línea de Investigación: Física de Partículas y Cosmología

Departament d'Estructura i Constituents de la Materia

Barcelona, noviembre de 2011

"It doesn't matter how beautiful your theory is, it doesn't matter how smart you are. If it doesn't agree with experiment, it's wrong."

"The worthwhile problems are the ones you can really solve or help solve, the ones you can really contribute something to. No problem is too small or too trivial if we can really do something about it."

Richard P. Feynman (1918-1988)

Acknowledgments

Many people have helped me during the years of my doctorate. I would like to express now my feelings of gratitude and appreciation.

First, I deeply thank Lluís Garrido and Hugo Ruiz for the opportunity to join the LHCb group at Universitat de Barcelona. Together with Ricardo Graciani and Eugeni Graugés, they provided continuous support along the years. I appreciate all the wisdom, encouragement and patience they have offered me.

I am grateful to Frederic Teubert, a true master in the art of making science, for the generous way in which he offered his time and advice during the long months at CERN. I have learned from his passion and dedication to Physics.

My work in the HLT relies on many ideas received from all the members of the trigger group. José Ángel Hernando provided me with invaluable help in the programming of the trigger algorithms. Many thanks to Hans Dijkstra, Gerhard Raven, Leandro de Paula and Miriam Gandelman for their suggestions and support, and to Johannes Albrecht and Vladimir Gligorov for our discussions, sometimes warm but always productive!

I would like to express my gratitude to Ulrik Egede and Mitesh Patel for their help and advice during the optimization of the muon+track algorithm for the selection of the $B_d \to K^* \mu^+ \mu^-$ decay, and their support to my work. My appreciation also goes to Gaia Lanfranchi, Diego Martínez, Xabier Cid and the whole group dedicated to rare decays and $B_s \to \mu^+ \mu^-$. I would also like to thank Jaap Panman, who allowed me to participate in the discussions of the luminosity measurement working group, introducing me to aspects of the experiment totally unknown to me.

I am grateful to Xavier Vilasis for his wise advice and the lively moments of interesting conversation during my stays in Geneva. A big thank you to Miriam Calvo for her help throughout the years, particularly during the first months in Barcelona, when I was ignorant of many things.

Un abrazo especial a Elías, con el que viajé por primera vez al CERN y a todos los compañeros de despacho en la UB, en particular Jordi y Miguel Angel, por su ayuda, consejos y siempre divertida conversación. Tambien al resto de los compañeros doctorandos de Barcelona: Ricci, Albert, Marc, Alessandro y Carlos por ayuda, consejos y buenos momentos a lo largo de todos estos años.

Agradezco a mis padres, hermano y toda mi familia su cariño y apoyo a lo largo de tantos años, y a mi tío José Ignacio Pérez Calero, por su ejemplo y consejos, los cuales me han permitido llegar hasta aqui. A los amigos en Sevilla. A José María Talavera, por mantenerme al corriente de todo lo que sucedía en mi ciudad durante las “estancias breves” en Ginebra.

Finalmente a René, sin cuyo amor no podría vivir. My love for you, my heart is true.

Contents

1 Introduction **1**

2 Theoretical Framework **3**
2.1 The Standard Model of Particle Physics 3
2.1.1 The CKM Matrix 5
2.2 Prospects and probes for Physics beyond the Standard Model 9
2.2.1 Limitations of the SM 9
2.2.2 Flavour Physics as a test for Standard Model extensions 11
2.2.3 New Physics constraints from CP violation 14
2.3 Muonic B decays in LHCb 21
2.3.1 $B_s \to \mu^+\mu^-$ 23
2.3.2 $B_d \to K^*\mu^+\mu^-$ 25
2.3.3 $B_s \to J/\psi(\mu^+\mu^-)\phi$ 26
2.3.4 $B_{d/s} \to X\mu\nu$ 29

3 The Beauty experiment at the Large Hadron Collider **33**
3.1 The Large Hadron Collider 33
3.1.1 Experiments at the LHC 35
3.2 The LHCb experiment 36
3.2.1 B Physics at the LHC 36
3.2.2 Tracking and vertexing detectors 43
3.2.3 Particle Identification detectors 49
3.2.4 LHCb software framework and applications 57

4 The LHCb Trigger System **59**
4.1 Need of a trigger system at LHCb 59
4.2 LHCb trigger strategy 62
4.2.1 Level 0 hardware trigger 64
4.2.2 High level software trigger 67
4.3 Muon triggers in HLT 69
4.3.1 HLT1 69
4.3.2 HLT2 73

5 Design and optimization of muon trigger lines with Monte-Carlo **77**
5.1 HLT1 muon+track alley 77
5.1.1 Benchmark channels 78

5.1.2 L0 muon and confirmation efficiencies 79
5.1.3 Study of muon+track discriminating variables 79
5.1.4 Performance at an example working point 82
5.2 HLT2 muon+track selection 85
5.2.1 Benchmark channel 85
5.2.2 L0 and HLT1 efficiencies 86
5.2.3 Optimization of discriminating variables 87
5.2.4 Trigger acceptance effects on $B_d \to K^* \mu^+ \mu^-$ 92
5.3 Global optimization of HLT2 inclusive muon selections in DC06 94
5.3.1 Objectives of the muon inclusive triggers 94
5.3.2 Benchmark channels 94
5.3.3 The three bandwidth division scenarios 95
5.3.4 Muon selections in the three scenarios 96
5.3.5 Working scenarios 98
5.4 HLT2 inclusive muon selections in MC09 100
5.4.1 Rate reduction scenarios for HLT2 100
5.4.2 Elementary muon selections 102
5.4.3 Inclusive muon strategies for the different reduction scenarios 103

6 Commissioning of muon triggers with data 109
6.1 Trigger strategy for the LHC startup 110
6.2 Commissioning of the L0 muon trigger 111
6.3 Commisioning of HLT1 muon alleys 113
6.3.1 L0 muon confirmation with T tracks 113
6.3.2 VELO track and vertex reconstruction 114
6.3.3 Selection variables for the HLT1 muon triggers 117
6.3.4 Minimum Bias retention results 124
6.4 Studies on signal Efficiency 124
6.4.1 First study of trigger performance on $J/\psi \to \mu^+ \mu^-$ 127
6.4.2 Prospects for evaluating trigger efficiencies of $B_s \to \mu^+ \mu^-$ using $J/\psi \to \mu^+ \mu^-$ 129
6.5 Later developments in HLT muon triggers 133
6.5.1 HLT1 single track trigger 134
6.5.2 Fast VELO reconstruction 135
6.5.3 HLT1 muon reconstruction 135
6.5.4 HLT2 inclusive B triggers 136
6.6 Dimuon spectra in the first LHCb data 137

7 Conclusions 141

A Resumen 143
Marco teórico 143
El detector LHCb del Gran Colisionador de Hadrones 144
El sistema de trigger del experimento LHCb 146
Desarrollo y evaluación de triggers muónicos con Monte-Carlo 148
Puesta en marcha y validación de los triggers muónicos 151
Conclusiones 155

List of Figures **157**

List of Tables **163**

Bibliography **165**

Chapter 1

Introduction

The origin of Particle Physics can be traced back to the study of the atom structure, natural radioactivity and cosmic radiation initiated by the pioneers of the field at the beginning of the 20th century. When the elementary particles we now call muons were first detected in cloud chambers and photographic emulsions, the discipline started to form an independent branch of what was until then basically atomic and nuclear physics.

Weak interactions had been known through its manifestation in β decays since the discovery of radioactivity. The first successful theory for this interaction was proposed by Fermi in 1934 by making use of the recently developed neutrino hypothesis. The Fermi model, with the introduction of a weak coupling constant, allowed decay amplitudes to be calculated. However, the theory was not renormalizable, and therefore did not permit the calculation of amplitudes beyond the tree level.

The careful study of interactions between elementary particles mediated by the weak interaction produced astonishing results when it was discovered that it did not comply with the assumed symmetry of spatial inversion (P) or its combination with the particle-antiparticle conjugation (CP). In order to incorporate these results in the theory, the intermediate boson model was used to propose a combined description for the weak nuclear force and electromagnetism. The theory for the unified electroweak interaction, developed in the 1960s, formed the basis of the Standard Model of Particle Physics, together with the theory for the strong interaction, formulated in the following decade.

On the experimental side, more powerful accelerators and better particle detectors were successively developed during the last decades of the past century. The experimental evidence supported the existence of vector bosons as mediators of the electroweak and strong interactions. New particles were discovered and predictions of the Standard Model, such as the phenomena of flavour oscillations, were also successfully scrutinized. The accurate description of all experimental results established the Standard Model as the modern paradigm for elementary particles and their interactions, even though a last key piece, the Higgs boson, still remains to be confirmed.

However, there are profound reasons to believe that the Standard Model can not be the ultimate theory, but an effective approximation below the TeV scale. Some of the reasons are: gravitation has not been incorporated to the theory; an important part of the dynamics of neutrinos is not understood; and the amount of CP asymmetry the Standard Model predicts is not sufficient to explain the evolution of the Universe from the assumed symmetric initial state to the matter-antimatter abundance asymmetry observed today.

Flavour Physics refers to the phenomena mediated by interactions that distinguish between the flavours of elementary particles, which within the Standard Model is associated to the weak and Yukawa interactions. In the last decades of the 20th century, the study of Flavour Physics allowed for the prediction of the quark content of the Standard Model and their respective masses before they were directly observed in experiment. In the similar spirit, the study of Flavour Physics has been identified by theorists as a key ingredient in our search for a more fundamental theory.

The LHCb experiment, which analyses the proton-proton collisions provided by the Large Hadron Collider, has been designed to continue the fertile approach of Flavour Physics in our quest for knowledge. In particular, the oscillation and decay of B mesons have been identified as an ideal laboratory for the exploration of New Physics, beyond the Standard Model, for both theoretical and experimental reasons.

B mesons are abundantly produced at the LHC, however they are diluted in a still more copious background. Profiting from the high B production therefore requires a careful identification of interesting decay modes.

The first stage of background rejection is achieved by the trigger mechanisms of the experiment, which examine events as they are produced in order to select only a small fraction of them for permanent storage and posterior analysis. Trigger algorithms based on the presence of muons have been designed to optimally select several muonic decays of key importance for the LHCb research program. The design, optimization and commissioning of such trigger selections is the subject of this work.

Chapter 2 of this thesis introduces the Standard Model and discusses its limitations. The role of Flavour Physics as a probe for New Physics is emphasized and several muonic B decays are presented, along with the first measurements and future expectations from the LHCb experiment.

Chapter 3 describes briefly the LHC and its experiments. The LHCb detector is presented in detail, providing a description for each of its sub-systems.

The global LHCb trigger strategy is summarized in Chapter 4. The requirements of performing precision measurements of heavy flavour decays in a hadronic collider, and how the LHCb trigger has been designed to meet them is discussed. Then, the muon trigger algorithms, subject of this work, are described thoroughly.

Chapter 5 presents the optimization process and the results obtained for the inclusive muon-based LHCb trigger strategy, as it was performed prior to the LHC start-up. A Monte Carlo based simulation was used for this purpose, tuned to different settings, which were adapted to reproduce the foreseen experimental scenarios expected to be met by LHCb.

Finally, Chapter 6 summarizes the commissioning of the trigger lines developed on simulation, once proton collisions were provided by the LHC. The first inspection of the data available suggested that some modifications with respect to the algorithms implemented were necessary. With these modifications in place, the performance of each muon trigger selection in terms of output rate reduction was carefully studied. A first evaluation of trigger efficiency on signal and its extrapolation to other important decay modes is also given.

Chapter 2

Theoretical Framework

This chapter describes the importance for the LHCb experiment of certain muonic decay channels of mesons containing beauty quarks (B mesons), which motivate the need for dedicated trigger mechanisms. A theoretical framework for this work is provided, by briefly introducing first the Standard Model (SM), current paradigm in Particle Physics. Then, the limitations of this theory and the role of Flavour Physics as a probe for Physics beyond the SM are discussed. In the last section, some muonic decay channels are introduced as examples of this approach. The expected sensitivity for several of the corresponding measurements by LHCb with the data from the first run of the LHC (2010-11) is given.

2.1 The Standard Model of Particle Physics

The Standard Model (SM) is a collection of quantum field theories that summarizes our current knowledge of the most fundamental constituents of matter and the interactions between them. The SM is a local gauge theory in which the building blocks of matter interact through the exchange of force carrier gauge particles, which are derived from the symmetry group

$$G_{SM} = SU(3)_C \times SU(3)_L \times U(1)_Y. \tag{2.1}$$

The electroweak symmetry $SU(3)_L \times U(1)_Y$ [1–3] is spontaneously broken by the Higgs field [4, 5], resulting in the electromagnetic and weak interactions which are mediated by massless photons and massive $W^{\pm}$ and Z^0 bosons respectively. The strong interaction derives from $SU(3)_C$ [6, 7] and its carriers are massless gluons. The fourth and weakest interaction in Nature, gravity, is not included in the Standard Model. The building elements of the SM can be then classified as fermions (quarks and leptons), gauge vector bosons (gluons, photon, $W^{\pm}$ and Z^0) and the Higgs scalar boson (see Tables 2.1 and 2.2). Their interactions are described by the fundamental SM Lagrangian

$$\mathcal{L} = \mathcal{L}(QCD) + \mathcal{L}(EW) + \mathcal{L}(Higgs) + \mathcal{L}(Yukawa), \tag{2.2}$$

where the Yukawa term includes the coupling of the Higgs to the fermion fields which, due to the non-null vacuum expectation value for the Higgs field, acquire mass. The three families of quarks and leptons, each containing two types of particles, are then copies with identical properties, except for their increasing masses. Quarks can be of positive electric charge (up, charm and top, collectively known as up-type quarks) or negative electric charge (down, strange, bottom, called down-type quarks). Leptons are either charged

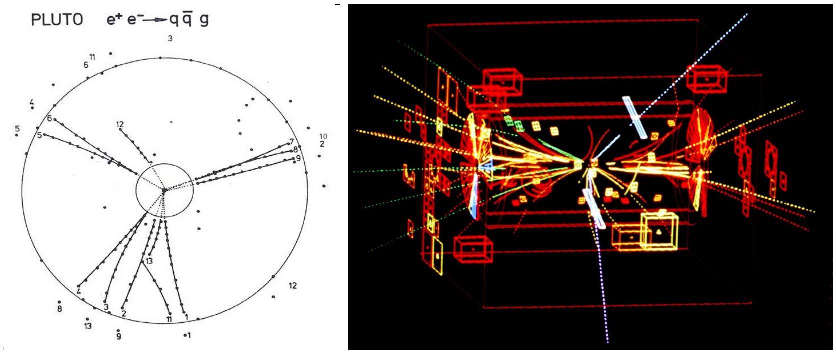

Figure 2.1: Three jet event interpreted as $q\bar{q}$+gluon from PLUTO data at Petra [9] (left). First detection of a Z^0 particle by UA1 [10] (right).

(electron, muon and tau) or neutral (electron, muon and tau neutrinos), as summarized in Table 2.1. Neutrinos are assumed to be massless in the SM. Antiparticles exist for each of these fermions with equal masses and decay times, but opposite additive quantum numbers.

Table 2.1: Fermion (quark and lepton) families in the Standard Model.

Charge	1st generation	2nd generation	3rd generation
+2/3	Up (u)	Charm (c)	Top (t)
-1/3	Down (d)	Strange (s)	Bottom (b)
0	Electron neutrino (ν_e)	Muon neutrino (ν_μ)	Tau neutrino (ν_τ)
-1	Electron (e)	Muon (μ)	Tau (τ)

Table 2.2: Boson content of the Standard Model [8].

Interaction	Boson	Charge	Mass
Electromagnetic	Photon (γ)	0	0
Weak (charged current)	$W^\pm$	±1	80 GeV
Weak (neutral current)	Z^0	0	91 GeV
Strong	Gluons	0	0
–	Higgs	0	>114 GeV

All fermion particles included in the SM have been detected along past decades. The description of fundamental interactions as mediated by the interchange of bosons in the SM has also been experimentally confirmed. Gluons are emitted in quark-quark interactions, then observed as additional jets in $q\bar{q}$ events (Fig. 2.1, left). W and Z bosons were detected by the UA1 and UA2 experiments at CERN (Fig. 2.1, right). However, the Higgs boson remains to be discovered, and hence, the proposed mechanism for spontaneous symmetry breaking for the electroweak interaction is still to be confirmed.

Quantum Chromodynamics (QCD) is the part of the SM which accounts for the strong interaction [11–13]. The charge of this interaction is a property of the quarks called color. This quantum number takes three values (commonly called red, green and blue) for quarks,

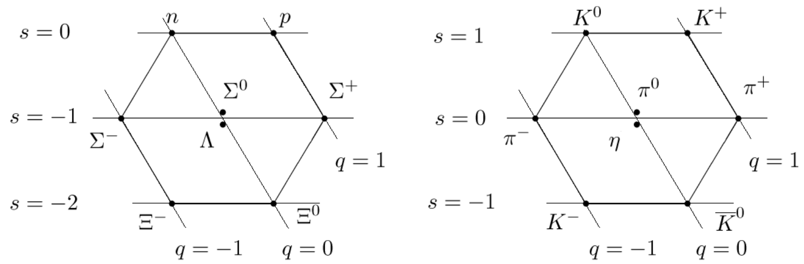

Figure 2.2: Classification of light baryons (left) and mesons (right) into octets according to their electric charge and strangeness.

and the corresponding anticolors for antiquarks (antired, antigreen and antiblue). Gluons carry both color and anticolor charges, changing the color of quarks when emitted and absorbed, while the flavour of the quark remains unchanged. The consequence of this is that quark production through the strong interaction conserves flavour, that is, always quark-antiquark combinations are produced. Quarks are bound into colorless objects, bound states collectively known as hadrons. They can be made up of either $q\bar{q}$ in color-anticolor combinations (mesons) or qqq in red-green-blue combinations (baryons). Figure 2.2 presents the lightest hadrons that can be formed by u, d and s quarks, and their antiparticles. These hadrons were the first to be discovered and their classification provided the first theoretical insight for the existence of quarks [14, 15]. Hadrons can also contain c and b quarks, while top quark decays before it can form a bound state with another quark. Particles containing b or anti-b quarks are of particular importance for the LHCb experiment and this thesis. They are produced in pairs by the strong interaction between colliding protons at the LHC (see Section 3.2.1).

The Electroweak Theory included in the SM comprises Quantum Electrodynamics (QED) and the theory for the Weak Interaction. The Higgs mechanism is the responsible for the breaking of the combined symmetry, causing the differences between the electromagnetic and weak interactions. Photons couple to electrically charged particles and their null mass causes the range of action for this interaction to be infinite. On the contrary, the other three massive intermediate bosons (W^+,W^- and Z) result into extremely short range interactions ($\frac{\hbar}{2m_{W,Z}c} \sim 10^{-18}$ m). The charged currents produced by the $W^\pm$ bosons couple to the flavour of the fermion fields, changing them from an up-type quark or antiquark ($|q| = 2/3$) to a down-type quark or antiquark ($|q| = 1/3$) and charged leptons into neutrinos, and viceversa. Neutral currents, mediated by the neutral Z boson, don't change the flavour or electric charge of the fermion fields.

2.1.1 The CKM Matrix

Fermion masses are originated by the Yukawa Lagrangian, the same Higgs mechanism which gives rise to gauge boson masses. The terms that couple the Higgs to fermion fields are

$$\mathcal{L}_Y = -\left(1 + \frac{H}{v}\right)\left[\bar{d}'_L M'_d d'_R + \bar{u}'_L M'_u u'_R + \bar{l}'_L M'_l l'_R + h.c.\right], \tag{2.3}$$

where H represents the Higgs field, v is the vacuum expectation value causing the spontaneous symmetry breaking, d', u' and l' are vectors in flavour space (e.g. d' refers to down-type quark fields) and M'_f are the mass matrices, defined as

$$(M'_f)_{ij} = -(C_f)_{ij}\frac{v}{\sqrt{2}}, \tag{2.4}$$

with $(C_f)_{ij}$ defining the couplings of fermion fields to the Higgs boson and $f = (d, u, l)$.

However, weak eigenstates which undergo the weak interaction are not, in general, the same that form bound states (hadrons), observable in experiments. Mass eigenstates are obtained by diagonalization of the mass matrices. This introduces the change of basis in fermion fields

$$f_L \equiv S_f f'_L \qquad f_R \equiv S_f U_f f'_R \tag{2.5}$$

produced by unitary matrices S_f and U_f. This results in the mass matrices

$$M_d = diag(m_d, m_s, m_b) \quad M_u = diag(m_u, m_c, m_t) \quad M_l = diag(m_e, m_\mu, m_\tau). \tag{2.6}$$

Since $\bar{f}'_L f'_L = \bar{f}_L f_L$ and $\bar{f}'_R f'_R = \bar{f}_R f_R$, neutral current terms of the Lagrangian are unchanged, causing the absence of Flavour Changing Neutral Currents or FCNC in the SM (GIM mechanism [16]). Charged current terms for quark interactions are however modified as $\bar{u}'_L d'_L = \bar{u}_L S_u S_d^\dagger d_L \equiv \bar{u} V_{CKM} d_L$. This defines the Cabibbo-Kobayashi-Maskawa matrix [17], V_{CKM}, which produces the mixing of the quark generations. Lepton terms are not modified, as $\bar{\nu}'_L l'_L = \bar{\nu}_L S_l^\dagger l_L \equiv \bar{\nu}_L l_L$, through the redefinition of neutrino flavours. This is possible as long as neutrinos are assumed to be massless. Neutrino mass terms would however introduce mixing also to the lepton sector.

The CKM matix can be written as

$$V_{CKM} = \begin{pmatrix} V_{ud} & V_{us} & V_{ub} \\ V_{cd} & V_{cs} & V_{cb} \\ V_{td} & V_{ts} & V_{tb} \end{pmatrix} \tag{2.7}$$

and contains the coefficients for the charged current terms $\bar{u}^i_L V_{ij} d^j_L$ that couple to the $W^\pm$ bosons. This complex matrix contains 18 parameters, which can be reduced applying unitarity constraints from which 9 unitarity relations arise

$$V_{CKM} V_{CKM}^\dagger = 1 \Rightarrow \sum_{k=1}^{3} V^*_{ki} V_{kj} = \delta_{ij}, \tag{2.8}$$

with V_{ij} as the coupling factor between quark states i and j. Five of these remaining nine CKM parameters are relative phases between the quark fields and can be absorbed by their redefinition. Finally, the resulting four free parameters are three rotation angles and one irreducible phase, which is the only source of CP violation phenomena in the SM. These are fundamental parameters of the SM. A standard expression for the matrix in terms of the four parameters is [18]

$$V_{CKM} = \begin{pmatrix} c_{12}c_{13} & s_{12}c_{13} & s_{13}e^{-i\delta} \\ -s_{12}c_{23} - c_{12}s_{23}s_{13}e^{i\delta} & c_{12}c_{23} - s_{12}s_{23}s_{13}e^{i\delta} & s_{23}c_{13} \\ s_{12}s_{23} - c_{12}c_{23}s_{13}e^{i\delta} & -c_{12}s_{23} - s_{12}c_{23}s_{13}e^{i\delta} & c_{23}c_{13} \end{pmatrix}, \tag{2.9}$$

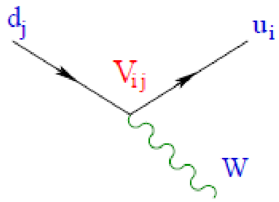

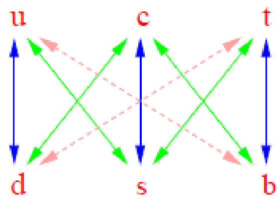

Figure 2.3: Charged current representation for the weak interactions between quarks: generic vertex (left) and generation mixing with coupling hierarchy according to the CKM matrix elements (right). Figure from [21].

with $s_{ij} = sin\theta_{ij}$ and $c_{ij} = cos\theta_{ij}$ and δ as the only phase.

Experiments have concluded that $s_{13} \ll s_{23} \ll s_{12} \ll 1$. This hierarchy can be explicitly shown using the parameter λ, defined as

$$\lambda = s_{12} = \frac{|V_{us}|}{\sqrt{|V_{ud}|^2 + |V_{us}|^2}} \tag{2.10}$$

to write the CKM matrix as an expansion (Wolfenstein parametrization). The λ parameter is related to the Cabibbo angle θ_C ($\lambda = \sin\theta_C$), which originally quantified the mixing between first and second generations. Quark generations mixing was first introduced by Cabibbo to explain kaon decay widths by the weak charged current between strange and up quarks, preserving the universality of the weak interaction [19]. Including terms up to fifth order in λ [20]:

$$V_{CKM} = \begin{pmatrix} 1-\lambda^2/2 & \lambda & A\lambda^3(\rho - i\eta + i\eta\lambda^2/2) \\ -\lambda & 1-\lambda^2/2 - i\eta A^2\lambda^4 & A\lambda^2(1+i\eta\lambda^2) \\ A\lambda^3(1-\rho-i\eta) & -A\lambda^2 & 1 \end{pmatrix} \tag{2.11}$$

where the additional parameters are defined by

$$s_{23} = A\lambda^2 = \lambda\left|\frac{V_{cb}}{V_{us}}\right| \qquad s_{13}e^{i\delta} = A\lambda^3(\rho + i\eta) = V_{ub}^* \tag{2.12}$$

and have experimental values [18]

$$\lambda = 0.2253 \pm 0.0007, \quad A = 0.808^{+0.022}_{-0.015}, \quad \rho = 0.132^{+0.022}_{-0.014}, \quad \eta = 0.341 \pm 0.013. \tag{2.13}$$

Figure 2.3 represents the hierarchy of the couplings between quarks. Vertical lines represent transitions within the same generation, corresponding to diagonal interaction terms with coupling factors close to unity. Couplings between first and second generation are of order λ, second and third of order λ^2, and first to third of order λ^3.

The CKM matrix is the key element for Flavour Physics, being the origin of the mixing of quark generations, FCNC which occur beyond the tree level, and CP violation in the SM. These phenomena would be absent from the SM if the relation between mass and flavour eigenstates were a real-valued diagonal matrix. In particular, CP non-conserving effects in the SM derive exclusively from the CKM complex phase, which is present at terms of order λ^3 or smaller.

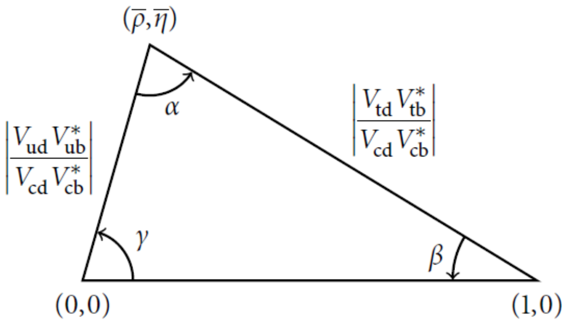

Figure 2.4: Unitarity condition for the CKM matrix associated to B_d system represented in the complex plane.

Each vanishing unitarity relation (eq. 2.8) between the CKM elements can be pictured as a triangle in a complex space. A total of six triangles of different shape but equal area can be constructed. This area is a parameter that measures the strength of CP violation in the SM [22]. Of particular interest are the triangles associated to the elements involved in the mixing of the B_d and B_s meson systems:

$$(b-d) \rightarrow V_{ud}V_{ub}^* + V_{cd}V_{cb}^* + V_{td}V_{tb}^* = 0, \tag{2.14}$$

$$(b-s) \rightarrow V_{us}V_{ub}^* + V_{cs}V_{cb}^* + V_{ts}V_{tb}^* = 0. \tag{2.15}$$

Dividing equation 2.14 by its first member and defining new parameters $\bar{\rho} \equiv \rho(1-\lambda^2/2)$ and $\bar{\eta} \equiv \eta(1-\lambda^2/2)$ yields

$$\bar{\rho} + i\bar{\eta} = -\frac{V_{ud}V_{ub}^*}{V_{cd}V_{cb}^*} \tag{2.16}$$

which leads to the triangle shown in Fig. 2.4. This triangle has similar sides, of order λ^3.

The following angles are defined:

$$\alpha = arg(-\frac{V_{td}V_{tb}^*}{V_{ud}V_{ub}^*}), \qquad \beta = arg(-\frac{V_{cd}V_{cb}^*}{V_{td}V_{tb}^*}), \qquad \gamma = arg(-\frac{V_{ud}V_{ub}^*}{V_{cd}V_{cb}^*}) \tag{2.17}$$

During the last decade, the task of B physics experiments, in particular "B factories" BaBar and Belle, has been measuring many observables in order to constrain the geometry of the unitarity triangle (UT). CKM fits use theory to convert experimental data to contours in the $\rho-\eta$ plane. In particular, branching ratios of semileptonic decays $b \rightarrow ul\bar{\nu}_l$ and $b \rightarrow cl\bar{\nu}_l$ and B meson mixing measure the sides of the triangle, that is, fix two circles centered in (0,0) and (1,0) in the complex plane. The indirect CP violation in neutral kaons is transformed into an hyperbola defined by the ε_K parameter (see [23] for a review of CP violation in neutral kaon). Measurements of CP violating observables (see Section 2.2.3) provide constraints to the angles of the UT. A successful example is the determination of the angle β from the study of CP violation in $B_d \rightarrow J\psi K_S$.

A departure from the unitarity relation expressed in this picture would mean that the CKM mechanism of the SM is not sufficient to explain flavour dynamics. For example, in the event of a hypothetical fourth generation of quarks, the three sides would not form a closed triangle. This could also lead to additional sources of CP violation apart from the single phase present in the CKM matrix. The current experimental picture of this unitary triangle is shown in Fig. 2.5, which confirms the CKM mechanism in the transitions of $b \to d$ quarks. However, more precise measurements of the angle γ are needed in order to over-constrain the triangle. This is one of the key objectives of the LHCb experiment.

In contrast to picture shown in Fig. 2.5, the triangle corresponding to eq. 2.15 has one side much smaller than the other two. This is the triangle linked to observables of the B_S system, which is yet to be precisely explored. In analogy to the previous definition in eq. 2.17, β_S is defined as

$$\beta_S = arg(-\frac{V_{ts}V_{tb}^*}{V_{cs}V_{cb}^*}) \tag{2.18}$$

In the Wolfestein parametrization $\beta_S \approx \eta\lambda^2$. β_S is currently poorly constrained experimentally and its measurement is another objective of the LHCb program (Section 2.3.3).

2.2 Prospects and probes for Physics beyond the Standard Model

This section discusses the limits of our current understanding and the challenges that appear today in Fundamental Physics. First, the frontiers of the SM are described. Secondly, the role of Flavour Physics as a laboratory to test SM extensions is discussed, followed by a brief introduction to the formalism commonly used in the field. This section ends with a description of CP violation in the context of B meson oscillations and decay, and the study of CP-violating observables, which would be affected by the presence of New Physics, and is one of the key objectives of the LHCb experiment.

2.2.1 Limitations of the SM

The SM summarizes our current understanding of most phenomena associated with elementary particles. Even if the SM has been extremely successful, in particular achieving the electroweak unification, there exist both experimental indications and theoretical considerations that leads us to believe that it can not be the final theory.

First, it does not incorporate gravity as one of the fundamental interactions, due to the lack of a successful quantum theory of gravitation. However, in the range of energies currently accessible in accelerators and cosmic rays, well below the Planck scale ($\sim 10^{19}$ GeV), gravity does not play any significant role.

Secondly, the fermion masses and the quark mixing parameters, which arise from the mass generating mechanism, are incorporated as free parameters of the theory. The SM does not explain mass hierarchies for quarks and leptons.

The SM does provide a mechanism for the origin of the masses of the constituent elements with the introduction of the Higgs auxiliary field. The quanta associated to this field have not yet been discovered, and its mass is not predicted by the theory. A fit of the direct searches at LEP excludes the existence of a Higgs boson with mass below 114.4 GeV at 95% CL [38], while a fit to the precise measurements of electroweak sector, such as W and top mass, sets an indirect upper limit at 186 GeV at 95% CL [38]. In order to accommodate these experimental limits within the theory, unnatural cancellations must occur to fix the Higgs mass in the order of the electroweak scale (set by the vacuum expectation value of the field, $v \sim 246$ GeV). This is often interpreted by considering that

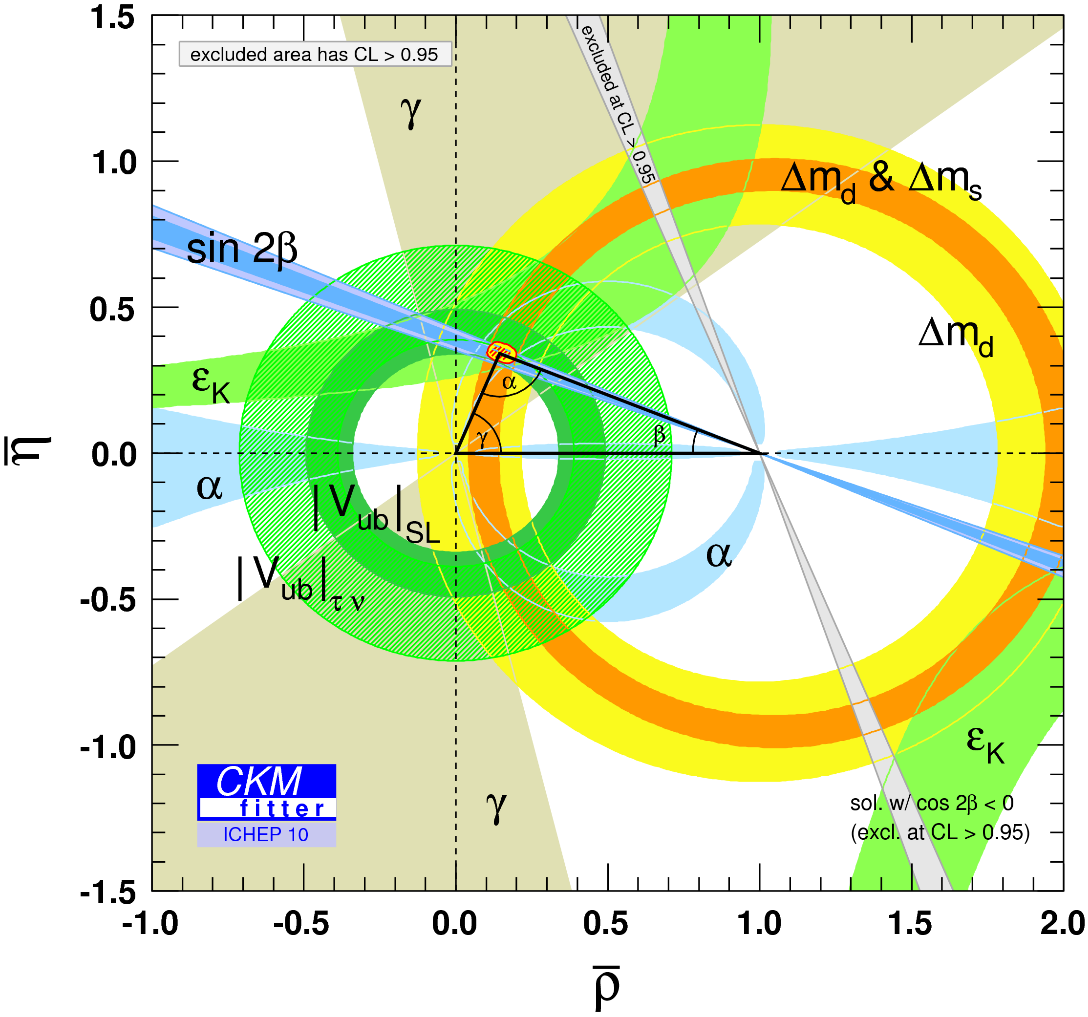

Figure 2.5: Current best fit for unitarity triangle for B_d system, from [24].

the SM is embedded in a more fundamental theory that accounts for the hierarchy between the electroweak and Planck scales. The validity of the SM as an effective theory up to the Planck scale is doubtful, with new physics expected to appear at the order or above the electroweak scale [38].

Supersymmetric (SUSY) extensions of the SM (see e.g. review [39]) provide a possible explanation to the fine-tunning problem of the Higgs mass. In these models, a new symmetry between fermionic and bosonic fields is invoked, assigning complex scalar bosonic fields for each fermion and fermionic fields for each boson. Fermions and bosons are grouped in supermultiplets and the new scalar fields couple to the Higgs. According to the spin-statistics theorem, these bosons have contributions of opposite sign with respect to fermions to the Higgs mass correction, producing the smallness of the Higgs mass. If this is the case, there must also exist a mechanism for supersymmetry breaking, as supersymmetric partners to SM particles have not been observed.

The Minimal Supersymmetric SM (MSSM) is the simplest extension of the SM to incorporate SUSY. In this model, the SM Higgs sector is enlarged to two Higgs fields that generate masses for the up and down quark families respectively. The electroweak symmetry breaking occurs when the two fields acquire vacuum expectation values v_u and v_d that verify

$$v_u^2 + v_d^2 = (246\ \text{GeV})^2, \tag{2.19}$$

with the ratio

$$\frac{v_u}{v_d} = \tan\beta \tag{2.20}$$

remaining as a free parameter.

Supersymmetric models also predict a distinct running for the coupling constants for the electromagnetic, weak and strong interactions, which are expected to converge at a certain energy scale (Grand Unification Theory [40]) as a manifestation of the origin of the gauge interactions in a common underlying symmetry. The SM does not predict this unification, in contrast with the MSSM (Fig. 2.6).

The SM also lacks an explanation to the nature of dark matter [41] and dark energy [42], which according to recent cosmological results, make up the vast majority of the known Universe [42]. SUSY models incorporate candidates for dark matter particles, known as weakly interacting massive particles (WIMPs) [41].

Finally, while the CKM mechanism of the SM describes correctly CP violation in the context of the weak interaction of quarks, as measured so far, it fails to account for the level of asymmetry needed in the process of baryogenesis [43], that led from a symmetric Big Bang to an asymmetric universe, dominated by matter over antimatter [44, 45]. This strongly suggests that additional sources of CP violation must be present. Evidence for neutrino masses and oscillations [46] could also imply that these new sources may appear in the lepton sector [47]. However, the SM does not even account for the neutrino mixing as there is no equivalent to the CKM matrix for the leptonic fields, due to neutrino masses being considered null in the SM. Models like the MSSM involve additional couplings and mixing parameters which could introduce new sources of CP violation [48].

2.2.2 Flavour Physics as a test for Standard Model extensions

Signatures of New Physics have two complementary sources: the direct observation of new particles and the measurement of indirect effects induced by virtual particles on sensitive

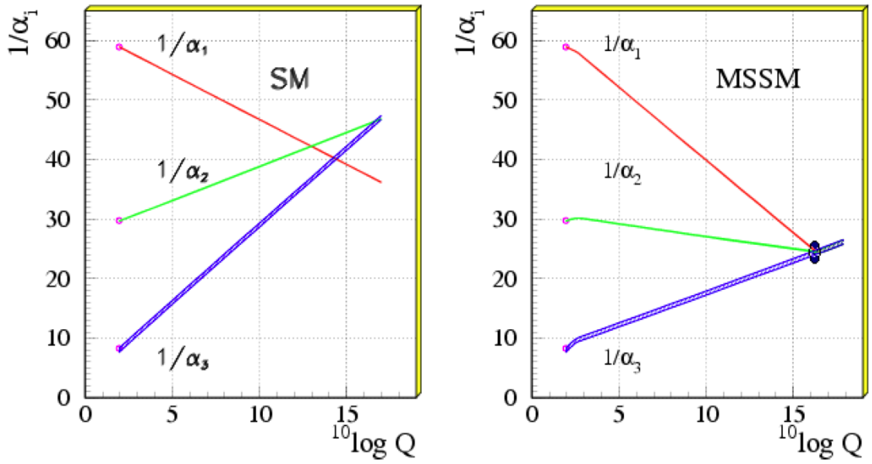

Figure 2.6: Evolution of the inverse of the coupling constants in the SM and the MSSM as a function of the energy scale. Only in the case of SUSY is unification achieved. Figure from [39].

observables. The construction of the SM profited from both approaches. Both methods are still valid to enhance our understanding of fundamental particles and interactions and to provide a test for the many models that have been proposed with the intention of solving the problems of the SM described in the previous section.

The first approach includes examples such as the search for supersymmetric particles or the Higgs boson at the general purpose experiments at the LHC (see Section 3.1.1). The second approach is based on the fact that the amplitude for a given process depends on all the virtual particles which contribute to it and their properties. The measurement of significant deviations from the SM predicted values for sensitive observables could be linked to the existence of new particles, as predicted in many models beyond the SM. The advantage of this approach is that studying new particles through their contribution to known processes rather than through their direct observation allows access to energy scales higher than the available energy. Some notorious precedents of this indirect method include:

- The observation of long lived particles, kaons (1947) [49] which decayed through weak processes. This led to the introduction of the strangeness quantum number and the flavour SU(3) quasi-symmetry [50] which was key to the development of the quark hypothesis in following decades.
- The suppression of some decay modes in neutral kaons ($K^0 \to \mu^+\mu^-$), explained as a consequence of the existence of an hypothetical partner to the strange quark. Charm quark was predicted and quark mixing established (GIM mechanism [16], 1970) before charm was directly observed [51, 52] (1974).
- The observation of neutral current effects such as the $\nu N \to \nu N$ scattering [53] (1973), before Z bosons were first produced at CERN [10] (1983).
- The proposal of a third generation of quarks [17] (1973) as a result of the small and unexpected CP symmetry violation observed in neutral kaon decays, before bottom [54] and top [55] quark were discovered (in 1977 and 1995 respectively).

- The prediction of a heavier top quark mass as a result of the unexpected observation of the B_d^0 mixing [56] (1987).

The b quark is the weak doublet partner of the heavy t quark. Hence, the weak decays of b-flavoured hadrons imply transitions through quark generations, which are CKM suppressed. In particular, transitions between b and d or s quarks are caused by flavour changing neutral currents (FCNC), forbidden at tree level in the SM. The time evolution and decay of b-flavoured hadrons are hence described at the lowest level by penguin and box diagrams, causing phenomena such as flavour oscillation and CP asymmetries and inducing many observables to be sensitive to New Physics.

B meson physics has been exploited by the B factories and this approach is continued by LHCb. In the case of the B_s^0 system, being the least constrained by data from B factories, these processes represent an ideal environment to look for sizable effects from New Physics. Examples of LHCb key measurements are given in Section 2.3.

Effective Hamiltonians and Operator Product Expansion

The Operator Product Expansion formalism (OPE, see [57]) is used to express the effective Hamiltonian describing transitions between b and d or s quarks in the form

$$H_{eff}^{b\to d(s)} = \frac{-4G_F}{\sqrt{2}} V_{tb}V_{td(s)}^* \sum_i (C_i O_i + C_i' O_i'), \tag{2.21}$$

where G_F is the Fermi coupling constant. The local operators $O_i^{(\prime)}$ govern the decay. They represent effective point-like vertices and connect initial and final state fields. Primed and unprimed operators are related by inverted handedness, the right handed part being suppressed in the SM. The Wilson Coefficients $C_i^{(\prime)}$ describe the strength with which a given operator enters the Hamiltonian (equivalent to coupling constants) and can be calculated perturbatively. They contain information about short distance physics, such as the masses of the particles entering the internal loops.

This formalism can be considered a generalization of the Fermi model for β decay [58], illustrated in Fig. 2.7. In this theory, the effective vertex originates from the degrees of freedom corresponding to the exchanged W boson being integrated out. In general, short range interactions involving the exchange of a heavy boson are replaced by point interactions. Due to the interplay of electroweak and strong interactions, the variety of operators (vertices) is much richer than in the Fermi model. Diagrams shown in Fig. 2.8 are examples of those typically found when describing FCNC processes within the SM. Operators in Eq. 2.21 originate from diagrams including those at tree level ($O_{1,2}$) and gluon (O_{3-6}), electroweak (O_{7-10}), scalar and pseudoscalar ($O_{S,P}$) penguin and box loops.

OPE formalism is particularly useful for the study of SM extensions. New operators, not found in the SM, could be introduced through new interactions or terms deriving from non-SM Lorentz structures such as couplings to pseudoscalar particles. New particles, such as charged Higgs bosons or supersymmetric partners found in SUSY models, could also contribute to loop terms which would modify the Wilson coefficients to existing operators. In both cases, changes in the effective Hamiltonian would translate into deviations from SM expectations of observables. Examples of this are discussed in Section 2.3.

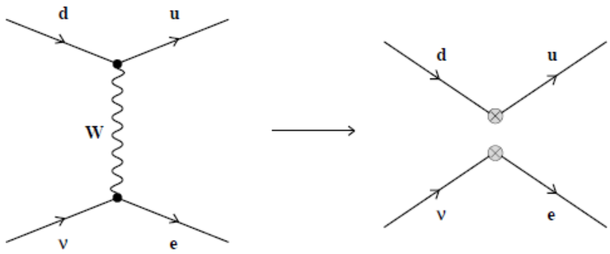

Figure 2.7: β decay at quark level in the elementary and effective (Fermi) theories.

2.2.3 New Physics constraints from CP violation

The CP transformation combines charge conjugation C, by which a particle is transformed to its antiparticle, with parity P, that changes the space coordinates $\vec{x} \to -\vec{x}$. For example, a left handed electron e^-_L is transformed into a right handed positron e^+_R. Phenomena mediated by the gravitational, electromagnetic and strong interactions are symmetric under both transformations and thus under the combined CP. On the other hand, weak interaction violates both C and P maximally [25, 26], as the W bosons only couple to e^-_L and e^+_R. CP was expected to be a symmetry until its violation was discovered in neutral kaon decays [27] in 1964. In 2001, CP violating effects were observed in the B_d system in the $B_d(\bar{B}_d) \to J/\psi K_S$ channel by the BaBar [28] and Belle [29] collaborations. This was the first observation of CP violation outside the kaon system, which was followed in 2004 by the detection of CP violation in the $B_d \to K^\pm\pi^\mp$, measured by Belle [30], Babar [31] and CDF [32]. CP violation has not yet been detected in B_s mesons.

The violation of the CP symmetry refers to the different probabilities for a particle and its antiparticle to undergo CP conjugated processes. The conservation of CPT, the combined transformation of CP symmetry and time reversal T, ensures that any CP violation effect must be produced by interfering amplitudes. For example, assuming there are two contributions to processes such as $M \to f$ and $\bar{M} \to \bar{f}$, then for each one the amplitude is $A = A_1 + A_2$ and $\bar{A} = \bar{A}_1 + \bar{A}_2$. While the phase for each component of the amplitude is arbitrary, the relative phase between them is not. Redefining the global phase for A_1 to be real, the amplitudes can be written as

$$\begin{aligned} A &= a_1 + a_2 e^{i\delta} e^{i\phi} \\ \bar{A} &= a_1 + a_2 e^{i\delta} e^{-i\phi}. \end{aligned} \tag{2.22}$$

The relative phase has been decomposed into two parts reflecting their different origins. The CP-odd phase ϕ originates from complex terms in the Lagrangian and in the SM it can only be produced by the weak interaction through the complex couplings of the $W^\pm$ bosons. For this reason, it is commonly referred to as weak phase. CP-even phase δ is generated by CP-invariant interactions, the dominant part being the strong interaction, and it is hence designated as the strong phase. The probability of the processes is then $\Gamma = AA^*$ and $\bar{\Gamma} = \bar{A}\bar{A}^*$. We can define the CP asymmetry as

$$A_{CP} = \frac{\bar{\Gamma} - \Gamma}{\bar{\Gamma} + \Gamma}, \tag{2.23}$$

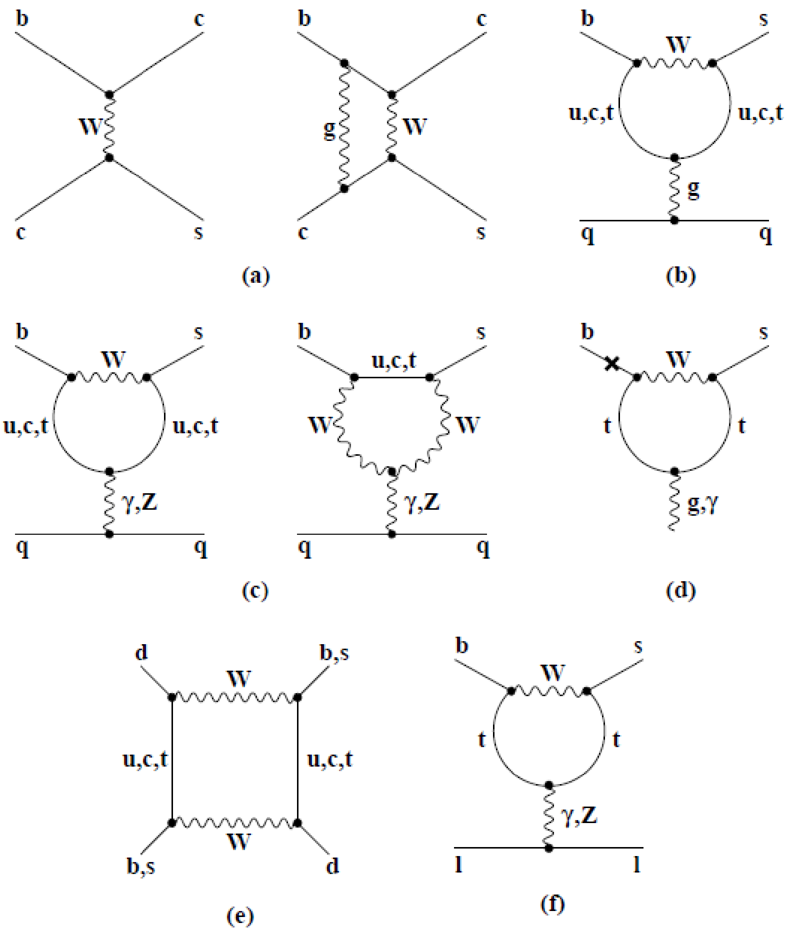

Figure 2.8: Examples of SM diagrams for FCNC transitions, figure from [57]

which results in

$$A_{CP} = \frac{2a_1 a_2 \sin\delta \sin\phi}{a_1^2 + a_2^2 + 2a_1 a_2 \cos\delta \cos\phi}, \tag{2.24}$$

clearly requiring the presence of two interfering amplitudes and both strong and weak types of phases to be non-zero. This is illustrated in Fig. 2.9, which shows that in these conditions $|A_1 + A_2| \neq |\bar{A}_1 + \bar{A}_2|$.

Time evolution of neutral meson systems

This section introduces the general formalism to describe CP violation in meson decay processes based on the reviews [23, 34]. Let us consider the decay amplitudes of a meson state M and its CP conjugated $\bar{M}$ to a final state f and its CP conjugated $\bar{f}$:

$$\begin{aligned} A_f &= \langle f | H_W | M \rangle \qquad \bar{A}_f = \langle f | H_W | \bar{M} \rangle \\ A_{\bar{f}} &= \langle \bar{f} | H_W | M \rangle \qquad \bar{A}_{\bar{f}} = \langle \bar{f} | H_W | \bar{M} \rangle \end{aligned} \tag{2.25}$$

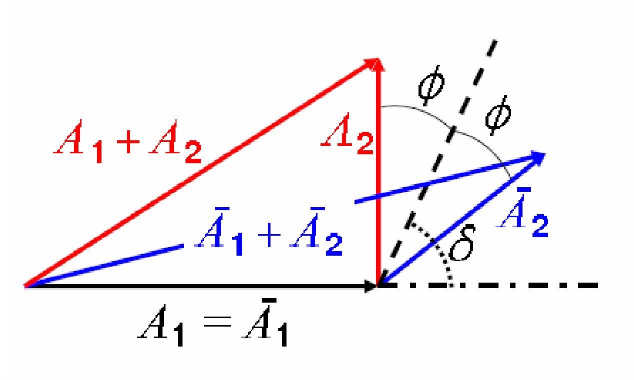

Figure 2.9: Interfering amplitudes producing CP violation. Figure from [33].

where H_W is the weak hamiltonian producing the decay. The effect of the CP operator is to interchange the states and to introduce additional phases:

$$\begin{aligned} CP\,|M\rangle &= e^{+i\xi_M}\,|\bar{M}\rangle \qquad CP\,|f\rangle = e^{+i\xi_f}\,|\bar{f}\rangle \\ CP\,|\bar{M}\rangle &= e^{-i\xi_M}\,|M\rangle \qquad CP\,|\bar{f}\rangle = e^{-i\xi_f}\,|f\rangle \end{aligned} \tag{2.26}$$

and of course $(CP)^2 = \mathbf{I}$. Phases ξ_M and ξ_f are arbitrary and if CP is conserved in the decay, amplitudes A_f and $\bar{A}_{\bar{f}}$ have the same magnitude, differing only in the phase ($\bar{A}_{\bar{f}} = e^{i(\xi_f - \xi_M)} A_f$).

In the case of neutral mesons (K, D, B_d and B_s) both mixing and decay processes occur, producing a variety of effects. A general case will be discussed here although the focus will be on B mesons. The time evolution of a superposition of neutral meson states $|M\rangle$ and $|\bar{M}\rangle$ is governed by the Schrodinger equation:

$$i\frac{\partial}{\partial t}\,|\psi(t)\rangle = (H_S + H_{EM} + H_W)\,|\psi(t)\rangle \tag{2.27}$$

where the total hamiltonian has been split into terms corresponding to strong, electromagnetic and weak interactions. The general solution is a time dependent wave function

$$|\psi(t)\rangle = a(t)\,|M\rangle + b(t)\,|\bar{M}\rangle + \sum_f c_f(t)\,|f\rangle \tag{2.28}$$

with $|f\rangle$ running on all final states accessible by weak decays. The unitarity condition for the hamiltonian implies that

$$|a(t)|^2 + |b(t)|^2 + \sum_f |c_f(t)|^2 = 1, \tag{2.29}$$

while initially $|a(0)|^2 + |b(0)|^2 = 1$. If all states $|M\rangle$, $|\bar{M}\rangle$ and $|f\rangle$ are eigenstates of $H_S + H_{EM}$, and H_W is treated as a perturbation, then an effective non-hermitian hamiltonian can be used to write the Schrodinger equation for $a(t)$ and $b(t)$ as

$$i\frac{\partial}{\partial t}\begin{pmatrix} a(t) \\ b(t) \end{pmatrix} = \mathbf{\Lambda}\begin{pmatrix} a(t) \\ b(t) \end{pmatrix}, \mathbf{\Lambda} = \mathbf{M} - \frac{\mathbf{i}}{\mathbf{2}}\mathbf{\Gamma} = \begin{pmatrix} M_{11} & M_{12} \\ M_{21} & M_{22} \end{pmatrix} - \frac{\mathbf{i}}{\mathbf{2}}\begin{pmatrix} \Gamma_{11} & \Gamma_{12} \\ \Gamma_{21} & \Gamma_{22} \end{pmatrix} \tag{2.30}$$

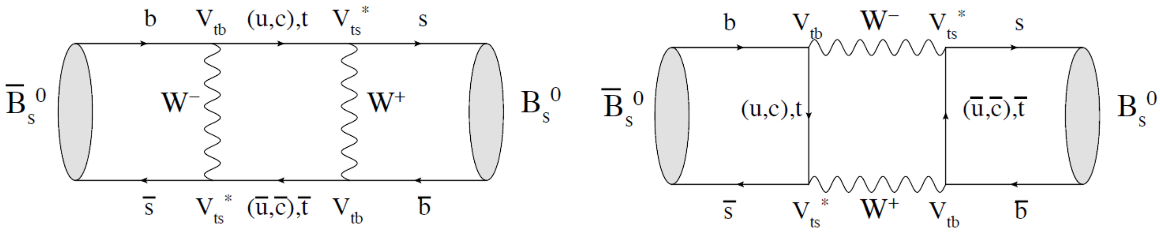

Figure 2.10: Dominant diagrams for B_s-$\bar{B}_s$ mixing in the SM.

The diagonal elements of $\mathbf{M}$ are

$$M_{11} = m + \langle M| H_W |M\rangle + \sum_f \frac{\langle M| H_W |f\rangle \langle f| H_W |M\rangle}{m - E_f}$$
$$M_{22} = m + \langle \bar{M}| H_W |\bar{M}\rangle + \sum_f \frac{\langle \bar{M}| H_W |f\rangle \langle f| H_W |\bar{M}\rangle}{m - E_f} \tag{2.31}$$

and in the case of $\mathbf{\Gamma}$

$$\Gamma_{11} = 2\pi \sum_f |\langle M| H_W |f\rangle|^2 \delta(m - E_f)$$
$$\Gamma_{22} = 2\pi \sum_f |\langle \bar{M}| H_W |f\rangle|^2 \delta(m - E_f), \tag{2.32}$$

with the values of m and E_f given by

$$(H_S + H_{EM})|M\rangle = m|M\rangle \quad (H_S + H_{EM})|f\rangle = E_f|f\rangle. \tag{2.33}$$

If CPT is a good symmetry, then $M_{11} = M_{22} \equiv M_0$ and $\Gamma_{11} = \Gamma_{22} \equiv \Gamma_0$, thus $\Lambda_{11} = \Lambda_{22} \equiv \Lambda_0$.

Off-diagonal terms for the $\mathbf{M}$ matrix are

$$M_{12} = \langle M| H_W |\bar{M}\rangle + \sum_f \frac{\langle M| H_W |f\rangle \langle f| H_W |\bar{M}\rangle}{m - E_f}, \tag{2.34}$$

while for $\mathbf{\Gamma}$

$$\Gamma_{12} = 2\pi \sum_f \langle M| H_W |f\rangle \langle f| H_W |\bar{M}\rangle \delta(m - E_f). \tag{2.35}$$

Final states $|f\rangle$ represents all those accessible to both M and $\bar{M}$ mesons, either off-shell (virtual states via dispersive transitions caused by $\mathbf{M}$ matrix) or on-shell (real states through absorptive transitions produced by $\mathbf{\Gamma}$ matrix). Figure 2.10 presents the main diagrams within the SM causing oscillations in the case of B_s mesons.

Since $M_{21} = M_{12}^*$ and $\Gamma_{21} = \Gamma_{12}^*$, matrices $\mathbf{M}$ and $\mathbf{\Gamma}$ are hermitian but the total hamiltonian $\mathbf{\Lambda}$ is not. Non hermiticity of the hamiltonian implies that $|a(t)|^2 + |b(t)^2|$ is not conserved, otherwise the mesons would oscillate but not decay.

Diagonalization of the hamiltonian leads to eigenstates $|M_H\rangle$ and $|M_L\rangle$, with well defined masses and decay widths represented by the real and imaginary parts of the eigenvalues $\lambda_\pm = \Lambda_0 \pm \sqrt{\Lambda_{12}\Lambda_{21}}$. They can be written in terms of the flavour eigenstates as

$$|M_H\rangle = p\,|M\rangle + q\,|\bar{M}\rangle \tag{2.36}$$
$$|M_L\rangle = p\,|M\rangle - q\,|\bar{M}\rangle\,, \tag{2.37}$$

with the condition $|p|^2 + |q|^2 = 1$. The difference in mass and decay widths are defined by

$$\Delta M = M_H - M_L, \qquad \Delta\Gamma = \Gamma_H - \Gamma_L, \tag{2.38}$$

with $\Delta M > 0$ by definition. The eigenvalues of $\mathbf{\Lambda}$ allow one to link measurable variables ΔM, $\Delta\Gamma$ and q/p to matrix elements M_{12} and Γ_{12} that can be calculated theoretically. In particular, the relation between q and p in terms of the eigenvalues is found to be

$$\left(\frac{q}{p}\right)^2 = \frac{M_{12}^* - i/2\Gamma_{12}^*}{M_{12} - i/2\Gamma_{12}}. \tag{2.39}$$

Eigenstates $|M_H\rangle$ and $|M_L\rangle$ have well defined masses and decay widths, but in general are not CP eigenstates. If a CP transformation is applied according to eq. 2.26, the condition for these states to be invariant is $|q/p| = 1$. In this case, mass eigenstates are also CP eigenstates and orthogonal ($\langle M_L|M_H\rangle = 0$, $|q|^2 - |p|^2 = 0$):

$$|M_H\rangle = |M_{CP}^{even}\rangle = \frac{1}{\sqrt{2}}(|M\rangle + e^{i\xi_M}\,|\bar{M}\rangle) \tag{2.40}$$
$$|M_L\rangle = |M_{CP}^{odd}\rangle = \frac{1}{\sqrt{2}}(|M\rangle - e^{i\xi_M}\,|\bar{M}\rangle). \tag{2.41}$$

In the SM, CP violation in mixing is small and the two mass eigenstates of B_d and B_s mesons are, to a good approximation, CP eigenstates.

Returning to eq. 2.28 and considering only the projection of $|\psi(t)\rangle$ on $|M\rangle$ and $|\bar{M}\rangle$, and under the initial condition $|\psi(0)\rangle = |M\rangle$ ($a(0) = 1$ and $b(0) = 0$), the evolution of the system follows the expression

$$|\psi(t)\rangle = f_+(t)\,|M\rangle + \frac{q}{p}f_-(t)\,|\bar{M}\rangle\,, \tag{2.42}$$

with the functions

$$f_\pm(t) = \frac{1}{2}(e^{-i\lambda_+ t} \pm e^{-i\lambda_- t}). \tag{2.43}$$

The probabilities for the system to remain in state $|M\rangle$ or having oscillated to $|\bar{M}\rangle$ at a time t are respectively

$$|\langle M|\psi(t)\rangle|^2 = |f_+(t)|^2 = \frac{1}{4}(e^{-\Gamma_H t} + e^{-\Gamma_L t} + 2e^{-\bar{\Gamma}t}cos\Delta Mt)$$
$$|\langle\bar{M}|\psi(t)\rangle|^2 = |\frac{q}{p}f_-(t)|^2 = \frac{1}{4}\left(\frac{q}{p}\right)^2(e^{-\Gamma_H t} + e^{-\Gamma_L t} - 2e^{-\bar{\Gamma}t}cos\Delta Mt), \tag{2.44}$$

with $\bar{\Gamma} = 1/2(\Gamma_H + \Gamma_L)$. The following parameters are useful to characterize the behaviour of neutral meson systems

$$x = \frac{\Delta M}{\bar{\Gamma}} \qquad y = \frac{\Delta\Gamma}{2\bar{\Gamma}}, \tag{2.45}$$

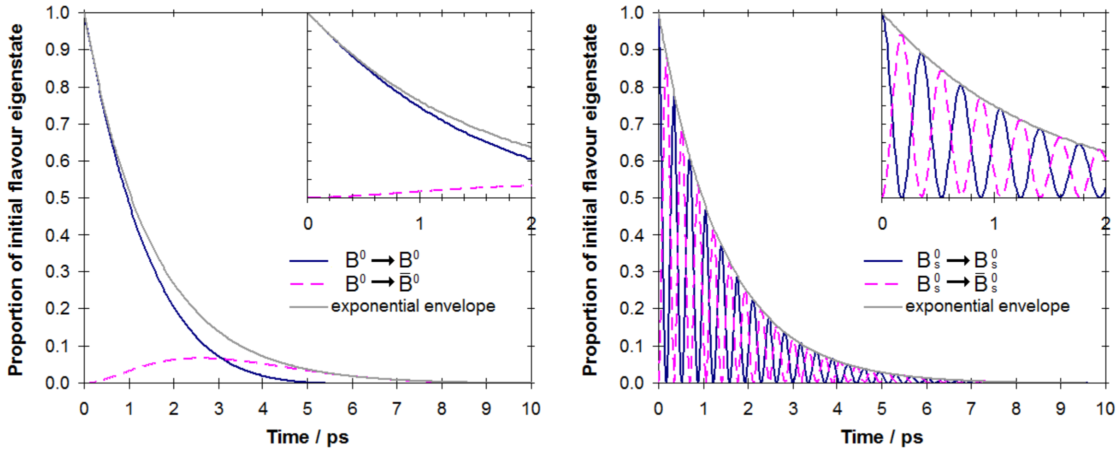

Figure 2.11: Oscillation and decay of neutral B mesons as described by equations 2.44: B_d^0 (left) and B_s^0 (right). Figure from [36].

as they compare mixing frequency and decay width splitting with the average lifetime. In the case of neutral B mesons [8]:

$$x_{B_d^0} = 0.774 \pm 0.008 \qquad x_{B_s^0} = 26.2 \pm 0.5. \tag{2.46}$$

The different evolution between both systems can be appreciated in Fig. 2.11, with the more rapid oscillations of the B_s^0 meson in spite of a similar lifetime.

The relative width splitting $\Delta\Gamma/\bar{\Gamma}$ is small in the case of B_d mesons, with a SM prediction of $\Delta\Gamma_d/\bar{\Gamma}_d \sim 0.2\%$ [35]. The situation is different for B_s, as the SM expectation for $\Delta\Gamma_s/\bar{\Gamma}_s$ is of order 10% [35], and for this reason, B_s meson lifetime needs to be carefully defined. One possible definition is $1/\bar{\Gamma}_s$, but in the case of flavour specific decays (see Section 2.2.3 for definition) such as semileptonic decays, lifetimes depend both on $\bar{\Gamma}_s$ and $\Delta\Gamma_s$.

Classification of CP violating effects

CP violation appears in the dynamics of B meson system in different processes which can be classified as:

- CP violation in the decay, observed if $|\bar{A}_{\bar{f}}/A_f| \neq 1$. This is the only possible source in the case of charged mesons. Some decay modes of neutral mesons are also affected and it has been observed by BaBar and Belle experiment and measured in the $B_d^0 \to K^+\pi^-$ decay mode. This decay has comparable contributions from both $b \to u$ tree level and $b \to s$ penguin diagrams, the interference between them resulting in direct CP violation.

- CP violation in mixing, which happens if $|q/p| \neq 1$, and can be observed in flavour specific decays of neutral mesons. If $B \to f$ and $\bar{B} \to \bar{f}$ are the allowed transitions, the decay $B \to \bar{f}$ can only proceed via intermediate oscillation $B \to \bar{B} \to \bar{f}$, and similarly for $\bar{B} \to f$. If there is no direct CP violation, then $|\bar{A}_{\bar{f}}/A_f| = 1$. In this case, any difference between the decay amplitudes for $B \to \bar{f}$ and $\bar{B} \to f$ must be

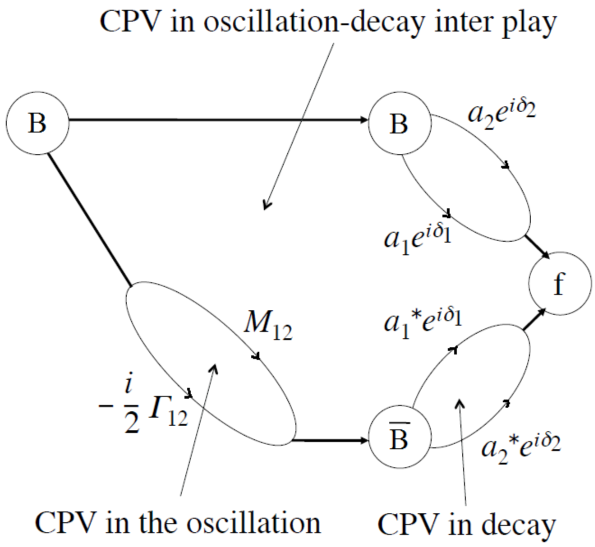

Figure 2.12: Different allowed transitions from a neutral meson initial state B to decay state f lead to diverse interfering amplitudes, which produce different types of CP violation. Figure redrawn from [34].

accounted for by the different rates of the $B \to \bar{B}$ and $\bar{B} \to B$ oscillations, which defines CP violation in mixing.

This effect is studied in semileptonic decays of neutral B mesons, caused in the SM by charged weak currents. W bosons link the lepton charge to the flavour of the decaying b quark ($B(d\bar{b}) \to l^+X$, and $\bar{B}(\bar{d}b) \to l^-X$). CP violation can be quantified here by the asymmetry in the "wrong-sign" decays (see Section 2.3.4), and is related to the mixing parameters p and q by

$$A_{SL} = \frac{\Gamma(\bar{B} \to \mu^+X) - \Gamma(B \to \mu^-X)}{\Gamma(\bar{B} \to \mu^+X) + \Gamma(B \to \mu^-X)} = \frac{1 - |q/p|^4}{1 + |q/p|^4}. \tag{2.47}$$

- CP violation in the interference between mixing and decay, which can be observed if final state f is both accessible through direct ($B \to f$) and mixing mediated ($B \to \bar{B} \to f$) decays (see Section 2.3.3). This is only possible for decay modes common to B and $\bar{B}$, in the case that

$$Im(\frac{q}{p}\frac{\bar{A}_f}{A_f}) \neq 0. \tag{2.48}$$

Figure 2.12 summarizes these phenomena. As previously discussed, interferences between amplitudes with non-zero relative weak and strong phases will produce CP violation effects. In the case of neutral mesons, different paths to a common final state may lead to CP violating effects being observed in the decay, oscillation or in the interference between mixing and decay.

New Physics in the mixing of neutral B mesons

The off-diagonal elements of the **M** and **Γ** matrices (eq. 2.34 and eq. 2.35) play a leading role in the discussion of mixing and CP violation. It is useful to write them as

$$M_{12} = |M_{12}|e^{i\phi_M} \qquad \Gamma_{12} = |\Gamma_{12}|e^{i\phi_\Gamma} \tag{2.49}$$

As described in previous section, both contribute to mixing and thus to the weak phase introduced in the process. However, the presence of New Physics affects them in different ways. As Γ_{12} includes terms generated by mixing through on-shell real states, it is dominated by light particle contributions. M_{12} however includes off-shell virtual states through loop processes and could get contributions from heavy particles such as those predicted by models including SUSY. Therefore, it is expected that if there is New Physics in B meson mixing, it would manifest itself in the mass matrix element. This can be parametrized in a model independent way with the introduction of a complex factor Δ (see for example [37]):

$$M_{12}^{tot} = M_{12}^{SM}\Delta_{d,s} = M_{12}^{SM}|\Delta_{d,s}|e^{i\phi_{d,s}^{\Delta}} \tag{2.50}$$

with different factors needed for B_d and B_s systems. The phase introduced is now $\phi_M = \phi_M^{SM} + \phi_{d,s}^{\Delta}$.

CP violating observables which can be used to measure New Physics contributions to B meson mixing include:

- The weak mixing phase defined by

$$\Phi \equiv -arg\left(\frac{q}{p}\frac{\bar{A}_f}{A_f}\right) \tag{2.51}$$

  that allows the extraction of New Physics phase through the interference between mixing and decay of B and $\bar{B}$ to a common final state f (see Section 2.3.3).

- The CP asymmetry in flavour specific semileptonic decays. In the case of both B_d and B_s mesons systems $|\Gamma_{12}/M_{12}| \ll 1$ and this observable can then be written as [23]

$$A_{SL} = \left|\frac{\Gamma_{12}}{M_{12}}\right| \sin(\phi_M - \phi_\Gamma), \tag{2.52}$$

  through which the weak phase is therefore accessible (discussed in Section 2.3.4).

The current experimental situation is displayed in Fig 2.13, which presents the constraints on the real and imaginary parts of the Δ factor for B_d and B_s respectively. Recent measurements at CDF and D0 of the B_s mixing phase in the channel $B_s \to J/\psi\phi$ and of a inclusive dimuon charge asymmetry at D0 suggest large contributions from New Physics (see Section 2.3.3 and 2.3.4). There is also a discrepancy of the measurements for B_d mixing phase with the SM hypothesis at the 2σ level.

2.3 Muonic B decays in LHCb

This section describes the relevance of several decay modes of B mesons for the LHCb indirect road [59] to discovery of New Physics. In the experimental conditions of proton-proton collisions at the LHC, decay processes of interest are diluted in QCD background.

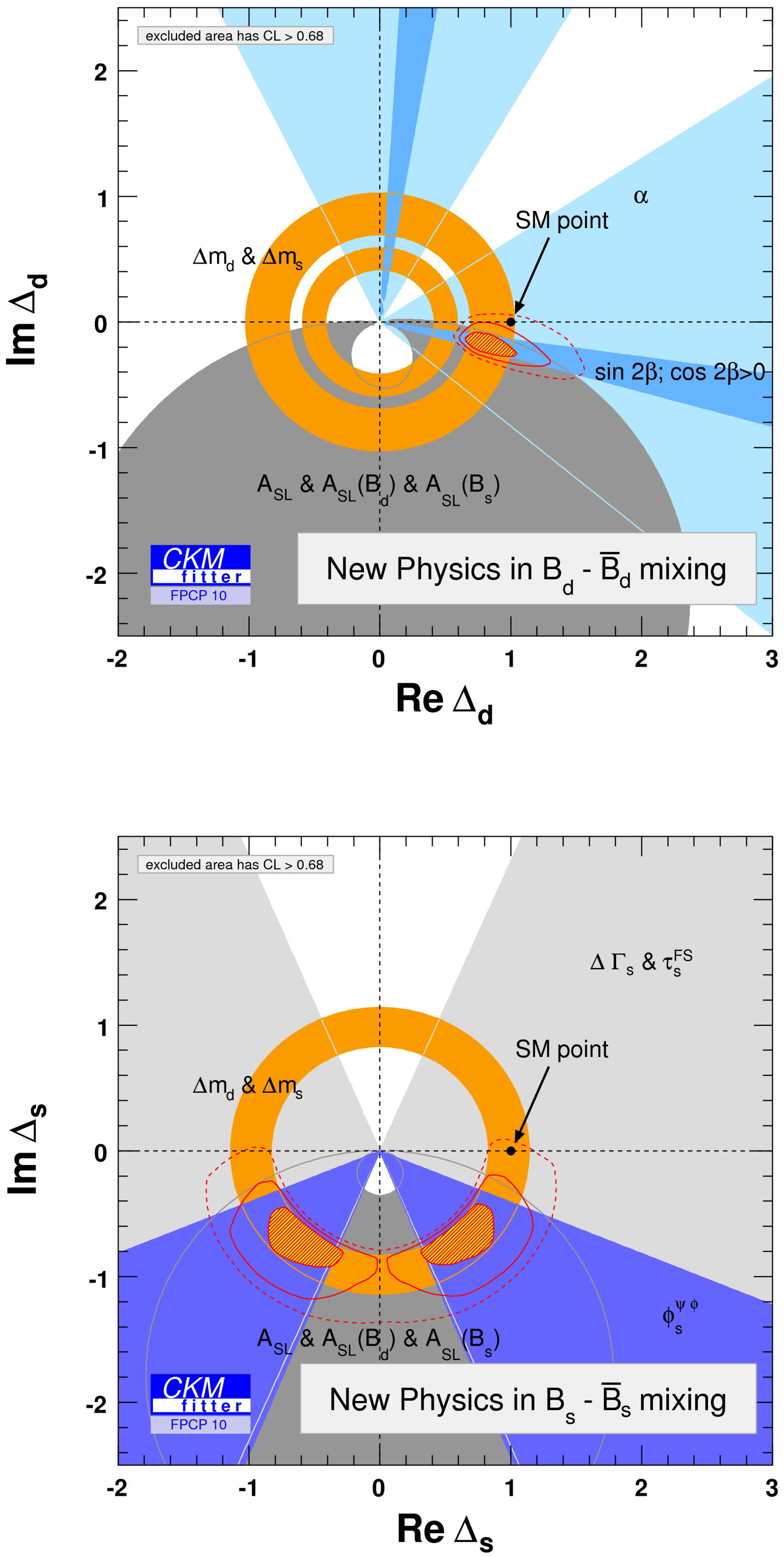

Figure 2.13: Experimental contraints to Δ_d and Δ_s parameters (see Eq. 2.50) for new physics in B_d and B_s mixing, indicating contours for σ, 2σ and 3σ uncertainties [24].

CP violating and rare decays present a wide range of branching ratios (10^{-2} to 10^{-6} or below). The later will also be masked by more probable B decays. The study of channels with muons as final products allows selections with the best background rejection. The relative low fraction of muons in the background means that they are a very helpful signature to identify signal candidates. The presence of muons is equally important at trigger level. Muon trigger algorithms have been designed to optimally select the decay modes discussed here, and the design, optimization and commissioning of these selections is the subject of this work.

The following subsections describe muonic decays of relevance for the LHCb physics programme. First, the two rare decays $B_s \to \mu^+\mu^-$ and $B_d \to K^*\mu^+\mu^-$, are introduced. The branching ratio of $B_s \to \mu^+\mu^-$ and the angular properties of $B_d \to K^*\mu^+\mu^-$ are expected to allow the discovery of New Physics or alternatively to provide constraints to New Physics models. Afterwards, the measurement of mixing-induced CP violation in the B meson sector at LHCb is described and this is used to show how semileptonic modes and $B_s \to J/\psi(\mu^+\mu^-)\phi$ can be used to explore the mixing asymmetries and constrain the phase ϕ_s. Other measurements of the LHCb program related to radiative or hadronic decays, such as the mentioned measurement of CKM angle γ, are discussed elsewhere [59].

2.3.1 $B_s \to \mu^+\mu^-$

The very rare decay $B_s \to \mu^+\mu^-$ may provide a decisive test on the contribution of the scalar sector to FCNC amplitudes. The lowest order contribution in the SM comes from the weak Z-penguin (see Fig. 2.14, left). The equivalent photon penguin is forbidden by C-parity conservation (as the final state is $J = 0$ and the initial state is a pseudoscalar meson) [60]. Electroweak box diagrams are suppressed by a factor M_W^2/m_t^2 with respect to the Z-penguin. Angular momentum conservation also produces the weak amplitude for pseudoscalar mesons decaying to lepton pairs to vanish in the limit of massless leptons, which introduces the additional factor $m_\mu^2/m_{B_s}^2$ to the decay rate (*helicity suppression*). The decay is also CKM suppressed by the element $|V_{ts}|^2$. The SM predicted [61] value for the branching ratio is thus very small, $\mathrm{BR}_{SM}(\mathrm{B}_s \to \mu^+\mu^-) = (3.2 \pm 0.2) \times 10^{-9}$. The current best limit is from CDF [62] (3.7 fb^{-1}) with BR$< 3.6 \times 10^{-8}$ at 90% C.L. This is still an order of magnitude above SM prediction and leaves room for the predictions of many New Physics models, which makes this decay very interesting for LHCb.

The SM electroweak loops described before contribute to the coefficient for the effective operator

$$O_A = \bar{b}_L \gamma^\alpha s_L \bar{\mu} \gamma_\alpha \gamma_5 \mu. \tag{2.53}$$

The helicity suppression makes $B_s \to \mu^+\mu^-$ a very sensitive probe for models with an extended Higgs sector. New scalar or pseudoscalar interactions would modify the coefficient for operators

$$O_S = m_b \bar{b}_R s_L \bar{\mu}\mu, \qquad O_P = m_b \bar{b}_R s_L \bar{\mu}\gamma_5\mu, \tag{2.54}$$

which are terms of negligible contribution in the SM. The effective hamiltonian can be written as

$$H^{eff}_{B_s\to\mu^+\mu^-} \propto V_{tb}^* V_{ts} \sum_{i=A,S,P} (C_i O_i + C_i' O_i') + (h.c.), \tag{2.55}$$

with primed operators indicating opposite chiralities for the quark currents. The decay amplitude can be significantly modified by these new terms in the hamiltonian. Enhancements in the decay rate are expected in several New Physics models, although some predict also suppression due to destructive interferences. In the MSSM, contributions from scalar penguins (Fig. 2.14, right) make the BR strongly dependent on $\tan\beta$ (the ratio of vacuum expectation values of the two neutral Higgs fields) in Eq. 2.20 [60]:

$$BR(B_s \to \mu^+\mu^-)_{MSSM} \propto \tan^6\beta. \tag{2.56}$$

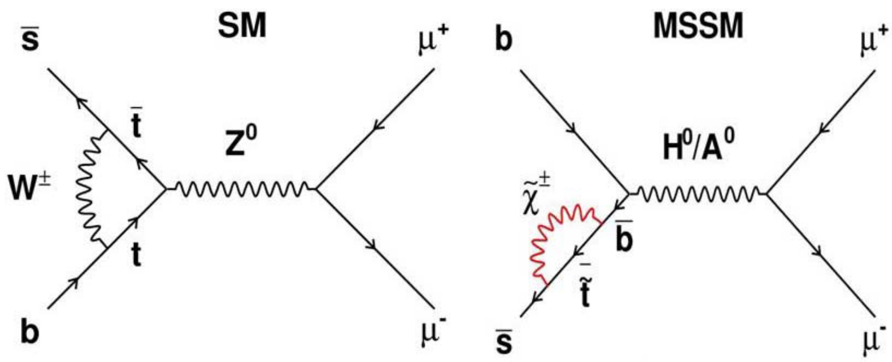

Figure 2.14: Examples of diagrams contributing to $B_s \to \mu^+\mu^-$: SM electroweak penguin (left) and possible scalar penguin in the MSSM (right). Figure from [59].

The strategy to search for this decay in LHCb [59] is based on an initial selection followed by the classification of events according to their likelihood of being signal or background built from three uncorrelated quantities: the invariant mass, the muon identification likelihood and the geometrical likelihood (GL). Several control channels have been selected to validate the method (e.g. $J/\psi \to \mu^+\mu^-$ for muon identification and trigger). The BR is extracted using normalization channels with well known BRs, such as $B_d^0 \to K\pi$ and $B^+ \to J/\psi K^+$, and for each case it can be written:

$$BR(B_s \to \mu^+\mu^-) = BR(Norm) \times \frac{N_{B_s\to\mu^+\mu^-}}{N_{Norm}} \times \frac{\epsilon_{Norm}(trig, rec, sel)}{\epsilon_{B_s\to\mu^+\mu^-}(trig, rec, sel)} \times \frac{f_{Bnorm}}{f_s}, \tag{2.57}$$

where the factors correspond to the number of observed events, the trigger, reconstruction and selection efficiencies (which, by the use of appropriate normalization channels, can be kept close to unity), and the ratio of hadronization fractions. The main systematic uncertainty affecting the measurement arises from the poorly measured f_d/f_s (with a relative uncertainty of $\sim$13%). A new method to measure this ratio at LHCb with improved resolution has been proposed [63].

As explained in the following chapters, the high B meson production rates at the LHC and the excellent vertexing, mass resolution and muon identification capabilities of the detector, make LHCb an ideal experiment to look for this decay. Already with about 37 pb^{-1} of integrated luminosity from the 2010 run, LHCb has reached sensitivities comparable to previous Tevatron limits with the results [64]

$$BR(B_s \to \mu^+\mu^-) < 4.3 \times 10^{-8}(90\%\, C.L.). \tag{2.58}$$

Figure 2.15 shows the promising LHCb potential. With the collisions expected to be provided by the LHC in 2011, the range of BRs down to 10^{-9} is to be explored in the near future.

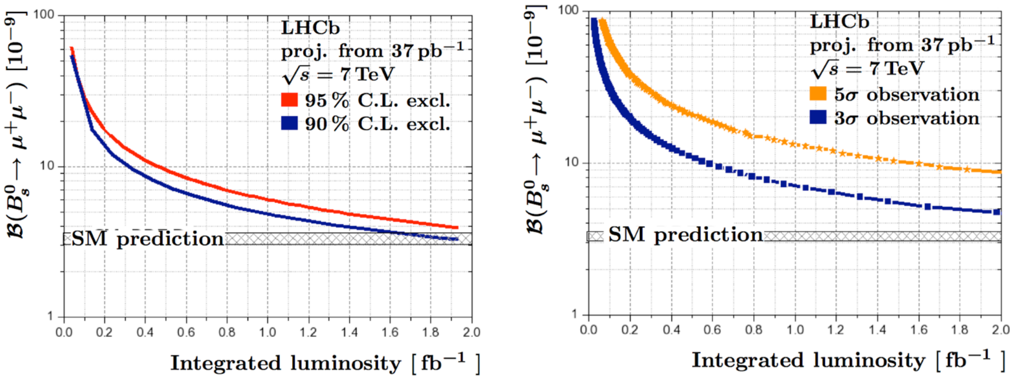

Figure 2.15: Expected sensitivity for the measurement of BR($B_s \to \mu^+\mu^-$) at LHCb: exclusion limit (left) and 3σ and 5σ observation (right) as a function of integrated luminosity.

Apart from $B_s \to \mu^+\mu^-$, other $B_q \to l^+l^-$ decay modes, with $q = d, s$ and $l = e, \mu, \tau$, are equally important. The decay $B_d \to \mu^+\mu^-$ is also accessible to LHCb, although its BR is expected to be one order of magnitude lower with respect to that of $B_s \to \mu^+\mu^-$, due to additional CKM suppression from V_{td}, which makes background rejection harder. Decays to electrons suffer from higher helicity suppression, due to the light electron mass, and the experimental reconstruction of electron momenta is complicated by photon radiation. $B_q \to \tau^+\tau^-$ decays are complicated by τ decays, with missing momenta from neutrinos or hadronic decay products, harder to identify compared to muon pairs.

2.3.2 $B_d \to K^*\mu^+\mu^-$

The rare decay $B_d \to K^*\mu^+\mu^-$ is another FCNC process, which in the SM occurs via electroweak penguin loops (Fig 2.16). As already discussed, this leads to small branching ratios $O(10^{-6})$ and high sensitivity to contributions from physics beyond the SM.

The angular distribution in the $B_d \to K^*\mu^+\mu^-$ decay is a source of observables sensitive to NP [65]. This decay can be completely described by the kinematic variables q^2 (invariant mass of the dimuon pair) and the three angles θ_L, θ_K and ϕ (described in Fig 2.17).

LHCb will first focus on the measurement of the forward-backward asymmetry $A_{FB}(q^2)$ (see [59, 66]). This theoretically clean observable is defined by the number of positive (negative) muons emitted from the decay of the B_d ($\bar{B}_d$) meson in forward or backward direction defined by θ_L in the rest frame of the dimuon system:

$$A_{FB}(q^2) = \frac{\int_0^{\pi/2} \frac{\partial^2\Gamma}{\partial q^2 \partial\theta_L} d\theta_L - \int_{\pi/2}^{\pi} \frac{\partial^2\Gamma}{\partial q^2 \partial\theta_L} d\theta_L}{\int_0^{\pi/2} \frac{\partial^2\Gamma}{\partial q^2 \partial\theta_L} d\theta_L + \int_{\pi/2}^{\pi} \frac{\partial^2\Gamma}{\partial q^2 \partial\theta_L} d\theta_L}. \tag{2.59}$$

This asymmetry is a function of the invariant mass of the muon pair. The most sensitive region ($1 < q^2 < 6$ GeV^2) is that where this asymmetry can be predicted precisely [67]. This function has a zero-crossing point ($q_0^2/A_{FB}(q^2) = 0$), and dominant theoretical uncertainties cancel in the determination of its position. The value is predicted in SM [68] as $4.36^{+0.33}_{-0.31}$ GeV^2.

Measurement of A_{FB} in the mentioned range and in particular at the zero-crossing point is sensitive to the interference between the contributions to the decay amplitude

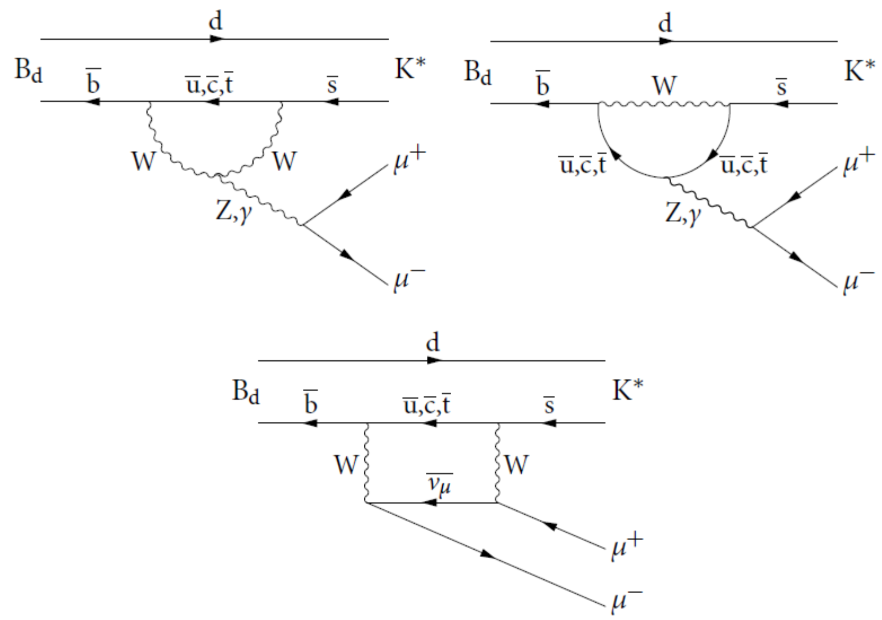

Figure 2.16: SM diagrams for the $\mathrm{B}_d \to K^*\mu^+\mu^-$ decay. Figure from [59].

from photon, vector and axial vector electroweak loop terms. It is therefore sensitive to effects from new physics, which would translate into the modification of the Wilson coefficients (C_7, C_9 and C_{10} [59]) associated to these effective vertices. Figure 2.18 shows A_{FB} prediction in the SM and and a variety of SUSY models.

Experimentally, the uncertainty on this measurement at B factories is still dominated by the small amount of data available. The expected sensitivity at LHCb is discussed in [66] and [69]. In the sensitive bin, and assuming Belle central value, with 1 fb^{-1}, LHCb will get statistical precision enough to exclude the SM A_{FB} average value by 4σ (Fig 2.19).

2.3.3 $B_s \to J/\psi(\mu^+\mu^-)\phi$

This decay is considered the "golden" mode for the extraction of the CP violating phase ϕ_s at LHCb. The decay amplitude is the result of the interference between direct decay and decay after oscillation of the B_s meson. The analysis is analogous to the extraction of the β CKM angle from the mixing and decay of $B_d \to J/\psi K_S$. The SM diagrams contributing to the decay are shown in Fig. 2.20. The tree diagram is dominant and introduces the weak phase $\phi_D = arg(V_{cs}V_{cb}^*)$. Before decaying, the meson can oscillate (according to Fig. 2.10 in the SM), adding the additional phase $\phi_M = 2 \cdot arg(V_{ts}V_{tb}^*)$. The weak phase difference between the interfering amplitudes is therefore $\phi_M - 2\phi_D$, hence, in the SM, the CP violating phase ϕ_s equals $-2\beta_s$, the smallest angle in the b-s unitarity triangle defined in eq. 2.18. This allows ϕ_s to be indirectly determined via global fits of the unitarity triangle to experimental data. The predicted value of this phase, which in the SM is one of the CP observables with smallest theoretical uncertainty, is [24]

$$\phi_s^{SM} = -2\beta_s = -0.036 \pm 0.002\, rad. \tag{2.60}$$

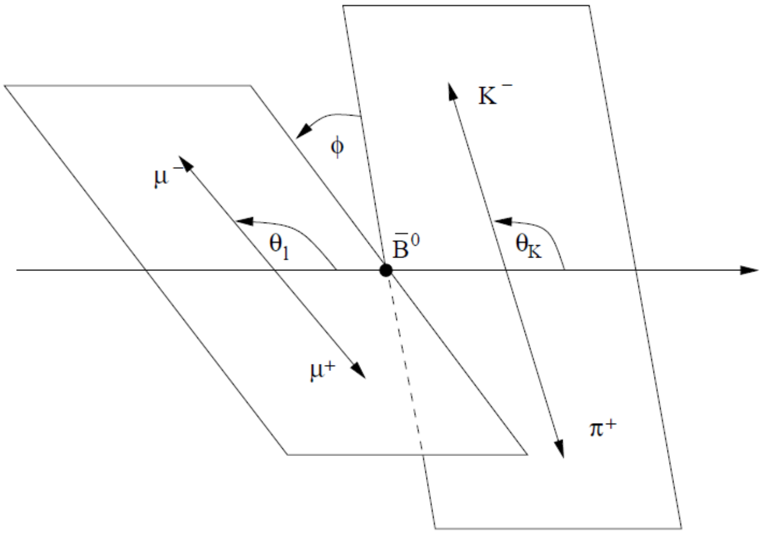

Figure 2.17: Definition of kinematic variables in the decay $B_d \to K^*\mu^+\mu^-$: The z-axis is the direction in which the $\bar{B}$ meson flies in the rest frame of $\mu^+\mu^-$. θ_l is the angle between the μ^- and the z-axis in the $\mu^+\mu^-$ rest frame, θ_K is the angle between the K$^-$ and the z-axis in the K* rest frame, and ϕ is the angle between the normals to the $\mu^+\mu^-$ and Kπ decay planes in the $\bar{B}$ rest frame. In the case of the B meson, the angles are defined relative to the μ^+ and the K$^+$. Figure from [59].

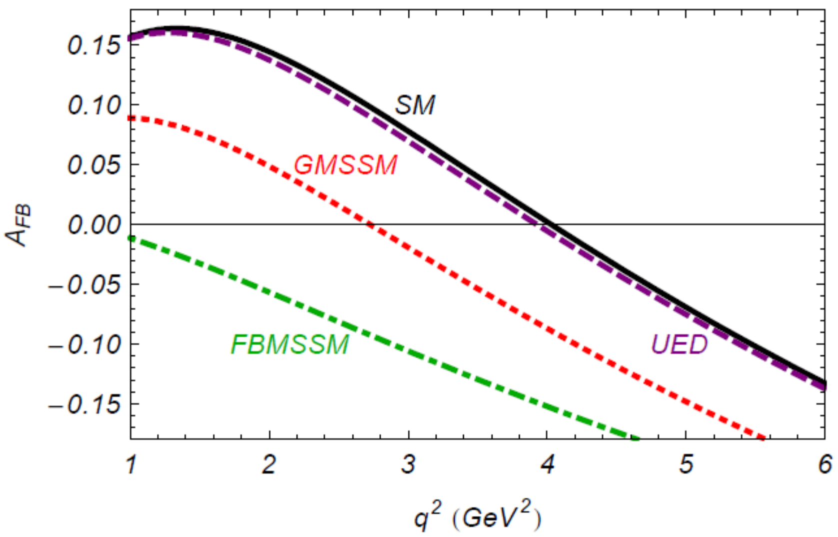

Figure 2.18: Theoretical A_{FB} curves as a function of q^2 for $B_d \to K^*\mu^+\mu^-$ in the SM and three models for New Physics. The solid lines give the SM prediction. The dashed lines show predictions from a universal extra dimensions (UED) model, a non-minimal flavour violating supersymmetric model (GMSSM) and a flavour blind supersymmetric model (FBMSSM) [59].

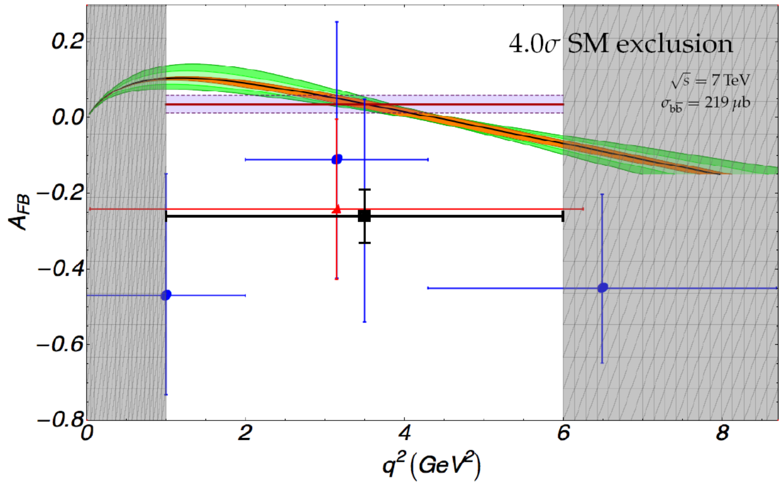

Figure 2.19: Expected sensitivity for the measurement of $A_{FB}(q^2)$ in $B_d \to K^*\mu^+\mu^-$ at LHCb with 1 fb^{-1} (black square) compared to current BaBar (red triangle) and Belle (blue circles) results and SM prediction and average in the $1 < q^2 < 6$ GeV^2 (colored bands show theoretical uncertainties). Figure from [69].

As the decay is a tree level process, the weak phase in the decay amplitude is expected to be dominated by the SM. However, the mixing phase, arising from the box diagrams, could be affected by New Physics contributions. The small theoretical uncertainty of the SM expectation for ϕ_s would allow a precise measurement to be discriminant and interpret deviations as a sign of New Physics. This measurement is hence one of the key elements in the indirect search for physics beyond the SM at LHCb.

The final states in $B_s \to J/\psi\phi$ decays are CP eigenstates, that is $CP\,|f\rangle = \eta_f\,|f\rangle$. The CP eigenvalue of the final state appears in the definition of λ_f as

$$\lambda_f = \frac{q}{p}\frac{\bar{A}_f}{A_f} = \eta_f e^{i(2\phi_D - \phi_M)}. \tag{2.61}$$

This allows the weak phase to be written as in eq. 2.51

$$\phi_s = -arg(\lambda_f). \tag{2.62}$$

If CP violation is negligible both in the decay ($|\bar{A}_f/A_f| = 1$) and the mixing ($|q/p| = 1$), then the decay rates can be written [59]

$$\begin{aligned}\Gamma(B_s(\bar{B}_s) \to f) \propto |A_f|^2 e^{-\bar{\Gamma}_s t}[&\cosh(\Delta\Gamma_s t/2) - Re(\lambda_f)\sinh(\Delta\Gamma_s t/2) \\ &-(+)Im(\lambda_f)\sin(\Delta m_s t)].\end{aligned} \tag{2.63}$$

Considering that $Im(\lambda_f) = \eta_f \sin\phi_s$ the phase ϕ_s can be measured from the time-dependent asymmetry between the decay rates of the B_s and $\bar{B}_s$ mesons. Equation 2.23 can in this case be written

$$A_{CP}(t) = \frac{\eta_f \sin\phi_s \sin\Delta m_s t}{\cosh\Delta\Gamma_s t/2 - \eta_f \cos\phi_s \sinh\Delta\Gamma_s t/2}. \tag{2.64}$$

The decay $B_s \to J/\psi\phi$ is a pseudoscalar to vector-vector process. Conservation of angular momentum allows relative orbital angular momentum between vector mesons with

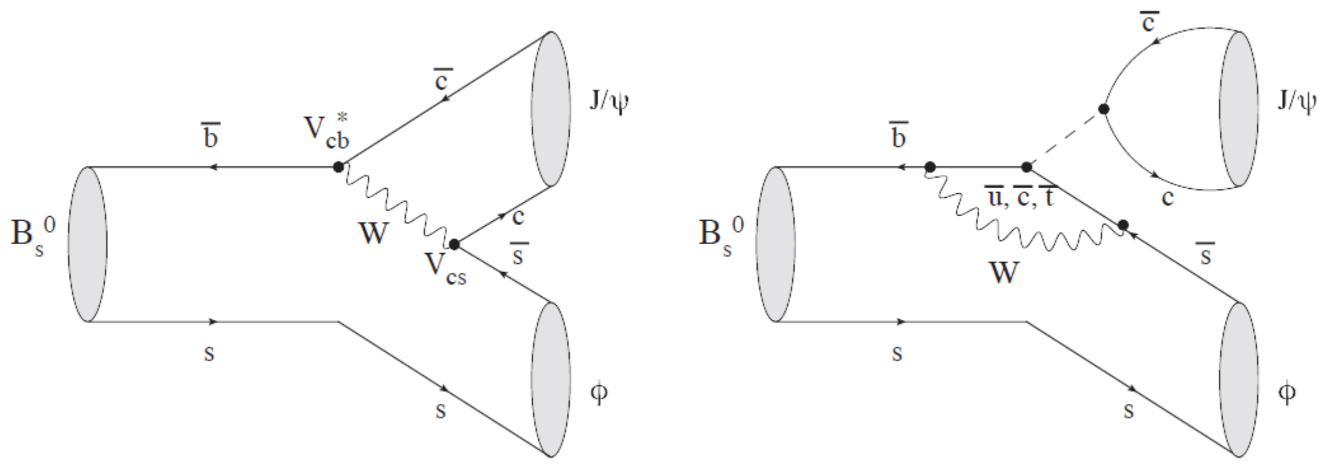

Figure 2.20: SM diagrams contributing to $B_s \to J/\psi\phi$ decays: tree (left) and penguin (right). Figure from [59].

values $l = 0, 1, 2$. The CP eigenvalue depends on l, and so the final state is a superposition of the three possible states, with CP-even ($l = 0, 2$) and CP-odd ($l = 1$) components. For this reason the analysis of this decay is more complex than the case of $B_d \to J/\psi K_S$, where only the CP-odd ($l = 1$) component is present (pseudoscalar to vector-pseudoscalar decay). An angular analysis is required to separate statistically the CP-odd and CP-even contributions. In the SM, $\cos\phi_s \approx 1$ and angular information separates mass eigenstates. Γ_L and Γ_H can be determined from the CP-even the CP-odd components respectively and thus $\Delta\Gamma_s$ can be simultaneously measured. The value of $\sin\phi_s$ acts as an amplitude to the flavour oscillation function $\sin\Delta m_s t$. As this terms have opposite signs for B_s and $\bar{B}_s$, flavour tagging is required to identify the flavour of the initial B_s meson and avoid cancellation of the ϕ_s information.

Figure 2.21 presents the latest results from CDF on B_s mixing phase, obtained with a $5.2 fb^{-1}$ data sample [70]. CDF results are displayed as contours in the β_s and $\Delta\Gamma$ plane (with $-2\beta_s = \phi_s$ and $\Delta\Gamma = \Delta\Gamma_s$ in their notation). The confidence interval quoted for β_s is [0.02,0.52] U [1.08,1.55] at the 68% C.L.

First results for ϕ_s and $\Delta\Gamma_s$ from data taken by LHCb during the 2010 run are shown in Fig. 2.22 [71]. Projected in ϕ_s axis LHCb measures $\phi_s \in [-2.7, -0.5]$ rad at 68% C.L. Extrapolating the current performance to 2011 data, a world best measurement can be expected.

2.3.4 $B_{d/s} \to X\mu\nu$

The D0 collaboration has published a possible evidence for NP from the measured charge asymmetry on semileptonic decays [72]. This is interpreted as a manifestation of CP violation in B mixing followed by flavour specific decays (introduced in Section 2.2.3).

In the SM, elements M_{12} and Γ_{12} can be calculated from the dispersive and absorptive parts of the box diagrams associated with B meson mixing (displayed in Fig 2.10 for the

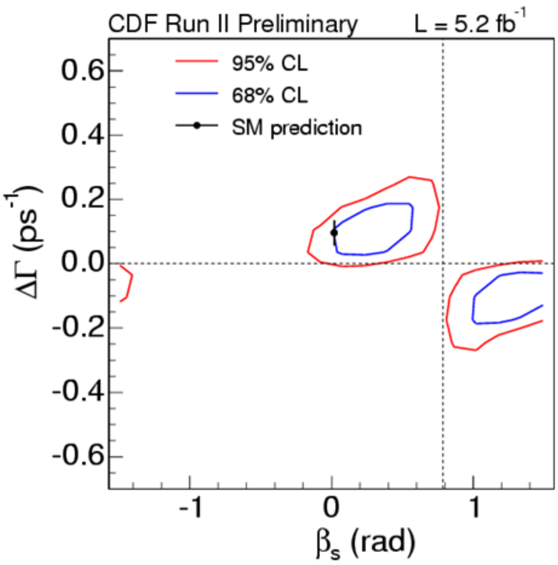

Figure 2.21: 68% and 95% confidence contours in the ϕ_s-$\Delta\Gamma_s$ plane determined by CDF for $5.2 fb^{-1}$, displaying point for SM values [70].

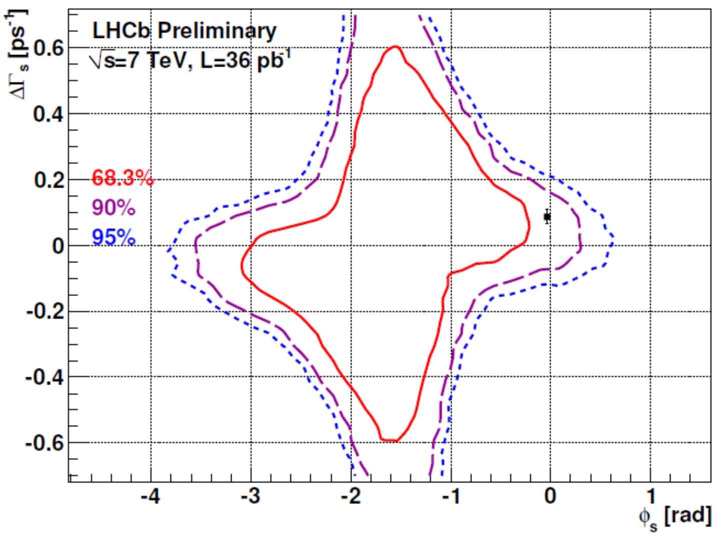

Figure 2.22: Confidence contours in the ϕ_s-$\Delta\Gamma_s$ plane as measured by LHCb with 2010 data. The point corresponds to SM expectations.

case of B_s). The ratio Γ_{12}/M_{12} can be probed with the *wrong* charge muon asymmetry

$$a_{SL}^q = \frac{\Gamma(\bar{B}_q \to \mu^+ X) - \Gamma(B_q \to \mu^- X)}{\Gamma(\bar{B}_q \to \mu^+ X) + \Gamma(B_q \to \mu^- X)} \approx \left|\frac{\Gamma_{12}^q}{M_{12}^q}\right| \sin(\phi_M^q - \phi_\Gamma^q) = \frac{\Delta\Gamma_q}{\Delta M_q} \tan(\phi_M^q - \phi_\Gamma^q), \tag{2.65}$$

with the index $q = d, s$ distinguishing B_d and B_s cases. The ratio Γ_{12}/M_{12} is suppressed and expected to be $O(m_b^2/m_t^2)$ and $\sin(\phi_M - \phi_\Gamma) \propto m_c^2/m_b^2$ so that $a_{SL}^{d,s}$ is suppressed by m_c^2/m_t^2 [73] which is $O(10^{-4})$. CP violation in B mesons mixing is thus expected to be tiny in the SM.

The measurement of a_{SL}^q is complicated by the need of flavour tagging to correctly select decays of *wrong* sign muons from the sample of semileptonic decays of b flavoured hadrons which reduces experimental sensitivity. What the D0 collaboration measured was instead the inclusive like-sign dimuon charge asymmetry for direct semileptonic $b \to \mu X$ decays, defined as

$$A_{SL}^b = \frac{N_b^{++} - N_b^{--}}{N_b^{++} + N_b^{--}}, \tag{2.66}$$

where N_b^{++} and N_b^{--} are the numbers of events containing two b hadrons decaying semileptonically and producing two positive or negative muons. This parameter A_{SL}^b is a function of both a_{SL}^d and a_{SL}^s and the hadronization fractions f_d and f_s. The relation is approximately found to be [72]

$$A_{SL}^b \approx \frac{a_{SL}^d + a_{SL}^s}{2}, \tag{2.67}$$

with a predicted value in the SM [72] of

$$A_{SL}^b = (-2.3^{+0.5}_{-0.6}) \times 10^{-4}. \tag{2.68}$$

The value measured by D0 is $A_{SL}^b = (-0.96 \pm 0.25 \pm 0.15)\%$, a result that differs by 3.2 standard deviations from the SM prediction (see Fig. 2.23).

At the LHC, the abundant B hadron production together with the high branching fractions make semileptonic (muonic) decays a source for a number of observables, including measurements of the $b\bar{b}$ production cross section [74] and of the CKM element V_{ub}, and a competitive and complementary measurement of the *wrong* charge muon asymmetry. To perform such a measurement at LHCb, a careful control of all asymmetries producing systematic effects is needed. These include background asymmetry, detector acceptance asymmetry and production asymmetry, the later due to the fact that the LHC is a proton-proton (and not a proton-antiproton) collider. Detection asymmetry can be controlled by regularly inversing the polarity of the LHCb dipole magnet. However, the production asymmetry is hard to control, introducing an expected systematic uncertainty greater than the effect intended to be measured.

To solve this problem, LHCb will use a novel time-dependent technique [36] that will allow the accurate measurement of the parameter

$$\Delta A_{SL} = \frac{a_{SL}^s - a_{SL}^d}{2}. \tag{2.69}$$

The expected sensitivities with 0.1 and 1 fb^{-1} are $\sigma(\Delta A_{SL}) = 5 \times 10^{-3}$ and 2×10^{-3}. This measurement is thus complementary to that of D0 and is expected to contribute to consolidate or dilute the tension between D0 observation and SM expectation (Fig. 2.24).

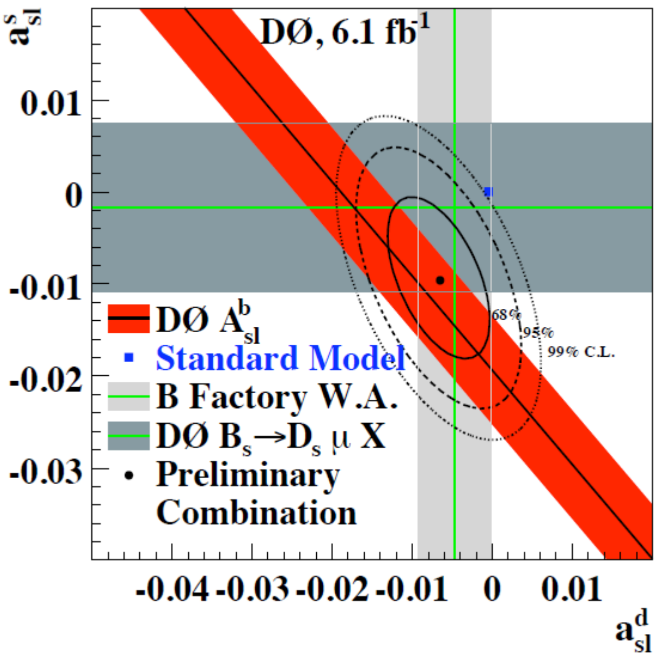

Figure 2.23: Mixing induced charge asymmetry $(a^d_{SL} + a^s_{SL})/2$ in semileptonic decays measured by D0, and results for a^d_{SL} averaged from Belle and BaBar measurements and a^s_{SL} at D0. Blue dot indicates SM prediction. Figure from [72].

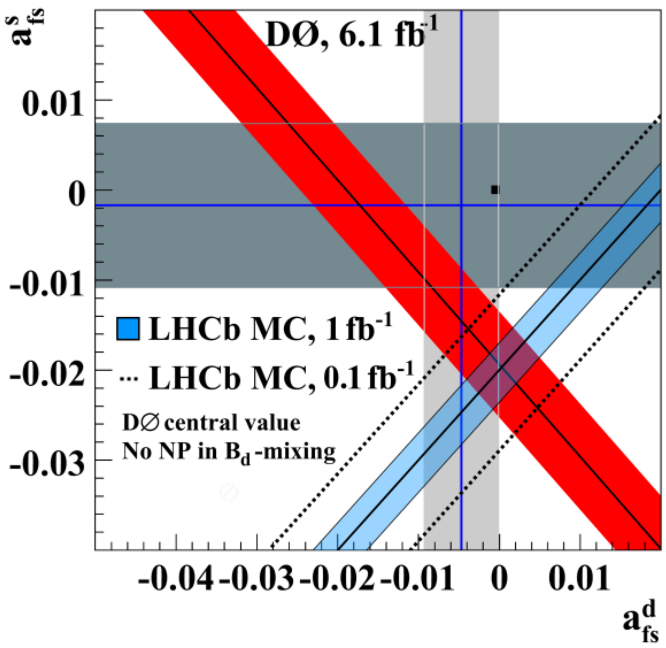

Figure 2.24: Expected sensitivity for mixing induced asymmetry in semileptonic decays parametrized by $\Delta A_{SL} = (a^s_{SL} - a^d_{SL})/2$ measured at LHCb for 0.1 and 1 fb^{-1} of integrated luminosity, compared to most recent results shown in Fig. 2.23. Figure from [75].

Chapter 3

The Beauty experiment at the Large Hadron Collider

LHCb is one of the four major experiments at the Large Hadron Collider at CERN, the European Laboratory for Particle Physics, in Geneva, Switzerland. This chapter briefly introduces the LHC and its other three detectors, and then describes LHCb and its subsystems.

3.1 The Large Hadron Collider

The Large Hadron Collider (LHC) [76], is the biggest, most advanced particle accelerator ever built, designed to provide unprecedentedly high energy and intensity beams. It accelerates two proton beams at world's highest energy and makes them collide at four interaction points where big particle detectors are located. The LHC has been built in the 27 km long, ring-shaped tunnel previously occupied by the Large Electron-Positron collider (LEP). The tunnel is located underground, at a maximum depth 170 m, across the French-Swiss border near the city of Geneva (Fig. 3.1).

The LHC is designed to circulate bunches of protons separated by 25 ns, which yields a nominal bunch crossing rate of 40 MHz. Figure 3.2 shows a cross section of the main dipole LHC magnets. Two sets of superconducting magnets make the two counter-rotating beams curve to follow circular trajectories. The coils are kept to a temperature below 2 K by cryostats, in order to achieve a magnetic field of up to the nominal 8.33 T required for the design energy of 7 TeV per beam. In addition, quadrupole magnets focus the beams and radiofrequency cavities increase the proton kinetic energy with repeating electromagnetic pulses.

The LHC ring is the last link in the chain of CERN accelerator systems (Fig. 3.3). LINAC2 produces low energy proton bunches for injection into the Proton Synchrotron (PS). The PS was CERN's first big particle accelerator, starting operations in 1959, with a circumference of 600 m. It has been used to accelerate protons, antiprotons, electrons, positrons and ions. Beams are then transfered to the Super Proton Synchrotron (SPS), which started operation as an accelerator in 1976 and was successfully configured as a collider in the early 1980s. The SPS provided the proton-antiproton collisions which resulted in the discovery of the W and Z bosons. It is now a key component of the LHC chain, injecting beams providing an energy of 450 GeV per beam.

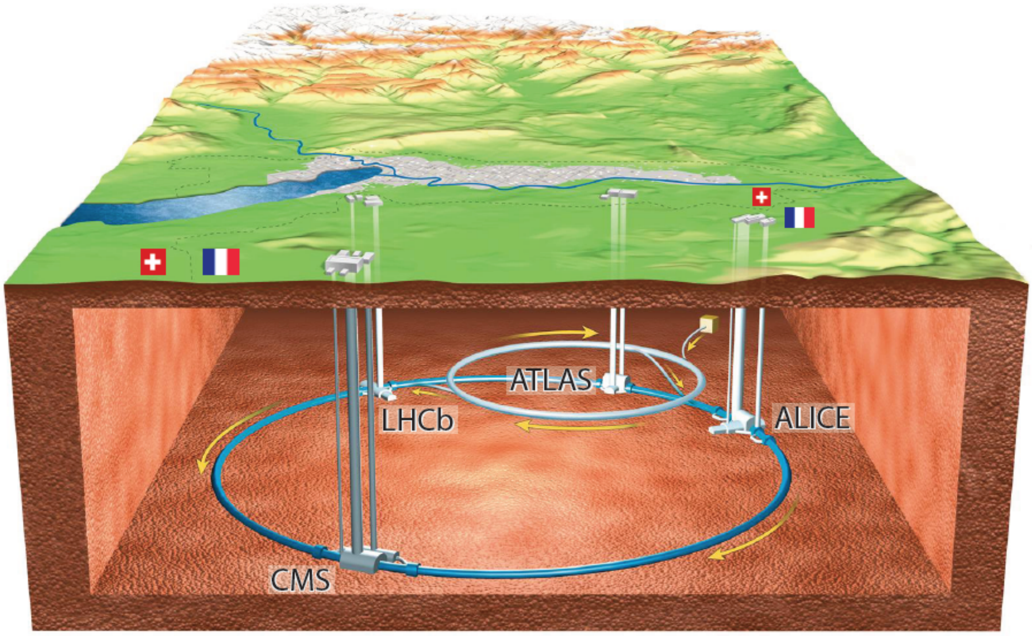

Figure 3.1: Schematic view of the LHC ring across the French-Swiss border near the lake and city of Geneva. The four main experiments (ATLAS, ALICE, CMS and LHCb) are located around the ring at the collision points.

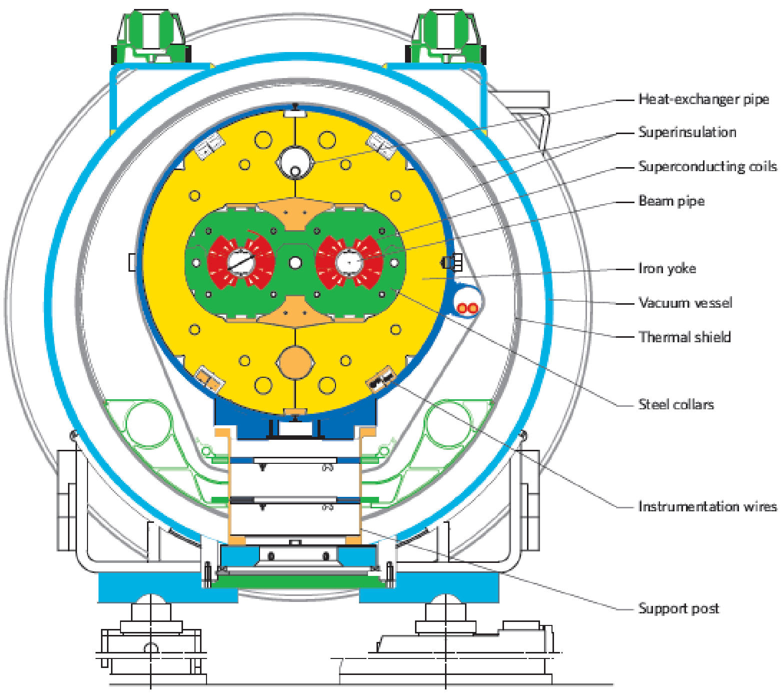

Figure 3.2: Cross section view of the LHC dipole magnets indicating its main components.

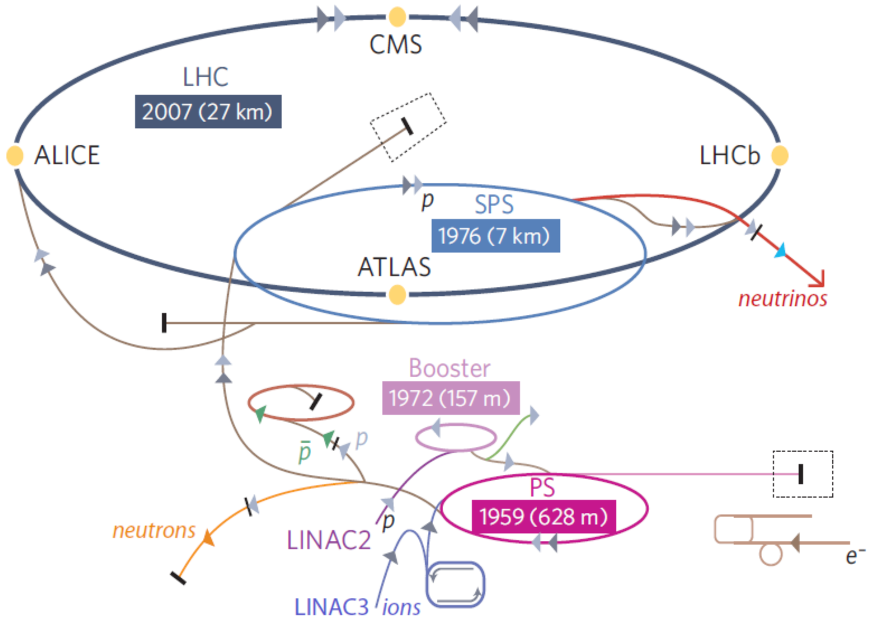

Figure 3.3: CERN accelerator chain used as injector system to the LHC.

Commissioning of the LHC started in 2008, with the collider initially circulating beams at the SPS injection energy. However, during powering tests, a faulty electrical connection between two of the magnets of the accelerator caused the release of helium from the cryogenic system and resulted in mechanical damage of one of the LHC sectors [77]. The system had to be repaired and after a recovery phase, in which additional safety measures where put in place, operation restarted achieving first proton collisions in late 2009. Collisions at the current center-of-mass energy of 7 TeV started on 30th March 2010, gradually increasing beam intensities since then. The LHC also accelerates and collides lead ions in dedicated runs. The first lead ion runs took place in November 2010.

3.1.1 Experiments at the LHC

Particle collisions at the LHC are recorded by several particle detectors of diverse sizes and complexities. ATLAS [78] and CMS [79] are two big general purpose detectors (depicted in Fig. 3.4). Their mission is to explore the results of the proton collisions looking for new massive particles, such as the yet undiscovered Higgs boson and those predicted by SUSY models, which are candidates for Dark Matter. Other topics in their research program include the search for extra dimensions and microscopic black holes. They share a similar barrel shaped design, although their main difference lies in the configuration of the magnetic fields. ATLAS (which stands for A Toroidal LHC ApparatuS) uses a solenoid for the inner detector and a large toroidal field for the muon chambers located in the outer layers of the detector. The CMS (Compact Muon Solenoid) design is based on a large solenoid magnet which produces a 4 T magnetic field. In both cases, the intense magnetic fields are achieved by the use of superconducting coils.

The ALICE collaboration focuses on the physics of strongly interacting matter, which can be studied in ion-ion collisions. The extreme energy densities produced in such collisions is expected to reproduce quark-gluon plasma, a phase of matter that probably existed just after the Big Bang. Studying the existence and properties of this form of matter is key to understand aspects of QCD, such as confinement. The ALICE detector [80] is also shaped as a barrel and uses the superconducting magnet of the former L3 experiment (Fig. 3.4).

Other smaller LHC experiments include TOTEM [81], LHCf [82] and MoEDAL [83]. The TOTEM detector, located close to CMS, has been designed to measure the total, elastic and diffractive cross sections in proton collisions. LHCf is a pair of detectors situated 140 m on either side of the ATLAS interaction point. Its aim is to study proton collisions looking for particles produced in the very forward region, which simulate and can be used to understand high energy cosmic ray events. Finally, MoEDAL, which is to be placed in the LHCb cavern, will look for magnetic monopoles and other exotic massive pseudo-stable ionizing particles.

The list of experiments at the LHC is completed with LHCb [84], which is the focus of this work and will be described in detail in the following section.

3.2 The LHCb experiment

The objective of the LHCb experiment is, as described in the previous chapter, the search for New Physics through the detailed study of the properties of decay processes of b-flavoured mesons. This will be done exploiting the huge numbers of B mesons produced at the LHC proton-proton collisions. This section starts with the discussion of the properties and yields of beauty production at the LHC.

Then, the LHCb detector is presented, describing its components in detail and summarizing the particle detection and event reconstruction principles it applies.

3.2.1 B Physics at the LHC

Pairs of $b\bar{b}$ quarks are produced as a result of the interaction between two partons of the colliding protons. Quark pairs production derives from several strong interaction processes, the most relevant being quark-antiquark annihilation and gluon fusion, displayed in Fig. 3.5. The $b\bar{b}$ production cross section at 14 TeV is two orders of magnitude smaller than the total interaction cross section, which, along with the relatively small branching fractions for interesting decay processes, introduce the need for a trigger system at LHCb (see Section 4.1).

At the high energies of the LHC, the amplitudes represented by the diagrams in Fig. 3.5 are favoured by an asymmetric relation of momenta between the colliding partons, and hence the $b\bar{b}$ pairs are boosted along the beam direction, following the parton of highest momentum. This causes b-flavoured hadrons to be produced mainly in angular regions of low angle with respect to the beam line (polar angle or θ), as shown in Fig. 3.6.

B hadrons are created when b quarks form bound states with lighter quarks, a process known as hadronization (see [35] for a review of B meson production). This is caused by the strong interaction between themselves and also with the debris of the proton-proton collision. B mesons contain a $\bar{b}$ quark combined with a u, d, s or c quark (for B^+, B^0, B_s and B_c^+ particles respectively), either in the ground or excited states. Antiparticles

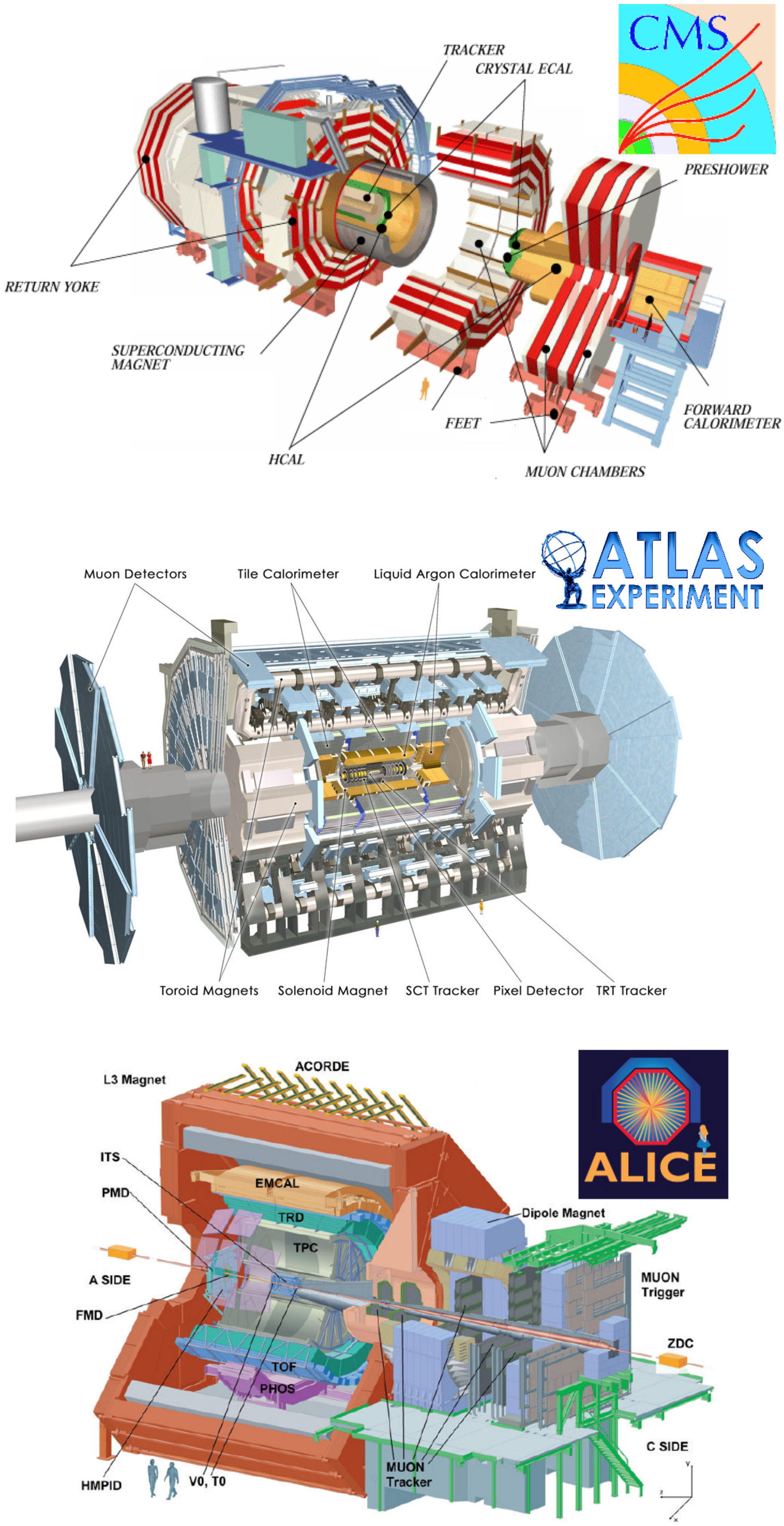

Figure 3.4: Schematic view of the CMS, ATLAS and ALICE detectors.

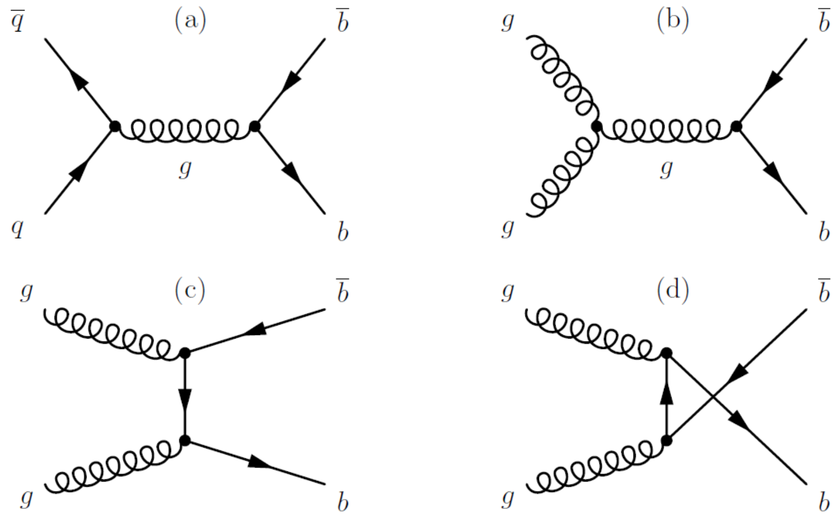

Figure 3.5: Main diagrams contributing to b quark production in the proton-proton collisions at LHC energies. Figure from [87].

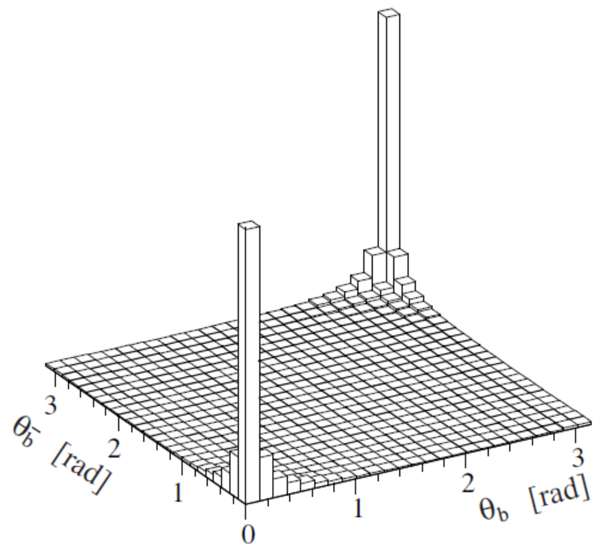

Figure 3.6: Probability distribution for the production of $b\bar{b}$ quark pairs versus momenta polar angles θ_b and $\theta_{\bar{b}}$. Both quarks are mostly produced with the direction of their momenta close to the beam pipe ($\theta = 0$ or $\theta = \pi$) [85].

to these contain the b quark. Bound states of a $b\bar{b}$ combination (commonly referred to as *bottomium*) are also produced in Υ ($l = 0$) and χ_b ($l = 1$) states. B-flavored baryons (Λ_b, Σ_b, etc) are also produced. In hadron colliders, each quark of the $b\bar{b}$ pair hadronizes incoherently.

The hadronization process is driven by strong dynamics in a non-perturbative regime and therefore it can not be reliably predicted. Thus, hadronization fractions for the different meson and baryon species (f_u, f_d, f_s, f_c and $f_{baryons}$ with $\sum_q f_q = 1$) must be determined experimentally. Isospin symmetry, reflected in the near equality of B_d and B_u masses, suggest that $f_u/f_d = 1$, which is generally assumed [35]. LHCb has recently measured the ratio of B_s production to the sum of those for B_d and B_u with the result [86]

$$\frac{f_s}{(f_u + f_d)} = 0.134 \pm 0.004^{+0.011}_{-0.010}. \tag{3.1}$$

LHCb has also used semileptonic decays $\Lambda_b \to X_c\mu$, where X_c represents a generic charmed hadron, to determine the ratio of Λ_b hadronization function (f_{Λ_b}) to the sum of those for B_d and B_u. This ratio has been found to vary with the transverse momentum (p_{T}) of the $X_c\mu$ system according to [86]

$$\frac{f_{\Lambda_b}}{(f_u + f_d)} = (0.404 \pm 0.017 \pm 0.027 \pm 0.105) \times [1 - (0.031 \pm 0.004 \pm 0.003) \times p_{\mathrm{T}}(\,\mathrm{GeV})]. \tag{3.2}$$

Finally, an estimate value of $f_c = 0.2\%$ has been obtained from B_c yields at Tevatron [35].

The number of collisions resulting in a given process is:

$$N = \sigma \times \int L dt, \tag{3.3}$$

where σ represents the cross section corresponding to the process and L is the instantaneous luminosity of the colliding beams. The luminosity, which is a measure of particle flux, depends on a number of beam parameters, and for Gaussian beam distributions can be written as [76]

$$L = \frac{N_b^2 n_b f_{rev} \gamma_r}{4\pi\epsilon_n\beta^*} F, \tag{3.4}$$

in which N_b is the number of protons per bunch, n_b is the number of colliding bunches per beam, f_{rev} is the revolution frequency, γ_r is the relativistic gamma factor, ϵ_n is the beam emittance, β^* is related to beam focusing at the interaction point, and F takes into account the effect on the luminosity of a crossing angle between beams.

The design luminosity for LHCb is lower than the maximum to be achieved by the LHC ($\sim 10^{34} cm^{-2}s^{-1}$). Running the experiment at a luminosity of $2 \times 10^{32} cm^{-2}s^{-1}$ produces events dominated by single pp interactions (see Fig. 3.7). This has several advantages, such as keeping the detector occupancies low and limiting radiation damage to the detector. The main advantage, however, is that these events are easier to analyse as the point of proton-proton collision (known as primary vertex or PV) can be distinguished from the decay point of the B particle (secondary vertex). Note that the extension of the luminous region along the beam axis is $\sigma_z = 5.3$ cm (see Fig. 3.10), while the typical B flight distance is ~ 1 cm. With a b production cross section estimated at 0.5 mb and the integrated luminosity of $2 fb^{-1}$ in a nominal year of data taking (10^7s), 10^{12} $b\bar{b}$ pairs are expected to be produced.

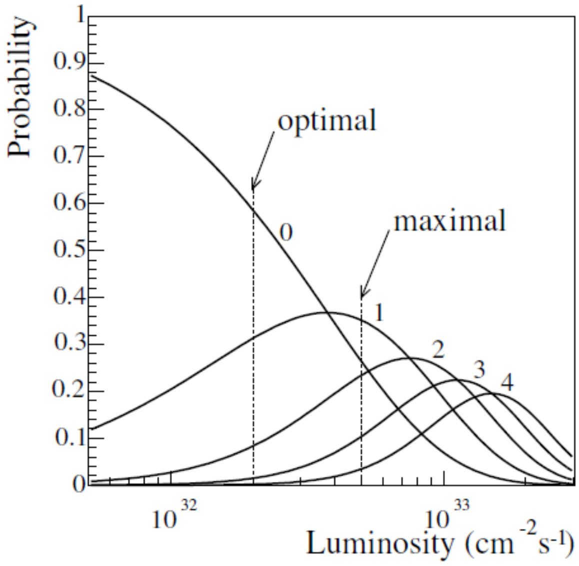

Figure 3.7: Probabilities for the number of proton-proton interactions per bunch crossing as a function of instantaneous luminosity. Design optimal and maximal operating luminosities are indicated [84].

B-flavoured hadrons are reconstructed from their stable or long lived decay products (*daughter* particles). The detectable final products of the decay are usually electrons, muons, proton, kaons, charged pions, photons and neutral pions, which decay immediately into two photons. Neutrinos, although stable, rarely interact with matter, hence they are not detectable at LHCb. The reconstruction of the original particle and the decay chain requires the daughter particles to be identified and their momenta to be measured. To achieve this, and due to the diverse mechanisms of interaction of these particles with matter, modern particle detectors, like the LHCb, are made up of several layers, with subdetectors of different technologies.

The angular distribution of the B mesons produced determines the shape of the LHCb detector as a single arm spectrometer covering the forward cone. The instrumented acceptance of the detector covers $10 < \theta < 250$ (300) mrad in the vertical (horizontal) plane, equivalent to a pseudorapidity coverage of $2.0 < \eta < 5.3$, with $\eta = -ln(\tan(\theta/2))$. In order for the detector to fit inside the existing underground area, previously used by the DELPHI experiment of LEP, and make best use of the available volume, the interaction point has been displaced by 11.25 m, via a modification of the LHC optics, from the center of the cavern. The LHCb detector occupies a total length of 20 m, a width of 6 m and a height of 5 m. The detector layout is shown in Fig. 3.8, which presents also the adopted system of coordinates. The positive z axis lies along the beam line, pointing from the interaction region to the muon stations (commonly referred to as *downstream* direction). The y axis corresponds to the vertical direction with positive sign pointing upwards. Finally, the x axis is chosen to be horizontal, with positive sign pointing away from the center of the LHC ring in order to complete a right-handed coordinate system.

The main requirements to be met by LHCb in order to perform high precision studies of heavy flavor decays are: excellent secondary vertex resolution for a precise determination of proper time, in order to resolve the fast oscillations of B mesons; precise charged particle

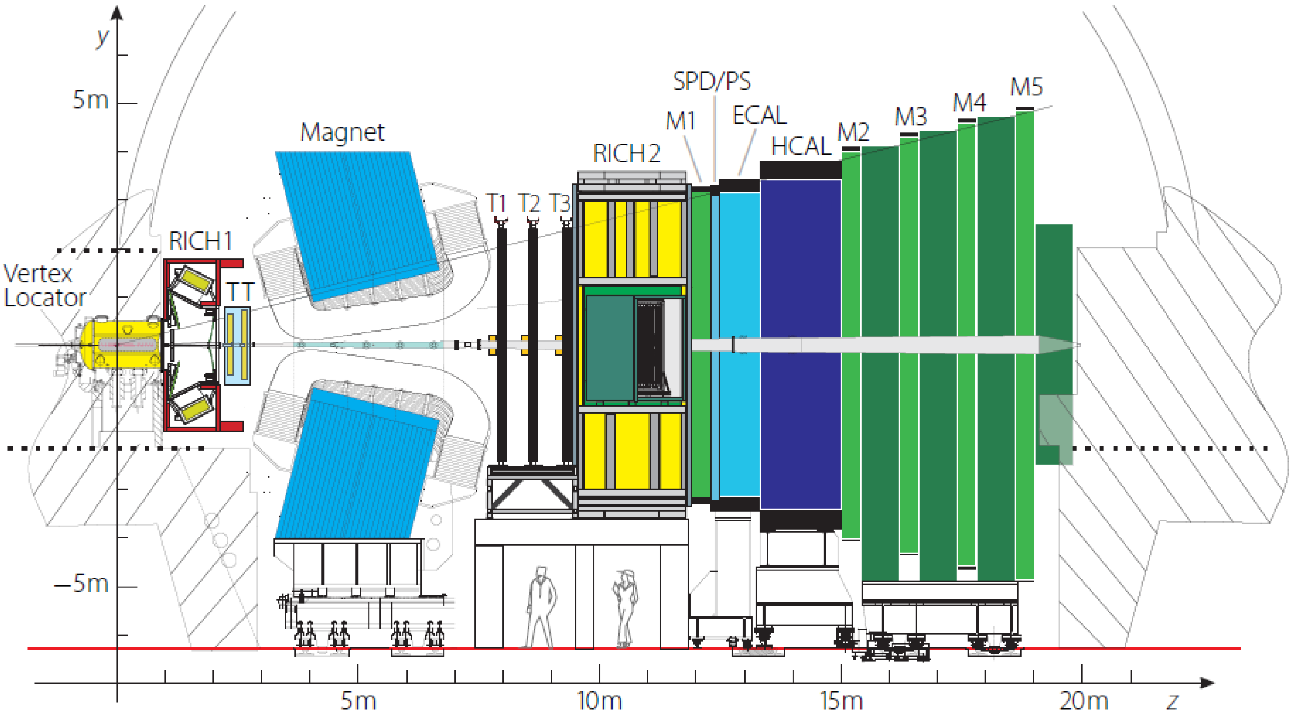

Figure 3.8: Schematic side view of the LHCb detector indicating its subsystems. From left to right: Vertex Locator (VELO) at the interaction region and coordinate origin, first Cherenkov detector (RICH1), tracker turicensis (TT), dipole magnet, tracking stations (T1, T2, T3), second Cherenkov detector (RICH2), first layer of the muon detector (M1), scintillating pad detector (SPD) and pre-shower (PS), electromagnetic calorimeter (ECAL), hadronic calorimeter (HCAL) and four muon stations (M2, M3, M4 and M5).

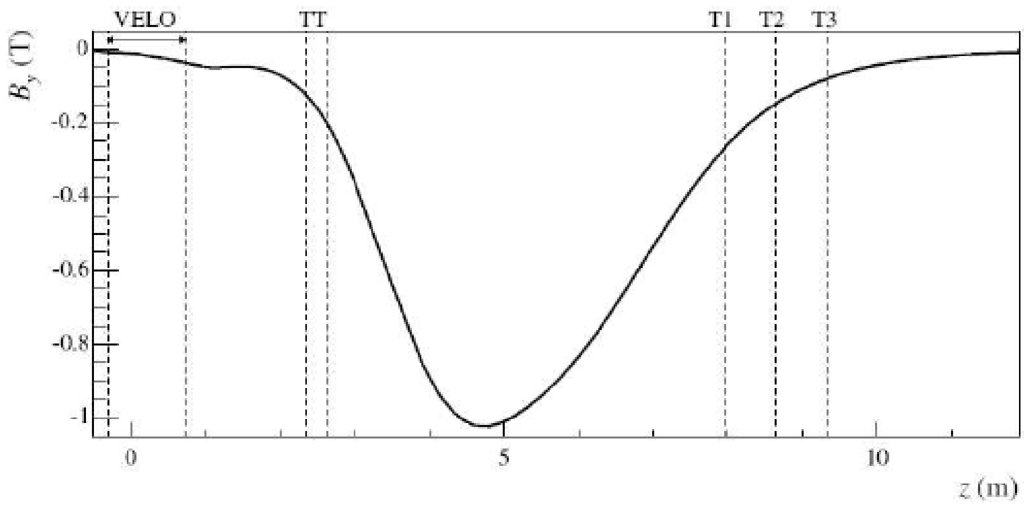

Figure 3.9: Main component of the magnetic field B_y as a function of the z coordinate. Figure from [84].

momentum measurement and neutral particle reconstruction for invariant mass resolution that enables a high background rejection; excellent particle identification (PID) capabilities which separates different hadronic decays of equivalent topology; a fast and efficient data acquisition system which provides high bandwidth and allows trigger mechanisms for fast analysis and rejection of non interesting events.

A key component of the spectrometer is the warm dipole magnet [88], which curves the trajectories of charged particles and thus allows their momenta to be measured. The dominant component of the magnetic field is in the y axis (B_y), with an integrated field of 4 Tm. Charged particles trajectories are hence deflected in the xz (horizontal) plane. Figure 3.9 presents B_y as a function of the z coordinate, showing that the magnetic field is mainly contained in the interior volume of the magnet, although some residual field is found in the interaction region and up to the main tracking stations.

The following subsections describe the systems which make up the LHCb detector, which according to their function can be classified as:

- Tracking detectors: VErtex LOcator (VELO), Tracker Turicensis (TT) upstream of the magnet and Inner Tracker (IT) and Outer Tracker (OT) which comprise each of the three Tracking Stations (TS) positioned downstream of the dipole magnet.

- Particle identification detectors: two Ring Imaging Cherenkov detectors (RICH1 and RICH2), the calorimeter system, Scintillator Pad Detector (SPD) and PreShower (PS), followed by the electromagnetic and hadronic calorimeters) and the muon detector, comprising five muon stations with the first one (M1) situated in front of the calorimeter and the rest (M2 to M5) behind it.

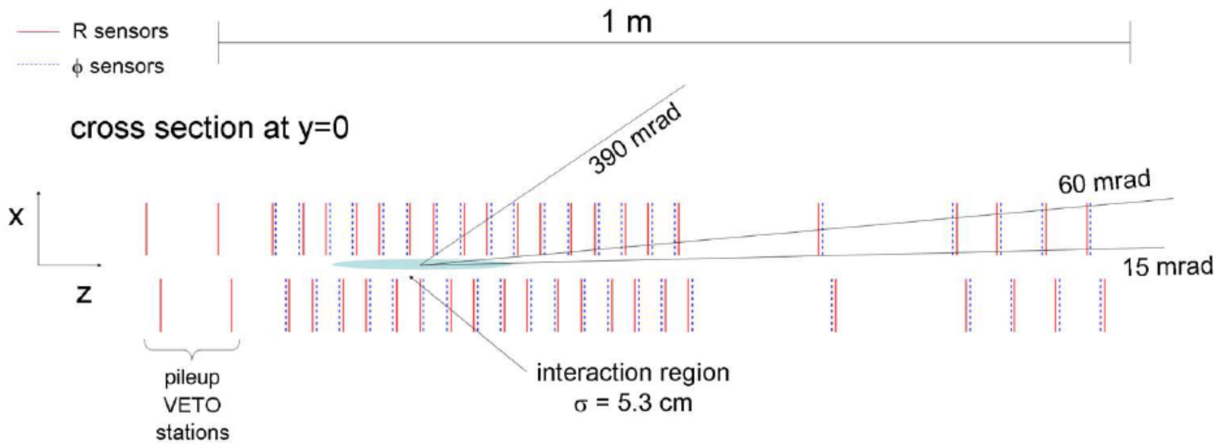

Figure 3.10: Cross section of the VELO silicon sensors in the xz plane. The spacing between sensors has been chosen to cover the LHCb polar angle acceptance from 15 to 300 mrad with the additional requirement that each particle must cross at least three modules. Two pile-up veto stations are located upstream of the VELO sensors.

3.2.2 Tracking and vertexing detectors

The tracking system is designed to reconstruct charged particles tracks as well as primary and secondary vertices. Together with the dipole magnet, it is used to measure particles' momenta. The VELO, TT and IT (the part of the tracking stations closest to the beam axis) use silicon microstrip technology. The TT and IT systems, developed in a common project, form the Silicon Tracker (ST) subsystem. The OT employs straw-tubes to cover the outer area of T1 to T3.

Vertex Locator (VELO)

The VELO [89] is the first tracking device that particles meet in their flight from the interaction region. It is made up of 21 stations placed along the beam axis (see Fig. 3.10), with sensitive elements placed at only 8 mm in radial distance with respect to the z axis. It uses precise measurements of track coordinates to reconstruct and identify displaced vertices, which correspond to decay vertices of long lived particles such as B or D mesons.

The VELO sensors are closer to the beam axis than the clearance required by the LHC during injection of the proton beams. For this reason, the VELO modules are retractable (Fig. 3.11) and are moved in to its operating position only after the beam properties are considered adequate (*stable beams*). Two additional sensor planes referred to as *pile-up veto* system, which are used in the first trigger level (see Section 4.2.1), are located upstream the VELO.

Each VELO module is a two-layer sensor with microstripes designed to measure the radial distance from the beam axis, r, and the azimuthal angle ϕ (Fig. 3.12). The layers measuring r are segmented and grouped into four 45° sectors in each half module, while ϕ sensors are divided into inner and outer regions, the outer having more strips, in order to avoid unacceptably high strip occupancies in the outer part. The z coordinate is taken from the known position of each sensor. The strip pitch for both r and ϕ sensors varies

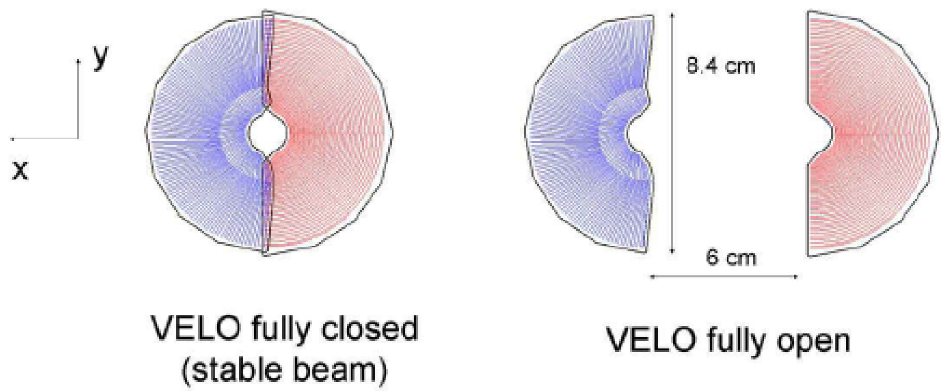

Figure 3.11: Velo modules shown in fully closed (operating) and open (beam injection) positions. The two halves of the VELO are designed to overlap partially in the fully closed position.

with the radial distance, as Fig. 3.12 shows. This causes hit resolution to depend on the radial distance as well, ranging from 10 to 25 μm [84] for both types of sensors.

The VELO system has been designed to make use of cylindrical geometry in order to enable the fast reconstruction of tracks and vertices in the LHCb trigger. Simulations showed that a rz (2D) partial reconstruction, which only requires the r strips to be read out, provided tracks and vertices of sufficient resolution to efficiently select events containing b hadrons. However, rz tracking imposes the constraint that circular strips must be centered as perfectly as possible around the beam axis, as the trigger performance rapidly degrades with r sensors misalignment [90].

Tracker Turicensis (TT)

The TT [84] is located upstream to the magnet and its main task is to provide track measurements for low momentum particles, which are bent out of the acceptance by the magnet, and particles produced by decays outside the VELO, such as K_S. It consists of two stations, each comprising two layers of silicon strip technology, for a total of four active planes covering the full acceptance. The strips of the four layers are arranged in a (x,u,v,x) configuration, which correspond to angles with respect to the vertical y axis of (0°,−5°,5°,0°). Figure 3.13 shows a representation of the vertical and stereo layers. The vertical orientation of the strips is chosen to obtain a better hit resolution in the bending plane. The presence of the angled u and and v strips allows the reconstruction of tracks in 3D. Hit resolution is about 50 μm [84].

Tracking Stations: Inner and Outer Trackers

The main tracking system, known as Tracking Stations or T-stations, comprises three modules (T1 to T3) approximately 6 m wide and 5 m high which are located downstream of the magnet. Each of this modules is in turn made up of two different technologies, used for regions of different particle flux. In the inner region, with higher particle occupancies, a higher resolution is needed and silicon strip detectors are used (Inner Tracker or IT). Outside this inner region, a detector based on straw tubes is employed (Outer Tracker or

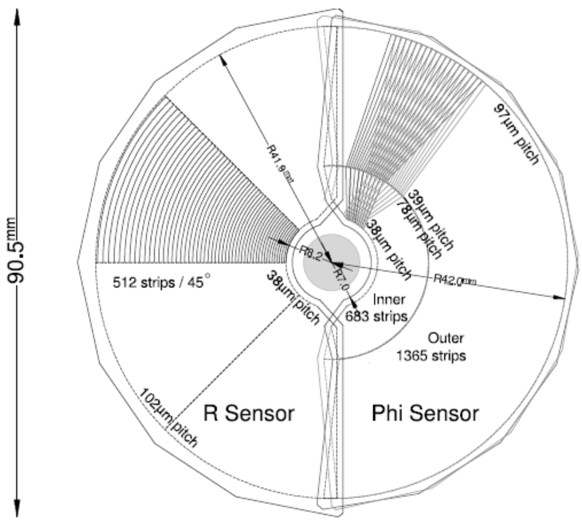

Figure 3.12: Velo module sketch showing the $r\phi$ geometry. Strips measuring r coordinate are segmented into 45° sectors. ϕ layers are divided into inner and outer regions with a higher number of strips in the outer region to avoid excessive occupancy.

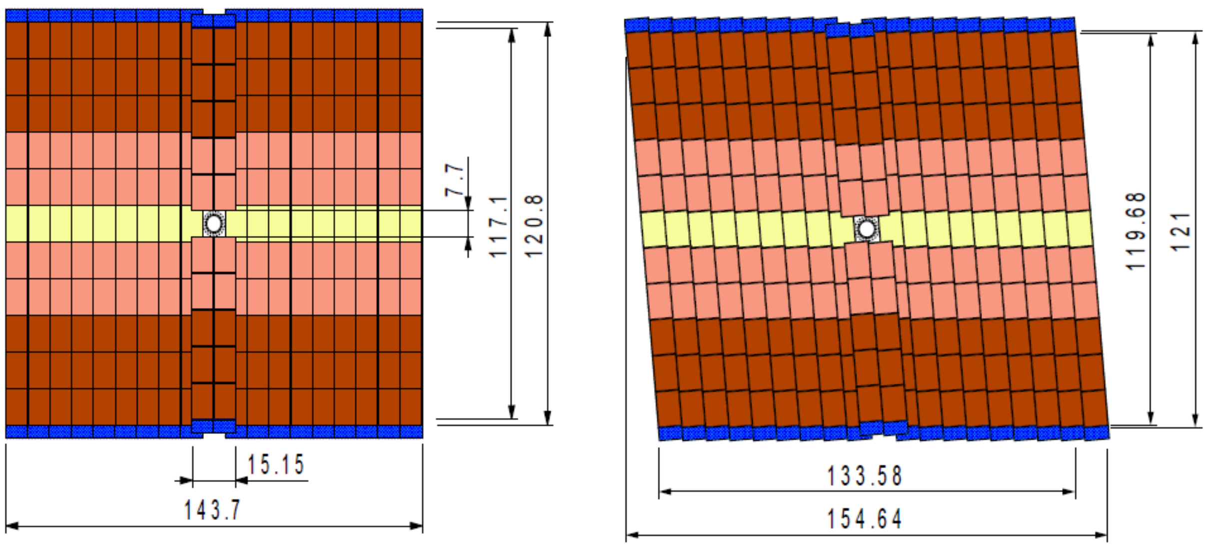

Figure 3.13: View of TT vertical (x) and stereo (v) layers. Different color shades indicate different readout sectors. Figure from [84].

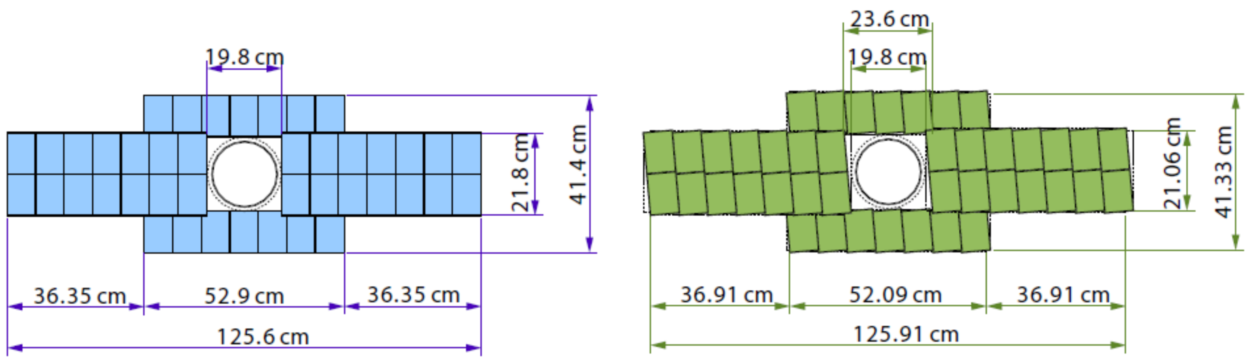

Figure 3.14: View of IT vertical (x) and second stereo (u) layers.

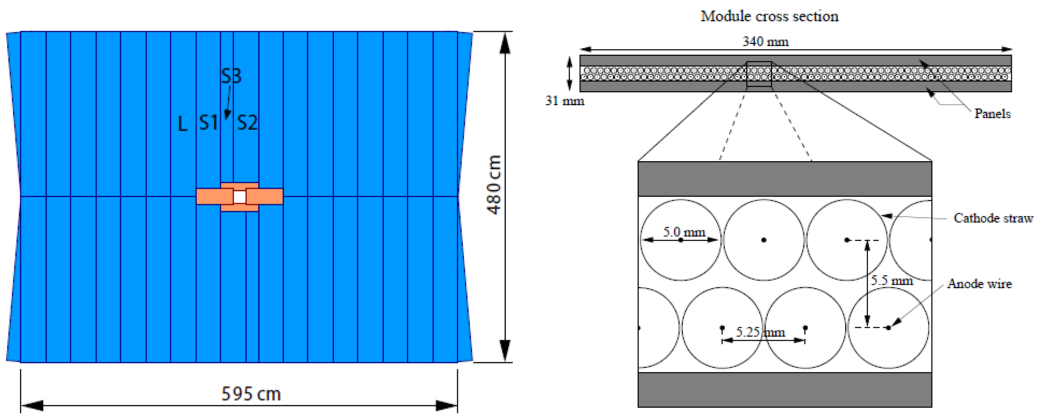

Figure 3.15: Front view of one of the OT stations (left) and cross section for one of the OT modules (right).

OT). The inner tracker (IT) [91] covers only 2% of the total surface of each T-station but receives about 20% of the particle flux within the LHCb acceptance.

Each of the three IT modules is divided into four boxes arranged around the beam pipe in a cross shape, as Fig. 3.14 shows. Each box contains four detector layers positioned in the same (x,u,v,x) geometry used in the TT. The hit resolution of the IT, as part of the ST is also about 50 μm [84].

The outer tracker (OT) [92] is a drift time detector (see Fig. 3.15 left). It has been designed as an array of individual straw tube modules. Modules contain 128 tubes arranged in two layers of 64 tubes (Fig. 3.15 right). Each OT tube measures 5 mm in diameter and is filled with a mixture of argon (70%) and CO_2 (30%). The modules are in turn positioned in layers, so that each of the three stations has four layers of modules in the previously described (x,u,v,x) configuration. The average hit efficiency is 98% and the spatial resolution of the OT is below 200 μm [84].

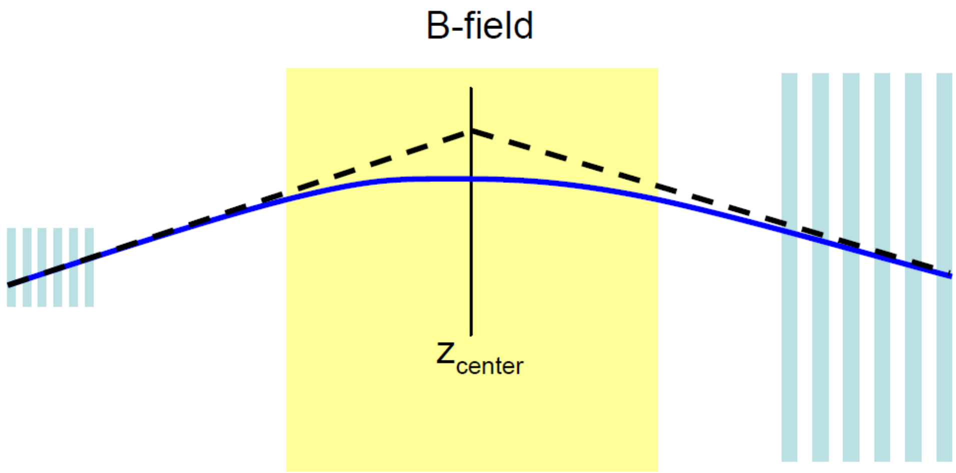

Figure 3.16: Tracking and momentum measurement principle: tracks can be made combining straight sections connected by a single kick by the magnetic field. Figure from [93].

Track reconstruction

Track reconstruction algorithms use hits in the VELO, TT, IT and OT detectors to deduce particle trajectories extending from the interaction region up to the calorimeters. The magnetic field that bend the trajectories is mainly present in the central section of the detector, so tracking devices are placed in approximately null field regions (Fig. 3.9). This implies that tracks in these regions can be essentially reconstructed as straight lines (Fig. 3.16).

Figure 3.16 also represents the basic principle of particle momentum measurement. The effect of the magnetic field can be approximated to first order by a single kick in the center of the magnet necessary to combine two straight segments. The momentum of the particle is inversely proportional to the difference in the slopes of the track segments at both sides of the magnet (*momentum kick* method).

Tracks can be classified according to their trajectories inside the spectrometer, as illustrated in Fig. 3.17:

- Long tracks, traversing the complete tracking system from the VELO to the T-stations. These are the best quality tracks for LHCb, as they have the most precise momentum determination.

- Upstream tracks, which traverse only the VELO and TT. These tracks correspond to low momentum particles, bent out of the acceptance by the magnet. Residual magnetic field in the TT region allows for a momentum determination, however with low resolution.

- Downstream tracks, which use the hits of the TT and T-stations, which allow the reconstruction of particles which decayed outside the VELO (mostly K_S and Λ).

- Velo tracks, measured in the VELO only. These are typically large angle and backward tracks used in the reconstruction of the primary vertices.

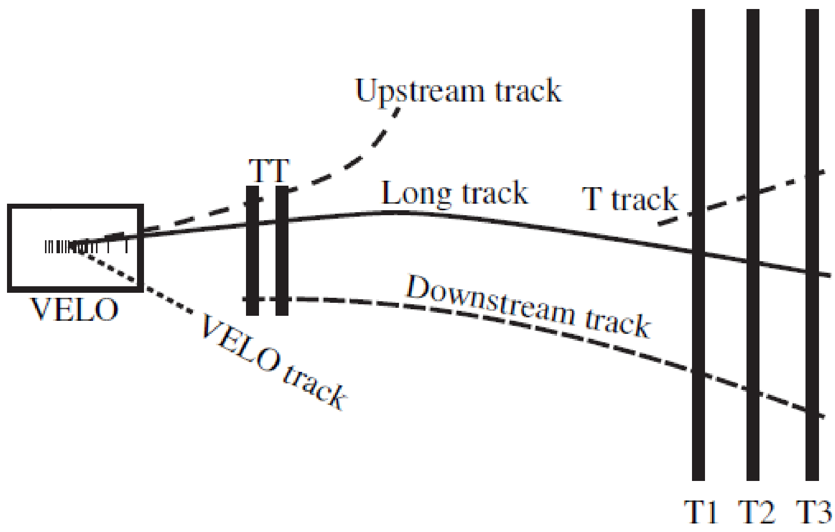

Figure 3.17: Types of tracks in the LHCb track reconstruction. Figure from [84].

- T tracks, which use T-station hits only. A crude momentum estimation can be made using T tracks and assuming they come from the coordinate origin. These tracks are useful for the global pattern recognition in RICH2.

The pattern recognition algorithms must reconstruct particle tracks with a high efficiency, while keeping a low yield of fake tracks made out of spurious combinations of real hits and/or detector noise (called *ghosts tracks*). On LHCb simulation studies, a track is considered a ghost if less than 70% of the hits are actually related to the same particle. An example of this would be a track made out of two real track segments in the VELO and T-stations that however correspond to different particles. Tracking algorithms also produce *clone tracks*. Two tracks are considered clones if they share more of 70% of their hits, and this is also to be avoided as it represents a duplication of the tracks associated to a unique particle.

The first algorithm run in the tracking reconstruction software of LHCb looking for long tracks starts from *seeds* produced by a standalone VELO track finding algorithm, which are then extended to the TT and T-stations. The VELO tracks are produced in a two-step sequence: first, a 2D reconstruction is performed using only the r sensors (VELO 2D or VELO rz tracks), then information from the ϕ sensors is added to each track to produce VELO 3D tracks. After VELO tracks are available, they are combined with hits in T1 and the possible trajectories are parametrized by a second order polynomial in y and a third order polynomial in x. Further T-station hits are looked for in a search window around the predicted position, and added to the track if found. The track candidates with higher number of hits are kept, and a likelihood is calculated in order to discard ghosts. Finally, hits in the TT are searched for and added to the track if they are close enough to the track passing through VELO and T-stations hits. This tracking algorithm is referred to as *forward tracking*.

To get the maximum number of tracks, a second and redundant track finding algorithm is used, called *track matching*. In this algorithm, standalone VELO and T tracks are first produced. Both track segments are then extrapolated to the bending plane of the magnet. If the position in both extrapolations in the center of the magnet and the change of track slopes satisfy a defined quality criteria, both segments are matched. Again, TT hits may be added if they are close to the resulting tracks. As many tracks are reconstructed by both methods, and hence duplicated, a *clone killing* algorithm is applied afterwards.

After long tracks have been found, they are refitted with a Kalman filter track fit [94,95]. This procedure starts from the position of a hit and the track slopes ($t_x = dx/dz$ and $t_y = dy/dz$) at this position, along with the uncertainties associated to these measurements. This set of information is referred to as a *track state*. This information is used to predict the next track state in the following detector plane. The information contained in this prediction and in the actual hit of the original track are combined to produce the new track state. The track is then updated substituting the original hit by this new track state. This process is repeated, adding one state at a time and using all the information available up to that point, until the last measurement is reached. This is mathematically equivalent to a least squares fit. The quality of the track is measured by the χ^2 of the track fit.

The fit can then be redone by starting from the other end of the track (*bidirectional fit*). Outlier states with the highest contribution to the χ^2 may be removed, in order to perform the second fit without the contribution from this hit. In the LHCb implementation of this procedure, three iterations of the bidirectional fit, are performed for a total of six iterations.

Changes is the trajectories produced by multiple scattering and corrections to the momentum due to dE/dx energy loss can be taken into account in this fit. This is achieved by modifying the uncertainties, which are parametrized according to the material to be traversed between two measurements.

A faster, simplified version of the Kalman Filter procedure has also been developed in order to be used in the trigger [93]. Some modifications to the algorithm described above include a simplified description of the material to be traversed, only one iteration to be done starting from the end of the spectrometer up to the VELO and with no outlier removal.

3.2.3 Particle Identification detectors

The identification of the final detectable particles (electrons, muons, kaons, protons, charged pions and photons) is a fundamental requirement for LHCb. Figure 3.18 summarizes the basic principle of particle identification (PID), which is the different ways in which different particles interact with matter. Charged particles differ from neutrals in that they produce hits in the tracking detectors. Electrons and photons differ from hadrons in the way they deposit their energy in the calorimeters. Muons can be distinguished from other charged particles by their greater penetration power, which makes them the only particles reaching the latest layers of a detector.

The LHCb objectives impose the need to disentangle between different hadronic particles. For this reason, LHCb design incorporates Cherenkov detectors, which are not present in the other main LHC experiments.

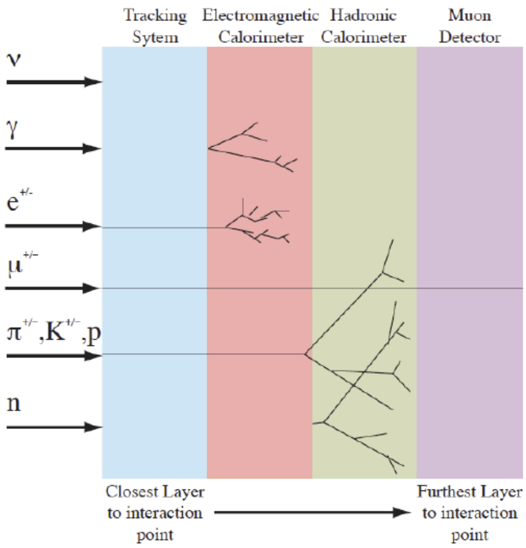

Figure 3.18: Different ways of interaction of different particles with successive layers of the detector are used to identify them. See text for a more detailed description. Figure from [96].

Ring Imaging Cherenkov detectors

Precise identification of hadrons, and in particular the separation of pions and kaons, is essential in order to disentangle some B decay channels which present the same topology. This is the task of the two Ring Imaging Cherenkov detectors (RICH) [97].

RICH detectors are based on the Cherenkov effect [98]. Cherenkov light is emitted when a charged particle traverses a dielectric medium, referred to as a *radiator*, at a speed higher than the speed of light in that medium, $v > c/n$. Emitted photons interfere coherently to produce a wavefront at a fixed angle θ_C with respect to the flight direction of the particle, originating a cone of light (Fig. 3.19).

By measuring the angle θ_C for a known radiator medium characterized by its refractive index n, the speed of the charged particle can be determined by the relation

$$\cos(\theta_C) = \frac{c}{nv}. \tag{3.5}$$

The measurement of the momentum of the particle allows the mass to be determined and hence the particle to be identified.

The LHCb detector makes use of two RICH detectors in order to cover different momentum ranges. Softer momenta are covered by the RICH1, situated between the VELO and the TT. Silica aerogel and C_4F_{10} radiators are employed to identify particles with momenta in the 1 GeV/c to 60 GeV/c range. The RICH2 detector is located between the T-stations and the calorimeter. It has a limited acceptance but covers the region at small polar angles, mostly traversed by high momentum particles. It contains CF_4 as a radiator, which can be used to explore the momenta from 15 GeV/c up to 100 GeV/c. Figure 3.20 summarizes the ranges of momentum for which the three different radiator materials allow for pion-kaon separation. The dependence of θ_C with particle momentum is shown to be different for the different species of charged particles.

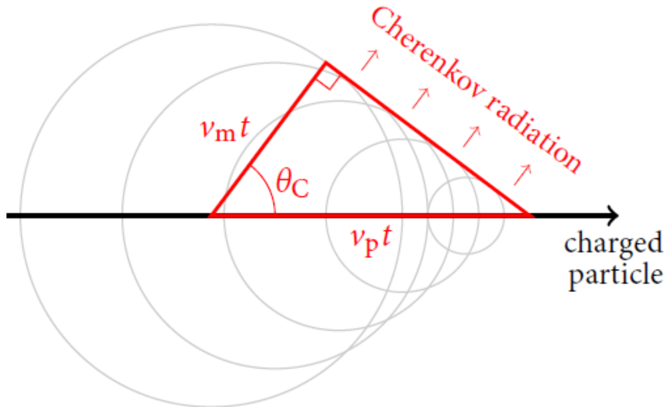

Figure 3.19: Cherenkov light shockwave cone.

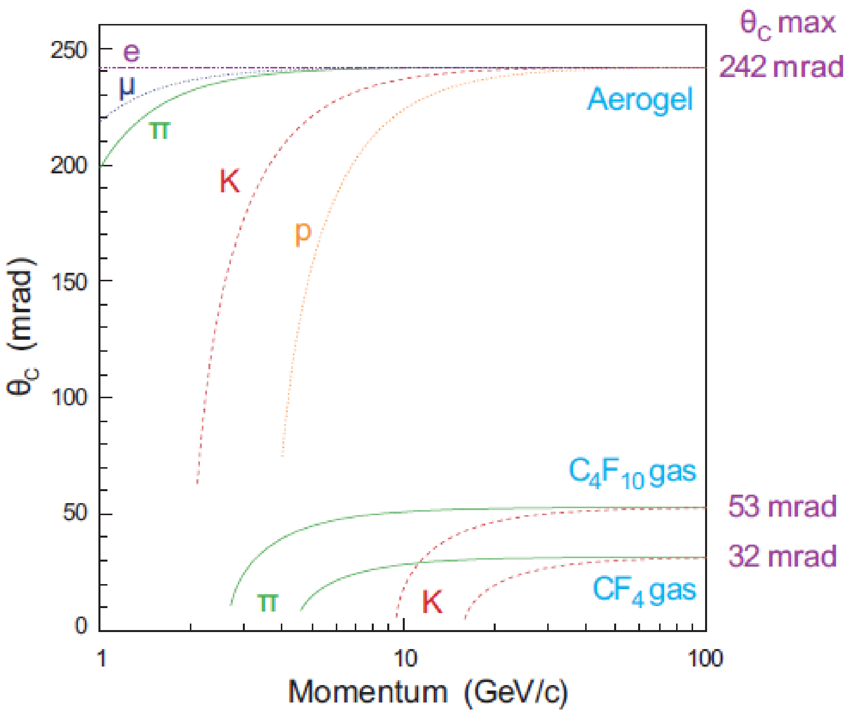

Figure 3.20: Cherenkov angle θ_C versus momentum for different particles and radiators used for particle identification [84].

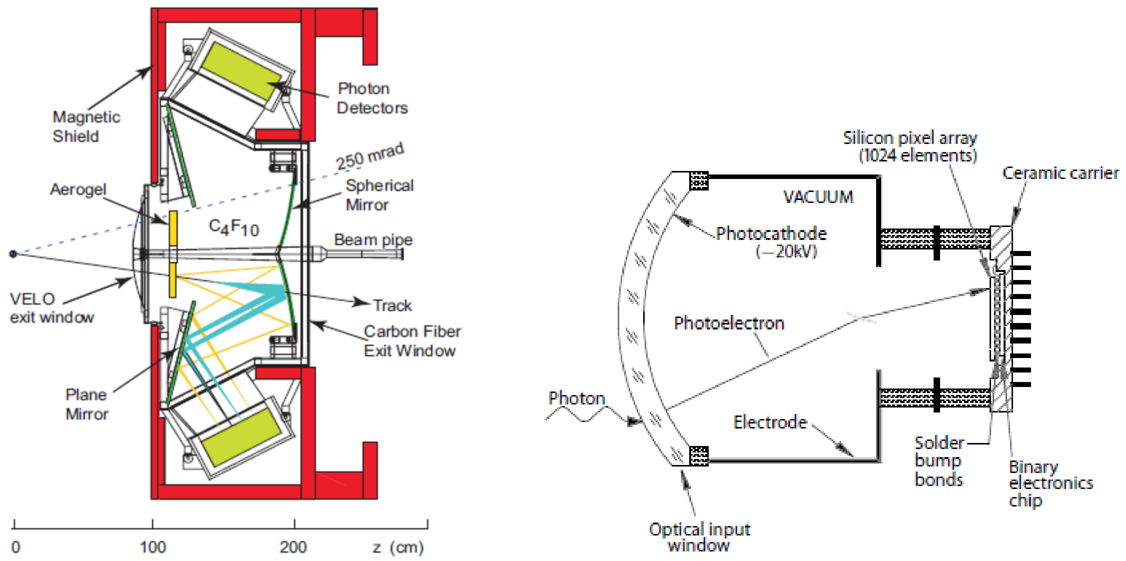

Figure 3.21: Side view schematic layout of the RICH1 detector (left). Sketch of pixel HPDs used in LHCb RICH detectors (right).

Cherenkov light is focused by a combination of flat and spherical mirrors which reflect the image to instrumented photon detector planes out of the detector acceptance, where it is collected in the shape of a light ring (see Fig. 3.21 left for a detailed view of RICH1 layout). The radius of this ring is a measure of the Cherenkov angle. In both detectors, photons in the wavelength range of 200-600 nm are collected using Hybrid Photon Detectors (HPD, see Fig. 3.21 right). The HPDs are surrounded by external iron shields that protect them from the intense magnetic field. The expected resolutions on the measurement of θ_C are 2.6 mrad for the aerogel and 1.5 mrad and 0.7 mrad for the C_4F_{10} and the CF_4 gaseous radiators respectively.

Calorimetry

The main task of the LHCb calorimeter system [99] is the identification of electrons, photons and hadrons and the measurement of their energies and directions. The reconstruction of prompt photons and π^0 is essential for the successful study of important decay channels for the LHCb physics program. In addition to that, the calorimeter selects high transverse energy candidates for the first level of the LHCb trigger.

When high energy particles traverse through dense media, their energy is released by the creation of new particles of lower energies, which in turn interact with the media to produce more particles. These cascades of secondary particles are commonly referred to as *showers*. Depending on the nature of the incoming particle, electromagnetic or hadronic showers can be produced.

Electromagnetic showers are produced by particles, mostly electrons and photons, through the electromagnetic interaction. Electrons radiate photons (*bremsstrahlung* or breaking radiation), while high energy photons interact with matter mainly by the creation of electron-positrons pairs. The effect of this interaction mechanisms is a multiplication of secondary particles until their energy is low enough to stop further particle creation. Beyond this point, energy is released by ionization or excitation of electrons in the media. This change of behavior is characterized by the critical energy E_c. The energy loss due to bremsstrahlung for an incoming electron of energy E is related to the radiation length X_0

$$-\frac{dE}{dx} = E/X_0. \tag{3.6}$$

From this expression, the average shower depth X produced by an incoming electron of energy E can be derived:

$$X = X_0 \ln \frac{E}{E_c}. \tag{3.7}$$

The radiation length is a property of the material and, in the case of media formed by a single chemical element, depends on the density and atomic number (Z).

Hadronic showers are produced when particles interact with atomic nuclei via the strong nuclear force. This results in successive inelastic collisions which excite the nuclei, which in turn release their excess of energy emitting pions. As a good fraction of the energy is transformed into neutral pions, which decay into photons, hadronic showers also have an electromagnetic component. The stopping power of a material through hadronic showers is characterized by a parameter analogous to the radiation length in the case of electromagnetic showers, the nuclear interaction length (λ). Interaction lengths are typically much larger than radiation lengths and therefore, larger amounts of material are required to stop hadronic showers.

The LHCb calorimetry system is designed in the usual structure of an electromagnetic calorimeter (ECAL) followed by a hadronic calorimeter (HCAL), which allows to absorb both electromagnetic and hadronic showers. Two additional detector layers, the Scintillator Pad Detector (SPD) and a PreShower (PS) have been placed in front of the ECAL. The SPD distinguishes between charged and neutral particles, with the main task of classifying electromagnetic showers as produced by a photon or an electron at the first level of the trigger, where no tracking information is available. The PS follows a 12 mm thick lead plane which initiates electromagnetic showers but is not thick enough to produce sizable hadronic showers, so it contributes to the separation between electromagnetic and hadronic showers.

The LHCb calorimeters are sampling calorimeters which alternate layers of radiator material (lead for the ECAL and iron in the case of HCAL) with scintillator tiles (Fig. 3.22). Shower particles ionize the scintillator material, which produces light that is collected by wavelength shifting fibers that direct the photons to photomultiplier tubes. The amount of collected light is proportional to the deposited energy. The SPD, PS and ECAL scintillator tiles are perpendicular to the beam axis, while those used in the HCAL run parallel to the beam axis

The SPD, PS, ECAL and HCAL have been designed with a variable segmentation in the xy plane to deal with different particle fluxes at different polar angles (Fig. 3.23). A segmentation into three zones of different cell sizes (inner, middle and outer) has been chosen for the ECAL and projectively for the SPD and PS. The HCAL uses larger cell sizes and has been segmented into two zones.

The ECAL depth accounts for 25 radiation lengths (X_0) and 1.1 hadronic interaction

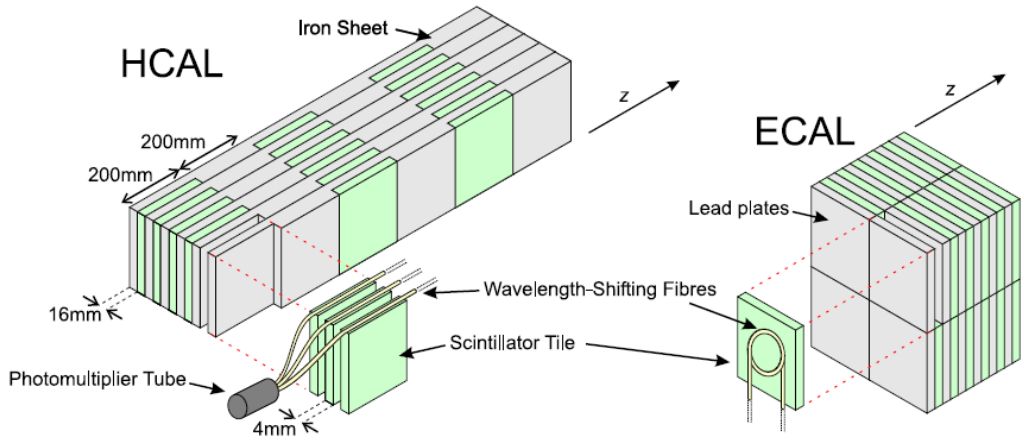

Figure 3.22: Calorimeter technology: both ECAL and HCAL are made up of a combination of a high density radiator material and scintillation tiles. Tiles are oriented differently for ECAL (normal to the beam axis) and HCAL (parallel to the beam axis). Light is collected by wavelength shifting fibers that transport the photons to photomultiplier tubes. The amount of light collected is a measure of the deposited energy.

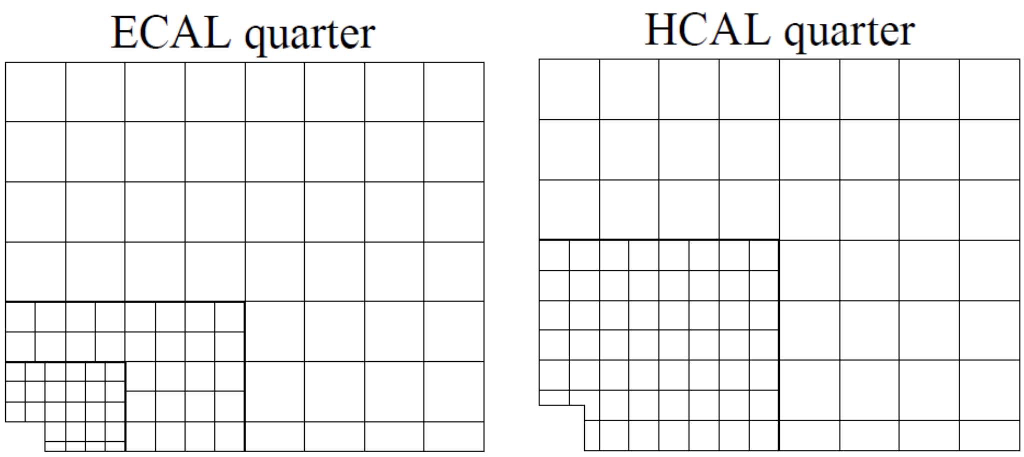

Figure 3.23: Segmentation for the Electromagnetic (left) and Hadronic (right) calorimeters.

lengths (λ). Its energy resolution is

$$\frac{\sigma(E)}{E} = \frac{10\%}{\sqrt{E/GeV}} \oplus 1.5\%. \tag{3.8}$$

In the case of the HCAL, the total depth is equivalent to 5.6 λ, and its energy resolution is

$$\frac{\sigma(E)}{E} = \frac{80\%}{\sqrt{E/GeV}} \oplus 10\%. \tag{3.9}$$

In both cases, the first term of the resolution corresponds to statistical fluctuations in the shower formation and the second is due to systematic uncertainty in the inter-calibration of the cells.

Muon stations

The LHCb muon detector system [100] is designed to fulfill two fundamental tasks: first, the identification of muons, which, as discussed in the previous chapter, are present in many key decay channels, and secondly, providing the LHCb trigger with muon candidates.

The muon system consists of five stations (Fig. 3.24). Four of these stations (M2 to M5) are located behind the calorimeters and interspersed with 80 cm thick iron walls (for a total of 20 λ) that stop any particles coming from calorimeter showers, leaving only the highly penetrating muons. The M1 station is placed in front of the calorimeter in order to provide a first measurement point avoiding additional multiple scattering caused by the calorimeter material. The minimum momentum for a muon to cross all five stations is approximately 6 GeV.

Each station is divided into four regions with different pad granularity, to accommodate to different particle fluxes (Fig. 3.25). Pad sizes vary from one station to another in such way that a projective geometry with respect to the coordinate origin is maintained.

The muon chambers make use of multi-wire proportional chamber (MWPC) detectors in all its stations, while Gas Electron Multiplier (GEM) technology is also employed in the innermost part of M1, the region with highest particle flux. This technology fulfills the requirement of a fast readout, essential for this detector to be used by the trigger.

Particle Identification

The information provided by the RICH detectors, calorimeters and muon stations is combined for the optimal identification of final particle types: hadrons (π, K, protons), electrons, muons, photons and π^0.

The algorithm developed for the identification of charged particles with the RICH detectors makes use of the tracking information. For each track with a measured momentum, the expected ring is produced for the electron, muon, pion, kaon and proton hypothesis. This prediction is compared to the observed patterns of hit pixels and a likelihood is calculated. This produces a best hypothesis for each track.

Muons are identified by extrapolating all tracks with momentum above 3 GeV/c to the muon stations, where hits are searched for in fields of interest (FOI) around the extrapolation of the track. The size of the FOIs depends on the track momentum, with a different parametrization for each station and region. A track is considered a muon candidate when

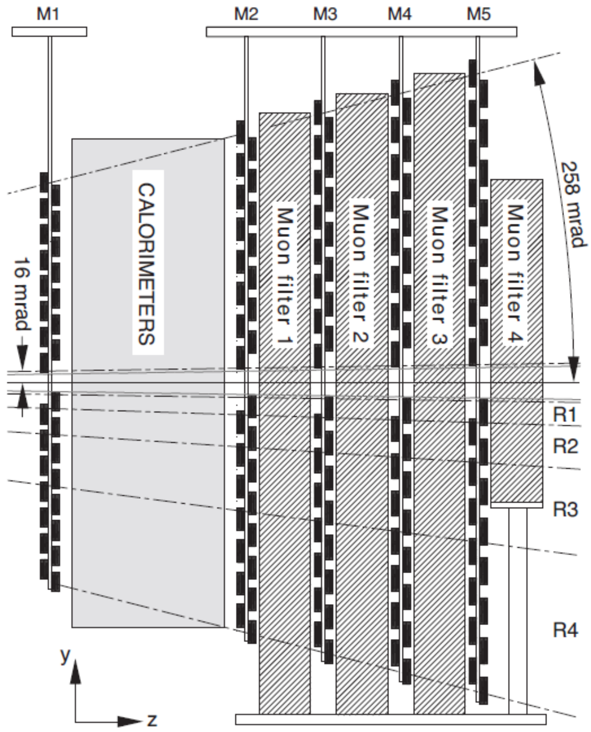

Figure 3.24: Side view of the LHCb muon stations layout. M1 is located in front of the calorimeter system, while M2 to M5 are placed behind it, with iron absorbers between them to remove particles other than the penetrating muons.

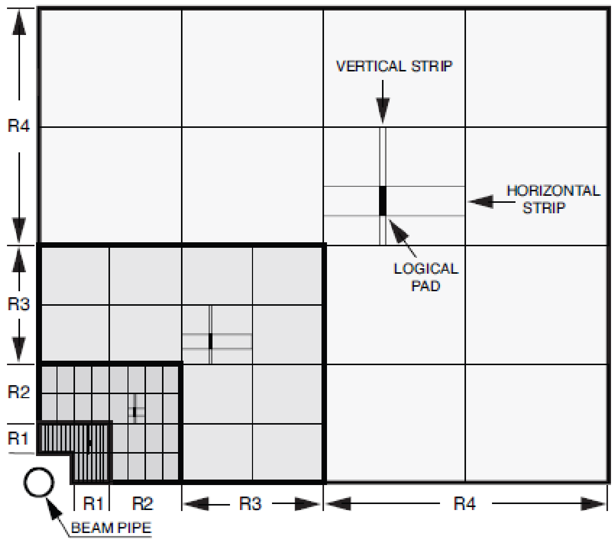

Figure 3.25: Schematic front view of one quadrant of a muon station. Each station is segmented into four regions of different pad sizes.

a minimum number of hits (2 to 4 depending on the momentum range) is found. Information from the RICH is also used to calculate a combined likelihood and a difference in likelihood with respect to the pion hypothesis. In the case of the online reconstruction, as performed by the trigger, a standalone algorithm has been implemented which produces *muon segments*. Hits in the last station, M5, are used as a starting point and they are combined with hits in M4. These segments are then extrapolated to M3, where hits are looked for in search windows. The process continues to include hits from M2 to M5 (but not M1, because of its high occupancy).

Electron identification is based on the ratio of the measured track momentum and energy of the associated charged cluster in the ECAL (which should be close to one for electrons), together with the quality of the matching between the extrapolation of the track and the center of the associated ECAL cluster. The energy of the charged cluster is corrected by adding the energy associated to bremsstrahlung photons that the electron could have emitted before the magnet deflected its trajectory. The VELO part of the track is extrapolated to the calorimeter, and if a neutral cluster is found, its energy is combined with that of the charged cluster to produce a corrected energy measurement. Further improvement is achieved by the addition of energy depositions in the PS and HCAL along the extrapolated particle trajectory. Finally, a global likelihood which combines calorimeter, RICH and muon detector information is produced.

Photon identification relies on electromagnetic showers not associated with any track. In order to improve energy resolution, photons are classified according to whether they converted in the material after the magnet (e.g. in the RICH2 or M1) by the presence of a hit in the SPD cell in front of the center of the ECAL cluster.

Finally, neutral pion reconstruction must consider two possible cases. The photons produced in the $\pi^0 \to \gamma\gamma$ decay may produce two separated ECAL clusters or end up in the same electromagnetic shower (merged photons). An algorithm that takes into account several variables describing the shower shape has been developed in order to disentangle pairs of photons merged into the same cluster from single photons.

3.2.4 LHCb software framework and applications

The LHCb experiment uses simulation of proton-proton collisions based on the Monte Carlo (MC) techniques [101] in order to accomplish certain tasks such as the optimization and study of the detector performance, reconstruction and analysis algorithms, etc.

Monte Carlo event generation and analysis require several steps, as summarized in Fig. 3.26. First the GAUSS application generates proton-proton collisions and the decay of the resulting particles (using the external programs Pythia [102] and EvtGen [103] respectively), followed by a simulation of the interaction of the radiation with the material of the detector (again thanks to the external package Geant4 [104]). The next step is performed by the BOOLE application, which simulates the response of the detector to the particles traversing it. At this point, simulation and raw data from real events have the same structure, so that the event reconstruction application, BRUNEL, can be equally applied to both. Complex objects such as tracks and calorimeter clusters are created at this stage. The output is stored in *Data Summary Tape* or DST files, which can then be analysed using the DAVINCI package. Particle identification algorithms are applied to each track which provides a PID hypotesis for these objects. Another type of algorithms is

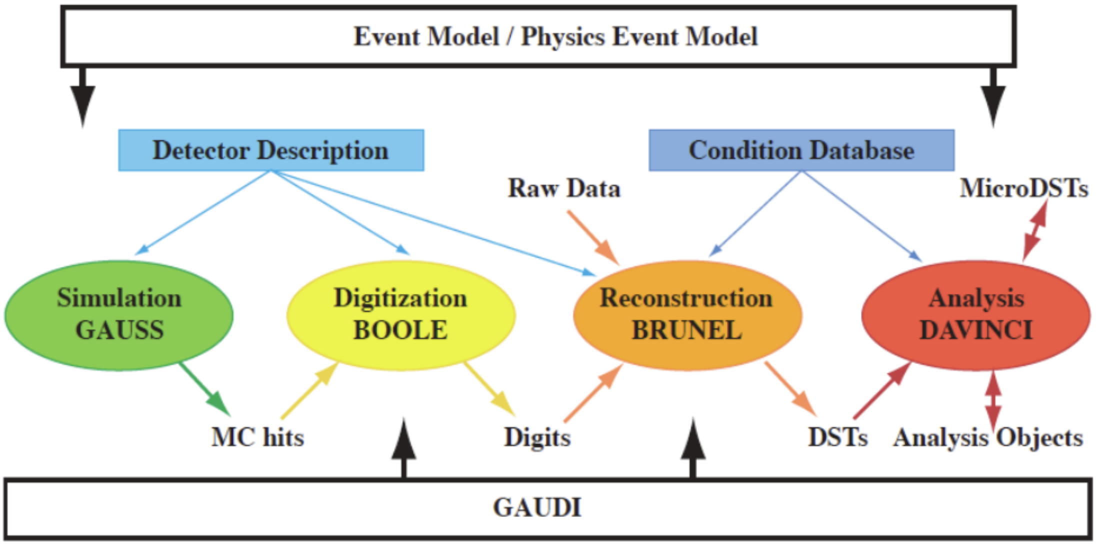

Figure 3.26: LHCb simulation and data processing applications. Reconstruction (Brunel) and analysis (DaVinci) stages are analogously applied both to simulated and real events.

then executed in order to combine these particle objects and try to reconstruct and select decays of interest.

The LHCb software framework [105] is implemented within the object oriented framework GAUDI [106], written in C++. All LHCb applications and their tasks as described above are embedded in GAUDI. Another application based on GAUDI, not mentioned before, is MOORE, which is executed online and performs the reconstruction and selection tasks required by the LHCb software trigger (described in the next chapter).

In order to design and study trigger performance, two basic types of simulated events are used. A number of events simulate generic proton-proton collisions that would be visible by LHCb (characterized by the presence of at least two charged particles producing reconstructible tracks in the detector). These are known as *Minimum Bias* events. They are used to calculate the retention of non interesting events by a given trigger algorithm. The other type of events is called *signal events*. These are events which simulate only one specific decay channel of interest and that have been selected by their respective analysis selection (*offline selected*). To evaluate the efficiency of a trigger algorithm (i.e. the ability to retain interesting events) the number of offline and trigger selected events is normalized with respect to all offline selected events entering the trigger selections. Both parameters, minimum bias retention and signal efficiency will be extensively used in the following chapters.

Chapter 4

The LHCb Trigger System

The LHCb experiment needs a trigger system, i.e. a set of fast mechanisms with the purpose of rejecting uninteresting events while efficiently selecting the small fraction of collisions which are actually useful for the LHCb research program. This chapter presents the requirements imposed by high precision studies of heavy flavor decays in the LHC environment, followed by a description of the solutions adopted by the LHCb experiment, with an emphasis on the strategies devised for the selection of events containing muons as decay particles.

4.1 Need of a trigger system at LHCb

QCD predictions for the cross sections for various processes at hadron collisions over a range of energies are summarized in Fig. 4.1. At the LHC nominal collision energy $\sqrt{s} = 14$ TeV, the total and $b\bar{b}$ production cross sections are respectively $\sigma_{tot} = 99.4$ mb while $\sigma_{b\bar{b}} = 0.633$ mb [107]. The ratio $\sigma_{b\bar{b}}/\sigma_{tot}$ corresponds to one $b\bar{b}$ event in approximately every 150 collisions.

The prediction of $\sigma_{b\bar{b}}$ has however large uncertainties [107], hence LHCb simulation studies at the nominal LHC collision energy of 14 TeV assume a conservative value of 0.5 mb [84]. At the design luminosity for LHCb ($2{\times}10^{32}\text{cm}^{-2}\text{s}^{-1}$), this value of $\sigma_{b\bar{b}}$ yields a $b\bar{b}$ quark pair production rate of 100 kHz. Typically, a fraction of 15% of those b hadrons and their decay products are found inside the detector acceptance. Furthermore, interesting decay processes are rare, typically with a relative probability of 10^{-4} or below, which are hence expected to occur at a maximum rate of 1 Hz.

The design time spacing between proton bunches at the LHC is 25 ns, which produces a peak crossing rate of 40 MHz. However, there are gaps with "empty bunches" needed for the LHC operation. The LHC beams at nominal intensity consist of a total of 2808 "full" bunches [76]. Due to the displacement of the interaction point in the LHCb cavern, a small fraction of the bunch crossings do not coincide with a bunch coming in th opposite direction, producing a total of 2622 colliding bunches at LHCb per LHC cycle. Because of the gaps, the average proton (*non-empty*) crossing rate, product of the number of bunches times the revolution frequency, at LHCb is 2622×11245 Hz $= 29.49$ MHz.

σ_{tot} can be broken down into the contributions from elastic ($p + p \to p + p$), diffractive ($p + p \to p + X$) and inelastic ($p + p \to X$) events. The elastic scattering of the protons and a fraction of the diffractive events is not seen by the detectors, as only hard inelastic

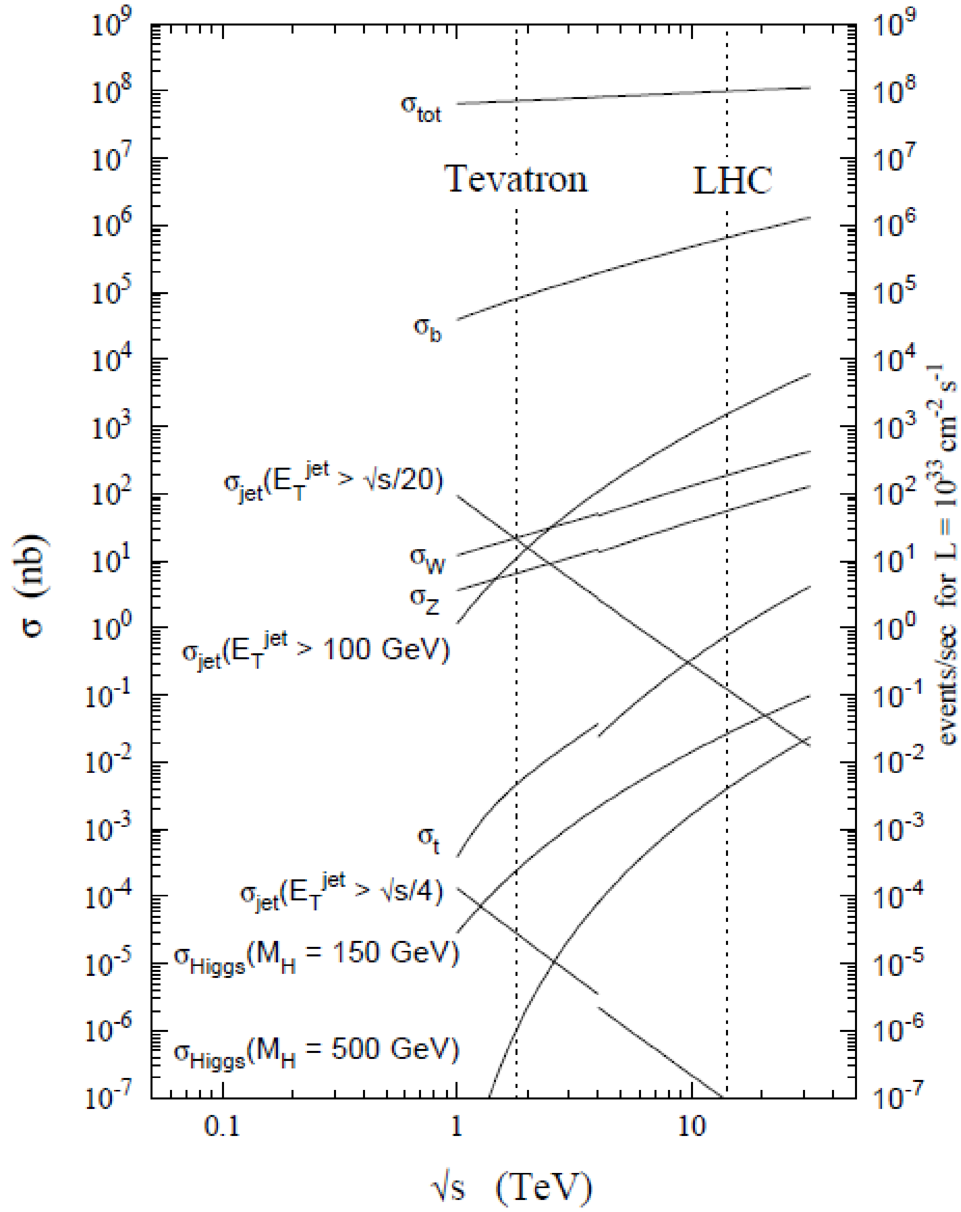

Figure 4.1: Cross sections and event rates as a function of collision energy for hard hadron scattering, indicating values for Tevatron (proton-antiproton) and LHC (proton-proton). At $\sqrt{s} = 14$ TeV, $\sigma_{tot} = 99.4$ mb and $\sigma_{b\bar{b}} = 0.633$ mb. Figure from [107].

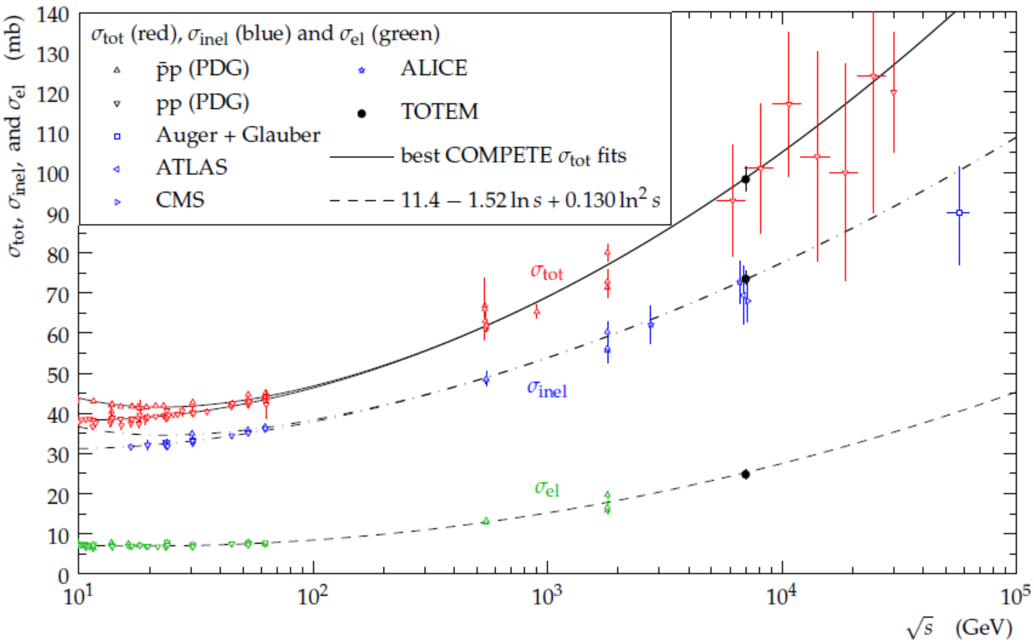

Figure 4.2: Total, elastic and inelastic cross sections as a function of collision energy for hard hadron scattering, including first values for LHC at 7 TeV center of mass collision energy, as measured by ATLAS, CMS, ALICE and TOTEM. Figure from [108].

scatterings give rise to particles at sufficient high angles with respect to the beam axis. Simulation studies at 14 TeV predict that the total rate of events visible by LHCb (those with at least two reconstructible tracks in the detector acceptance) is ∼14 MHz. This is the rate assumed for minimum bias events, used in the trigger optimization studies based on simulation described in the next chapter.

The TOTEM experiment has recently produced a first measurement of the proton-proton cross sections at the current LHC energy of 7 TeV [108]. Non-elastic cross section (including inelastic and diffractive processes) has been measured as $\sigma_{ne} = 73.5 \pm 0.6^{+1.8}_{-1.3}$ mb), while the result for elastic collisions is $\sigma_{el} = 24.8 \pm 0.2 \pm 1.2$ mb, for a total $\sigma_{tot} = 98.3 \pm 0.2 \pm 2.8$ mb (see Fig. 4.2). This measurement for σ_{ne}, at LHCb nominal luminosity, corresponds to a non-elastic event rate of 14.7 MHz. The rate of minimum bias events for LHCb with the LHC running at $\sqrt{s} = 7$ TeV is therefore similar to the value assumed in trigger optimization studies based on simulation.

In summary, from the nominal bunch crossing rate of 40 MHz, non-empty bunch crossings occur at 30 MHz from which 14 MHz are visible. The rate of interesting b events, as discussed above is of 1 Hz, which implies that signal events are hence diluted by background in a proportion of one to ten million at best. The purpose of the LHCb trigger system is therefore to reject the majority of the collisions, which are uninteresting events, preventing them from being stored for further analysis.

LHCb trigger system examines proton collisions looking for b hadron decay signatures which derive from its relatively heavy mass and long lifetime. The main signature of particles coming from B decays are the relatively high transverse momentum (p_T), due to the large B mass, and the significant impact parameter (IP) with respect to the proton-

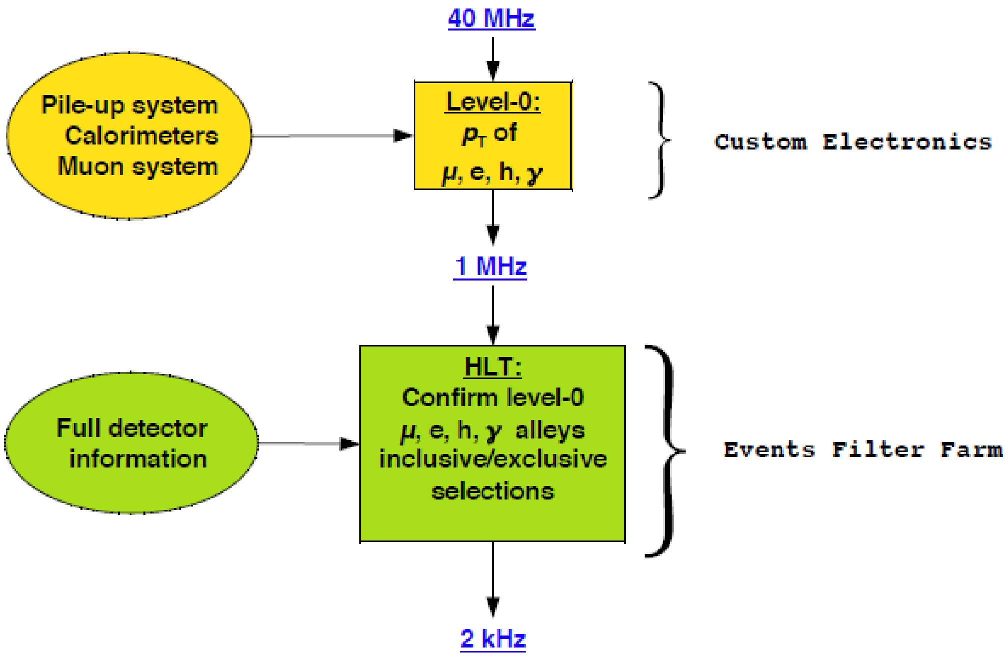

Figure 4.3: LHCb trigger levels.

proton collision vertex, due to the long B lifetime.

4.2 LHCb trigger strategy

Data taking at LHCb is constrained by two conditions. First, the full readout of the detector is designed to work at a maximum rate of 1.1 MHz. Secondly, available offline storage and analysis resources have been estimated to be sufficient to process a number of events equivalent to a sustained rate of 2 kHz of events being stored during a nominal year (10^7 s) of operation.

The LHCb trigger [84, 109] is hence divided into two stages (Fig. 4.3). The first one (Level zero or L0) is implemented in custom electronics and controls detector readout. Some LHCb subdetectors can be read-out through a specific L0 trigger path, which is independent of the normal data acquisition chain and synchronous to LHC clock at 40 MHz. The information from these subdetectors is used to trigger the full detector readout. Events then flow into a second stage (High Level Trigger or HLT), which consists of software algorithms running on a cluster of 1000 multicore CUPs (for a total of 16000 processors) named the Event Filter Farm (EFF). The HLT regulates data storage, as it produces the final decision to discard or retain the event. Figure 4.4 represents the two stages of the LHCb trigger in the context of the data acquisition (DAQ) and experiment control (ECS) systems.

General purpose detectors at the LHC run at a luminosity of $10^{34}\text{cm}^{-2}\text{s}^{-1}$. This luminos-

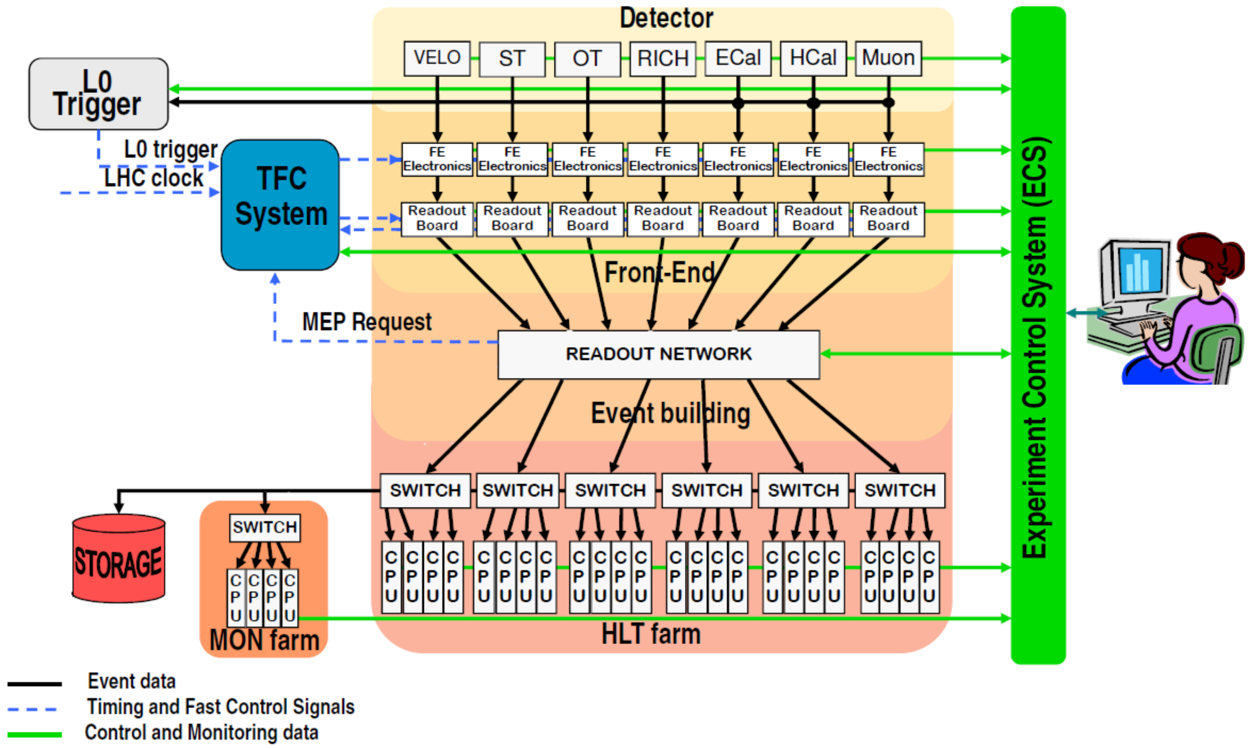

Figure 4.4: Diagram of the LHCb trigger stages integrated in the LHCb DAQ and ECS elements showing data flow. Complete description of the diverse elements can be found in [84]. Information from the calorimeters, muon detectors and pile veto system is used by the L0DU to produce a trigger decision. A positive decision is sent to the Trigger and Fast Control (TFC) system, which in turn sends it to the readout boards of all subdetectors, where information from the relevant events is stored in buffers. Multi event packets (MEP) are sent through the network built on a gigabit Ethernet to the event filter farm (EFF). Event fragments contained in the MEPs are then combined to rebuild the events. Events are distributed to the CPUs of the EFF, which are running the HLT application. Finally, if the decision of the HLT is positive, the event is sent to permanent storage. Figure from [84].

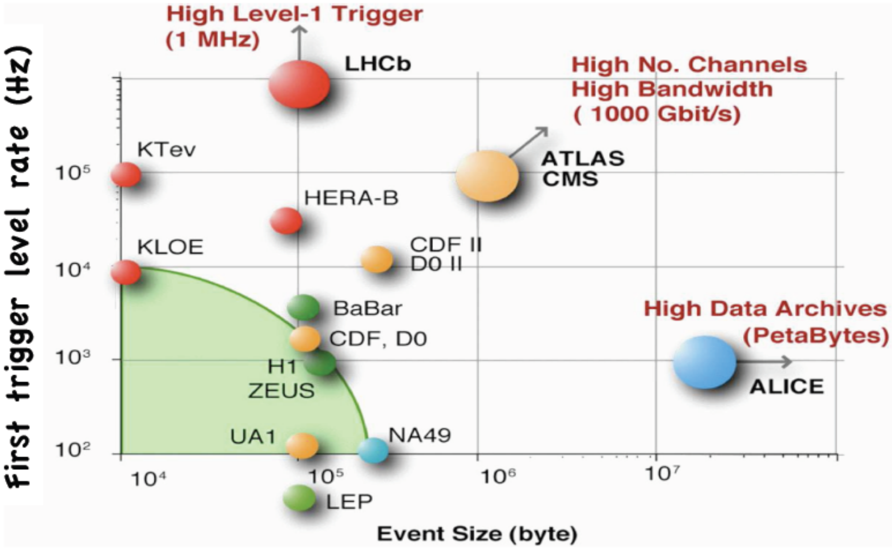

Figure 4.5: LHCb trigger strategy compared to other experiments. Running at low luminosities produces small size events which allows LHCb to read the full detector at an unprecedented rate.

ity produces on average ~23 inelastic events per bunch crossing, with a visible interaction rate of ~700 MHz. Events of higher complexity, as compared to those analysed by LHCb, force CMS and ATLAS to achieve a greater rate reduction before the full detector can be readout (Fig. 4.5). Table 4.1 summarizes LHCb, ATLAS and CMS running parameters and trigger requirement. Small event size at LHCb (35 kB on average) also allows a high rate of events being written to storage (output of the software trigger), while the actual data flow (70 MB/s) is lower than that of ATLAS and CMS. The consequence of this is that ATLAS and CMS must set higher thresholds in order to achieve a greater event reduction, which makes LHCb unique in accessing, for instance, particles of lower transverse momentum or those closer to the beam axis.

Experiment	L ($cm^{-2}s^{-1}$) (ν)	Proton interaction rate	DAQ readout	Event size	Rate to storage
LHCb	2×10^{32} (0.7)	14 MHz	1 MHz	35 kB	2 kHz (70 MB/s)
ATLAS	10^{34} (23)	700 MHz	75 kHz	1.6 MB	200 Hz (320 MB/s)
CMS	10^{34} (23)	700 MHz	100 kHz	1 MB	100 Hz (100 MB/s)

Table 4.1: Comparison of LHCb, ATLAS and CMS running parameters and trigger requirements: instantaneous luminosity and average number of hard proton collisions per bunch crossing, proton interaction rate, DAQ readout rate, average event size and rate of events finally written to permanent storage.

4.2.1 Level 0 hardware trigger

The purpose of the L0 trigger is to reduce the event rate to 1.1 MHz. Its decision relies on the presence of candidates of high transverse momentum (p_T) or energy (E_T) in the muon

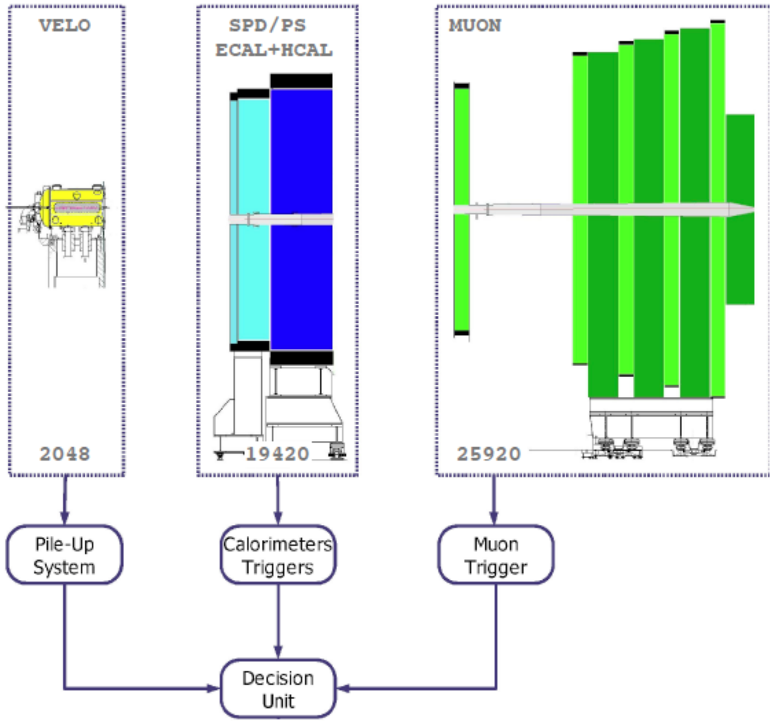

Figure 4.6: The pile up system, calorimeters and muon chambers can be read out at 40 MHz. The information from these subdetectors is employed to produce the L0 decision.

and calorimeter systems respectively. Additionally, in order to reject high multiplicity events or those with multiple interactions (pile-up events), some general variables that characterize the complexity of a particular event (*global event cuts* or GEC), may be required. These variables are the total transverse energy deposited in the calorimeters, and the multiplicities of the pile system planes located in the VELO and of the SPD layer of the calorimeter. Figure 4.6 shows the subdetectors involved in the L0 decision.

Calorimeter clusters are formed by combining energy deposited in regions of 2×2 cells. According to energy deposition in different calorimeter layers, clusters can be classified as electrons, photons, charged hadrons and neutral pions, and the highest E_T candidate of each type is considered (Fig. 4.7).

Muon candidates are track segments reconstructed by searching for straight line combination of hits in muon stations (Fig. 4.8). Assuming they are produced at the nominal origin, for a known magnetic field, segment slopes given by M1 and M2 hits can be used to compute p_T with a resolution of 20%. The two highest p_T candidates found per detector quadrant are selected (Fig. 4.9) for a maximum of eight candidates.

A custom built L0 decision unit (L0DU) [109] combine all the information received into a trigger decision. The L0 system is fully synchronous with the 40 MHz bunch crossing signal of the LHC. The time interval between the pp interaction and the arrival of the L0 decision which triggers the readout (*latency*) is fixed at 4 μs.

The L0 decision is obtained by applying different thresholds (*cuts*) to the measured p_T or E_T to each type of L0 object. In the case of the muon candidates, there are two

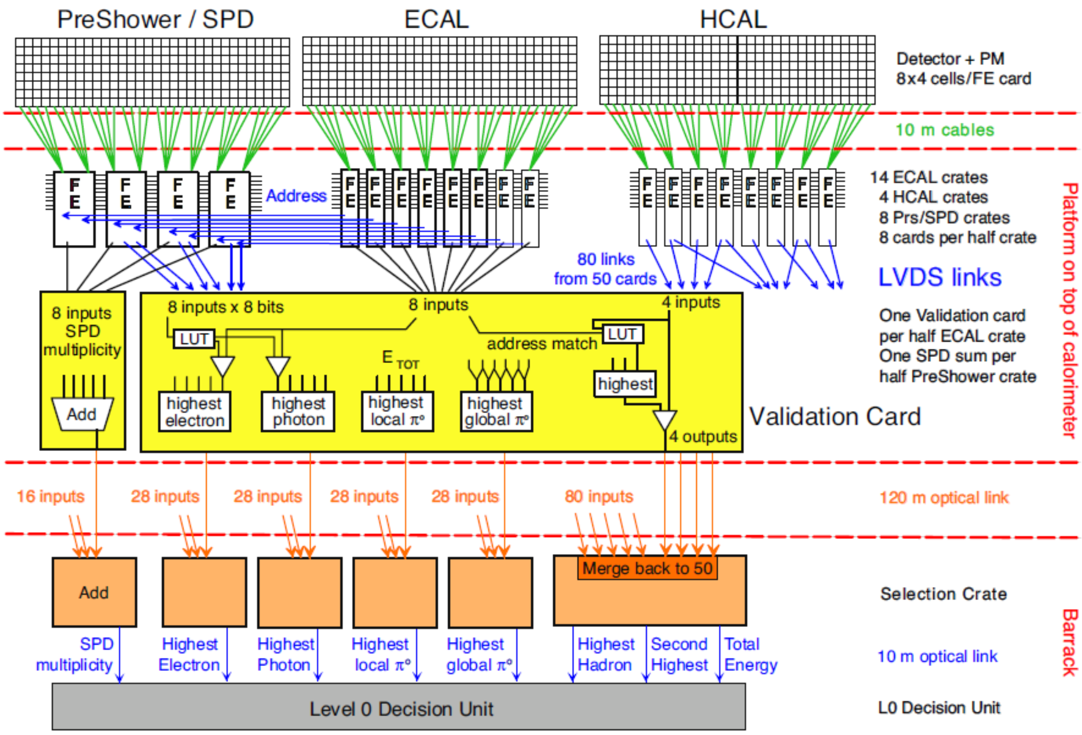

Figure 4.7: Level 0 calorimeter architecture: clusters made up by 2×2 cells are classified according to the information from every calorimeter layer. Highest E_T candidates of each type and the total multiplicity of the SPD are passed on to the L0 decision unit.

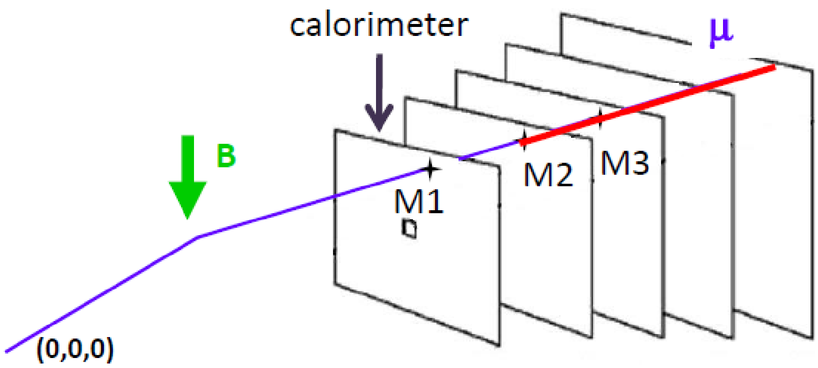

Figure 4.8: Level 0 muon candidate reconstruction and momentum estimate: starting from hits in M3, straight lines connecting each hit with the origin are defined. Each line is extrapolated to M2, M4 and M5, where hits are looked for in search windows around the extrapolation. If hits are found in the four detectors, the track position in M1 is determined by an straight line from M2 and M3 hits, selecting the hit in M1 closest to the extrapolation. M1 and M2 hits are then used in the p_T measurement of the candidate, from the change on the track slopes assuming the particle was produced at the origin and a single kick in the magnetic field.

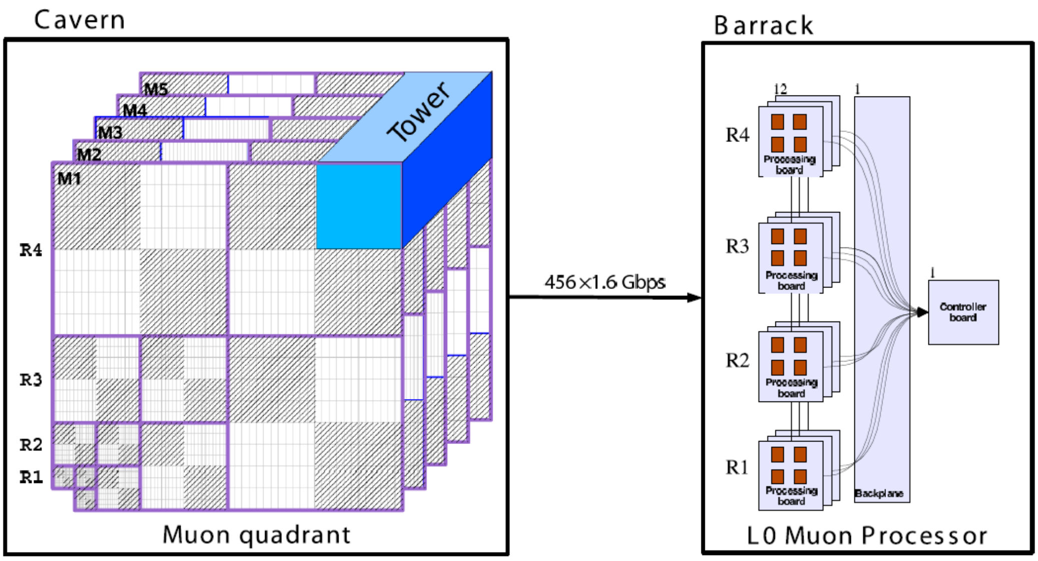

Figure 4.9: Level 0 muon architecture: each quadrant of the muon detector is connected to a L0 muon processor, which reconstruct the muon candidates. The two highest p_{T} candidates found in the quadrant are then selected and sent to the L0DU.

possibilities: each candidate is tried separately (*L0Muon*) or may be combined with the other candidate from the same quadrant so that the discriminating variable is now $p_T(1)+p_T(2)$ (*L0DiMuon*). The cuts applied reduce both the event rate and the number of candidates per event to be further processed. The L0DU produces the logical OR of several trigger conditions, each consisting on a threshold on $E_{\mathrm{T}}/p_{\mathrm{T}}$ for a type of candidate with optionally some GEC condition, and may introduce prescale factors in any of them. Passing candidates are then used as seeds for the HLT.

4.2.2 High level software trigger

After a positive decision of the hardware trigger, the detector is fully readout and the information is sent via a gigabit Ethernet to the EFF [110] (see Fig 4.4). The HLT is a C++ application (called *Moore*) running at the nodes of the EFF, which is built from general purpose CPUs (Fig 4.10). The HLT has access to full event information and could in principle execute the offline selection algorithms. However, due to the CPU power limitations, a complete reconstruction of the event is not possible at 1MHz, and a two-step process is needed.

The first stage (HLT1) must rely on a partial reconstruction of the events to reduce the minimum bias rate down to ∼40 kHz. The L0 decision produced for each event determines which sequences of algorithms (*alleys*) will be tried. Their common strategy consists of trying to confirm the L0 seeds with information from the tracking devices, namely T stations and VELO, in order to find high p_{T} tracks associated to them (step referred to as *L0 confirmation*). Primary vertices from pp collisions (PVs) are reconstructed at this stage, so cuts on the IP of the matched tracks can be applied as well. Finally, additional companion tracks can also be used in order to access new discriminating variables for improved performance.

Figure 4.10: View of a section of the LHCb Event Filter Farm, where the software trigger is executed.

The HLT1 alleys alternate selection and reconstruction algorithms in order to minimize the time spent per event. Each alley decision is independent of the others, so logically they can be imagined as running in parallel. However, they actually run in a sequence, so algorithms are designed to perform common tasks only once per event.

If an event is accepted by any of the alleys in HLT1, it then enters the second stage (HLT2), executed at a maximum rate of 40 kHz, in order to further reduce the event rate to the final trigger output rate of 2 kHz. HLT2 starts with the full reconstruction of the event, based on the forward tracking algorithm described in Section 3.2.2. Tracking at HLT2 thus represents an intermediate stage between HLT1 and offline reconstructions, in that all tracks are reconstructed, however with a simplified version of the offline tracking procedure (called fast track fit), which produces less precise measurements of the track parameters.

The HLT2 decision relies on *inclusive selections*, which search for generic signatures (displaced vertices, dilepton pairs, etc) of interesting b decays, as well as *exclusive selections*, where fully reconstructed b decays are looked for. Inclusive selections are generally robust against tracking inefficiencies and also allow to trigger interesting decays and its control channels with a single trigger line. By design, some redundancy between inclusive lines enables to perform cross checks for a better understanding of trigger acceptance effects. The disadvantage with respect to exclusive lines is that in order to be equally efficient for a given decay channel, the required output rate is higher.

HLT strategies have been optimized to efficiently select signal channels related to the main objectives of LHCb (for instance, in the case of HLT1, hadron [111], electromagnetic [112] and muon [113, 114] alleys have been developed). However, it must be noted that, since the HLT is fully implemented in software, it is very flexible and can adapt to changes in event reconstruction and selection software, and also evolves according to the physics priorities of the experiment. For example, an alternative strategy to the confirmation scheme of HLT1 has been recently developed, based on a refined tracking strategy [115].

HLT1 decision is then based on the presence of a single high p_T and IP track (*track trigger*), not necessarily associated to the object which triggered L0. This new approach is specially advantageous in the case of highly populated and pile-up events, where the reconstruction of all possible tracks which would confirm a L0 object is particularly time-consuming.

4.3 Muon triggers in HLT

This section describes the HLT strategies for generic B event selection based on the presence of muons in the b meson decay tree (HLT1 muon alleys and HLT2 inclusive muon selections), whose optimization and commissioning is the subject of this work.

4.3.1 HLT1

HLT1 muon triggers are only executed if the event was selected at L0 by the L0Muon or L0DiMuon conditions. Events passing the L0Muon condition enter the single muon, dimuon and muon+track alleys, while those selected by L0DiMuon follow only the dimuon selection sequence.

L0 muon confirmation with tracks

The first step in any HLT1 muon selection is the confirmation of muon segments found in L0 (either from L0Muon or L0DiMuon) with long tracks [116]. This is done by means of the following steps:

- A search for track segments is performed in the T stations trying to match the L0 muon candidates. Hits are looked for in search windows on both position and slopes compatible to the muon segment (Fig. 4.11). Once confirmed with T segment, the resolution on the measurement of muon candidates momenta has improved rfom the L0 value of 20% to $\sigma(p) = 2.3\%$ (Fig. 4.12, left).
- If any candidate is found, the complete 2D VELO tracking is performed.
- 2D VELO segments matching the T confirmed muon tracks are searched for.
- Matching VELO 2D segments are used as seeds for a VELO 3D reconstruction, by adding to them the information from the ϕ sensors.
- If VELO 3D segments are successfully reconstructed, its correspondence to the muon candidate is re-checked. The momentum resolution for muon candidates now confirmed with the VELO and T stations information has improved again, now to $\sigma(p) = 1.3\%$ (Fig. 4.12, right).

A robust, although slower, alternative to the last steps of the process involves skipping the 2D VELO matching step. Instead, the full VELO 3D reconstruction may be performed and VELO 3D segments tried to match with the T confirmed muons.

L0Muon candidates passing this process, in any of its two versions, are said to be confirmed. If no L0Muon or L0DiMuon candidate is confirmed, the HLT1 muon alleys are not executed.

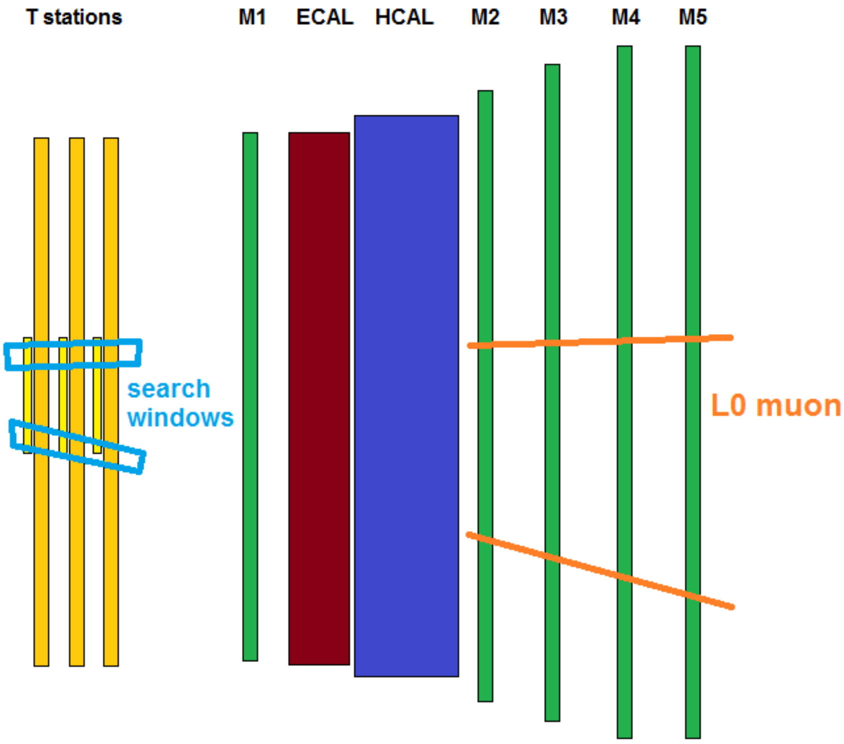

Figure 4.11: L0 muon candidate confirmation with T-tracks, Figure redrawn from [117].

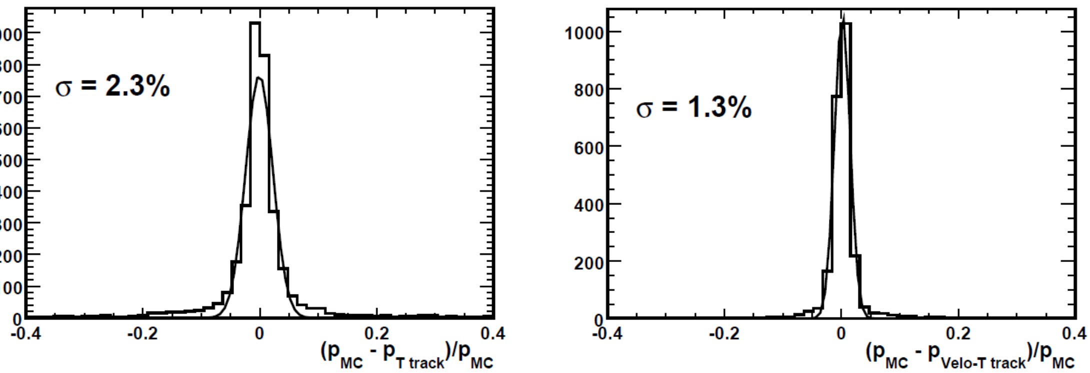

Figure 4.12: Momentum resolution of L0 muon candidates after confirmation with T-tracks and T+VELO tracks, calculated from p_{MC}, the true momentum of the MC particle, and p_{Ttrack} and $p_{Velo-Ttrack}$, momentum measurements after both stages of the confirmation process respectively. Figure from [113].

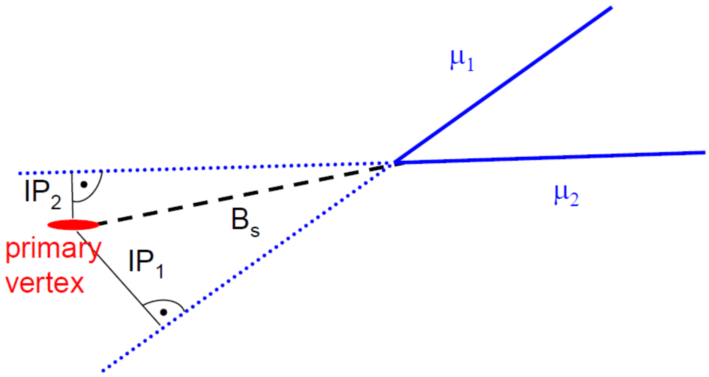

Figure 4.13: Impact parameter of muon tracks, for the example of a $B_s \to \mu^+\mu^-$ event.

Single muon strategy

Confirmed muon candidates have improved momentum resolution and therefore a new cut on p_{T} can be applied. After primary vertex reconstruction, the IP information is also available, hence a minimum value for the IP with respect to any PV may be required. Figure 4.13 illustrates the geometrical definition of the IP as the minimum distance between a straight line and a point, in this case between the tracks of the muon daughters in a $B_s \to \mu^+\mu^-$ decay and the PV.

Two variants of the single muon trigger have been implemented: an inclusive trigger for muonic B and D decays, which uses both p_{T} and IP cuts, and an *electroweak* trigger for muons coming from $W^{\pm}$ and Z^0 decays, which needs to trigger on prompt muons (and therefore does not use IP cuts) but exploits their very high p_{T}.

Dimuon strategy

The dimuon alley has the purpose of efficiently selecting decay processes with two muons in the final state, such as $B_d \to J/\psi(\mu^+\mu^-)K^*$. The triggering muon pairs may have been already selected by L0, in the form of two L0Muon candidates or one L0DiMuon candidate. In order to improve the performance, *muon segments* can also be reconstructed in HLT1. Straight segments in the muon stations are searched for, starting from hits in M5 to M2. The duplication of objects is avoided by excluding the hits already used by other candidates. The muon pair is in this case made up of a L0Muon triggering candidate and a recovered muon segment.

In the three cases, the first step is the confirmation of both muon segments as long tracks. Then, the distance of closest approach (DOCA) between them is used as a discriminating variable, as the confirmed muons in the pair are required to form a good vertex. Finally, both lifetime-biased (with cuts on the IP of both muons and a minimum invariant mass required) and unbiased selections (which employ a stronger cut in the invariant mass, hence referred to as *heavy dimuon*) are used. A total of six dimuon lines have been implemented.

Muon+track strategy

The muon+track alley presents some advantages with respect to the previously described single and dimuon alleys: first, the performance of a selection of events based on the presence of a single muon can be improved by adding further information from the decay; secondly, even if decays containing two muons are efficiently selected by the dimuon alley, the muon+track strategy provides a complementary trigger for multi-body decays, which adds robustness ensuring a good performance in the event of inefficiencies, either intrinsic to the muon chambers or due to the reconstruction process; finally it provides a sample of dimuon events without the requirement of particle identification for one of them (*tag and probe* method), useful to study the muon identification performance.

After the L0 muon has been confirmed, as in the case of the single muon selection, cuts on p_{T} and IP with respect to any PV are applied. The next step involves the reconstruction of the companion track, which is executed in a sequence of algorithms alternating reconstruction and filtering steps. If at any point in the sequence no candidate survives, the process is interrupted and the next strategy (if any) will be tried. The addition of information from the extra track is performed in the following steps:

- full VELO 3D reconstruction: VELO 3D tracks are reconstructed from the already available VELO 2D seeds.

- VELO 3D companion filter: VELO 3D tracks are filtered according to the likelihood of the companion track candidate to belong to a B decay together with the confirmed muon. The selected variables are: the minimum IP of the track to any PV, the DOCA between the two tracks and the difference in z coordinate (DZ) between the secondary vertex formed by the muon and companion track with respect to any PV.

- forward tracking: surviving VELO 3D companion tracks are extrapolated to the T stations.

- muon+long track filter: if any combination remains, further cuts can be applied on variables which use the momentum information from both tracks. A p_{T} cut is applied to the companion track. If the companion track is assigned the rest mass of a muon, the invariant mass of the pair can be calculated and required to be above a certain threshold. Finally, for a particle reconstructed from its decay products, the pointing variable [111] is defined as

$$Pointing = \frac{|\vec{p}|\sin\theta}{\sum\limits_{tracks} p_T^i + |\vec{p}|\sin\theta}, \tag{4.1}$$

  where $\vec{p}$ is the (partially) reconstructed mother momentum, θ is the angle between $\vec{p}$ and the direction defined by the primary and secondary vertices, and p_T^i are the transverse momenta of the daughter particles with respect to this direction. This variable, which exploits the conservation of momentum perpendicular to the flight direction of the mother particle, takes values in the [0,1] interval, with correctly reconstructed decays accumulated at 0. It is computed for the muon and companion track pair with respect to any PV, and the minimum is required to be below a certain cut.

Simplified track fitting

After HLT1 muon selections have been applied and both the event rate and the number of surviving candidates have been reduced, some extra rejection may be gained if the triggering tracks undergo a fast track fit (see Section 3.2.2). After the track fit, bad quality tracks may be rejected cutting on the track χ^2. As the track fit improves the extrapolation of the VELO part of the track to the beam axis, the resolution on the impact parameter is also improved and a new cut on IP may be applied (*afterburn cuts*). For muon tracks, the component of the track χ^2 which comes from the hits in the muon stations can be studied separately, acting as an estimate of the likelihood of the identification as a muon and helping in the rejection of candidates formed by spurious hits in the muon stations.

4.3.2 HLT2

As previously discussed, the input rate to the HLT2 is low enough so that its sequence of algorithms starts with the full reconstruction of the event, by producing primary vertices and long tracks. Inclusive muon selections in HLT2 are basically equivalent to those found in HLT1 alleys, except for the better quality tracking, which allows the rate of uninteresting events to be further reduced, while selecting efficiently signal events.

Single muon

The single muon selection in HLT2 requires either high IP and/or p_T cuts or a prescale factor in order to produce the sufficient minimum bias rejection to fit into the final 2 kHz. Its output is a high purity $b \to \mu X$ sample. Triggering events in the decay products of the B particle that accompanies the one which is the subject of our study (referred to as "opposite B", see Fig. 4.14) has a double interest. First, this selection produces b and c enriched data samples, important for posterior *data mining* of decay processes without dedicated trigger selections. Secondly, as the event has been selected by the trigger independently of the signal (named TIS events, see Fig. 4.15), it produces a trigger unbiased sample, useful to understand trigger efficiencies and acceptance effects, and in particular the possible correlations between trigger and tagging [118].

As in the case of the HLT1, a very high p_T single muon selection is used to trigger on muons from electroweak production processes.

Dimuon

Again, two tracks identified as muon are required to form a good vertex. Lifetime biased and unbiased selections have been implemented. Due to the improved tracking performance, momentum and mass resolutions are now close to offline values. This allows HLT2 to incorporate several lifetime unbiased dimuon selections dedicated to particles decaying into a pair of muons, such as $J/\psi \to \mu^+\mu^-$ and $\psi(2S) \to \mu^+\mu^-$. Rate reduction is achieved selecting only dimuon pairs with invariant mass inside a strict window around the particle's rest mass.

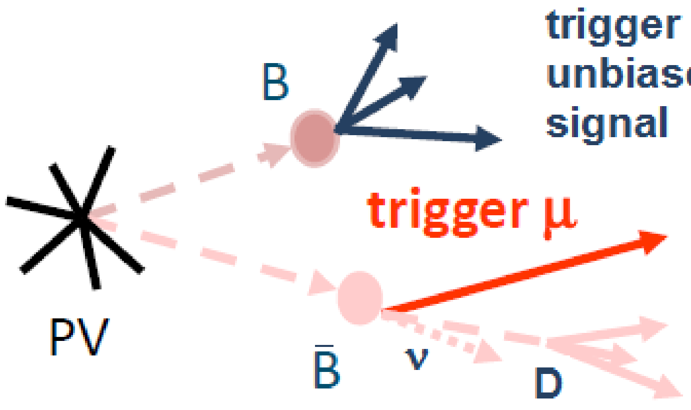

Figure 4.14: Event selected by the single muon trigger independently of the signal particle (B), as the triggering muon is a product of the semileptonic decay of the companion $\bar{B}$.

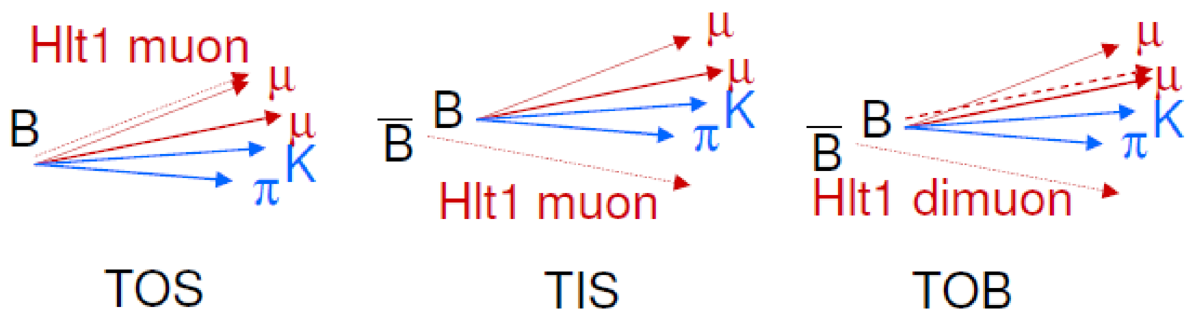

Figure 4.15: Trigger decision is classified in relation to signal, according to whether tracks corresponding to the particles in the signal decay chain have been involved in the trigger selection: single muon trigger on signal (TOS), single muon trigger independent of signal (TIS) and dimuon trigger on both (TOB) signal and opposite B decay products.

Muon+track

As in the case of HLT1, an inclusive selection based on the same muon+track strategy is implemented in HLT2. Again, it provides robustness and redundancy to the dimuon triggers, dedicated to trigger the main LHCb muonic channels. However, like the single muon selection, the muon+track strategy in HLT2 has the additional advante of yielding high purity samples of generic B decays and TIS events.

Chapter 5

Design and optimization of muon trigger lines with Monte-Carlo

This chapter summarizes the design, optimization and development of the HLT muon selections performed using simulated events until the start-up of the LHC.

This work was done in two phases. The first phase was devoted to the initial setup of the HLT. HLT1 alleys were implemented and their performance was tested on signal samples from the Data Challenge 06 (DC06) simulation, at the nominal LHC energy of 14 TeV. Once a relatively stable HLT1 was deployed, the design of the first HLT2 inclusive selections started.

The second phase was performed after the LHC incident in September 2008. It had been decided that the LHC would run initially at a lower energy and thus new simulation samples were produced, at the then presumed safe maximum collision energy of 10 TeV (MC09). In this second phase, a re-evaluation the performance of the HLT on these new conditions was required. In addition, some new studies were dovoted to establish different working scenarios according to the foreseen evolution of the LHC luminosity.

The sections of this chapter follow these two stages, starting with the design of the HLT1 muon+track alley and the HLT2 muon+track selection with DC06. The integration of HLT2 inclusive muon selections into a coordinated strategy for muonic channels is then discussed, first for stable long term running conditions, represented by the DC06 samples, and secondly, for different LHC luminosity scenarios, corresponding to successive steps in the LHC start-up, using MC09 simulation.

5.1 HLT1 muon+track alley

This section describes the study leading to the initial optimization of the muon+track HLT1 alley, as described in [114]. Once a set of discriminating variables has been chosen (see Section 4.3.1), the performance of the strategy is evaluated. A wide range of values for each of the cuts is studied in order to determine the best possible performance and an example working point is provided.

5.1.1 Benchmark channels

Semileptonic b decays, which contain one muon and other charged decay products, have been chosen as benchmark to study the performance of the muon+track alley. The study of semileptonic decays contributes to the measurement of the CP violation in B system mixing (Section 2.3.4). Due to their large branching fraction, semileptonic decays are also used by LHCb as control channels to calibrate the performance of flavour tagging algorithms [119], which aim for the determination of the B hadron flavor at production. The channels used here are two, $B_d \to D^{*-}(D(K^+\pi^-)\pi^-)\mu^+\nu_\mu$ and $B_s \to D_s^-(K^+K^-\pi^-)\mu^+\nu_\mu$ [120, 121]. They both correspond to neutral B mesons, hence they are equally useful for calibrating same-side and opposite-side tagging methods.

The MC samples used are part of DC06-phys-v2-lumi2, simulated for an instantaneous luminosity of $2\times10^{32}\text{cm}^{-2}\text{s}^{-1}$ with packages Gauss v25r8, Boole v12r10 and Brunel v30r14. Signal samples include both direct decays and events with intermediate decays such as $\tau^- \to \mu^-\nu_\tau\bar{\nu_\mu}$ and $D_s^{*-} \to D_s^-\gamma$. On these signal samples, the selection criteria shown in Table 5.1, optimized by the developers of the physics selections ([36, 122]), are applied, resulting in 1220 and 985 signal events for the $B_s \to D_s^-\mu^+\nu_\mu$ and $B_d \to D^{*-}\mu^+\nu_\mu$ channels respectively. In order to estimate the trigger rate, one million minimum bias events have been used. This sample amounts for 13.2 μb^{-1}, which is equivalent to 0.066 seconds of collisions at design luminosity.

	Cut	$B_d \to D^{*-}\mu^+\nu_\mu$	$B_s \to D_s^-\mu^+\nu_\mu$
	p>	2000 MeV/c	2000 MeV/c
D/D_s daughters	p_T >	300 MeV/c	500 MeV/c
	IPS >	2	3
Soft pion	IPS >	1	
Muon	p_T >	1000 MeV/c	1000 MeV/c
	IPS >	2	2
	χ^2 <	25	
D	Δm_D <	25 MeV/c^2	
	p_T >	1200 MeV/c	
	FS >	2.5	
	χ^2 <	25	10
	$\Delta z(D_s - PV)$ >		1 mm
D^*/D_s	IPS >		3
	p_T >	2000 MeV/c	1500 MeV/c
	$\Delta m_{D^*/D_s}$ <	50 MeV/c^2	20 MeV/c^2
	$m_{D^*} - m_D$	143.74 - 147.25 MeV/c^2	
	χ^2 <	20	5
	$\Delta z(D - B)$ >	0 mm	
B/B_s	$\Delta z(B - PV)$ >	0.5 mm	
	$\cos(\theta_B)$ >		0.999
	m_{B/B_s}	(3, 5.4) GeV/c^2	(3, 5.7) GeV/c^2

Table 5.1: Selection criteria for the benchmark semileptonic decays considered. See references [36,122] for full explanation of selection criteria.

HLT algorithms and structure used in this study are those found in the HltSys v4r3 and HltConf v1r5 packages, implemented to run on DaVinci v20r3.

5.1.2 L0 muon and confirmation efficiencies

Table 5.2 shows the partial efficiencies of the trigger steps preceding those studied here: the L0 single muon selection (p_{T} >1 GeV/c) and the muon confirmation sequence, for both signal channels. Efficiencies for these steps on minimum bias events determine their trigger rate. The output rate of the L0 single muon line is 279 ± 2 kHz, while the output rate of the muon confirmation is 142.9 ± 1.5 kHz.

For the optimization of the trigger selection, only events in which the trigger decision is based on particles from the signal decay are used (TOS, see Fig. 4.15). The association between reconstructed trigger tracks and Monte Carlo particles is based in a cut in the angle between the directions at the interaction region (at 0.001 radians). Table 5.2 shows in addition the percentage of TOS events amongst those passing L0 and muon confirmation as well as the final cumulative L0 × Muon confirmation × TOS efficiency. The efficiencies given in the coming section always refer to events passing both the L0 single muon line and the muon confirmation as TOS.

	L0Muon	Muon Confirmation	TOS	Cumulative
$\epsilon(B_d \to D^{*-}\mu^+\nu_\mu)$ (%)	83	93	96	74
$\epsilon(B_s \to D_s^-\mu^+\nu_\mu)$ (%)	79	94	97	72

Table 5.2: Partial efficiencies for L0 single muon, muon confirmation and for the additional requirement of both L0 and muon confirmation to be TOS for both semileptonic channels. Last column indicates cumulative efficiency for the three requirements.

5.1.3 Study of muon+track discriminating variables

The strategy to illustrate the effect of each individual cut and to find a benchmark set of cuts is the following: signal efficiency versus minimum bias output rate is studied for pairs of related variables. For each pair of variables, the most stringent pair of cuts retaining ~100% efficiency is selected, and applied in the study of the remaining parameters. The choice of the cuts while still on the efficiency plateau ensures that the conclusions are independent of the order in which the cuts are studied, since each individual cut does not introduce significant biases to the sample. The figures shown correspond to $B_s \to D_s^-\mu^+\nu_\mu$, but a similar behavior is found for every variable in the case of $B_d \to D^{*-}\mu^+\nu_\mu$.

Figure 5.1 shows the signal efficiency versus rate for combinations of the p_{T} cut for the muon and the additional tracks used in this selection (*companion tracks*). The most stringent p_{T} combination is 1 GeV for the muon and 0.8 GeV for the additional track. These are the values used in the next steps.

Cuts in DOCA are not useful to reduce rate in the absence of a DZ cut, as every pair of tracks originating from the primary vertex does have low DOCA. But this variable reduces the number of candidates to consider, improving timing performance, and also prevents triggering on a combination of decay products from the two B mesons present in the event (TOB, see Fig. 4.15). When both vertex cuts are combined, along with the best combination of muon and track p_{T} cuts, a clear plateau behavior appears, as Fig. 5.2 shows. From the end of the plateau, the best combination is chosen, with the result of DOCA cut at 0.4 mm and DZ at 1.5 mm.

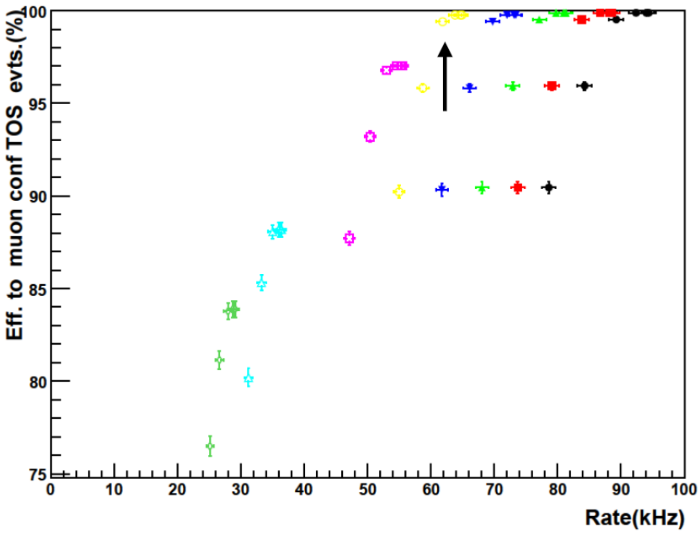

Figure 5.1: $B_s \to D_s^- \mu^+ \nu_\mu$ efficiency vs. rate for combinations of muon and companion track p_T cuts. Different shape indicate different muon p_T cuts, with values [0, 400, 600, 800, 1000, 1200, 1600, 1800] MeV. Different entries for the same shape indicate different values of the companion p_T cut, with values [0, 400, 600, 800, 1000, 1200] MeV. The combination selected is indicated with an arrow.

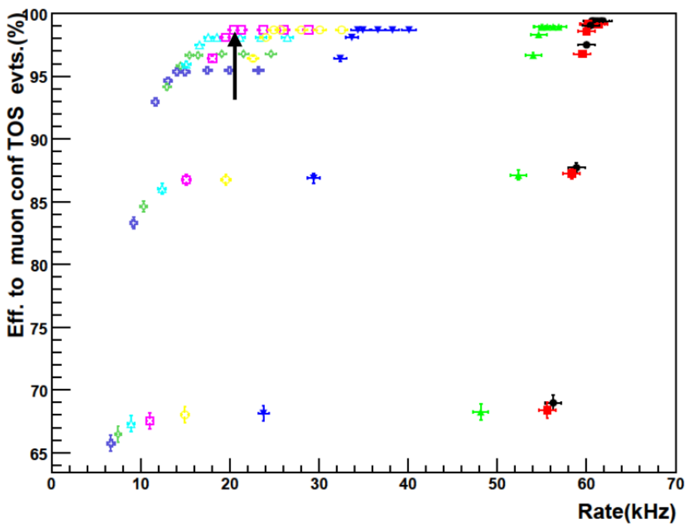

Figure 5.2: $B_s \to D_s^- \mu^+ \nu_\mu$ efficiency vs. rate for different DZ and DOCA cuts applied simultaneously, after cuts on muon and track p_T have been applied at 1 and 0.8 GeV respectively. Different DZ cuts, with values [no cut, -2, 0, 0.5, 1, 1.5, 2, 2.5, 3] mm are indicated by different shapes. Different entries for the same shape indicate different values of the DOCA cut at [no cut, 2, 1, 0.5, 0.4, 0.3, 0.2, 0.1, 0.05] mm. The combination selected is indicated with an arrow.

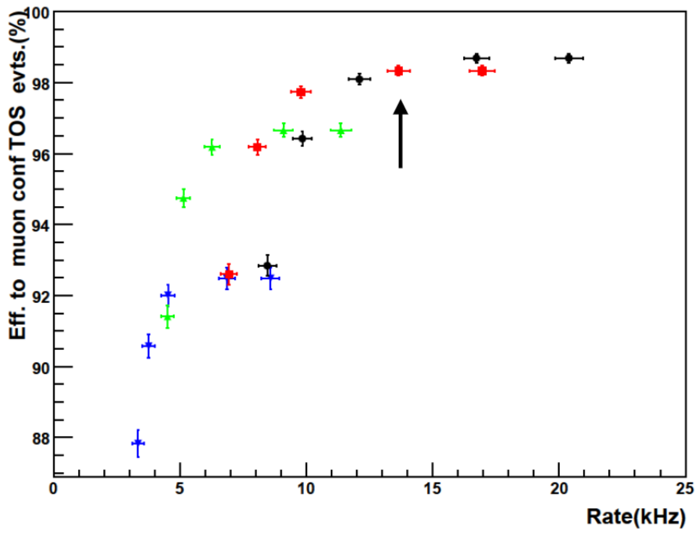

Figure 5.3: $B_s \to D_s^- \mu^+ \nu_\mu$ efficiency vs. rate for combinations of muon and track minimum IP, after cuts on muon and track p_T have been applied at 1 and 0.8 GeV respectively plus a DZ cut at 1.5 mm and in DOCA at 0.4 mm. Different cuts on muon IP are indicated by different shape with values of [0, 25, 50, 75] μm. Different entries for the same shape indicate different cuts on the companion track IP, with values of [0, 50, 100, 150, 200] μm. The combination selected is indicated with an arrow.

Then, cuts on minimum value of muon and track IP to any reconstructed PV are applied on events passing the chosen combination of muon and track p_T and vertex DOCA and DZ cuts. Results are shown in Fig. 5.3. Best values are 25 μm for the muon and 50 μm for the extra track.

Figure 5.4 shows the effect of additional cuts on vertex pointing variable (see Eq. 4.1) and invariant mass. Cuts are chosen at 0.4 for the pointing variable and 1 GeV for invariant mass.

Table 5.3 shows the effect of each of the selected cuts when considered individually on both signal samples, as a percentage of passing TOS events with respect to muon confirmed TOS events. The efficiencies are high, although slightly lower for $B_d \to D^{*-} \mu^+ \nu_\mu$, mainly for the DZ cut, which can be explained by the different criteria applied in the selection of the secondary vertex. As the pointing cut also requires the secondary vertex to be sufficiently far from the primary vertex (in order to better determine the flight direction of the B meson), the efficiency is also slightly worse for this channel.

The previous steps allow us to determine the end-of-plateau point. This point corresponds to the maximum rate reduction that the muon+track alley is capable of, while still being nearly 100% efficient on signal. The next objective is to study the maximum efficiency that the alley can provide as a function of the allowed rate. In order to do that, all parameters are varied simultaneously in regions around the end-of-plateau point. Three scenarios have been considered:

- simple cuts: individual track cuts (p_T and IP) plus DOCA and DZ.
- the above simple cuts plus invariant mass cuts.

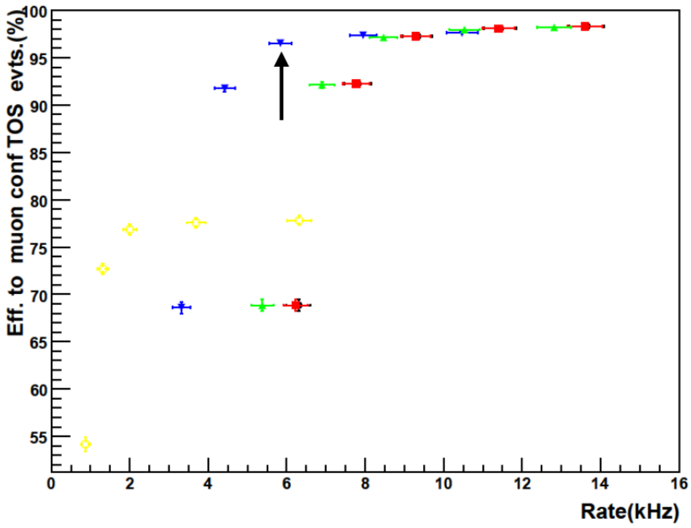

Figure 5.4: $B_s \to D_s^- \mu^+ \nu_\mu$ efficiency vs. rate for combinations of cuts on muon+track vertex pointing variable and invariant mass, after cuts on p_T and IP have been applied at 1 GeV and 25 μm for the muon and 0.8 GeV and 50 μm for the companion track, plus a DZ cut at 1.5 mm and in DOCA at 0.4 mm. Different cuts on the pointing variable are shown as different shapes with values at [1, 0.8, 0.6, 0.4, 0.2]. Different entries for the same shape indicate different cuts on invariant mass, with values [0, 500, 1000, 1500, 2000] MeV. The combination selected is indicated with an arrow.

- the above simple cuts plus invariant mass, plus pointing cuts. This option is studied separately due to the non trivial correlations between pointing and lifetime that could in principle disfavor the use of this parameter.

Figure 5.5 shows the best performance for each scenario for a range of alley output rates. Note that the first scenario, with simple variables, provides equal results than more complicated choices above ∼14 kHz. However, already at 10 kHz the results are better if the mass or the mass and pointing cuts are included. The third strategy is undoubtedly the best if the final desired rate is of 5 kHz or below.

For comparison, results obtained with a trigger line based only on the properties of a confirmed muon, with cuts on p_T and IP (single muon alley) are also presented. It is clear that using information from the extra tracks allows the rate to be reduced while retaining higher efficiencies.

5.1.4 Performance at an example working point

Efficiencies and rate

Table 5.4 shows the signal partial and cumulative efficiencies, minimum bias retention and number of candidates processed per filtered event, as well as the output rate for each algorithm, when the discriminating parameters are set to the values for the end-of-plateau point proposed in the previous section.

Signal is shown to be efficiently selected by the algorithms and cut values that make up the muon+track alley. The highest loss of signal events is produced at L0 (with a

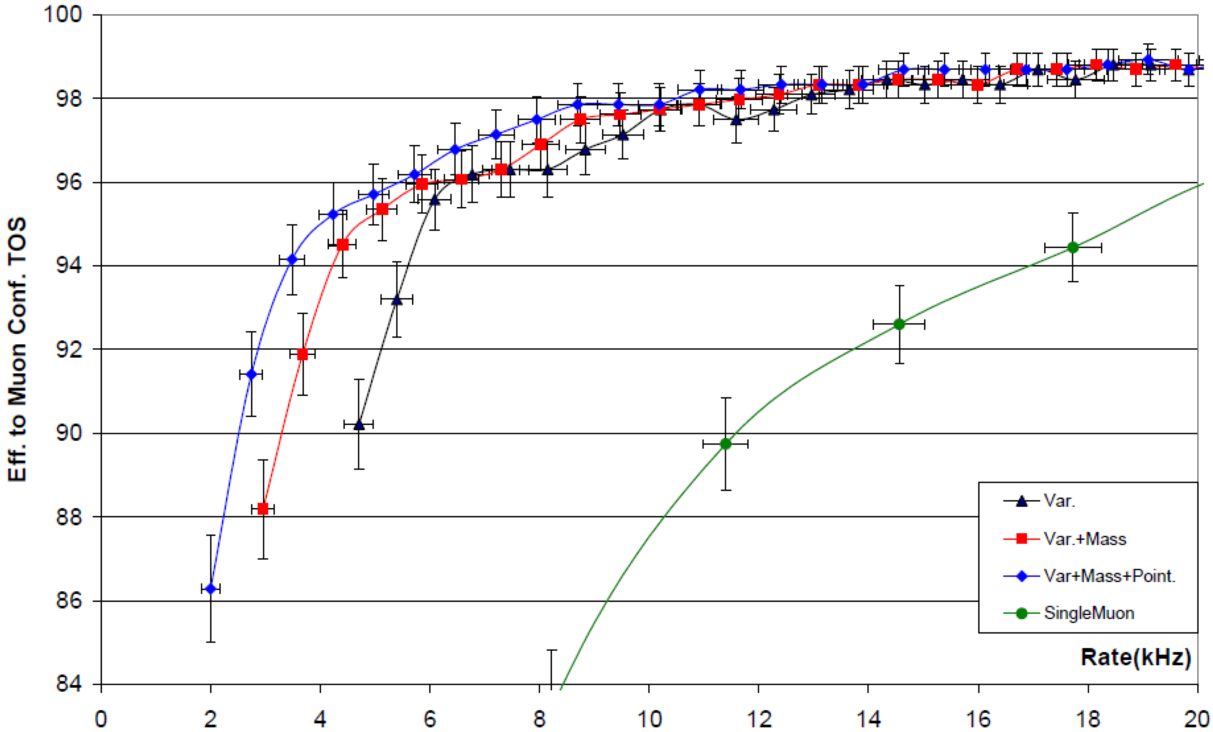

Figure 5.5: $B_s \to D_s^- \mu^+ \nu_\mu$ best efficiency vs. rate taken from all combinations of cuts on simple variables (p_{T}, IP, DOCA and DZ), these variables plus invariant mass (Var.+Mass), and simple variables plus mass and pointing (Var.+Mass+Point.). For comparison, the best results for a single muon line based in one confirmed muon with p_{T} and IP cuts are shown. Note that uncertainties in different curves are correlated.

Variable	Cut value	$\epsilon(B_s \to D_s^- \mu^+ \nu_\mu)$ (%)	$\epsilon(B_d \to D^{*-} \mu^+ \nu_\mu)$ (%)
Muon p_T >	1 GeV/c	99.8	99.7
Track p_T >	0.8 GeV/c	99.5	99.4
|Muon IP| >	25 μm	99.5	99.4
|Track IP| >	50 μm	99.9	99.6
Vertex DZ >	1.5 mm	99.4	98.1
Vertex DOCA <	0.4 mm	99.9	99.7
Vertex Pointing <	0.4	99.5	99.0
Inv. Mass >	1 GeV/c^2	99.5	99.6

Table 5.3: Percentage of events retained for each of the chosen cuts individually for both signal channels with respect to muon confirmed TOS events.

p_T threshold equal to the cut applied by both physics selections but poorer momentum resolution), and at the L0 confirmation with tracks, stages that are common to the single muon alley. The following steps, exclusive to the muon+track alley, explain the differences in performance with respect to the single muon selection shown in Fig. 5.5.

Minimum bias rate is largely reduced by the cuts applied in the muon+track sequence, from a starting of 143 kHz (muon confirmation) to final 7 kHz, i.e. a reduction factor ~20. Note that the algorithms filtering VELO tracks do not reduce the rate significantly, but they still play an important role in the timing performance of the alley, as they reduce the number of VELO segments that will be used as seeds for tracking in the T stations.

Algorithm	$\epsilon(B_s \to D_s^- \mu^+ \nu_\mu)$		$\epsilon(B_d \to D^{*-} \mu^+ \nu_\mu)$		Minimum Bias		
	%	%	%	%	Retention	Candidates	Rate (kHz)
L0 single muon	82.6	82.6	78.8	78.8	1.84		279
L0 muon confirmation	92.6	76.5	93.6	73.7	51.1		143
Muon p_T and IP cuts	98.0	75.0	97.9	72.2	43.3	1.2	61
VELO 3D reconstruction	100	75.0	100	72.2	100	70.4	61
Track IP and DOCA cuts	100	75.0	100	72.2	100	28.4	61
Vertex DZ cut	99.9	74.9	100	72.2	91.0	7.1	55
Forward tracking	99.9	74.8	99.8	72.1	87.1	5.4	48
Track p_T cut	99.3	74.3	98.0	70.7	35.3	2.4	17
Vertex mass cut	99.0	73.6	99.4	70.3	67.8	1.8	12
Vertex pointing cut	98.4	72.4	97.5	68.6	54.6	1.8	7

Table 5.4: Muon + track algorithm sequence with partial and cumulative efficiencies for signal channels and partial retention, average number of candidates filtered by each algorithm per minimum bias event and equivalent rate.

Timing

Table 5.5 summarizes the time consumption of algorithms (total and average on events in which they are invoked) and the overall time spent by the alley on 150,000 minimum bias events. The selection parameters are those of the end-of-plateau working point described in the previous section. Time measurements were performed on a PC with a speed about 2.73 times higher than that of a 2.8 GHz Xeon, similar to the CPUs integrated in the EFF.

The most time demanding algorithms by far are those related to reconstruction, that is,

Algorithm	Average time per event (ms)	Min (ms)	Max (ms)	Times executed	Total (s)
Muon track pT and IP cuts	0.009	0.005	0.1	1400	0.012
VELO 3D reconstruction	2.293	0.222	94.1	603	1.383
Extra track IP and DOCA cuts	0.088	0.016	0.7	603	0.053
Muon + extra track vertex maker	0.1	0.028	1.0	603	0.063
Vertex DZ cut	0.021	0.006	0.1	603	0.013
Forward tracking of extra track	4.274	0.070	32.4	550	2.351
Final muon+track decision	0.018	0.007	0.1	478	0.009
Total	2.774			1400	3.884

Table 5.5: Algorithm timing results for the end-of-plateau cuts, after running on 150,000 minimum bias events. Average processing time per event, as well as maximum and minimum processing times, are shown. Taking into account the number of times that each algorithm was executed, the total time consumption per algorithm over the whole sample and the final time required for the entire sequence are shown in the last column.

the complete VELO 3D track reconstruction and the upgrade of the selected segments to complete tracks by extrapolating them to the T stations. In contrast, selection algorithms spend a tiny fraction of the total time.

Note that the values of the selection parameters of this working point have been selected to maximize the efficiency for a given rate, without any restriction on the alley time consumption. It is possible to improve the time performance of the alley by just tightening the cuts before reconstruction stages, although at the expense of some inefficiencies. As an example, if the cut on the muon track IP is increased from 25 to 50 μm, the time per event is reduced from 2.774 ms to 1.403 ms, while the final rate decreases from 7 to 5 KHz and the efficiency by only 2%.

5.2 HLT2 muon+track selection

This section describes the implementation and optimization of the muon+track strategy in the context of HLT2.

5.2.1 Benchmark channel

Preliminary tests indicated that minimum bias rate can be effectively reduced by the inclusive lifetime-unbiased dimuon triggers [125], which rely on cuts on the dimuon invariant mass with values typically over 2 GeV/c^2. These triggers select efficiently decays such as $B_s \to \mu^+\mu^-$ and $B_s \to J/\psi(\mu^+\mu^-)\phi$.

Such a strategy is not possible in the case of $B_d \to K^*(K^+\pi^-)\mu^+\mu^-$, due to its softer dimuon invariant mass distribution (with the region identified for maximum sensitivity to the measurement of the forward-backward asymmetry starting at 1 GeV/c^2, see Section 2.3.2). A lifetime-biased dimuon selection substituting mass cuts by impact parameter requirements can be considered as the alternative trigger. However, Fig. 5.6 shows that low momentum muons are not efficiently reconstructed by HLT2, which is less efficient compared to the more sophisticated offline reconstruction and muon identification procedures. The requirement of finding two HLT2 muon tracks TOS is only 88% efficient with respect

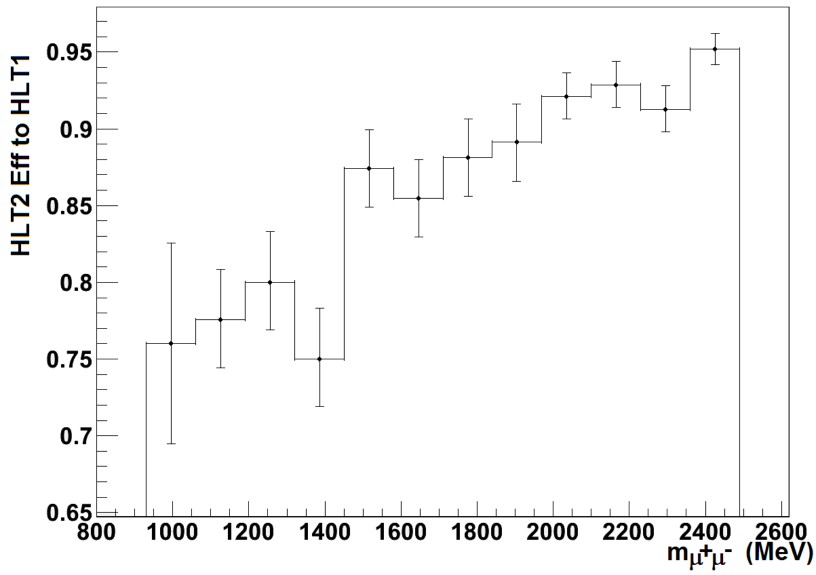

Figure 5.6: HLT2 efficiency to reconstruct two muon tracks TOS as a function of the invariant mass of the MC muon pair, for offline selected $B_d \to K^*\mu^+\mu^-$ events, calculated with respect to those passing any L0 and HLT1 selection. The overall efficiency is 88%.

to events passing any L0 and HLT1, in contrast to decays such as $B_s \to J/\psi(\mu^+\mu^-)\phi$, which is 94% efficient. A lifetime-biased dimuon selection for this channel would therefore suffer from poor HLT2 muon reconstruction.

In contrast to dimuons, Fig. 5.7 shows the efficiency to find a TOS combination of a muon and a track associated to another charged particle from the decay with respect to events passing any L0 and HLT1, which is above 95% even in the bins corresponding to lower momentum muons. The integrated efficiency is 98%. The muon+track selection is hence considered an alternative to dimuon lines for this channel, and in general for the selection of decays with relatively soft muons. $B_d \to K^*\mu^+\mu^-$ is chosen as the benchmark channel for the optimization of the HLT2 muon+track selection.

A sample of 1000 signal events, offline selected and provided by the authors of the physics selections [123, 124], is used for the optimization of the selection. The minimum bias output rate is computed from a sample of 15,000 events passing L0 and HLT1 [126] at a rate of 36.5 kHz. Analysis software for this work is DaVinci v23r0p1.

5.2.2 L0 and HLT1 efficiencies

Table 5.6 shows minimum bias rate and signal efficiencies for L0 and HLT1 muon lines. The HLT1 muon+track provides higher signal retention than single muon and dimuon alleys while consuming a small fraction of the rate. This proves the advantage that the muon+track strategy represents for $B_d \to K^*\mu^+\mu^-$ at HLT1. The overall HLT1 efficiency with respect to L0 is 92%, while the cumulative L0 and HLT1 efficiency is 82%.

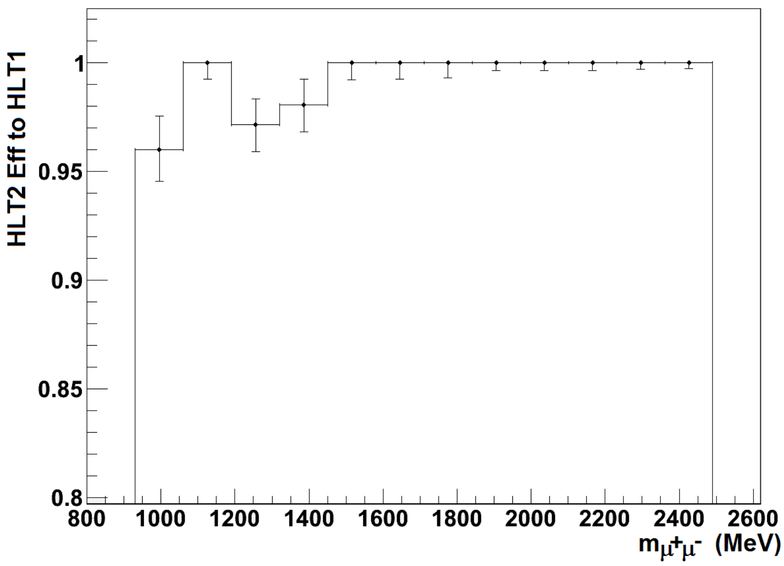

Figure 5.7: HLT2 efficiency to reconstruct a muon and companion tracks TOS as a function of the invariant mass of the MC muon pair, for offline selected $B_d \to K^*\mu^+\mu^-$ events, calculated with respect to those passing any L0 and HLT1 selection. The overall efficiency is 98%.

Trigger lines	$\epsilon(B_d \to K^*\mu^+\mu^-)$ (%) relative to L0	cumulative	Minimum bias rate (kHz)
L0 any	-	89.5	-
HLT1 single muon	73	65	7.4
HLT1 dimuon	58	52	7.6
HLT1 muon+track	76	68	1.7
HLT1 all	92	82	36.5

Table 5.6: L0 and HLT1 muon alleys $B_d \to K^*\mu^+\mu^-$ efficiencies (relative to L0 and cumulative) and minimum bias rate. Efficiencies and rates for single muon and dimuon alleys take into account both lifetime-biased and lifetime-unbised selections.

5.2.3 Optimization of discriminating variables

The optimization is performed in a similar manner to the HLT1 case. The same parameters are employed, although with increased discriminating power, given the improved track reconstruction used by HLT2. Additional parameters such as the momentum or transverse momentum of the muon+track combination have also been considered, although they are not finally used as they do not improve the discriminating power of the variables presented in the HLT1 alley.

The optimization is again performed by selecting trigger tracks associated to signal decay products, that is, computing TOS efficiencies. As previously discussed, requiring one muon+track candidate to be reconstructed in HLT2 is 98% efficient TOS for $B_d \to K^*\mu^+\mu^-$, while it reduces the output rate from 36.5 kHz to 27 kHz. This represents the starting point of the optimization process. In the following, efficiencies have been calculated with respect to all signal events passing L0 and any HLT1 alley.

Figure 5.8 presents the dependency of the signal efficiency and rate for different cuts on

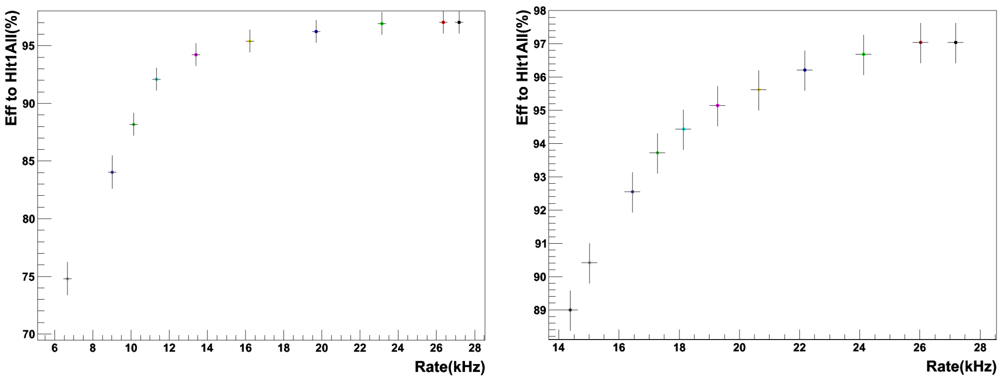

Figure 5.8: $B_d \to K^*\mu^+\mu^-$ efficiency vs. rate for muon p_{T} with values [0, 200, 400, 600, 800, 1000] MeV/c (left) and IP cuts with values [0, 20, 40, 60, 80, 100] μm (right).

muon p_{T} and IP independently. Cuts on both variables are then applied simultaneously and the combinations providing best efficiency amongst those producing comparable rates, within the statistical uncertainty, are chosen (shown in Fig. 5.9). With moderate cuts, p_{T} $>$ 800 MeV and IP$>$ 60 μm, $\sim$98% of the events are selected (94% taking into account the initial reconstruction efficiency), while the rate has been reduced to 8-10 kHz.

After p_{T} and IP cuts are applied on the muon track, the DZ and DOCA variables of the muon+track vertex are explored. Figure 5.10 shows the plateau on signal efficiency with increasingly restrictive DOCA cuts. The best efficiency at every rate for combinations of DOCA and DZ is displayed in Fig. 5.11. A working point is selected for a DZ cut at 1 mm and a DOCA cut at 0.15 mm, with an accumulated efficiency of $\sim$92%, with an output rate of 5 kHz.

After requiring DZ and DOCA, the pointing variable for each muon+track combination is studied with respect to any PV. A plateau behavior is observed in Fig. 5.12, up to values around 0.4, which is selected as the working value.

The next variable considered is the muon+track invariant mass, computed with the assignment of the muon rest mass for the companion track, as defined for HLT1. In order to prevent any possible acceptance effects from this cut to the $B_d \to K^*\mu\mu$ q^2 distribution (see [seccion AFB]), the contribution to the trigger selection from neutral and charged combinations is studied separately. Figure 5.13 shows that in both cases, there exists an efficiency plateau up to $\sim$2 GeV/c^2. A cut value at 2.2 GeV/c^2 is chosen.

At the values chosen for the cuts, the rate has been reduced to $\sim$1 kHz while the TOS signal efficiency, including the reconstruction of the muon, is $\sim$90% with respect to HLT1.

This rate is however excessive for an HLT2 selection, which should fit into a total minimum bias rate of 2 kHz. Further rate reductions are obtained at the expense of higher efficiency losses. In order to fine tune the cuts for a particular working rate, a simultaneous variation of the variables with bigger impact on selection rate is performed. Figure 5.14 summarizes the best efficiency at any working rate for combinations of cuts on the muon and companion track p_{T} and IP and on the pointing variable for the muon+track pair. A working point is chosen, with cuts on p_{T} and IP at 1000 MeV/c and 80 μm for the muon and 600 MeV/c and 100 μm for the track. The cut on pointing variable remains at 0.4. This set of cuts produces a TOS signal efficiency of 87% for a rate of 0.7 kHz.

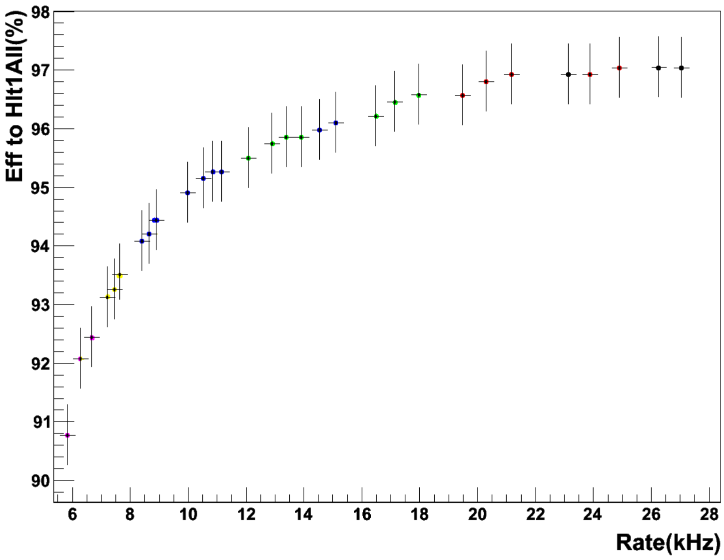

Figure 5.9: $B_d \to K^* \mu^+ \mu^-$ best efficiency vs. rate for the combinations of muon p_{T} and IP cuts given in Fig. 5.8. Same color indicates combinations for the same p_{T} but different IP cuts.

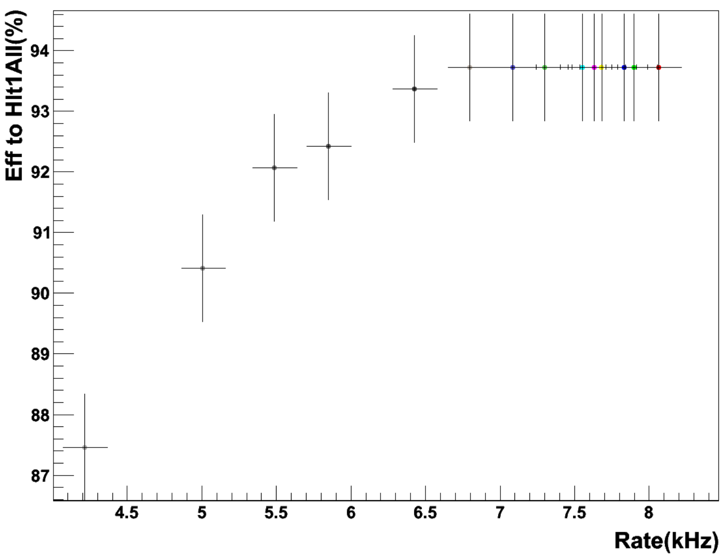

Figure 5.10: $B_d \to K^* \mu^+ \mu^-$ efficiency vs. rate for muon+track DOCA cuts with values [no cut, 5, 2, 1.5, 1, 0.8, 0.6, 0.4, 0.3, 0.25, 0.2, 0.15, 0.1, 0.08, 0.06] mm.

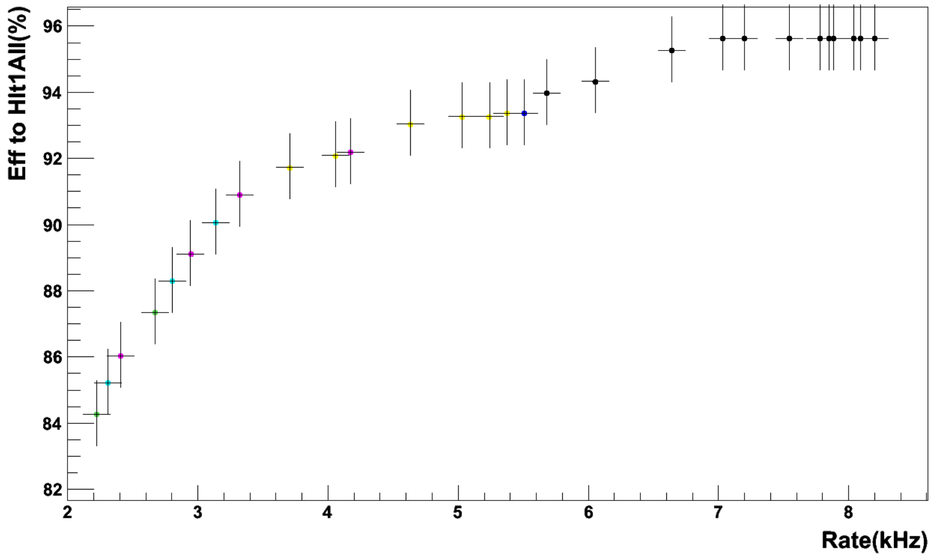

Figure 5.11: $B_d \to K^*\mu^+\mu^-$ best efficiency vs. rate for muon+track vertex DOCA and DZ combinations of cuts. Color indicates combinations for the same DZ threshold, with cuts at [no cut, 0.5, 1, 1.5, 2, 2.5] mm, and different DOCA cuts (listed in Fig. 5.10).

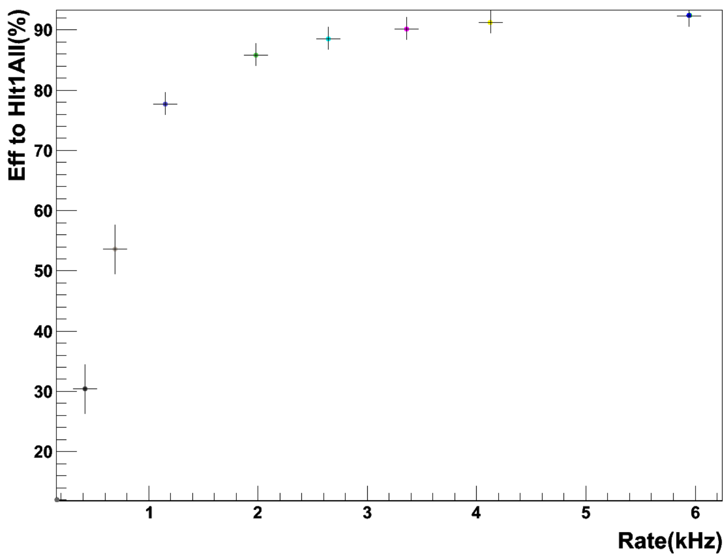

Figure 5.12: $B_d \to K^*\mu^+\mu^-$ efficiency vs. rate for muon+track pointing cuts with values [1, 0.8, 0.6, 0.5, 0.45, 0.4, 0.35, 0.3, 0.25, 0.2, 0.15, 0.1]. The first four values produce identical results, represented by the first point.

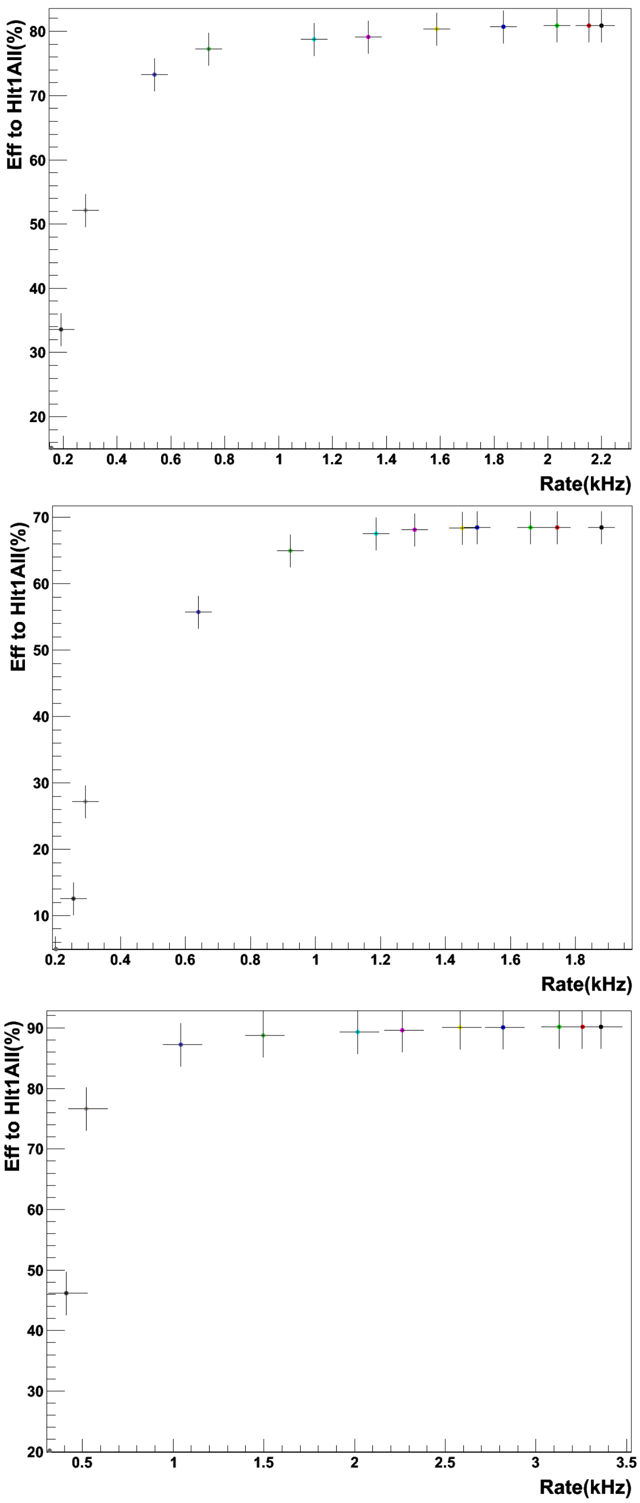

Figure 5.13: $B_d \to K^*\mu^+\mu^-$ efficiency vs. rate for muon+track invariant dimuon mass cuts with values [0, 0.4, 0.6, 1, 1.2, 1.6, 1.8, 2.2, 2.6, 3, 3.4, 3.8] GeV/c^2 for opposite (top), same (middle) and both (bottom) charge combinations.

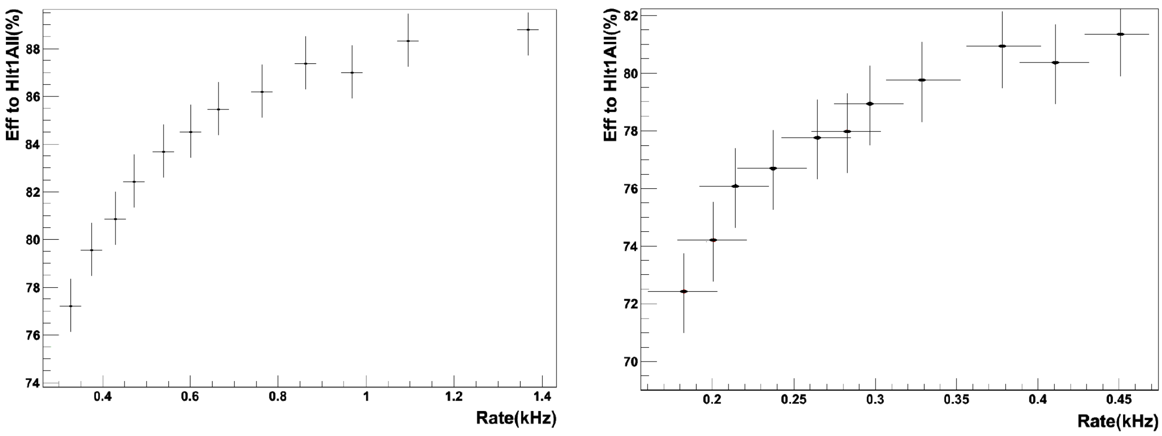

Figure 5.14: $B_d \to K^*\mu\mu$ best TOS efficiency vs. rate for LHT2 muon+track selection, calculated from combinations of cuts on p_T and IP for both muon and companion tracks and on the combination pointing.

5.2.4 Trigger acceptance effects on $B_d \to K^*\mu^+\mu^-$

When muon+track candidates passing the HLT2 selection are matched to MC particles for the true $B_d \to K^*\mu^+\mu^-$ decay, their composition results in 56% muon+kaon, 41% muon+pion and 3% muon+muon. If the invariant mass constraint (2.2 GeV/c^2) is removed, the composition changes to 41% muon+kaon, 34% muon+pion and 23% muon+muon. The cut on invariant mass, helpful in the rejection of minimum bias events tends to remove the dimuon candidates. With this cut, the muon+track is basically a muon+kaon or a muon+pion trigger.

This represents in fact the advantage of avoiding trigger-induced biases on the q^2 distribution ($= m^2_{\mu\mu}$, $1 < q^2 < 6$ (GeV/c)^2 in the region of maximum A_{FB} sensitivity), which is crucial for the $B_d \to K^*\mu^+\mu^-$ analysis. Figure 5.15 shows the invariant mass distribution for the MC muon pair passing each stage of the trigger. No significant differences are observed. The acceptance effects of the HLT2 muon+track selection are shown in Fig. 5.16 (left) while the acceptance of the complete trigger sequence (any L0, any HLT1 and HLT2 muon+track selection) with respect to all offline selected events is presented in Fig. 5.16 (right). In both cases neither the HLT2 muon+track selection itself nor the full trigger sequence introduce significant effects on the q^2 distribution.

Further discussion about acceptance effects on the $B_d \to K^*\mu^+\mu^-$ angular distributions due to reconstruction, offline selection and the diverse trigger alternatives can be found in [127]. The conclusion of that study is that, after the HLT2 muon+track optimization process previously described, the favoured combination of trigger selections corresponds to L0 single muon $\times$ HLT1 muon+track $\times$ HLT2 muon+track, which provides $\sim$75% of the total trigger efficiency for this channel while not introducing any significant acceptance effect.

In summary, due to the soft $B_d \to K^*\mu^+\mu^-$ dimuon spectrum, HLT2 inclusive selections based on a pair of muons are not very efficient for this channel. The muon+track strategy has been developed for HLT2 and optimized to be the main inclusive trigger for decays with soft momentum muons as in the example. By effectively selecting the events on combinations of a muon plus a hadron from the decay, in addition to high signal retention,

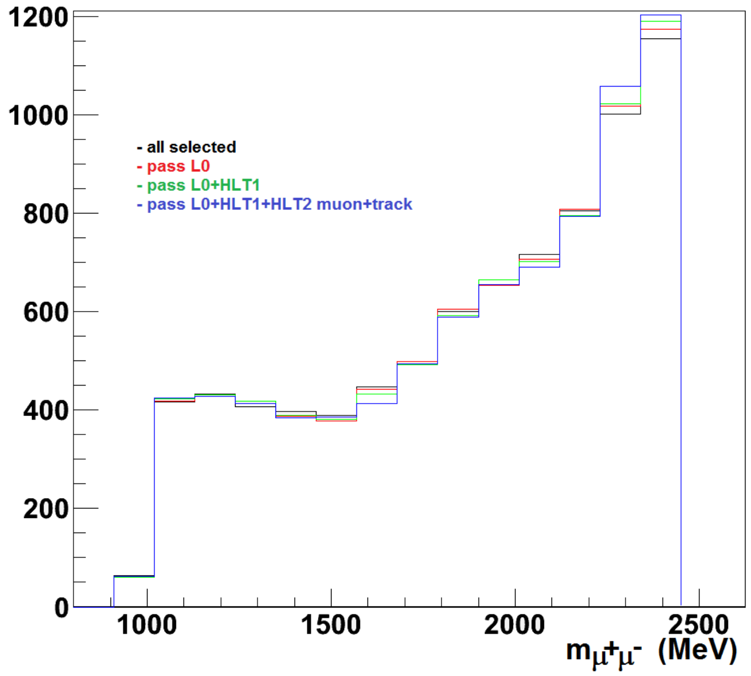

Figure 5.15: Invariant mass distributions for MC muons from the $B_d \to K^*\mu^+\mu^-$ decay for all offline selected events (black), offline selected events passing any L0 trigger (red), offline selected events passing any L0 and HLT1 alley (green) and offline selected events passing any L0 and HLT1 and the HLT2 muon+track selection. Curves are normalized to the same area.

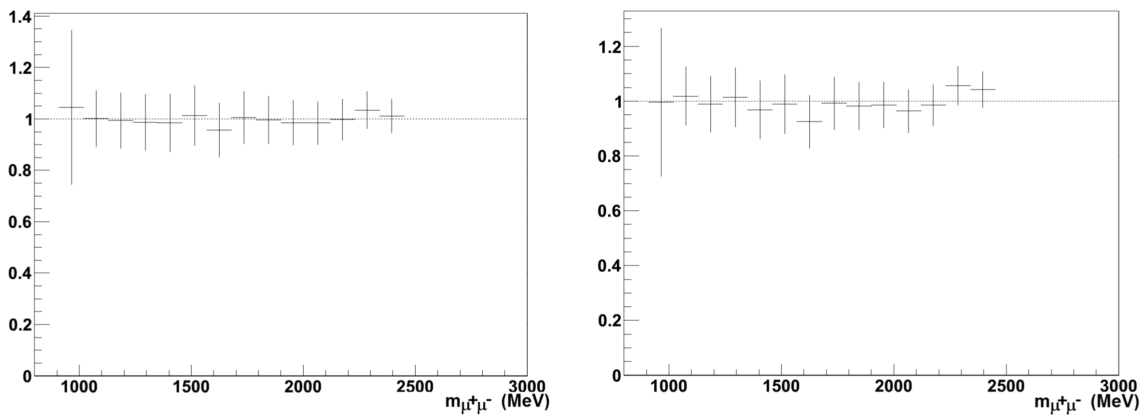

Figure 5.16: Ratios of equally normalized invariant mass distributions for MC muons from the $B_d \to K^*\mu^+\mu^-$ decay: effect of the HLT2 muon+track selection with respect to events passing the offline selection, L0 and HLT1 (left) and effect of the trigger chain L0, HLT1 and HLT2 muon+track with respect to all offline selected events (right).

acceptance affects are avoided.

5.3 Global optimization of HLT2 inclusive muon selections in DC06

The objective of the work described in this section is the simultaneous optimization of the different HLT2 muonic selections in order to make the best use of the total trigger bandwidth dedicated to muon channels. As mentioned in the previous chapter, single muon, muon+track and dimuon (with lifetime biased and unbiased versions) selections have been developed. The selection cuts for each one of them as well as their individual and combined performances will now be summarized.

5.3.1 Objectives of the muon inclusive triggers

The objectives for the integration of the individual selections into a combined inclusive muon strategy are:

- Provide the highest efficiency for the key muonic channels, allowing for sufficiently relaxed sidebands and samples for control channels.
- Trigger signal in different ways in order to understand and minimize trigger induced biases and provide robustness to the strategy
- Select TIS events of non-muonic B decays, which are important to many physics studies, as in the case of the $B_s \to \mu^+\mu^-$ analysis, which uses TIS $B_d \to K^+\pi^-$ events as a calibration channel.
- Provide a high b-purity sample, including trigger unbiased b decays and semileptonic decays for flavour tagging studies, and useful for posterior data mining.

This study tries to find an efficient solution for the regime of steady long term running. The problem of coping with initial states of the LHC, with consecutive phases of increasing luminosity, is left for the next section of this chapter.

5.3.2 Benchmark channels

Several B muonic decays, which represent key measurements of the LHCb program (Section 2.3) have been selected as benchmark channels to optimize the inclusive trigger strategy. The list of channels, together with the corresponding L0 and HLT1 efficiencies, is given in Table 5.7. In each case, samples containing $\sim$1000 offline selected events have been prepared by the authors of the physics selections.

For $B_s \to \mu^+\mu^-$, a sample has been selected considering events in the most sensitive region of the geometrical likelihood variable (GL above 0.5, see Section 2.3.1). Samples for the calibration and control channels of this analysis, $B^+ \to J/\psi(\mu^+\mu^-)K^+$ and $B_d \to K^+\pi^-$, have also been provided.

For the rare decay $B_d \to K^*\mu^+\mu^-$, a sample of events weighted according to their sensitivity for the measurement of A_{FB} has been used.

For the case of $B_s \to J/\psi(\mu^+\mu^-)\phi$, which will be used in CP violation studies, both lifetime-biased and lifetime-unbiased offline selections have been proposed.

Finally, trigger rates are computed using 60,000 minimum bias events passing L0 and HLT1 at 36.5 kHz. In each case, the MC content for each passing event is inspected and the b purity of the output is measured as the fraction of events that contain a b quark. This study has been carried out with DaVinci v23r2p1 analysis software.

	ϵ(L0×HLT1) (%)
$B_s \to \mu^+\mu^-$	97
$B^+ \to J/\psi(\mu^+\mu^-)K^+$	92
$B \to hh$ TIS	3.8 ± 0.2
$B_s \to J/\psi(\mu^+\mu^-)\phi$ Unb.	86 (75)
$B_s \to J/\psi(\mu^+\mu^-)\phi$ Bias.	88
$B_d \to K^*\mu^+\mu^-$	83

Table 5.7: L0 and HLT1 efficiencies for benchmark signal channels (uncertainty is ±1%). Efficiency for the lifetime-unbiased $B_s \to J/\psi(\mu^+\mu^-)\phi$ sample in parenthesis takes into account events passing only lifetime-unbiased HLT1 muon selections.

5.3.3 The three bandwidth division scenarios

In order to develop the global LHCb trigger strategy, it is necessary to define priorities between the different samples to be triggered, which follow the physics analysis priorities agreed by the collaboration. In addition to leptonic lines, LHCb trigger uses inclusive topological selections, aiming at selecting multi-body displaced vertices from b decays, an inclusive ϕ trigger, which identifies $\phi \to K^+K^-$ decays, and inclusive topological selections for charm decays. A small fraction of the bandwidth (100 Hz) is reserved to exclusive selections dedicated to individual channels, as the complete reconstruction of a particular decay provides them with higher minimum bias reduction.

Table 5.8 summarizes the predefined scenarios that were defined by the collaboration [128]. The priority is given to leptonic b decays, hadronic b decays and charm physics respectively. Taking into account the total trigger output rate of 2 kHz, the inclusive muon strategy has to fit into 1200 Hz in the leptonic scenario, 600 Hz in the charm scenario and 400 Hz in the hadronic scenario.

Trigger lines	Trigger scenarios		
	Leptonic	Hadronic	Charm
Leptons	60%	20%	30%
Topological	20%	50%	20%
Inclusive ϕ	5%	10%	5%
Topo charm	10%	10%	40%
Exclusive	5%	5%	5%

Table 5.8: Proposal for bandwidth division scenarios: fraction of the total output to be filled by each selection category in each of the scenarios.

For each working scenario, efficiency and acceptance effects must be evaluated.

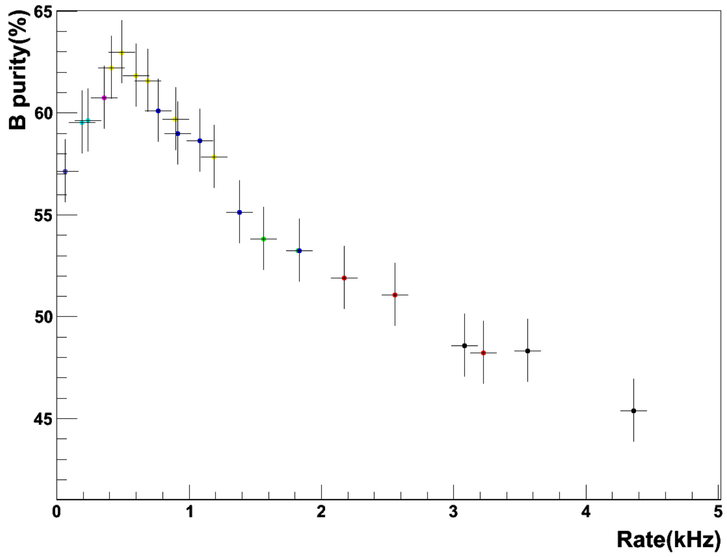

Figure 5.17: Maximum percentage of minimum bias events containing a b quark as a function of output rate for the HLT2 single muon selection based on combinations of p_{T} and IP cuts. Color indicates p_{T} cuts. Best purity is obtained requiring p_{T} >3GeV/c and IP>300 μm.

5.3.4 Muon selections in the three scenarios

Single muon

A trigger based on a single muon track is not discriminating enough to retain signal events from our benchmark channels with high efficiencies keeping a rate fitting into the HLT2 envelope. The HLT2 single muon strategy is therefore optimized for best b purity (Fig. 5.17). Requiring cuts on p_{T} >3GeV/c and IP>300 μm for the muon tracks selects events which in a (67 ± 2)% of cases contain a b quark. The selection is subsequently downscaled to fit into the bandwidth requirements with an output rate of (200 ± 10) Hz.

Muon+track

Three versions of the muon+track selection are designed following the method described in the previous section, in order to provide increasing rate reductions. Table 5.9 shows the threshold values in each case.

The performances of the three versions are shown in Table 5.10. $B_s \to \mu^+\mu^-$ is efficiently selected even at lower rates. B purity increases with harder cuts, to almost 90%, although $B_d \to K^*\mu^+\mu^-$ and $B_s \to J/\psi(\mu^+\mu^-)\phi$ with the lifetime-biased selection suffer from decreasing efficiencies.

Lifetime-biased dimuons

Two alternative selections, one based on harder mass cuts and the other on harder lifetime cuts, have been considered [129–131]. In both cases, one of the muons is required to have $p_{\mathrm{T}} > 700$ MeV/c and cuts on the dimuon pair lifetime (τ >0.1 ps) and vertex quality (vertex $\chi^2 < 4$) are applied. Then, cuts are applied on $\mathrm{m}_{\mu\mu}$ >2.9 GeV/c^2 and IP> 20

Variable	High	Mid	Low
Muon p_{T} >	1 GeV/c	1 GeV/c	1.2 GeV/c
Track p_{T} >	0.6 GeV/c	0.8 GeV/c	0.8 GeV/c
|Muon IP| >	80 μm	80 μm	120 μm
|Track IP| >	100 μm	125 μm	150 μm
Vertex DZ >	1 mm	1 mm	1 mm
Vertex DOCA <	0.15 mm	0.15 mm	0.15 mm
Vertex Pointing <	0.4	0.4	0.3
Inv. Mass >	2.2 GeV/c^2	2.2 GeV/c^2	2.2 GeV/c^2

Table 5.9: Cut values for the three versions of the HLT2 muon+track selection.

	High	Mid	Low
Rate	660 ± 20 Hz	330 ± 14 Hz	266 ± 13 Hz
B purity (%)	70 ± 1	84 ± 2	89 ± 2
$\epsilon(B_s \to \mu^+\mu^-)$ (%)	97	95	95
$\epsilon(B^+ \to J/\psi(\mu^+\mu^-)K^+)$ (%)	93	86	82
$\epsilon(B_s \to J/\psi(\mu^+\mu^-)\phi$ Bias.) (%)	80	63	58
$\epsilon(B_d \to K^*\mu^+\mu^-)$ (%)	90	83	78

Table 5.10: Performance of HLT2 muon+track variants : efficiencies relative to L0×HLT1 (%) for signal channels (uncertainty is ±1%) and rate and b content fraction of minimum bias.

μm or, $m_{\mu\mu}$ >1.2 GeV/c^2 and IP> 50 μm. The final decision is the logical OR of both selections, to be used for the three bandwidth division scenarios.

The performance of both lines separately and the combined performance are summarized in Table 5.11. The rate is almost the same for the two alternatives, with little overlap. The value for the b-purity in the combined performance corresponds to the average of the two selections. The cut on invariant mass is a better strategy for most channels except for $B_d \to K^*\mu^+\mu^-$, which is almost entirely removed by the mass cut.

	Dimuon Mass	Dimuon IP	OR
Rate	93 ± 8 Hz	131 ± 9 Hz	209 ± 11 Hz
B purity (%)	54 ± 4	65 ± 3	60 ± 3
$\epsilon(B_s \to \mu^+\mu^-)$ (%)	94	46	94
$\epsilon(B^+ \to J/\psi(\mu^+\mu^-)K^+)$ (%)	89	38	89
$\epsilon(B_s \to J/\psi(\mu^+\mu^-)\phi$ Bias.) (%)	83	33	83
$\epsilon(B_d \to K^*\mu^+\mu^-)$ (%)	2	34	35

Table 5.11: Performance of HLT2 lifetime-biased mass-based and IP-based variants and logical OR of the two: efficiencies relative to L0×HLT1 (%) for signal channels (uncertainty is ±1%) and rate and b content fraction of minimum bias.

Lifetime-unbiased dimuons

Dimuon selections with no lifetime or IP requirements have been developed [93, 130, 131]. The dimuon vertex is required to satisfy χ^2 <20 and then three selections are considered:

- J/ψ selection, with a mass window of 70 MeV around the J/ψ rest mass (equivalent to 3σ of the HLT2 mass measurement), $p_{\mathrm{T}} > 0.5$ GeV/c for both muons and $p_{\mathrm{T}} > 1$ GeV/c for the dimuon combination.

- $\psi(2S)$ selection, with a mass window of 70 MeV around the $\psi(2S)$ mass, $p_{\mathrm{T}} > 1.5$ GeV/c for both muons and $p_{\mathrm{T}} > 1$ GeV/c for the dimuon.
- Heavy dimuon selection, for any dimuon forming a good vertex and with the invariant mass requirement of $m_{\mu\mu}$ >5.2 GeV/c^2.

In addition to these signal triggers, any dimuon combination above $m_{\mu\mu}$ >2.9 GeV/c^2 is accepted by a control selection with a prescale of 5%. The final decision is the logical OR of all four selections.

The rate of the combined selection is dominated by the $J/\psi \to \mu^+\mu^-$ line, with ∼72% of the total lifetime-unbiased dimuon trigger. The heavy dimuon line contributes ∼27% to the combined rate, while the contribution of the $\psi(2S)$ line is negligible (smaller than 1%). In order to reduce the combined output for the hadronic scenario, instead of increasing cut values in the J/ψ line, which would cause trigger acceptance effects (for example in the angular distributions due to strong p_{T} cuts), a downscale factor of 25% is applied.

Table 5.12 presents the results for the combination of these selections, to be used in the high and medium rate scenarios, and, once the downscale factor is applied to the J/ψ line, in the low rate scenario. B purities are relatively low in both cases. The $J/\psi \to \mu^+\mu^-$ line, which triggers mainly on prompt J/ψ, selects only ∼13% of the events containing a b quark, while the fraction of those passing the heavy dimuon selection is 25%, for a combined b-purity of 16%. The combined b-purity increases to 20% when the J/ψ selection is prescaled. All channels except $B_s \to \mu^+\mu^-$ lose most of its efficiency with this change. Due to the mass cuts, $B_d \to K^*\mu^+\mu^-$ events are almost entirely rejected.

	High/Mid	Low
Rate	338 ± 14 Hz	160 ± 10 Hz
B purity (%)	16 ± 2	20 ± 2
$\epsilon(B_s \to \mu^+\mu^-)$ (%)	94	94
$\epsilon(B^+ \to J/\psi(\mu^+\mu^-)K^+)$ (%)	85	21
$\epsilon(B_s \to J/\psi(\mu^+\mu^-)\phi$ Unbias.) (%)	93	26
$\epsilon(B_s \to J/\psi(\mu^+\mu^-)\phi$ Bias.) (%)	85	22
$\epsilon(B_d \to K^*\mu^+\mu^-)$ (%)	1	1

Table 5.12: Performance of HLT2 lifetime-unbiased selections: efficiencies relative to L0×HLT1 (%) for signal channels (uncertainty is ±1%) and rate and b content fraction of minimum bias.

5.3.5 Working scenarios

For each scenario, a combination of selections from the different categories described above is used. The choice of selections tries to cover all benchmark channels while fitting into the rate allowed for each of the scenarios. The studied combinations are:

Leptonic scenario (1.2 kHz): all muon selections are used

Charm scenario (600 Hz): the inclusive muon strategy for this scenario contains the muon+track selection, in its "medium rate" version, and the lifetime-unbiased dimuon lines.

Hadronic scenario (400 Hz): it allows a maximum rate of 400 Hz which is filled by the "low rate" muon+track selection and the lifetime-unbiased dimuon lines.

The performance of the inclusive muon strategy for each scenario is shown in Table. 5.13. In the leptonic scenario, efficiencies with respect to L0 and HLT1 for all samples is above 90% and b purity is 54 ± 1 %. The fraction of TIS events has however been reduced to 40% of those passing HLT1, which represents a final TIS efficiency of 1.5%, coming essentially from the muon+track line. $B_s \to \mu^+\mu^-$ and $B_s \to J/\psi(\mu^+\mu^-)\phi$ lifetime-unbiased selection samples are efficiently triggered by unbiased dimuon lines. The muon+track line, together with the lifetime-biased dimuon selection, provide efficiency for $B_d \to K^*\mu^+\mu^-$ and $B_s \to J/\psi(\mu^+\mu^-)\phi$ biased selection. In general, channels are triggered in multiple ways, which will useful to understand possible trigger biases and commission the trigger lines. The single muon selection has been replaced as a trigger providing generic b samples by the muon+track selection.

In the charm favoured scenario, the single muon and the lifetime-biased dimuon selections have been removed, and therefore $B_d \to K^*\mu^+\mu^-$ and data mining samples are now only triggered by the muon+track, whose rate has been reduced by 50%. Efficiencies are above 90%, except for this channel, which suffers from the tighter cuts on muon+track line, and in particular from harder track p_T cuts, with possible acceptance effects. B purity is ∼50%, provided now almost exclusively by the muon+track line. The same is true for TIS events.

Going to the hadronic scenario, both muon+track and unbiased dimuon selections have their bandwidth reduced to approximately 200 Hz each. The inclusive $J/\psi \to \mu^+\mu^-$ lifetime unbiased selection has been prescaled, instead of constrained by harder cuts in order to avoid trigger biases. In this situation the most successful $B_s \to J/\psi(\mu^+\mu^-)\phi$ sample corresponds to the lifetime-biased selection, which can be triggered by the muon+track. B purity is again ∼50%, provided by the muon+track line. Both $B_s \to \mu^+\mu^-$ and its control channel $B^+ \to J/\psi(\mu^+\mu^-)K^+$ have good efficiencies from the heavy unbiased dimuon and the muon+track selections.

This last scenario forces additional trigger biases and implies a significant loss of efficiency. At this point, the advantages of the inclusive approach have been lost and exclusive selections should be used to go even further in rate reduction.

	Leptonic	Charm	Hadronic
Rate	1260 ± 30 Hz	650 ± 20 Hz	420 ± 16 Hz
B purity (%)	54 ± 1	49 ± 2	63 ± 2
$\epsilon(B_s \to \mu^+\mu^-)$ (%)	98	97	97
$\epsilon(B^+ \to J/\psi(\mu^+\mu^-)K^+)$ (%)	98	96	85
$\epsilon(B \to hh)$ (%) TIS	39	29	26
$\epsilon(B_s \to J/\psi(\mu^+\mu^-)\phi$ Unb.) (%)	95	95	27
$\epsilon(B_s \to J/\psi(\mu^+\mu^-)\phi$ Bias.) (%)	97	92	66
$\epsilon(B_d \to K^*\mu^+\mu^-)$ (%)	93	84	78

Table 5.13: Performance of the combination of muonic selections used for each rate scenario: HLT2 inclusive muon efficiencies relative to L0×HLT1 (%) for signal channels (uncertainty is ±1%) and rate and b content fraction of minimum bias. The final TIS efficiencies for $B \to hh$ are 1.5%, 1.2% and 1% respectively. Efficiency for the lifetime-unbiased $B_s \to J/\psi(\mu^+\mu^-)\phi$ sample is computed with respect to events passing lifetime-unbiased muon selections in HLT1.

5.4 HLT2 inclusive muon selections in MC09

At the LHC start-up LHCb trigger needs to adapt to the increasing beam intensities. Several important steps in the LHC beam intensity have been foreseen [132] corresponding to increasing number of circulating bunches.

The number of colliding bunches at LHCb, the number of protons per bunch and the beam focusing at the LHCb interaction point determine the maximum instantaneous luminosity. The predicted value of σ_{tot} at the foreseen collision energy of $\sqrt{s} = 10$ TeV is 94 mb. Going in several steps from one pair of colliding bunches to 468 translates into visible bunch crossing (i.e. minimum bias) rates going from 1.2 kHz to 2.7 MHz.

The event filter farm is not to be completed until the stable running phase (2011). Given its reduced size and capabilities (approximately one third of the total number of CPUs) the maximum rate of events that can be processed by the HLT is estimated to be 300 kHz.

The initial trigger studies with MC09 samples [133] suggested that, in order to maximize the trigger efficiency on charm physics and hadronic b channels, and as long as the luminosity allows it, the LHCb trigger should be configured keeping a minimal L0 and HLT1 [132–134]. Then, the additional rate reduction would rely on the HLT2 selections. The configuration of L0 and HLT1 is expected to remain stable, which requires HLT2 to be deployed in different versions according to the luminosity regime.

In the luminosity scenario with 68 colliding bunches, the rate of visible events is 320 kHz. The task of the soft L0 triggers (selecting single muon candidates with p_{T} above 400 MeV/c) is to identify the L0 candidates to be used by the HLT1 confirmation and to reduce the rate into the EFF to 300 kHz. Relaxed cuts on the HLT1 muon alley (with a single selection of muon-confirmed tracks with p_{T} above 1 GeV/c and no IP cuts) reduce the rate to 10 kHz to be processed by the HLT2. The rate of events passing HLT1 muon alley is $\sim$2.7 kHz while signal efficiencies for the benchmark muon channels is typically above 95%. This scenario has been chosen as the starting point to develop HLT2 lines.

5.4.1 Rate reduction scenarios for HLT2

The rate reduction factors to be achieved by the whole HLT2 on top of HLT1 are predicted as 5, 10 and 20 for the successive luminosity steps at the LHC start-up. These factors have to be combined with the proposed bandwidth division scenarios discussed in the previous section (see Table 5.8). Table 5.14 shows the combinations of global HLT2 reduction and inclusive muon bandwidth division requirements. Inclusive muon strategy must hence be optimised to produce rate reductions by factors 8, 17, 25, 33, 50 and 100.

Figure 5.18 shows the dependence of signal efficiency with minimum bias reduction, for several simple muon (single muon, dimuon and muon+track) selections for some benchmark channels. The conclusion is that less inclusive selections should only be used when further reduction is needed.

Keeping the inclusive approach developed for HLT2 for long term running, the objective of the study based on MC09 is to find efficient combinations of elementary selections which are capable of providing increasing rate reductions. HLT2 inclusive muon is therefore to be implemented using increasingly more selective muon lines. In the following, the selections proposed are described and tested.

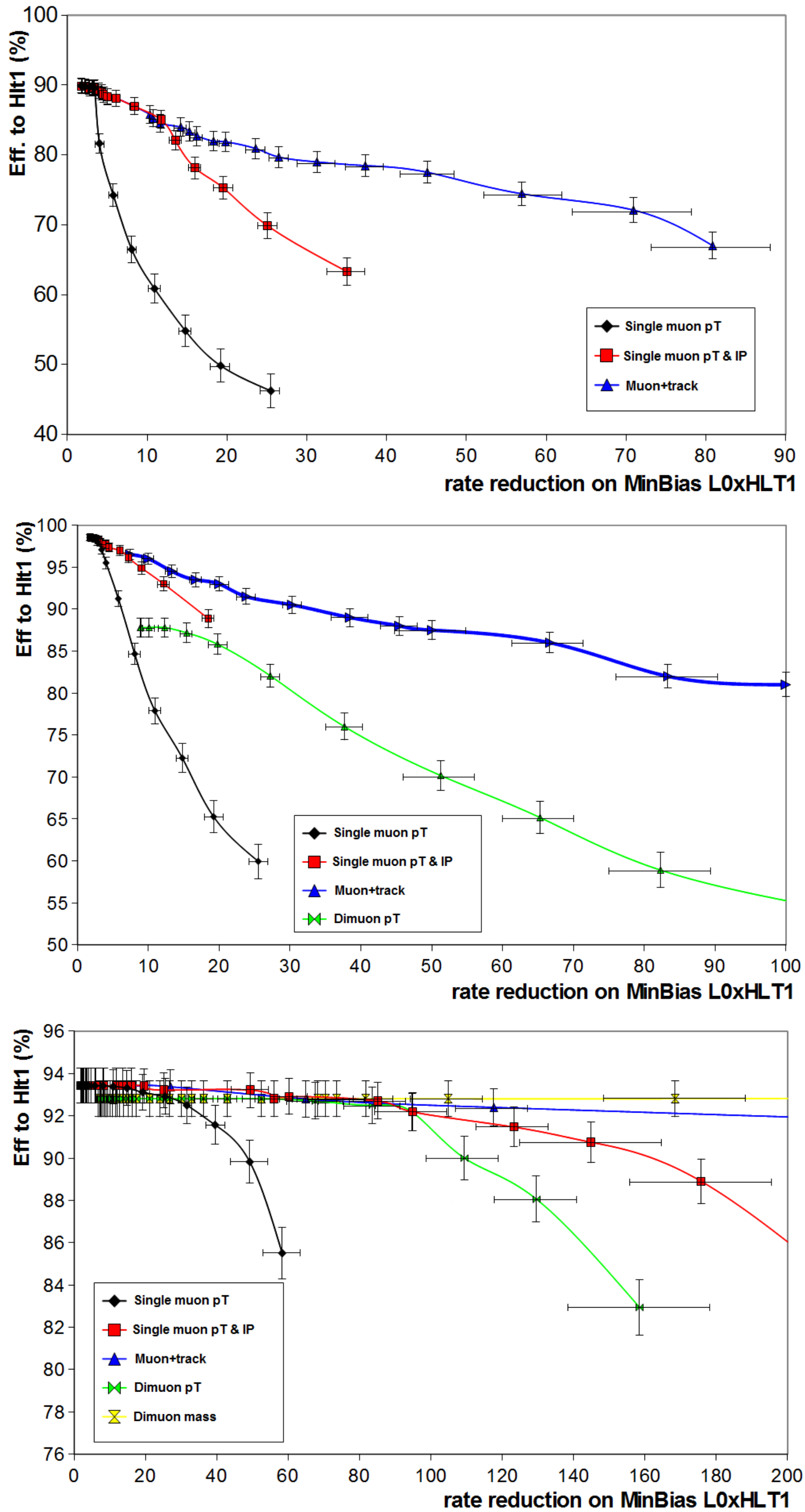

Figure 5.18: Best efficiency for individual muon selections as a function of minimum bias reduction factor with respect to HLT1 rate for $B_d \to D^* \mu\nu$ (top), $B_d \to K^* \mu\mu$ (middle) and $B_s \to \mu\mu$ (bottom).

	Leptonic (60%)	Charm (30%)	Hadronic (20%)
Factor 5	8 (1.2 kHz)	17 (0.6 kHz)	25 (0.4 kHz)
Factor 10	17 (0.6 kHz)	33 (0.3 kHz)	50 (0.2 kHz)
Factor 20	33 (0.3 kHz)	67 (0.15 kHz)	100 (0.1 kHz)

Table 5.14: Combinations of global HLT2 rate reduction factors 5, 10 and 20 combined with bandwidth division proposals determine the required inclusive muon rate reduction factor, and maximum rate for 10 kHz of HLT1 output. Inclusive muon strategy must hence be optimised to produce rate reductions by factors 8, 17, 25, 33, 50 and 100. Given the similarity in rate between the 50 and 67 rate reduction scenarios, only the first case is analysed.

5.4.2 Elementary muon selections

The selection of a single muon in HLT2 is the starting point for the muon trigger strategy. Given the different reconstruction used in HLT2 and the fact that no IP cuts are applied to muons in HLT1, HLT2 single muon selections have been designed with relatively soft cuts on p_{T} and IP (Table 5.15). A high p_{T} single muon selection is dedicated to electroweak $W \to \mu\nu$ decays.

Selection	p_{T} cut	IP cut
Single muon p_{T}	1 GeV/c	
Single muon high p_{T}	10 GeV/c	
Single muon p_{T} and IP	1 GeV/c	80 μm

Table 5.15: Inclusive single muon selections.

Two muon+track selections have been developed, with relaxed cuts compared to DC06 lines (see Table 5.16). In particular, the less restrictive selection has a reduced invariant mass cut (above 0.8 GeV/c^2, to be compared with the typical 2.2 GeV/c^2) which allows it to trigger on the charm rare decay $D \to \mu^+\mu^-$, of similar physics interest as $B_s \to \mu^+\mu^-$.

Variable	Muon+track	Muon+track tight
Muon p_{T} >	1 GeV/c	1 GeV/c
Track p_{T} >	0.4 GeV/c	0.6 GeV/c
|Muon IP| >	80 μm	80 μm
|Track IP| >	100 μm	100 μm
Vertex DZ >	1 mm	1 mm
Vertex DOCA <	0.2 mm	0.15 mm
Vertex Pointing <	0.4	0.4
Inv. Mass >	0.8 GeV/c^2	2.2 GeV/c^2

Table 5.16: Cut values for the two versions of the HLT2 muon+track selection.

Dimuon selections are described in Table 5.17. The most simple selection is the requirement of two tracks to be reconstructed and identified as muons in HLT2. Cuts on vertex quality and on the higher p_{T} of the combination can then be applied. Subsequent selections use a combination of invariant mass and vertex displacement requirements. Two special purpose selections are added, aiming to trigger on the $D \to \mu^+\mu^-$ decay.

Selection	Higher p_T	DOCA	Mass	DZ
Dimuon p_T	1 GeV/c	200 μm		
Dimuon mass	1 GeV/c	200 μm	0.8 GeV/c^2	
Dimuon mass disp.	1 GeV/c	200 μm	0.8 GeV/c^2	1 mm
Dimuon mass heavy	1 GeV/c	200 μm	2.7 GeV/c^2	
Dimuon for $D \to \mu\mu$	1 GeV/c	200 μm	1.6 to 2.1 GeV/c^2	
Dimuon for $D \to \mu\mu$ disp.	1 GeV/c	200 μm	1.6 to 2.1 GeV/c^2	1 mm

Table 5.17: Inclusive dimuon selections.

The study of the trigger rate for these selections is performed with analysis software DaVinci v24r4, using 10,000 minimum bias events passing L0 and HLT1 in the configuration identified as 320Vis-300L0-10HLT1-Nov09 [135]. The rates and rate reduction factors achieved by the elementary selections are summarized in Table 5.18. The rates are calculated assuming 10 kHz on total HLT1 output rate.

The selection requiring a single muon with a p_T cut essentially reproduces the HLT1 result, with a rate of 2.4 kHz. Note that the rate of events with at least one muon reconstructed is ~4.7 kHz, higher than the HLT1 single muon rate. This is due to events with reconstructible muons coming from other HLT1 alleys. The requirement of loose IP cut reduces the rate down to 600 Hz, while the bandwidth taken by the high p_T muon line is negligible.

Two muons are reconstructed and identified at a rate of ~1.2 kHz, which is reduced to below 500 Hz if the two muons are required to form a vertex, and one of them to have a p_T above 1 GeV/c. If soft invariant mass and displacement with respect to any PV is required or harder invariant mass cuts applied, the rate of the dimuon selections is below 100 Hz.

Finally, if the single muon with IP and p_T cuts and the muon+track selections are compared, the addition of a companion track fulfilling the requirements described above reduces the rate to 140 Hz. If stronger mass cuts are applied, the rate goes down to ~40 Hz.

5.4.3 Inclusive muon strategies for the different reduction scenarios

Taking into account the conclusions of the DC06 study, the elementary selections described above are combined into selection sets which defined the proposed inclusive muon strategy for each on the reduction factor scenarios identified in Table 5.14. The proposal for the grouping of selections is as follows (Fig. 5.19):

- reduction factor 8: a simple trigger is obtained using the single muon line with p_T and IP cuts together with the dimuon p_T selection.

- factor 17: in order to reduce the rate the single muon selection is substituted for the muon+track line, used in addition to the dimuon p_T selection.

- reduction factor 25: at this stage, additional rate reduction is achieved requiring a loose cut on the dimuon combination invariant mass. This selection is used together with the muon+track line.

		Minimum Bias
	Rate (kHz)	reduction from 10 kHz
Single muon (all)	4.7	2.1
Single muon p_{T}	2.4	4.1
Single muon high p_{T}	4×10^{-3}	2.5×10^{3}
Single muon p_{T} and IP	0.59	17
Muon+track	0.14	70
Muon+track low	0.04	280
DiMuon (all)	1.2	8.4
DiMuon p_{T}	0.47	21
DiMuon mass	0.39	26
DiMuon mass disp.	0.084	120
DiMuon mass heavy	0.033	300
DiMuon for $D \to \mu\mu$	0.11	90
DiMuon for $D \to \mu\mu$ disp.	0.016	630

Table 5.18: Performance of individual muon selections: minimum bias rate and rate reduction factor with respect to HLT1 at 10 kHz.

- reduction factor 33: in the next step, the dimuon selection is split in two, triggering both on heavy dimuons and displaced low mass dimuons. Again these selections are combined with the muon+track line.
- reduction factor 50: the displaced dimuon with low invariant mass is only useful at this stage to trigger on $D \to \mu^+\mu^-$, therefore a mass window around the D rest mass is required for displaced dimuon combinations. Additional triggers in this stage are the muon+track and the heavy dimuon lines.
- reduction factor 100: final rate reduction is achieved tightening the cuts on the muon+track selections. Heavy combinations of dimuons and the displaced dimuons for D decays are also kept.

A high p_{T} single muon line is added at every stage. Its contribution to minimum bias rate is negligible.

Note that organized in this fashion, each stage represents a subsample for the preceding one. If needed, while running in any of these scenarios the precedent selection could be also be executed with a downscale factor in order to provide samples for the study of possible trigger acceptance effects.

Table 5.19 summarizes the performance in terms of rate reduction for the proposed combination of selections. In all cases (except for the combination aimed at a reduction factor 25, which results in ~20) the expected rate reduction is achieved or improved.

In order to test these selections, signal samples have been provided by the LHCb physics working groups for rare decays [136], CP violation [137] and flavour physics [138]. In addition to the benchmark channels studied in the previous section, several samples have now been included motivated by physics objectives for the initial running scenarios, such as the study of the inclusive production of J/ψ and $\psi(2S)$. Efficiencies discussed in the following are calculated with respect to events passing L0 and HLT1.

Figure 5.20 shows the efficiency as a function of rate reduction factor for the samples provided by the rare decays WG. It is observed that the efficiency for $B_s \to \mu^+\mu^-$ remains

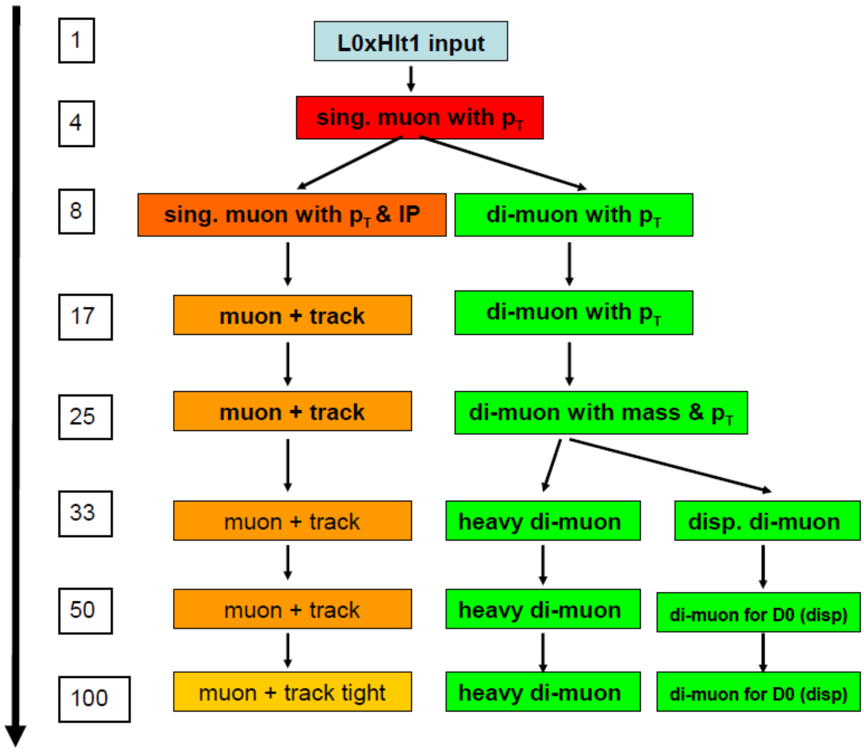

Figure 5.19: Evolution of the HLT2 inclusive muon trigger strategy in terms of selections as a function of the required rate reduction factor on minimum bias passing L0 and HLT1. A high p_{T} single muon line of negligible rate contribution is added at every stage.

		Minimum Bias
	Rate (Hz)	reduction from 10 kHz
Inclusive muons, factor 8	970	10
Inclusive muons, factor 17	580	17
Inclusive muons, factor 25	500	20
Inclusive muons, factor 33	240	43
Inclusive muons, factor 50	190	53
Inclusive muons, factor 100	85	118

Table 5.19: Performance for combinations of muon selections: minimum bias rate and rate reduction factor with respect to HLT1 at 10 kHz for each designed scenario.

unchanged, above 96% in all cases. $B_d \to K^*\mu^+\mu^-$ efficiency suffers from the increasingly less favorable dimuon selections. However, its efficiency remains above 90% thanks to the muon+track tight selection. In the case of the proposed $D \to \mu\mu$ samples, the difference in trigger efficiencies is caused by the different offline selections.

Figure 5.21 presents the performance of the designed inclusive muon scenarios on the samples for CP violation studies. All channels containing a $J/\psi \to \mu^+\mu^-$ decay are efficiently selected (above 95%) by the heavy dimuon line even in the most extreme scenarios. Semileptonic decays however suffer a considerable efficiency loss in the most restrictive case due to the increased mass requirement on the muon+track selection.

In the case of the samples provided by the flavour physics WG, Fig. 5.22 (top) shows again that decay modes which contain the decay of a J/ψ or a $\psi(2S)$ particle into a muon pair are efficiently triggered by the heavy dimuon line. Figure 5.22 (bottom) presents the results for the electroweak $W \to \mu\nu$, $Z \to \mu\mu$ and Drell-Yan processes. In most cases, efficiencies are above 95%, except for the sample corresponding to dimuon pairs from Drell-Yan production selected with a mass threshold at 2 GeV/c^2, which is affected by the mass cut on the heavy dimuon pair at 2.7 GeV/c^2.

In conclusion, this study demonstrates that inclusive muon strategies for increasing rate reduction requirements can be built from a few elementary selections combined to fit into each rate envelope. As this section has shown, this method provides a successful strategy to achieve high efficiencies for a wide variety of decay modes in the early running stages of the LHC.

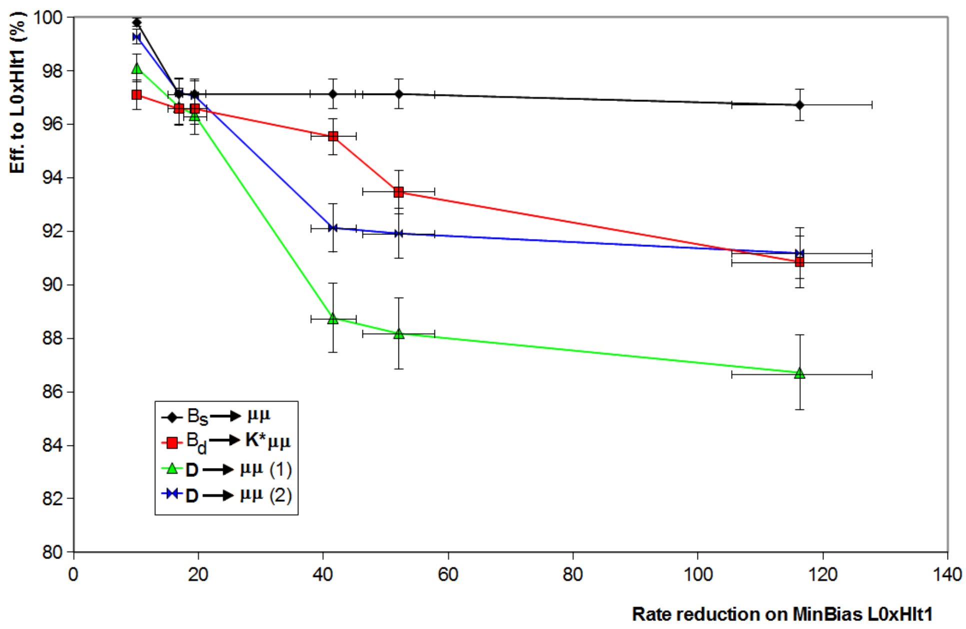

Figure 5.20: Evolution of the HLT2 inclusive muon trigger efficiency as a function of the rate reduction factor for the samples provided by the Rare Decays working group: $B_s \to \mu^+\mu^-$, $B_d \to K^*\mu^+\mu^-$ and two different selections for the $D \to \mu\mu$ charm rare decay.

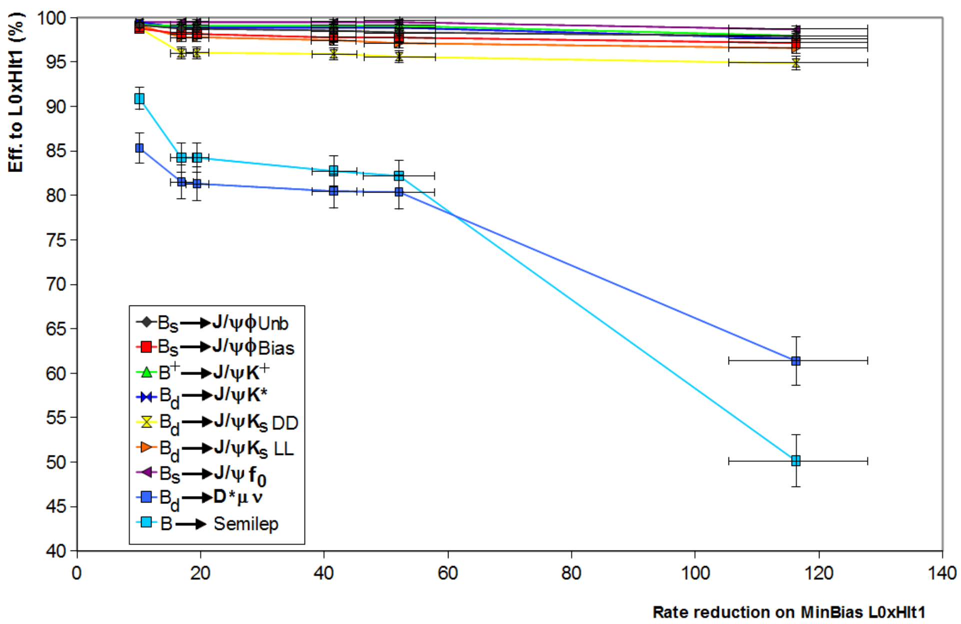

Figure 5.21: Evolution of the HLT2 inclusive muon trigger efficiency as a function of the rate reduction factor for the samples provided by the CP violation working group: $B_s \to J/\psi(\mu^+\mu^-)\phi$ in lifetime unbiased and biased selections, $B^+ \to J/\psi(\mu^+\mu^-)K^+$, $B_d \to J/\psi(\mu^+\mu^-)K^*$, $B_d \to J/\psi(\mu^+\mu^-)K_s$ with selections reconstructing the K_s from long or downstream track pairs, $B_s \to J/\psi(\mu^+\mu^-)f_0$, and semileptonic samples for $B_d \to D^*\mu\nu$ and the generic $B \to \mu X$ decay.

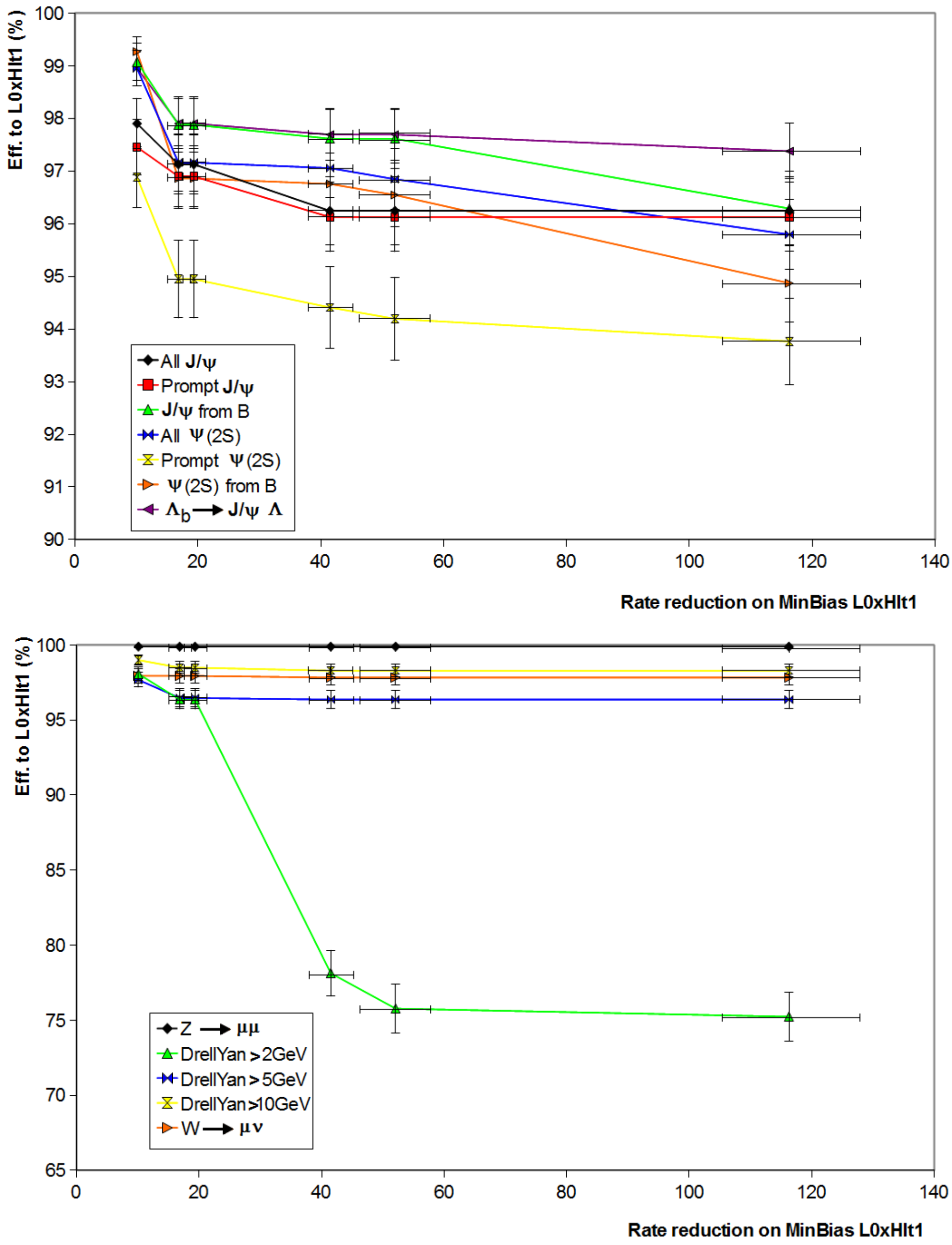

Figure 5.22: Evolution of the HLT2 inclusive muon trigger efficiency as a function of the rate reduction factor for the samples provided by the Flavour Physics working group: Inclusive, prompt and detached $J/\psi \to \mu^+\mu^-$, Inclusive, prompt and detached $\psi(2S) \to \mu^+\mu^-$, and $\Lambda_b \to J/\psi(\mu^+\mu^-)\Lambda$ (top); electroweak $W \to \mu\nu$ and $Z \to \mu\mu$ processes and dimuon from Drell-Yan production with invariant mass thresholds at 2 GeV/c^2, 5 GeV/c^2 and 10 GeV/c^2 (bottom).

Chapter 6

Commissioning of muon triggers with data

On Monday November 23$^{\text{th}}$ 2009 the LHCb experiment recorded the first proton-proton collisions at the LHC injection energy ($\sqrt{s} = 0.9$ TeV). The transversal size of the beam at this energy did not allow to close the VELO to its nominal position, and during most of the 2009 run ($\sim$7 μb^{-1}) the data was collected with the two sides of the VELO open by $\sim$15 mm in x axis instead of the nominal overlapping position. Even under such conditions, these data were extremely useful to commission the first steps of the HLT1 muon algorithms, namely the confirmation of the L0-muon candidates in the T-stations.

On Tuesday March 30$^{\text{th}}$ 2010 the LHCb experiment recorded the first proton-proton collisions at a world record energy ($\sqrt{s} = 7$ TeV). With the VELO closed and all the detector taking data in nominal conditions it was possible to commission the whole HLT1 muon trigger. The muon IP resolution was at first worse than expected from MC, and the culprit was identified to be the reconstruction of the PV using only RZ tracks (see Section 3.2.2) in the VELO (PV2D). Given the low interaction rate, and even though the EFF was not yet fully deployed (limiting the maximum L0 output to $\sim$300 kHz), the available CPU power allowed to skip this step and directly reconstruct the VELO tracks including the ϕ-sensors, as done in the HLT2 and offline event reconstructions. Therefore, the PV2D were replaced by the PV3D reconstruction in the trigger algorithms.

The first $\sim$15 nb^{-1}, were taken with a trigger configuration where most of the bandwidth (if not all) was devoted to minimum bias triggers, hence it was possible to evaluate the muon trigger efficiencies on data, by running offline the HLT algorithms on samples of $J/\psi \to \mu^+\mu^-$ events. This efficiency could also be compared with the evaluation using TIS events, hence validating the main LHCb strategy to measure trigger efficiencies.

In the last stages of the 2010 run, the LHC luminosity parameters evolved in such a way that the number of visible interactions per bunch crossing at the LHCb interaction region exceeded by a factor 6 its design value. This resulted in much more populated events which increased the HLT algorithms processing time. The HLT strategy had to be reviewed and new methods explored in order to adapt to these circumstances.

This chapter describes the HLT muon commissioning work sketched above. The trigger configurations used are first described. The minimum bias retention of each trigger step is compared with simulation expectations, and the trigger reconstruction is then modified in order to reach a reduction factor close to the MC expectations. The trigger performance is then evaluated on offline selected $J/\psi \to \mu^+\mu^-$ events and extrapolated to the $B_s \to \mu^+\mu^-$ decay, for a first estimation of the trigger efficiency for this rare decay. Finally, latest developments concerning the muon selections in the HLT, motivated by the change in LHCb running luminosity conditions, are described.

6.1 Trigger strategy for the LHC startup

As the instantaneous LHC luminosity in 2009 was much below its design value, the LHCb trigger was initially setup in order to record all minimum bias events. Only L0 was in rejection mode, selecting events with the requirement of a minimal amount of activity in the detector (*Minimum Bias* trigger). The L0 parameters used are shown in table 6.1. The reference trigger configuration key (TCK [139]) for this setup was 0x1309. The full trigger settings can be found under the nickname *Physics_MinBiasL0_PassThroughHlt_09Dec09* (TCK 0x00011309), used in HLT project v8r2.

L0CALO	E_T in Hadron calorimeter	>	240 MeV
	and SPD multiplicity	>	2
L0Muon	muon candidate with p_T	>	480 MeV/c
L0PU	PU sensors multiplicity	>	7

Table 6.1: L0 settings under TCK 0x1309. An event was accepted if one of the three requirements was fulfilled.

During April and May 2010, the LHC delivered $\sim$15 nb^{-1}, as shown in Fig. 6.1. The very first data, in region labeled **1** in Fig. 6.1, was delivered with an instantaneous luminosity that still allowed LHCb to record all minimum bias events. During this period the L0 settings for the minimum bias trigger was similar to the ones used in 2009 and the parameters are shown in Table 6.2. Additionally, the L0 lines for the LHCb physics were run in parallel, using the parameters shown in Table 6.3, in order to provide candidates for the HLT1 alleys. During this period, HLT1 ran with a special line, *pass through*, accepting all events triggered by L0, while the rest of the HLT1 lines were run in parallel rejecting events, in order to evaluate their performance.

In addition to the trigger path based on positive L0 decisions, an alternative path was implemented on L0 random triggers. A trigger line was introduced in HLT1, running only on such L0 triggers, with the only requirements that at least one track was reconstructed either in the VELO or in the T-stations (*micro-bias trigger*). Minimum bias and micro-bias triggers were both extremely useful for the commissioning work described in this chapter. The full trigger settings used in this period can be found under the nickname *Physics_MinBiasL0_PassThroughHlt_Apr10* (TCK 0x00031810) used in HLT project v9r2.

After the first $\sim$2 nb^{-1} were delivered, the increase in LHC instantaneous luminosity did not allow LHCb to record all minimum bias events anymore. The output rate of the HLT1 pass through line was hence limited to 1 kHz via a random downscaling. HLT1 physics triggers, including single muon, dimuon and muon+track alleys, filled the additional bandwidth for a total trigger rate of 2 kHz. This corresponds to region 2 in Figure 6.1. The trigger settings used are described under the nickname *Physics_25Vis_25L0_2Hlt1_ExpressHlt2_Jun10* (TCK 0x000e2810, used in HLT project v10r7).

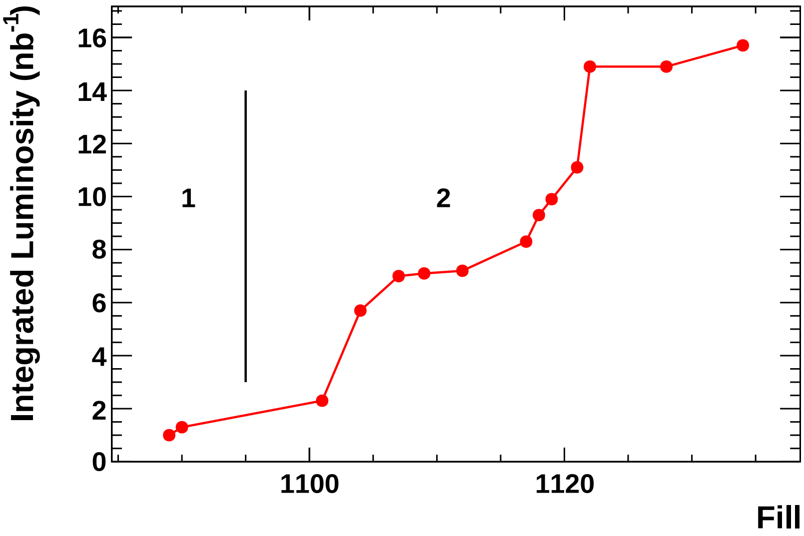

Figure 6.1: First 15 nb^{-1} recorded in 2010 as a function of fill number. For the period indicated in region **1**, data taken with L0 minimum bias triggers. After the increase in the LHC instantaneous luminosity, L0 minimum bias triggers were accordingly downscaled (region **2**).

L0CALO	E_T in Hadron calorimeter	>	240 MeV
	and SPD multiplicity	>	2
L0Muon,minbias	muon candidate with p_T	>	240 MeV/c
L0PU	PU sensors multiplicity	>	3
L0SPD	SPD multiplicity	>	2

Table 6.2: L0 settings under TCK 0x1810 - Minimum bias triggers. An event was accepted if one of the listed requirements was fulfilled.

6.2 Commissioning of the L0 muon trigger

For the studies presented here, the relevant L0 decision are L0Muon and L0DiMuon, which provide the input candidates for the HLT1 muon alleys. This section describes the commissioning of the L0 muon triggers [140], performed with collision events triggered by the microbias lines. Data from the inclusive dimuon stripping stream (which selects events with a pair of muons with an invariant mass above 2.7 GeV/c^2) were filtered with the requirements described in [140] to select $J/\psi \to \mu^+\mu^-$ events. Figure 6.2 displays the dimuon invariant mass distribution for the resulting sample. The number of $J/\psi \to \mu^+\mu^-$ signal events contained in the sample is estimated as 3619 ± 71.

L0 muon trigger is then compared between the data sample described above and on an inclusive $J/\psi \to \mu^+\mu^-$ MC sample. The efficiency on data is corrected from background contributions by using sidebands. Figure 6.3 shows the L0 muon efficiency for data and MC samples as a function of the highest p_T of the two muon daughters and as a function of p_T of the reconstructed J/ψ candidates. In both cases there is a reasonable agreement, with efficiencies for data slightly above those for MC. The integral L0 muon efficiency is measured as $(95.5 \pm 1.3)\%$ for data and $(93.7 \pm 0.1)\%$ for MC.

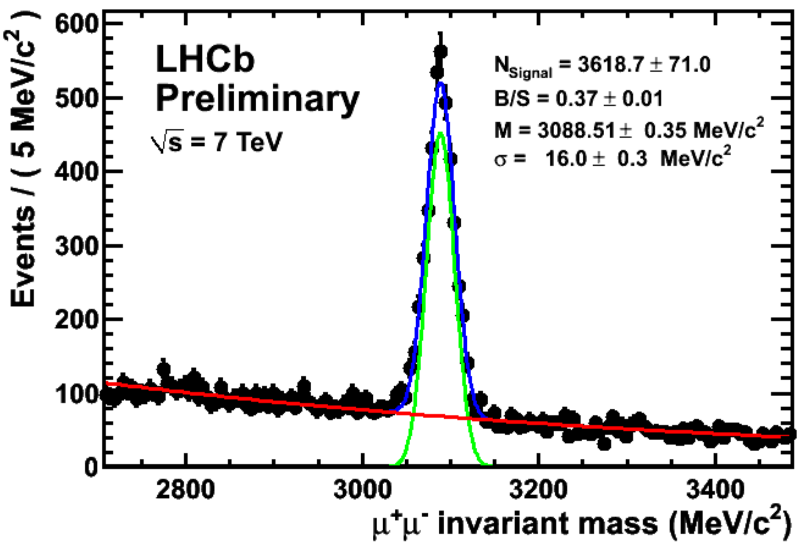

Figure 6.2: Dimuon invariant mass distribution for $J/\psi \to \mu^+\mu^-$ event sample used for L0 muon commissioning. Figure from [140].

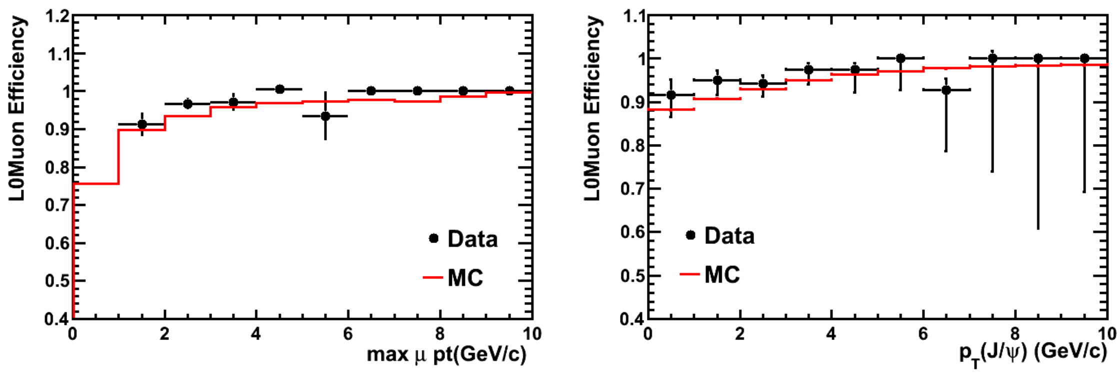

Figure 6.3: L0 muon efficiency comparison for $J/\psi \to \mu^+\mu^-$ events from data and MC samples: as a function of the highest p_T between the two muon daughters (left) and as a function of p_T for the reconstructed J/ψ candidates (right). Figure from [140].

L0Hadron	E_T in Hadron calorimeter	$>$	1220 MeV/v
L0Muon	muon candidate with p_T	$>$	320 MeV/c
L0DiMuon	two muon candidates with sum p_T	$>$	320 MeV/c
	second muon candidate with p_T	$>$	80 MeV/c
L0Muon,lowMult	muon candidate with p_T	$>$	320 MeV/c
	SPD multiplicity	$<$	20
L0DiMuon,lowMult	Two L0 μ candidate with p_T	$>$	80 MeV/c
	SPD multiplicity	$<$	20
L0Electron	E_T (charged cluster) in ECAL	$>$	750 MeV
L0Photon	E_T (neutral cluster) in ECAL	$>$	2700 MeV

Table 6.3: L0 settings under TCK 0x1810 - L0 trigger for the LHCb core physics program. An event was accepted if one of the listed requirements was fulfilled.

6.3 Commisioning of HLT1 muon alleys

This section describes the commissioning of the HLT1 muon trigger algorithms. Track and vertex reconstruction sequences are first discussed, followed by the study of the performance of the different selection variables used by the muon triggers. Finally, a summary of the study on rate reduction is given. This work was based on minimum bias samples from collision data (reco04-strip05) and MC 2010 (sim04-reco03), each containing 0.5 million events.

6.3.1 L0 muon confirmation with T tracks

The first part of the HLT1 muon trigger is the confirmation of the L0 muon candidate with a track reconstructed in a field of interest in the T-stations (*T-Confirmation*). This part could be completely commissioned using the 2009 data. For the early data taking conditions, both the detector alignment and the OT calibrations were shown to be non-optimal. This resulted in a track confirmation efficiency of the order of 60 - 70%.

To account for the residual misalignment of the tracking stations, the HLT1 tracking parameters used in the confirmation algorithm were modified [117, 141]:

- the search windows opened around the extrapolated L0 seed were extended to 10σ, where σ is the parameterized resolution of the L0 extrapolation. Previous MC studies (DC06) had found a slightly smaller 8σ to be the optimal compromise between efficiency and background retention.
- the search windows and χ^2 requirements inside the pattern recognition were loosened as well as the minimal requirements of hits per detector layer.

These modifications improved the track confirmation efficiency to above 90%, comparable to the performance measured on MC.

During the first half of the 2010 run, both the detector calibration and alignment improved in several iterations. The relevance of the loose pattern recognition tuning therefore diminished, with a review of the changes showing that the improvement with respect to design parameters had become minute (below 1% in the yield of triggered J/ψ events). The effect on rate reduction was marginal.

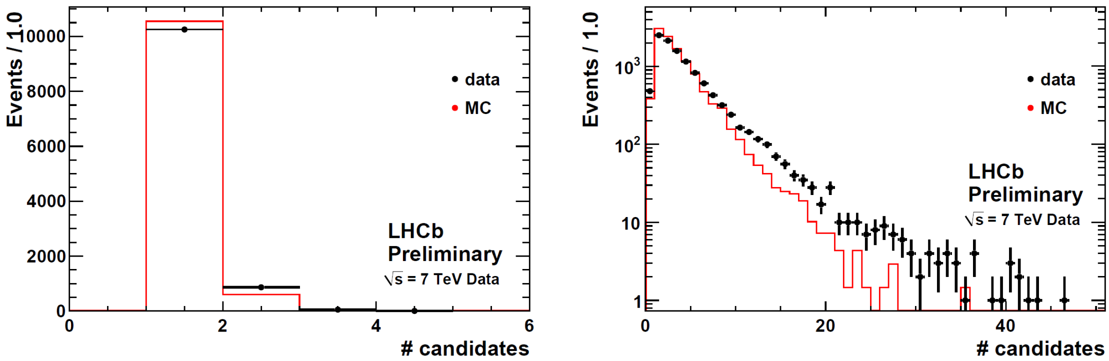

Figure 6.4: Comparison between data and MC of the L0-muon confirmation with T stations: number of L0 candidates passing L0 single muon p_T threshold (left) and number of matched candidates in the T-stations (right).

However, when running conditions evolved towards higher pile-up, the CPU time performance was significantly degraded. It was then decided to tighten the pattern recognition parameters to their tuning to nominal values.

Figure 6.4 shows the comparison between data and MC of the relevant quantities in the L0-muon confirmation with the T-stations, namely the distribution of the number of L0 candidates and the number of candidates matched to the T-stations. While the agreement is reasonable, more T-tracks were found to match the L0 muon candidates in data (4.0 tracks per candidate on average) than MC (3.2 tracks per candidate). Studies of particle production suggested that track multiplicities were underestimated by the simulation [142]. The increased number of T-matched muon candidates found in data is thus related to the higher occupancies observed in the T-stations.

6.3.2 VELO track and vertex reconstruction

Once the L0 muon candidate has been confirmed in the T-stations, the HLT muon lines perform the VELO reconstruction. A preliminary study of the 2D VELO reconstruction algorithm and its integration on the muon confirmation procedure was performed using 2009 data [143], however with the VELO halves retracted from their nominal position. The data accumulated in 2010 at $\sqrt{s} = 7$ TeV allowed for a detailed comparison with MC expectations, as the VELO detector was completely closed.

The original HLT1 strategy as described in [84] was to reconstruct the PV using only the VELO r sensors. The ϕ sensors were to be added only to a subset of selected tracks, thus minimizing the time spent in the VELO reconstruction. It turned out, however, that the implementation of the PV2D algorithm had several assumptions that were not a good approximation with real data, namely the beam position was not centered along the z-axis.

As a consequence, early studies [144] showed that the measurement of track impact parameter with respect to PV2D, as used in the HLT1, was degraded in data with respect to MC simulation. The observed disagreement is shown in Fig. 6.5 for the case of muon tracks, which also shows the difference between the expected trigger rate reduction as a function of the IP cut.

As a solution, the HLT1 VELO reconstruction strategy was modified and instead all

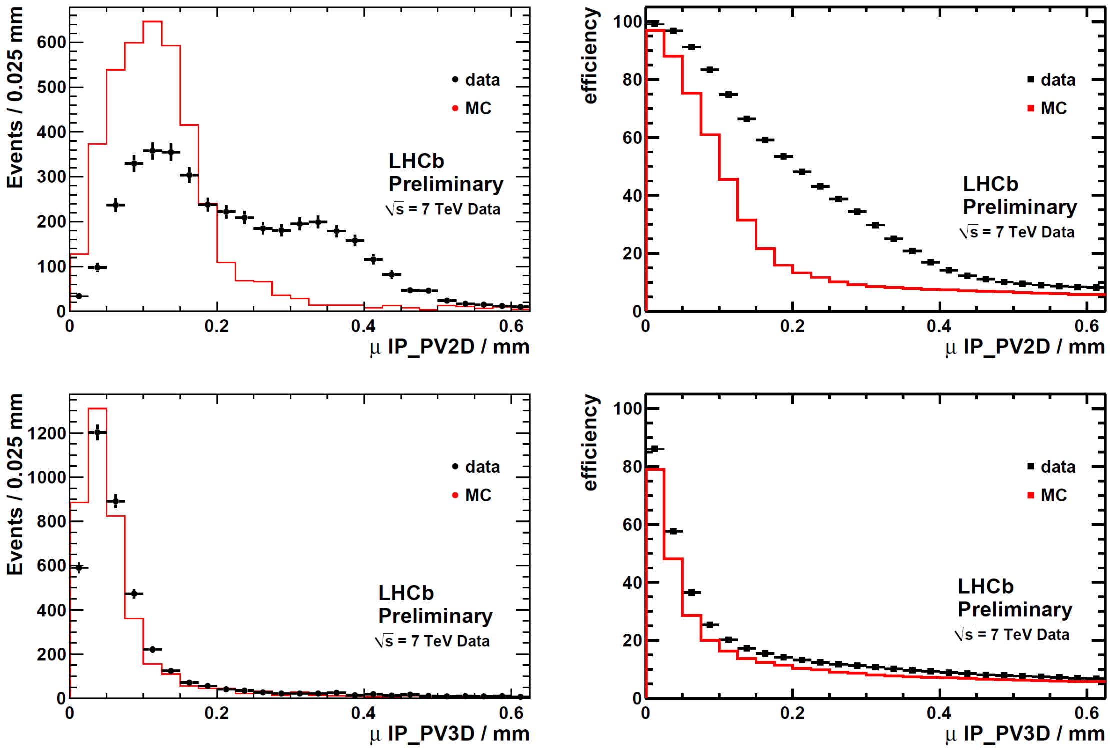

Figure 6.5: Highest impact parameter amongst the muon tracks and event retention fraction as a function of the cut for data and MC minimum bias events: measured with respect to PV2D (top) and with respect to PV3D (bottom).

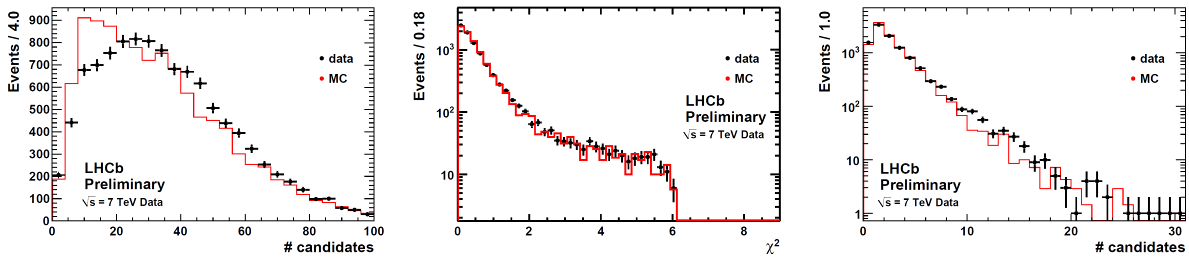

Figure 6.6: Comparison between data and MC of VELO reconstruction and matching between VELO segments and T stations: number of (non-backwards) reconstructed 3D Velo tracks (left), lowest χ^2 of T+Velo track matching (center), and number of T+Velo matched candidates (right).

tracks in the VELO were reconstructed in 3D using the r and ϕ sensors. The vertex reconstruction sequence was therefore unified in both HLT stages, as now HLT1 and HLT2 used 3D VELO tracks to find the PVs (PV3D). Figure 6.5 shows that with this substitution, the IP distribution for muon tracks and the effect of the IP cut became much closer to MC predictions.

As indicated in Section 3.2.2, an intermediate step in the confirmation process involved a compatibility check between the T-confirmed muons and the RZ VELO tracks. Only those tracks passing this requirement were then to be upgraded to 3D tracks. This confirmation sequence was commissioned successfully using the first data samples [145]. However, the muon confirmation procedure had to be modified because of the need to fully reconstruct the 3D VELO tracks in order to solve the PV reconstruction issue. This step was hence removed, and the muon confirmation algorithm described in this section makes use of 3D VELO tracks exclusively.

In Figure 6.6 the number of VELO tracks, the lowest χ^2 match between VELO and T, and the number of candidates matched are compared with MC expectations. Adding the VELO information seems to improve the agreement between data and MC on the number of candidates matched. The detailed numbers are given in Table 6.4 together with the retention rate after each confirmation step.

	Event retention (%)		Candidates: average(RMS)	
	data	MC	data	MC
Decode L0 Muon Cand.	100	100	1.09(0.31)	1.06(0.24)
T Confirmation	95.7 ± 0.2	96.6 ± 0.2	4.0(4.2)	3.2(2.9)
3D VELO tracks	99.4 ± 0.1	99.8 ± 0.1	36(24)	33(22)
T+3D VELO match	85.4 ± 0.3	86.5 ± 0.4	2.5(2.6)	2.3(2.3)
Total L0 muon Confirmation	81.2 ± 0.4	83.5 ± 0.4		

Table 6.4: Event retention and number of candidates in the HLT1 single muon confirmation sequence.

The L0-muon confirmation is the first step common to all HLT1 muon triggers. The confirmation of a single L0 muon candidate is shared by the single muon and muon+track lines. In the case of the dimuon selections, three different types of L0 seeds are considered, hence retention after this step differs between them. In Table 6.5 the overall event retention is compared with MC expectations for each L0 input, and the agreement is very reasonable in all cases.

	data (%)	MC (%)
Single muon / Muon+Track lines	81.2 ± 0.4	83.5 ± 0.4
Dimuon from L0 Dimuon lines	51.5 ± 1.2	47.6 ± 1.7
Dimuon from 2 L0 lines	81.2 ± 0.4	83.5 ± 0.4
Dimuon from L0Seg lines	42.7 ± 0.5	41.0 ± 0.6

Table 6.5: Event retention of muon confirmation sequences for data and MC classified according to the L0 seed types.

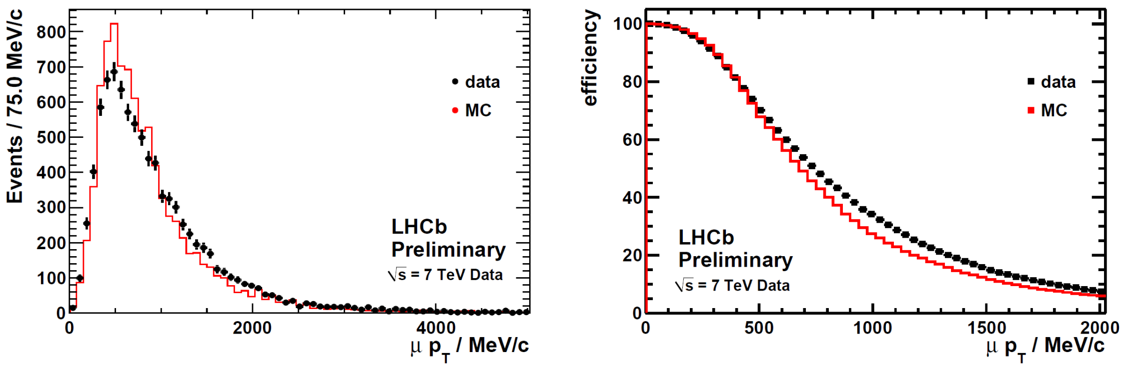

Figure 6.7: Highest p_{T} amongst the muon tracks in each event (left) and retention vs. p_{T} cut (right) for data and MC minimum bias events.

6.3.3 Selection variables for the HLT1 muon triggers

The selection variables in which the different HLT1 muon lines apply cuts are below compared in detail with the MC expectations. As the cuts are applied sequentially and that they are correlated, the distributions and efficiencies for a given cut on a variable are presented after all previous cuts have been applied, following the order of the trigger sequence.

Single muon alley

As described in Section 4.3.1 there are two single muon lines, one with cuts only on p_{T} and the other with cuts on both p_{T} and IP. The distribution of the muon candidate p_{T} is shown in Figure 6.7 and is in reasonable agreement with MC expectations. The IP distribution for muon tracks has already been shown in Figure 6.5. However, in the single muon line with IP cuts, a fast Kalman fit (Section 3.2.2) is performed for the muon candidates, resulting in an improved resolution. This IP distribution for fitted tracks can be seen in Fig. 6.8. Figure 6.9 shows the χ^2 per degree of freedom for the fitted tracks and the contributions from the Muon chambers and the rest of hits used in the track reconstruction (VELO, TT and T-stations) are explicitly shown. The agreement with MC expectations is good.

Dimuon alley

As described in Section 4.3.1, there are two parallel sequences of HLT1 DiMuon decision algorithms. One is based on a cut in the invariant mass of the two muon candidates while the second relies on IP cut and mass cuts. In each case there are three different seeds for

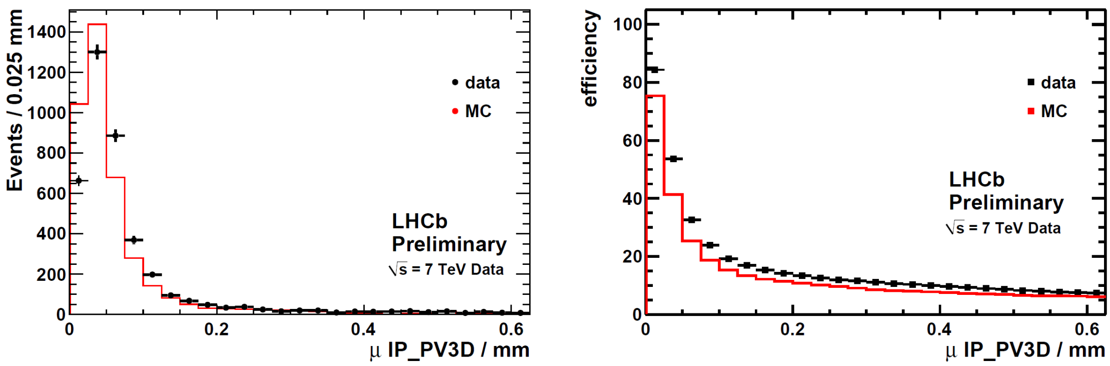

Figure 6.8: Highest impact parameter measured to PV3D amongst the muon tracks in each event after track Kalman fit (left) and retention as a function of the cut (right) for data and MC minimum bias events.

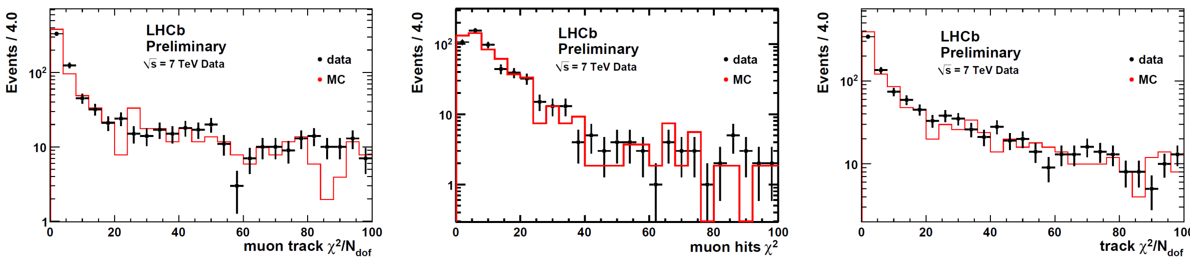

Figure 6.9: Quality of fitted muon tracks: lowest χ^2 per degree of freedom for fitted muon candidates including all measurements used in the track (left), contribution to track χ^2 from hits in muon chambers (center) and track χ^2 per degree of freedom excluding hits in muon chambers (right) for data and MC.

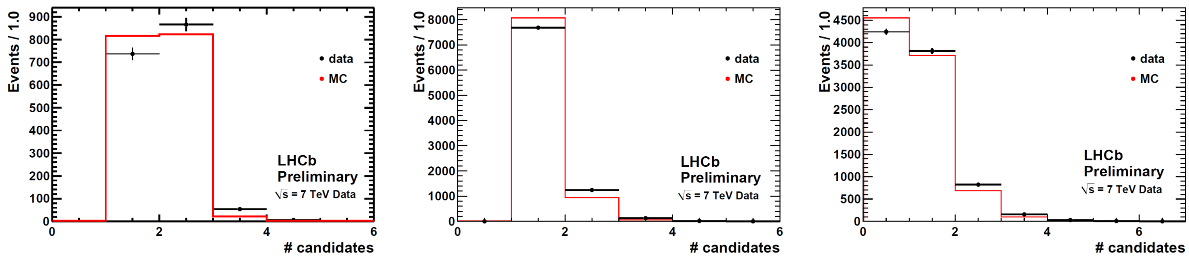

Figure 6.10: Number of input candidates for dimuon lines: L0 candidates for events passing L0 dimuon (left), all L0 muon candidates above the minimal requirement $p_{\mathrm{T}} > 80$ MeV/c (center) and stand-alone reconstructed muon segments not sharing hits in M3 with the main muon (right) for data and MC.

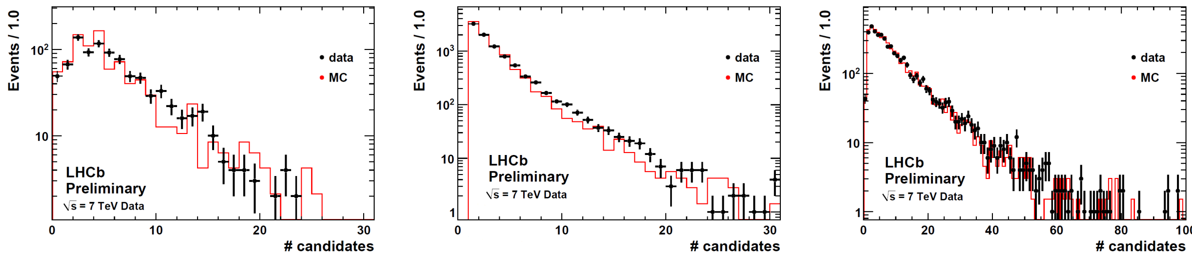

Figure 6.11: Confirmation of candidates with T+3D VELO tracks in the dimuon lines: number of T+Velo passing candidates matched to muons from L0 dimuon pairs (left), to all L0 candidates above the minimal requirement $p_{\mathrm{T}} > 80$ MeV/c (center) and to recovered muon segments (right) for data and MC.

those lines: a L0DiMuon candidate, two L0Muon candidates and a L0Muon together with a muon segment.

Figures 6.10 and 6.11 show the number of input candidates for dimuon lines. Both the presence of L0 seeds and their confirmation with T and VELO tracks are reasonably well predicted by MC for the three dimuon algorithms.

After the confirmation step, the first requirement for dimuons is on the DOCA between the two muon tracks. The distribution of this variable is shown in Fig. 6.12 for the different dimuon seeds, compared with MC expectations. Again there is good data-MC agreement.

After this, each trigger sequence splits into two, depending if an IP cut is applied or not. The lines with no IP cut rely on a cut on the invariant mass of the dimuon. The lines with IP cuts reconstruct first the 3D PV and then the tracks are fitted to improve the resolution on IP. With the help of the IP cuts, the cuts on the invariant mass can be relaxed.

The invariant mass is studied separately for no-IP (Figure 6.13) and IP dimuons lines (Figure 6.14) due to the difference in track quality after the fast track fit. No significant differences in retention can be observed with respect to MC performance in any of the categories. Dimuon mass distributions show a peak at twice the muon mass, arising from combinations in which both tracks are clones corresponding to the same particle. The peak appears a bit higher for data than MC, due to the fact that muon confirmation produces more tracks in data, thus increasing the probability to find clones. These combinations are however removed by the mass cut itself, well above this value in all dimuon lines.

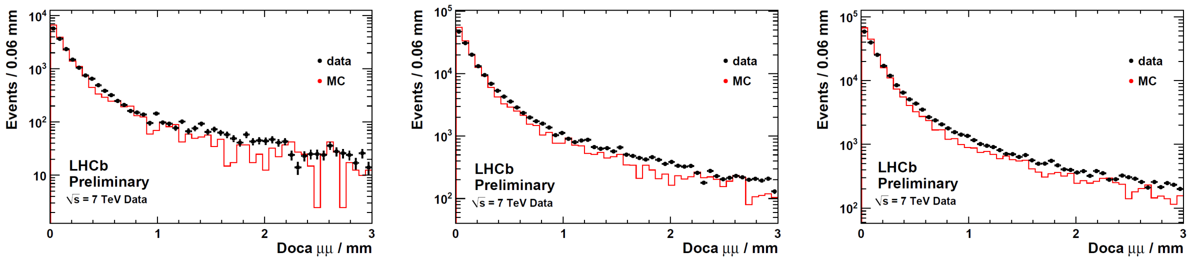

Figure 6.12: DOCA between confirmed muon tracks in a dimuon pair: from L0 Dimuon candidates (left), from two L0 muon candidates (center) and from one L0 muon candidate and a recovered muon segment (right) for data and MC.

The comparison of the IP and track χ^2 variables for the fitted tracks used in the dimuon with IP lines is very similar to what has been already discussed for the single muon with IP line.

Muon+track alley

The HLT1 muon+track alley starts with a confirmed L0 muon (see Section 4.3.1). Cuts on p_{T} and IP are applied to the muon track, as in the single muon case. The commissioning of these variables has been described above for single muon line.

The presence of one additional unidentified track coming from the same decay tree as the muon is then required. Only those VELO tracks sufficiently close to the muon candidate in DOCA and with significant IP are to be reconstructed in the forward direction as long tracks. The vertex defined by the muon and its companion track has to be in the forward direction with respect to any reconstructed PV. The distributions for the DOCA, IP and DZ variables used by the muon+track alley are shown in Fig. 6.15 together with the event retentions as a function of the cuts, compared with MC expectations. A reasonable agreement is observed, although with slightly higher event retention for data than MC.

The number of muon+track pair candidates before and after the extrapolation to the T-stations of the companion track is shown in Fig. 6.16, comparing data results with MC expectations. In both cases a good agreement is found.

At this stage of the selection sequence, kinematic information about the muon+track candidates is available. Cuts on companion tracks p_{T}, the invariant mass of the pair (with a muon mass hypothesis for the companion) and the pointing of the muon+track vertex with respect to any PV are applied. In Fig. 6.17 these distributions are compared to MC expectations as well as the event retention after cuts, which is slightly higher for data than MC for the p_{T} and invariant mass cases.

After the cuts on kinematic variables, muon and companion tracks in the surviving candidates are fitted. In the case of the muon, the discussion is analogous to what has already been shown for the single muon line, where the different components of the muon track fit χ^2 have been described (Fig. 6.9). In the case of the additional track, Fig. 6.18 compares the quality of the companion long tracks after the fast fit for data and MC. Due to residual detector misalignment, the track χ^2 distribution for data is slightly shifted towards higher values than in the case of MC, which causes event retention in data to be smaller than that of MC.

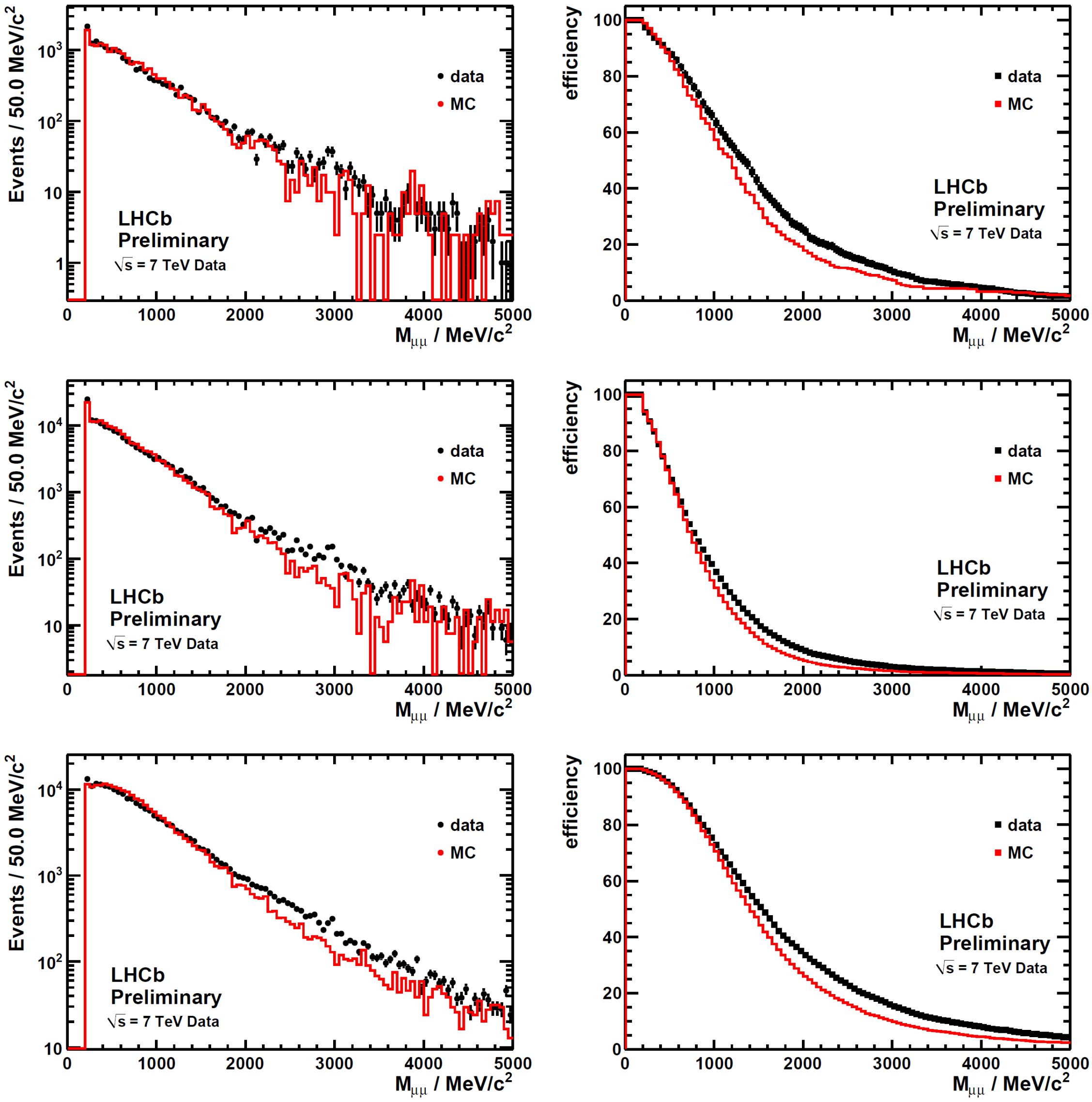

Figure 6.13: Invariant mass (left) and event retention vs. cut (right) for unfitted muon tracks for dimuon lines with no IP cuts from L0 dimuon (top), two L0 muon candidates (center) and one L0 muon candidate and a recovered muon segment (bottom) for data and MC.

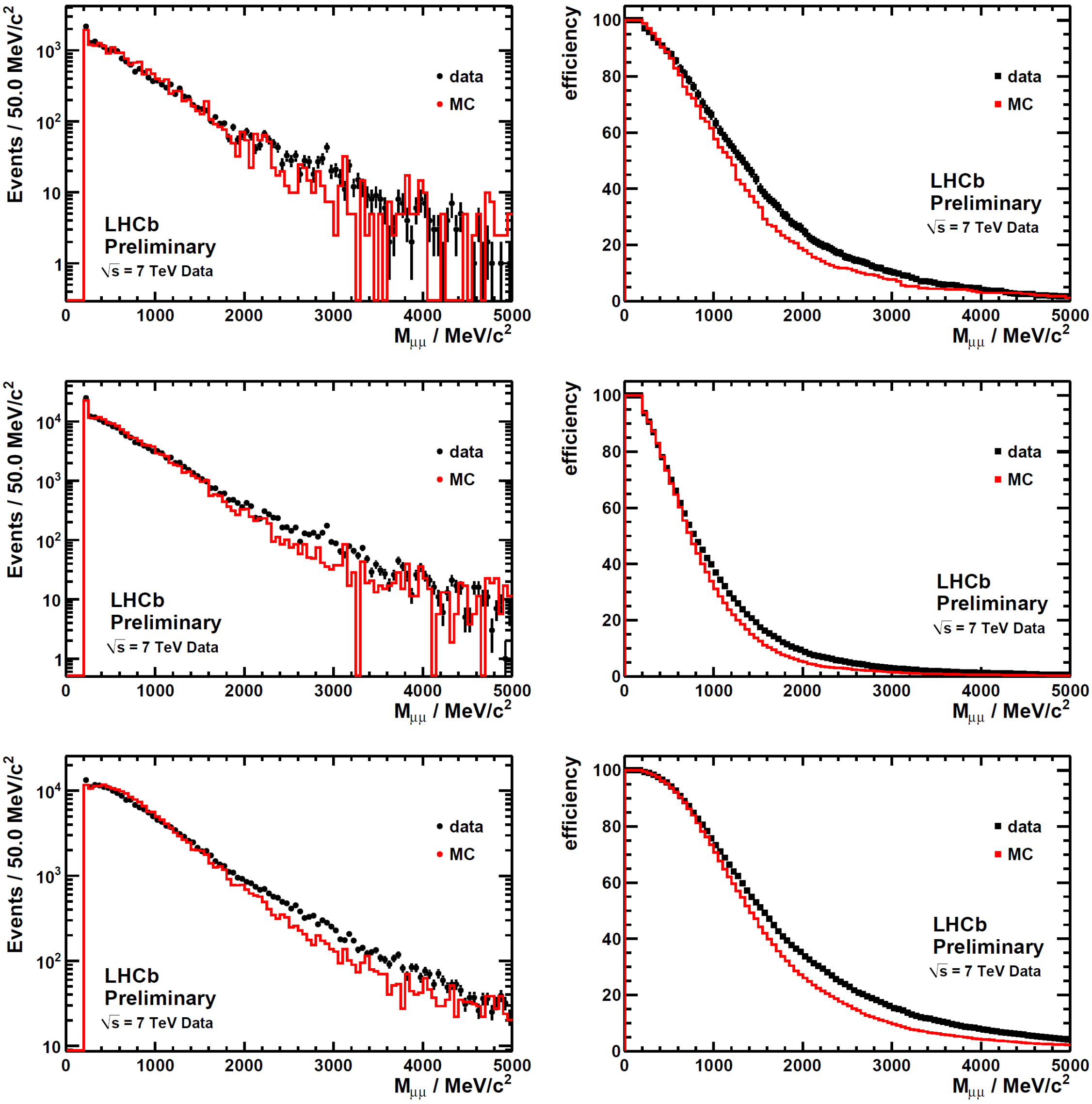

Figure 6.14: Invariant mass (left) and event retention vs. cut (right) for fitted muon tracks for dimuon lines with IP cuts from L0 dimuon (top), two L0 muon candidates (center) and one L0 muon candidate and a recovered muon segment (bottom) for data and MC.

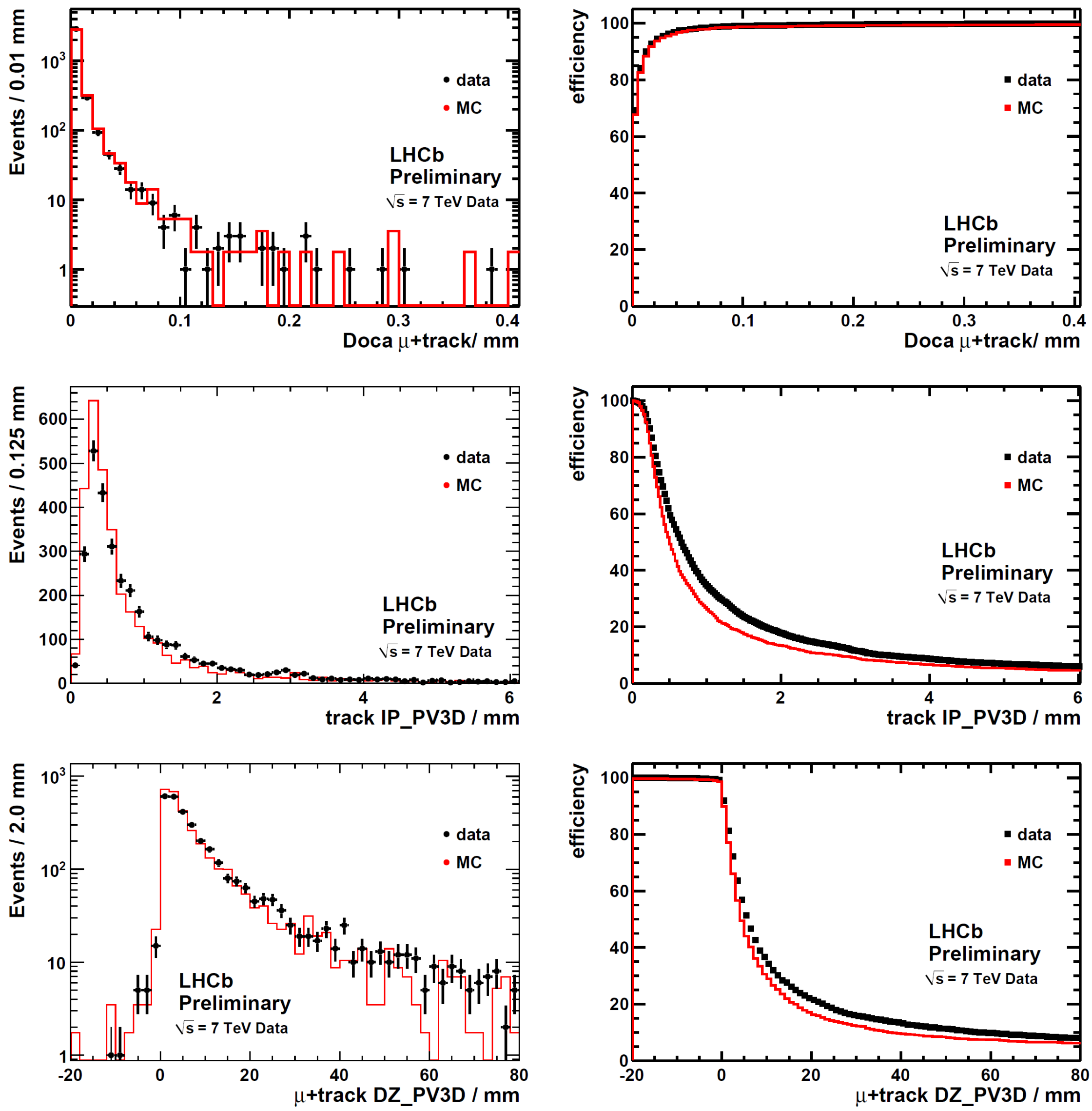

Figure 6.15: Muon+track VELO filtering: distributions (left) and event retention after cuts (right) for the lowest DOCA between a velo track and the muon confirmed track (top), highest IP of velo tracks with respect to any PV3D (center) and highest DZ of combined muon+velo track with respect to any PV3D (bottom) for data and MC.

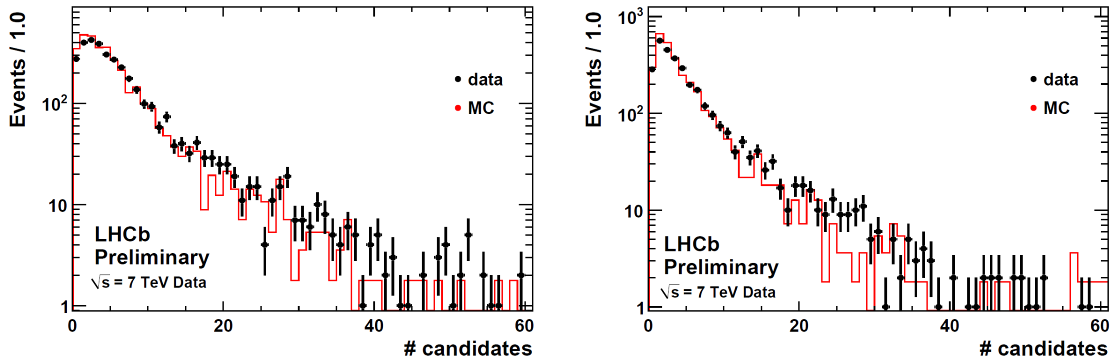

Figure 6.16: Forward reconstruction of the companion track in the muon+track alley: number of muon+velo candidates surviving the IP, DOCA and DZ cuts tracks (left) and muon+long track pairs after the forward tracking of the companion velo track (right) for data and MC.

Again, the resolution of variables which depend mostly in the reconstruction of the VELO segment of the track improve after the fast track fit. Fitted muon track IP has already been discussed for single muon trigger, hence only the comparison for the IP of the companion fitted track is shown in Fig. 6.19. Applying cuts on DOCA and IP for fitted tracks at the same value as for the unfitted tracks allows the rate to be further reduced, resulting in 20% less minimum bias retention in data to be compared with 25% in MC.

6.3.4 Minimum Bias retention results

The small disagreements between the observed retentions and the MC expectations cause the rate reduction observed in data to be slightly lower than MC expectations, as shown in Table 6.6.

	data (%)	MC (%)
Single muon	11.3 ± 0.3	8.0 ± 0.3
Single muon No IP	17.6 ± 0.4	14.3 ± 0.4
Muon+track	3.8 ± 0.2	2.2 ± 0.2
Dimuon from L0Di	33.8 ± 1.2	29.5 ± 1.6
Dimuon from L0Di No IP	7.1 ± 0.6	4.7 ± 0.7
Dimuon from 2 L0	26.9 ± 0.4	25.1 ± 0.5
Dimuon from 2 L0 No IP	2.6 ± 0.2	1.4 ± 0.1
Dimuon from L0Seg	33.9 ± 0.4	32.1 ± 0.5
Dimuon from L0Seg No IP	9.1 ± 0.3	6.1 ± 0.3

Table 6.6: Retention of HLT1 muon lines for data and MC.

6.4 Studies on signal Efficiency

In parallel to the commissioning of the muon triggers in terms of minimum bias rejection described above, studies with the aim of an initial evaluation of trigger efficiency on signal

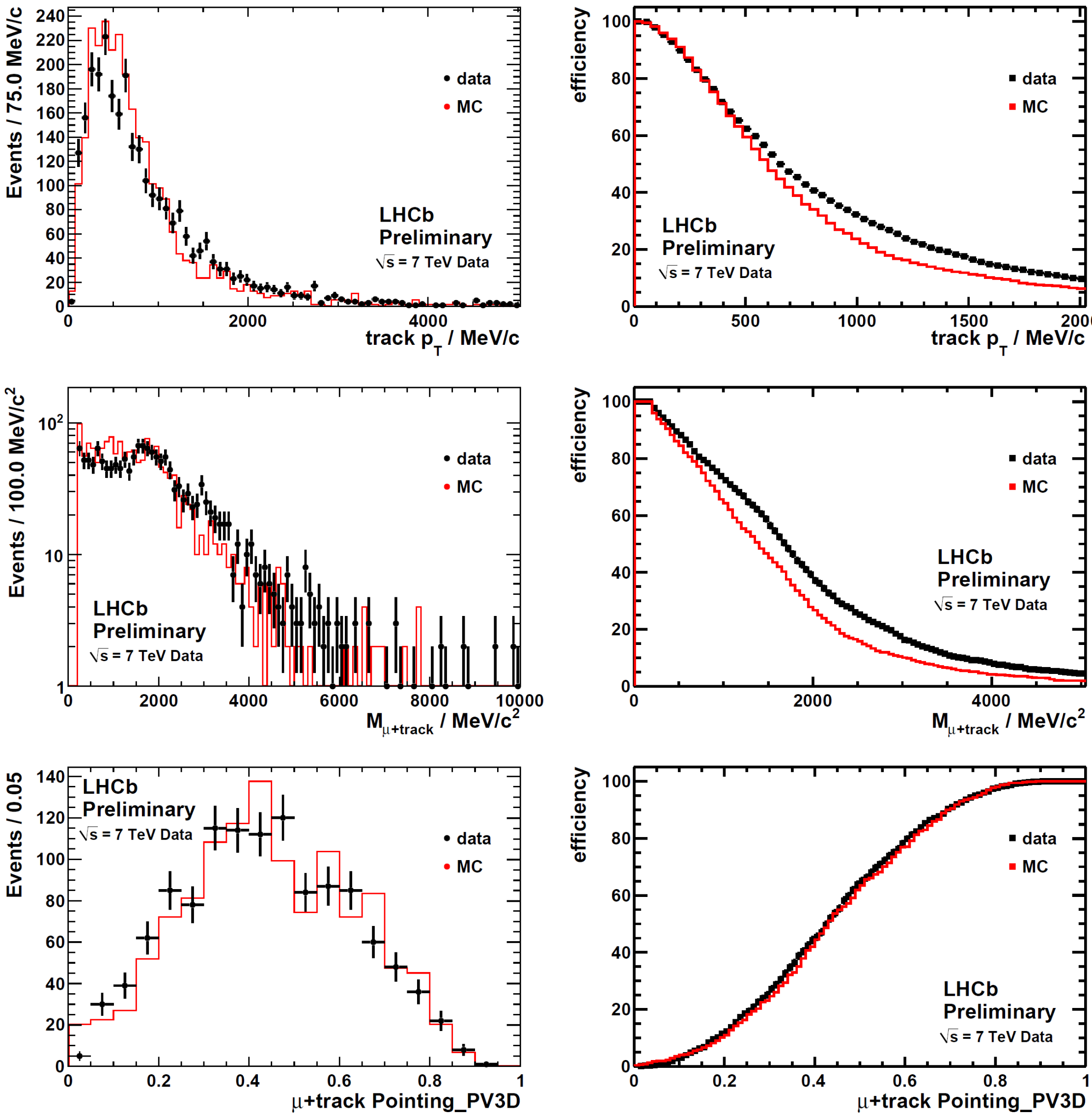

Figure 6.17: Kinematic filtering after forward reconstruction of companion tracks in the muon+track alley: distributions (left) and event retention after cuts (right) for the companion track highest p_T (top), highest invariant mass for muon+track pair as a dimuon (center) and lowest muon+track pointing variable to any PV3D (bottom) for data and MC.

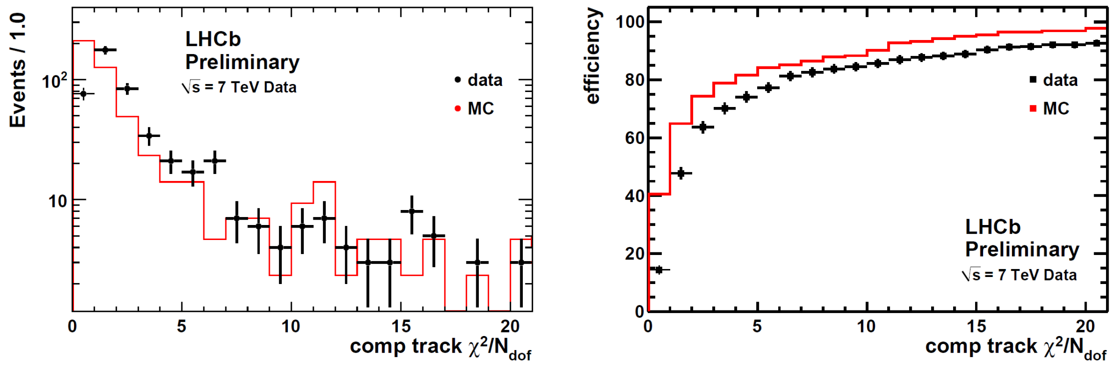

Figure 6.18: Quality of the track fit for companion tracks in the muon+track alley: lowest track χ^2 per degree of freedom (left) and event retention as a function of the applied cut (right) for data and MC.

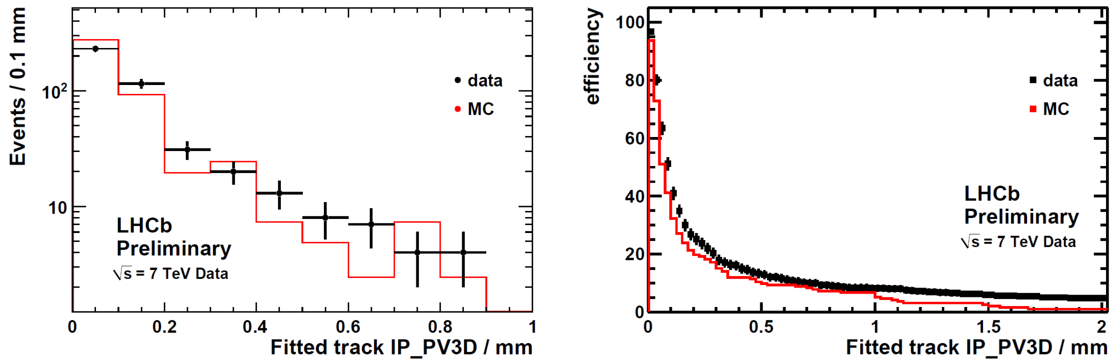

Figure 6.19: Distribution (left) and event retention as a function of the cut (right) for the highest IP with respect to any PV3D amongst the companion tracks in the muon+track alley after the fast track fit for data and MC.

were performed. The $J/\psi \to \mu^+\mu^-$ process provided the first abundant source of signal decays with muons and was therefore used to study trigger efficiencies.

The majority of these decays are caused by prompt J/ψ particles, either produced at the primary collision or as the result of the decay of heavier charmonium states. Prompt decays hence lack separation from the PV that would allow testing the performance of muon trigger lines developed for the selection of B meson decays. This work is therefore mainly testing the performance of the reconstruction and selection algorithms involved in the lifetime-unbiased muon lines, namely the reconstruction of the muon candidates and the measurement of their momenta and invariant mass.

6.4.1 First study of trigger performance on $J/\psi \to \mu^+\mu^-$

A first study of trigger performance on signal events was conducted using data events from the reco-strip03 sample and MC2010 simulated events [146]. Table 6.7 shows the criteria used in the selection of $J/\psi \to \mu^+\mu^-$ events, applied both to data and MC samples. An additional requirement on MC is the rejection of pile up events in order to better simulate the low luminosity conditions for the initial data taking. If more than one candidate is found in a given event, the one with the lowest sum of χ^2 per degree of freedom of the two muon tracks is kept.

$J/\psi \to \mu^+\mu^-$ selection:		
$\mu^\pm$:	ISMUON	
	p_T	$> 0.9\,\mathrm{GeV}/c$
	minimum p	$> 6\,\mathrm{GeV}/c$
	maximum p	$> 10\,\mathrm{GeV}/c$
	DLL$\mu\pi$	> -5
J/ψ:	χ^2_vtx/nDoF	< 25
	$\lvert M(\mu\mu) - M(J/\psi)\rvert$	$< 60\,\mathrm{MeV}/c^2$

Table 6.7: $J/\psi \to \mu^+\mu^-$ sample selection criteria for the initial estimation of trigger performance on signal.

This selection results in samples containing ∼3500 data and ∼5000 MC events. The MC sample is almost background free, while for data $S/B \sim 4$. No background subtraction was applied to either sample and therefore signal and background events within the signal peak are kept. The trigger conditions present in this work were those found under the trigger nickname Physics_25Vis_25L0_2Hlt1_2Hlt2_May10, running in Moore v9r1p2.

L0 single muon candidates in this trigger version are selected with $p_\mathrm{T} > 320$ MeV/c. The L0 single muon efficiency for both data and MC samples is measured to be 95%. The L0 dimuon is an entirely redundant trigger in these conditions of low p_T thresholds for the individual muons, compared to typical values of 1 GeV/c.

The muon confirmation sequence is first studied. This work was developed before the modification of the confirmation algorithms related to the PV2D issue described above and therefore includes the intermediate candidate confirmation with RZ VELO tracks. This version of the confirmation also includes the enlarged search windows and the mentioned modifications to the PatSeeding algorithm in the T confirmation. Table 6.8 summarizes the results for the different confirmation steps, both in terms of event retention and average number of candidates found in each stage. The confirmation efficiency is high in both

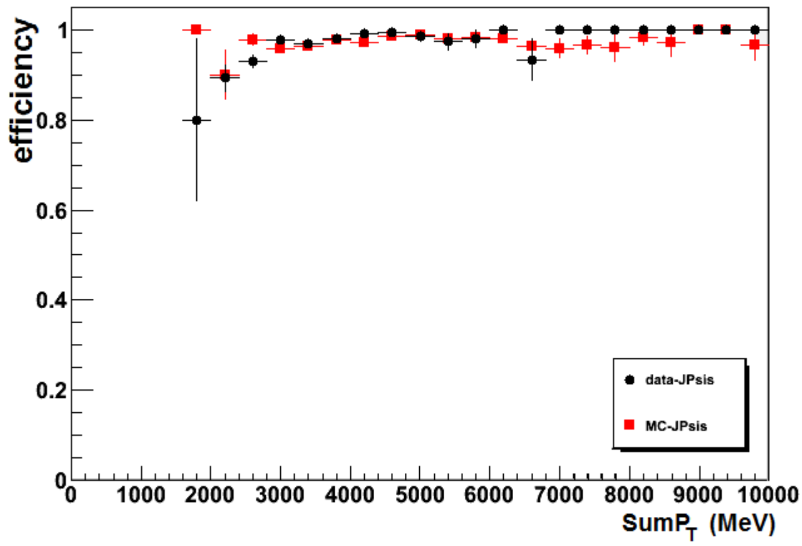

Figure 6.20: HLT1 muon efficiency with respect to L0 muon as a function of the sum of the p_{T} for both muons from $J/\psi \to \mu^+\mu^-$ sample comparing data and MC.

cases. The number of candidates is comparable at each step, although slightly higher for data than MC.

	$J/\psi \to \mu^+\mu^-$ data		$J/\psi \to \mu^+\mu^-$ MC	
	retention (%)	candidates	retention (%)	candidates
T confirmation	99.6	7.3	98.9	4.8
RZ VELO	100	56	100	47
RZ VELO-T filter	100	13	100	10
RZ VELO upgrade	100	13	100	9.5
3D VELO-T match	99	4.6	99	3.8
Total	98.9	4.6	98.4	3.8

Table 6.8: Summary of L0 muon confirmation performance on signal: event retention at each step and average number of passing candidates for $J/\psi \to \mu^+\mu^-$ data and MC samples.

Figure 6.20 shows the inclusive HLT1 muon triggers efficiency with respect to L0 muon selected events as a function of the sum of the p_{T} of both muons from the decay (Σp_{T}). The integral value is 97% in both data and MC. The main contribution comes from the no-IP versions of the dimuon alley, triggering on masses above 2.5 GeV/c^2 (92% of the total HLT1 efficiency for data y MC). The second most efficient selection, with big overlap to dimuons, is the single muon line, with a p_{T} cut at 1.3 GeV/c (providing 88% of the total efficiency for data and 93% on MC).

Figure 6.21 displays the inclusive HLT2 muon efficiency with respect to HLT1 muon triggered events again as a function of Σp_{T}. The corresponding integral value is 94% on data and 98% on MC.

Finally, Fig. 6.22 summarizes the combined performance of muon triggers for L0 + HLT1 + HLT2 with respect to all selected events, as a function of Σp_{T}. The integral

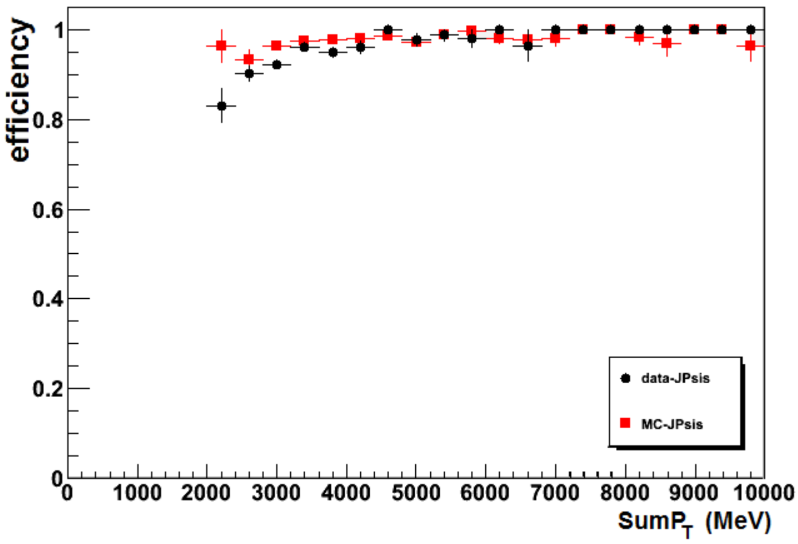

Figure 6.21: HLT2 muon efficiency with respect to HLT1 muon as a function of the sum of the p_T for both muons from $J/\psi \to \mu^+\mu^-$ sample comparing data and MC.

efficiency is 87% on data and 90% on MC.

The conclusions from this preliminary work were that high efficiencies were found at every trigger level for the $J/\psi \to \mu^+\mu^-$ signal decay. In general, trigger performances on data and MC showed good agreement at every stage, although with slightly better results for MC.

6.4.2 Prospects for evaluating trigger efficiencies of $B_s \to \mu^+\mu^-$ using $J/\psi \to \mu^+\mu^-$

The objective of the work summarized in this section was the evaluation of the trigger efficiency on offline selected $J/\psi \to \mu^+\mu^-$ and its extrapolation to the $B_s \to \mu^+\mu^-$ decay, as described in [147]. In contrast to the previous section, the modified version of the muon confirmation algorithm, not using RZ VELO tracks, was employed.

The trigger efficiency on $J/\psi \to \mu^+\mu^-$ can be used to estimate the trigger efficiency of the rare decay $B_s \to \mu^+\mu^-$ assuming that the only relevant quantities for the trigger efficiency are the properties of the dimuon final state. The triggers studied here select the events on the basis of the p_T of the muons. The trigger efficiency for $J/\psi \to \mu^+\mu^-$ events, measured in bins of Σp_T, can be then converted into a trigger efficiency for $B_s \to \mu^+\mu^-$ by re-weighting it to reproduce the harder spectrum of $B_s \to \mu^+\mu^-$.

The careful estimation of trigger efficiencies on signal can be then compared to the main strategy used by LHCb to extract trigger efficiencies, evaluated using TIS events [148], thus validating the strategy. This method is essential for the normalization of the BR($B_s \to \mu^+\mu^-$) with respect to its controls channels (see Section 2.3.1), which requires the evaluation of the ratio of trigger efficiencies on signal and control channels.

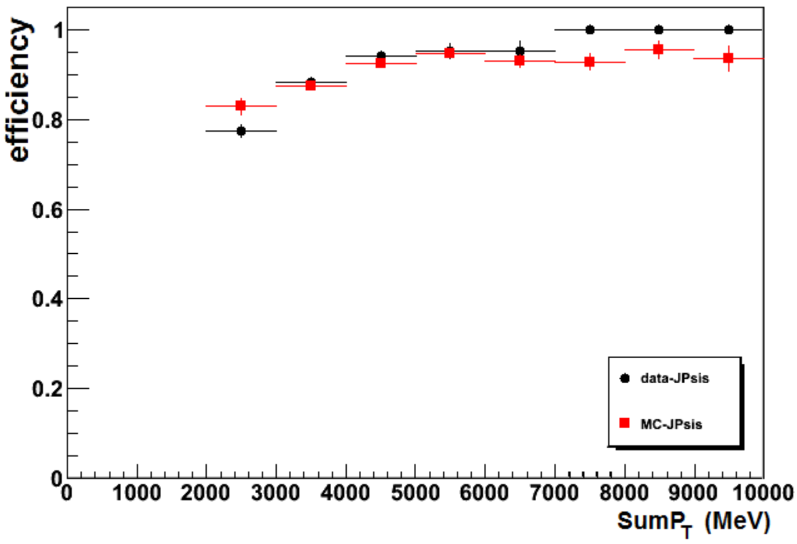

Figure 6.22: L0+HLT1+HLT2 muon triggers efficiency with respect to all selected events as a function of the sum of the p_{T} for both muons from $J/\psi \to \mu^+\mu^-$ sample comparing data and MC.

Signal selection

The selection of $J/\psi \to \mu^+\mu^-$ candidates was performed with criteria close to the one discussed in chapter 4 of [59], similar to the selection described in previous section. They are summarized in Table 6.9.

The selection was applied to the then available data from the 2010 run ($15\,\mathrm{nb}^{-1}$) from the dimuon stripping stream and to 10,000 simulated inclusive J/ψ MC 2010 (sim01-reco01) events. The dimuon mass spectra of the selected samples are shown in Fig. 6.23.

$J/\psi \to \mu^+\mu^-$ selection:		
$\mu^{\pm}$:	ISMUON	
	p_{T}	$> 1\,\mathrm{GeV}/c$
	minimum p	$> 6\,\mathrm{GeV}/c$
	maximum p	$> 10\,\mathrm{GeV}/c$
	$\chi^2_{\mathrm{track}}/\mathrm{nDoF}$	< 5
	DLL$\mu\pi$	> -5
J/ψ:	$\chi^2_{\mathrm{vtx}}/\mathrm{nDoF}$	< 15
	$\lvert M(\mu\mu) - M(J/\psi)\rvert$	$< 300\,\mathrm{MeV}/c^2$

Table 6.9: Summary of the $J/\psi \to \mu^+\mu^-$ selection criteria.

In MC, the $J/\psi \to \mu^+\mu^-$ sample selected is almost background free. In data, however, the background is significantly higher. For the analysis of data events, the signal had to be corrected for background. The invariant mass was fitted with a Gaussian for the signal region and a straight line for the background. The signal fraction was extracted from the core ($\pm 30\,\mathrm{MeV}/c^2$) of the Gaussian and the background from the straight line fit. The signal to background ratio was evaluated in bins of Σp_T, summarized in Table 6.10. For the bins above $6\,\mathrm{GeV}/c$, the background contribution is consistent with zero.

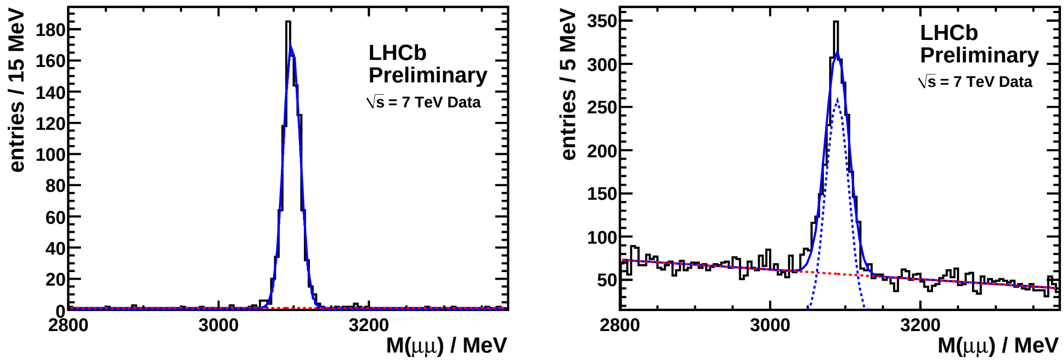

Figure 6.23: Mass of $J/\psi \to \mu^+\mu^-$ in data and minimum bias MC. A linear fit to the background and a gaussian fit to the signal is included.

Σp_T	2-4 GeV/c	4-6 GeV/c	6-8 GeV/c	8-10 GeV/c	above 10 GeV/c
S	1180	535	131	42	53
B	608	71	≈0	≈0	≈0
S / B	1.94	7.54	-	-	-

Table 6.10: Signal and background fractions as determined from the mass fit.

$J/\psi \to \mu^+\mu^-$ trigger efficiency for L0 $\times$ HLT1

As first step, the J/ψ trigger efficiency is determined on TIS events. To measure the trigger efficiency, the Σp_{T} distribution of TIS events which are also triggered on signal by the lifetime unbiased single or dimuon triggers is divided by the same distribution of all TIS events.

Figure 6.24 shows the trigger efficiency for events in the central region around the J/ψ mass (± 30 MeV/c), and for the upper and lower sidebands. Note that the efficiency for the sidebands in the low Σp_{T} region is significantly lower than the efficiency for the signal region.

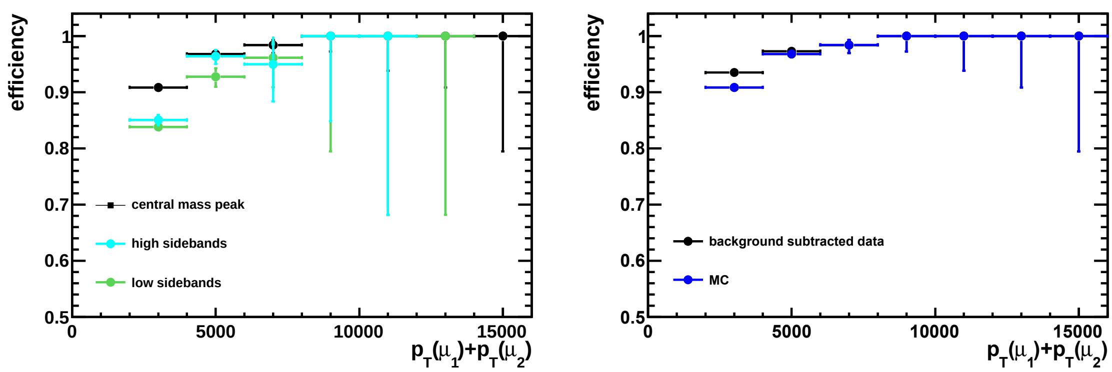

Figure 6.24: Trigger efficiency for events in the signal region and in the sidebands (left) and trigger efficiency with background correction applied, compared to the MC trigger efficiency.

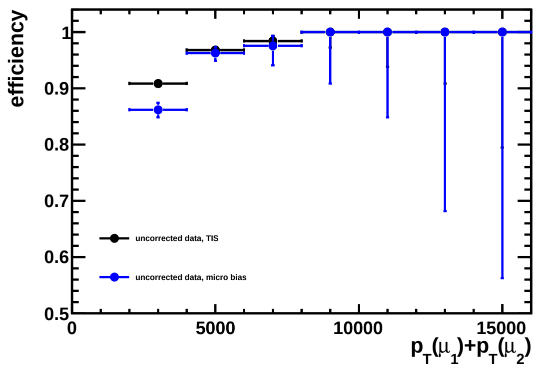

Figure 6.25: Trigger efficiency $\epsilon(S+B, J/\psi)$ measured with the TIS and micro bias methods.

The trigger efficiency can be corrected for background using the signal to background fraction shown in Tab. 6.10. The signal efficiency for each bin of Σp_{T} ($\epsilon(S)_i$) can be calculated as

$$\epsilon(S)_i = \frac{S_i + B_i}{S_i} \times (\epsilon(S+B)_i - \frac{B_i}{S_i + B_i} \times \epsilon(B)_i), \tag{6.1}$$

where, for each for each bin of Σp_{T}, S_i and B_i are the number of signal and background events as estimated by the fit, $\epsilon(S+B)_i$ the efficiency in the central region of the mass peak (which includes signal and background), and $\epsilon(B)_i$ the trigger efficiency determined as average of the lower and upper mass sidebands.

The background-corrected trigger efficiency is shown in Fig. 6.24 together with the MC trigger efficiency. The background correction gives only a significant contribution in the lowest Σp_{T} bin. Data and MC differ in the lowest bin by 3% whereas the agreement is excellent for higher Σp_{T}. The integrated trigger efficiency for $J/\psi \to \mu^+\mu^-$ is determined to be

$$\begin{aligned} \epsilon_{trg}(J/\psi)_{data} &= 94.9 \pm 0.2\%, \\ \epsilon_{trg}(J/\psi)_{MC} &= 93.3 \pm 0.2\%, \end{aligned}$$

where only the statistical error is given.

This result can be cross-checked using the fact that a large fraction of the data were recorded using the micro-bias triggers. The data sample recorded with these triggers is to a good approximation trigger-unbiased. Only the trigger efficiency uncorrected for background is compared. Figure 6.25 shows that in the lowest Σp_{T} bin, the TIS method gives a trigger efficiency ∼5% higher than the estimation from the micro-bias sample. For higher Σp_{T}, the agreement between the two methods is very good.

Extrapolation to $B_s \to \mu^+\mu^-$

The trigger efficiency just determined on $J/\psi \to \mu^+\mu^-$ data events can be used to estimate the trigger efficiency on $B_s \to \mu^+\mu^-$. The efficiency, measured in bins of Σp_{T}, is applied to a MC $B_s \to \mu^+\mu^-$ sample according to its harder spectrum. The precision of this method can be evaluated on MC. The trigger efficiency determined on MC $J/\psi \to \mu^+\mu^-$ events is also applied to the Σp_{T} spectrum of $B_s \to \mu^+\mu^-$. Both efficiencies, obtained with data and

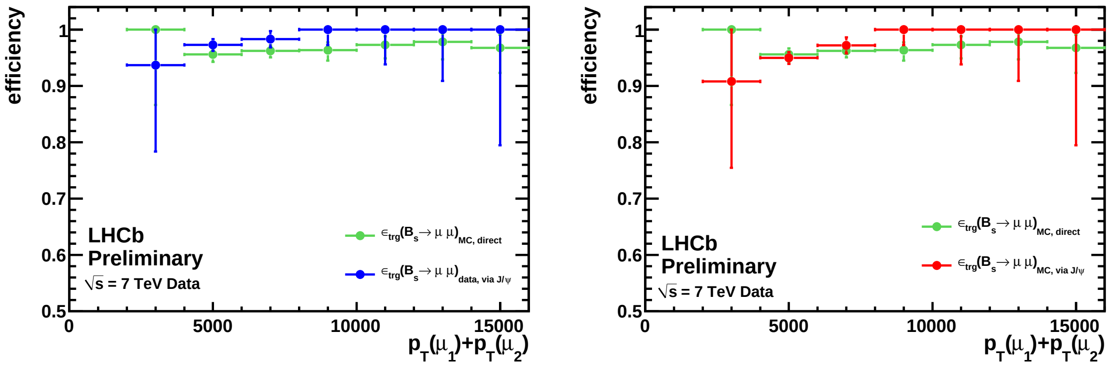

Figure 6.26: Trigger efficiency evaluation for $B_s \to \mu^+\mu^-$: the directly determined MC efficiency is compared to that obtained via the extrapolation of the efficiency on selected $J/\psi \to \mu^+\mu^-$ events from data (left) and MC (right) samples.

MC $J/\psi \to \mu^+\mu^-$ samples can be compared to the trigger efficiency determined directly from MC (Fig. 6.26).

The integrated trigger efficiencies from MC are determined as

$$\begin{aligned} \epsilon_{trg}(B_s \to \mu^+\mu^-)_{MC,direct} &= 96.4 \pm 0.2\%, \\ \epsilon_{trg}(B_s \to \mu^+\mu^-)_{MC,viaJ/\psi} &= 95.1 \pm 0.2\%. \end{aligned}$$

They agree within 1.3%, which quantifies the precision of the method.

The integrated trigger efficiency on $B_s \to \mu^+\mu^-$, determined from $J/\psi \to \mu^+\mu^-$ data events is determined to be

$$\epsilon_{trg}(B_s \to \mu^+\mu^-)_{dataJ/\psi} = 98.8 \pm 0.2(stat) \pm 1.3(syst)\%,$$

where the systematic uncertainty has been taken from the precision obtained above.

6.5 Later developments in HLT muon triggers

LHC running conditions evolved rapidly through the 2010 run [149, 150]. As the LHC luminosity increased, tighter trigger conditions were required while the available CPU power of the EFF was fully exploited.

About 3/4 of the total data collected in the 2010 run ($\sim$38 pb^{-1}) was recorded during the last month of operation of 2010 (October). In these last stages, the instantaneous luminosity peaked at about 1.7×10^{32} cm^{-2}s^{-1}, close to the LHCb nominal running luminosity. However, this value was achieved with only 344 colliding bunches, instead of the nominal 2622 bunches discussed in Section 4.1. These running conditions corresponded to an average number of visible interactions per bunch crossing (μ) of up to 2.5 (Fig. 6.27), much higher than the design value $\mu = 0.4$.

Higher μ values means more vertices and tracks per event, higher readout rates and increased event size and processing time. The main limitation was found in the CPU time consumption in the partially installed EFF to process the very busy events. This section describes the modifications implemented in the HLT motivated by the need to dealing with increasingly more complex events.

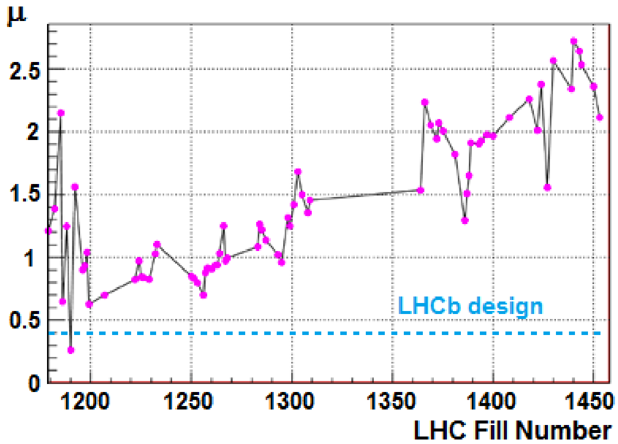

Figure 6.27: Evolution of the average number of visible interactions per bunch crossing at LHCb (μ) from July 2010 to the end of the 2010 data taking period. The design value of 0.4 is displayed.

Contrary to the case of the muon triggers, the performance of hadron triggers was found to be extremely dependent on the particular running circumstances. This forced the confirmation principle to be abandoned for HLT1 hadronic triggers and an alternative, based on a single track trigger, to be deployed by the second half of the 2010 run.

The EFF was completely installed in the 2010/2011 winter shut-down. The experience gained coping with the harsh environment of the late 2010 run inspired the modifications in the VELO and HLT1 muon track reconstructions and the development of a re-optimized version of the inclusive HLT2 topological triggers. These modifications, implemented for the 2011 run, have allowed to run the LHCb experiment at luminosities higher than initially foreseen.

6.5.1 HLT1 single track trigger

HLT1 hadronic triggers were known to be vulnerable to contamination from ghost tracks, particularly in the presence of pile up [151]. The commissioning of these triggers in the early 2010 run showed that this was a real problem. An alternative strategy for HLT1, departing from the idea of L0 confirmation was implemented, aiming for the selection of events based on a single detached high momentum track (*track trigger*) [115]. The main features of this strategy, and its implication for muon triggers will now be described.

The main requirements for the new strategy were to fit into the timing envelope considered acceptable for HLT1 event processing (estimated in [ref Vava] to be 10 ms) and its performance to remain stable with the changing LHC conditions, in particular with respect to μ in order to allow LHCb to run at higher luminosities than expected. Some limiting conditions to the event saturation were imposed, removing events with extremely high occupancies in the VELO, OT and IT.

The strategy is based on the fact that all decays considered interesting at LHCb contain at least two charged tracks in the final state, which, given the long lifetime and heavy mass of the B mesons, present large IP and higher momentum and p_{T} than light quark hadrons produced at the PV.

VELO tracks with significant IP with respect to any PV are first selected and an additional requirement of sufficient VELO hits is applied. Passing VELO tracks are used as seeds for the forward tracking. Minimum p and p_{T} values are implicit in the reconstruction parameters, which allow to reduce the search windows used in the T-stations. This limits the reconstruction time to below 10 ms and makes this time basically independent of μ.

Cuts on p and p_{T} are then applied to the tracks in order to reduce the rate. The remaining candidates are fitted using a Kalman filter procedure with outlier removal. This allows tracks to be filtered according to an offline-like track χ^2, as well as computing a IP χ^2 which is also used as a discriminant variable. A cut on the track fit χ^2 enables the trigger to reject ghost tracks. Cuts on both variables determine the final rate reduction.

These steps constitute the general track trigger selection, which is applied to all events regardless of their L0 origin.

The performance results for the track trigger presented in*track trigger* indicate that the output rate increases only slowly with μ and that the trigger always selects a good track, proving it to reject ghosts being essentially unaffected by pileup.

In the case of decays involving muons, an additional cut is available, based on the muon identification algorithm. This fact is exploited and an alternative selection (*track-muon*) is applied in parallel to the main one for events triggered by the L0 muon or dimuon lines. The identification of the track as a muon allows to relax most of the cuts used in the selection.

Including the track-muon line, the single track trigger provides a fast and totally inclusive trigger for HLT1. However, as lifetime-biasing cuts are essential to this strategy, an alternative is needed to trigger on decays used in analyses preferring lifetime-unbiased selections, for example $B_s \to J/\psi(\mu^+\mu^-)\phi$. These decays are covered by the implemented lifetime unbiased dimuon selections.

6.5.2 Fast VELO reconstruction

A new implementation of the VELO pattern recognition algorithms was developed to cope with the new requirements for the HLT tracking [152]. First, the HLT1 is not to perform the PV reconstruction from RZ tracks, but from 3D tracks instead. This requires the full 3D reconstruction to be executed in every event. Secondly, the increased occupancy deriving from the higher values of μ implies that the algorithm needs to be revisited in order to re-tune it for this context.

The performance of the new algorithm was tested on a MC sample simulating data taking at $\mu = 2.5$. Results in terms of ghost rate and track efficiencies improved with respect to the previous implementation reducing the total time per event by 30%.

6.5.3 HLT1 muon reconstruction

The sequence of reconstruction and selection of muon candidates in the HLT1 muon alleys has been recently reviewed [153]. The confirmation strategy of L0 candidates with T and VELO track segments, which had to deal with different L0 inputs, has been replaced by a unified muon reconstruction sequence executed on all events passing either L0 single or dimuon triggers.

The fast VELO reconstruction procedure described above is first executed. The reconstruction of non-pointing tracks is however not implemented in HLT1 but left for HLT2.

The compatibility of the VELO tracks with the muon hypothesis is then tested with a new fast muon identification algorithm, and only the tracks remaining are to be used as seeds in the forward reconstruction to long tracks.

The novelty in the most recent version of the HLT1 muon triggers is the fast muon identification of VELO candidates. This reconstruction algorithm is based on the facts that the LHCb magnet does not change the vertical component of the momentum of particles, a low occupancy is found in the muon stations and that a particle must have a momentum at least of 6 GeV/c to cross all muon detectors. For each VELO candidate, a search region is considered in M3. The center of this region corresponds to the extrapolation of the VELO track. In order to account for multiple scattering, which causes the deviation of the track from its VELO extrapolation, the region of interest is defined in the vertical direction with a width twice the size of a detector pad in the outer region on M3. In the horizontal direction, the maximum possible deflection for a 6 GeV/c particle is considered, for both charge hypothesis. Any hits found are used to make track candidates used to look for extra hits in M2, M4 and M5. Candidates containing at least one additional hit are accepted. The track obtained is then projected on the horizontal plane and a linear fit is used to reject candidates with a large χ^2.

VELO track candidates associated successfully to enough muon hits are used in the forward tracking reconstruction. As in the case of the track trigger described above, implicit cuts are applied on the reconstruction settings requiring track p>6 GeV/c and p_{T} > 0.5 GeV/c, in order to speed up the tracking algorithm.

Finally, successful candidates are fitted with a fast Kalman filter and the offline muon identification, which makes use of fitted tracks, is applied achieving further rate reduction.

6.5.4 HLT2 inclusive B triggers

The set of inclusive B trigger lines used in HLT2 is based on the topological selection of 2, 3 or 4 tracks forming a displaced vertex. In the most recent version of HLT2, the muon+track selection has been unified with the topological lines, extending the strategy in fact to “n muons + m tracks”, with n+m={2, 3, 4}. This section summarizes the strategy and performance results described in [154].

The execution of HLT2 starts with the full event reconstruction. All VELO tracks are used as seeds to reconstruct long tracks using the forward pattern recognition algorithm, again with implicit cuts to reduce processing time, followed by a track fit and particle identification algorithms.

The selection of candidates is performed in several steps. First, 2-body vertices are selected using discriminating variables essentially analogous to those described for the muon+track strategy. An additional requirement is however that at least one of the tracks in the pair passed the HLT1 inclusive track trigger. In the next steps, additional tracks may be added to the trigger candidate filtering them in DOCA and requiring them to be associated to the same PV. The associated PV is defined for each track as the one which minimizes its IP.

Candidates with 2, 3 and 4 tracks, with at least one of them passing the HLT1 track trigger, are then filtered using a multivariate selection (*boosted decision tree*), a stage which produces most of the rejection of the topological lines.

The muon variants of the topological strategy require that at least one of the particles in the candidate has been identified as a muon. This reduces the number of candidates and allows for softer selection requirements.

Combined with the HLT1 track trigger, the HLT2 topological lines have been found to provide a rate reduction from 1 MHz at L0 output down to 1 kHz. The b purity in the selected events is close to 100% [154].

Again, as described for HLT1, lifetime-unbiased muon trigger lines are used in HLT2, with their latest implementation described in [153].

6.6 Dimuon spectra in the first LHCb data

This section illustrates the excellent performance achieved by the LHCb detector and the online and offline reconstruction and selection strategies, including the dedicated HLT muon triggers discussed in this work.

Figures 6.28 and 6.29 show the full dimuon mass spectrum up to the Z^0 mass as observed by LHCb in the 37 pb^{-1} collected during the 2010 run and in the 70 pb^{-1} collected during the initial months of the 2011 run respectively [155].

Figures 6.28 and 6.29 also show the contributions to the dimuon mass spectra for both data samples from the different HLT2 triggers, by requiring a TOS decision of each specific HLT2 line or set of lines. The various discontinuities observed in some trigger categories correspond to the overlap of lines with different explicit invariant mass cuts and prescale factors.

Finally, Fig. 6.30 shows the standard LHCb display of a reconstructed event, recorded on June 14$^{\mathrm{th}}$ 2011, in which the candidate most compatible with $B_s \to \mu^+\mu^-$ is found.

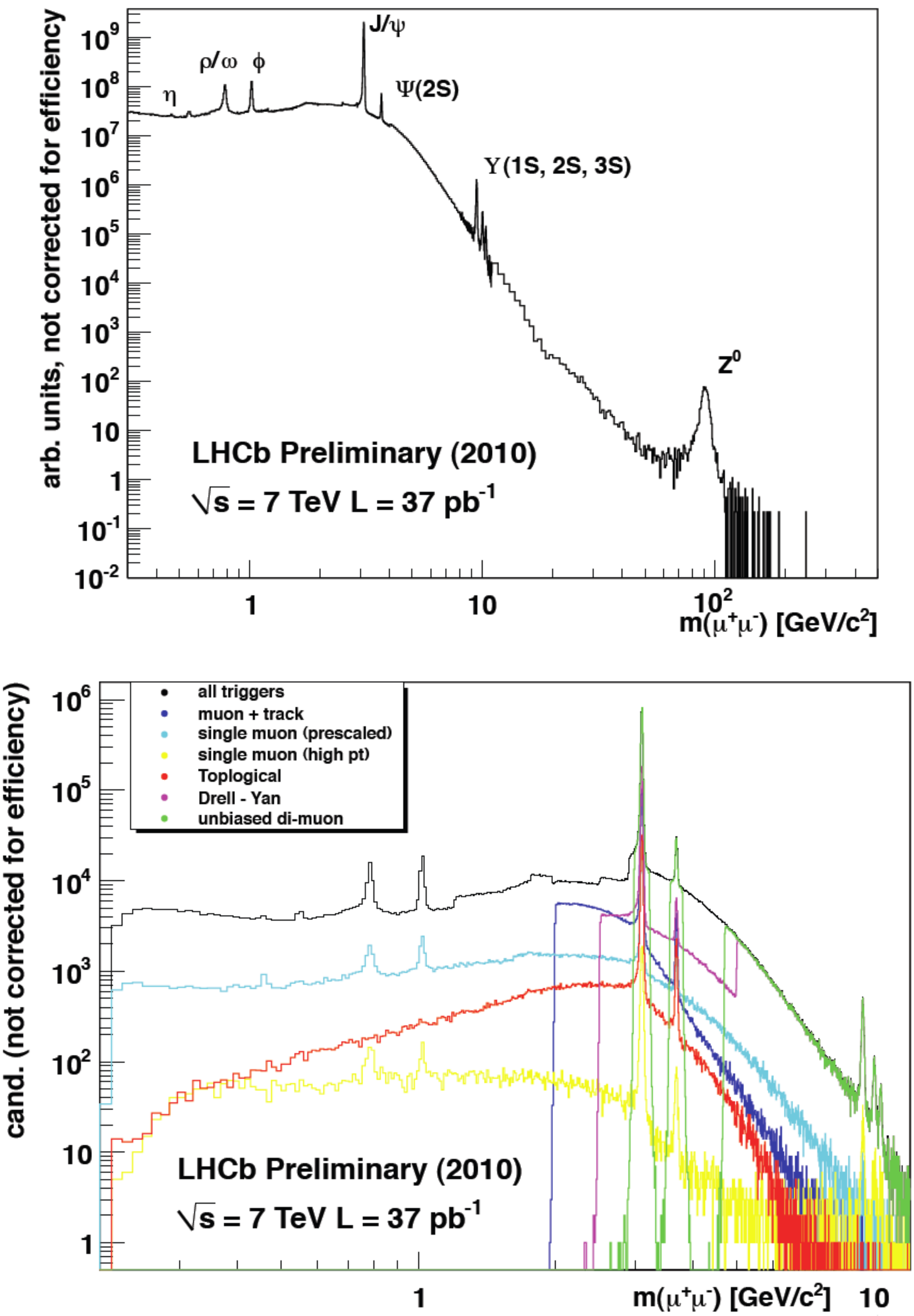

Figure 6.28: Dimuon spectrum from the $\sim$37 pb^{-1} recorded in 2010 (top) and contributions from the different HLT2 lines (bottom). Figures from [155].

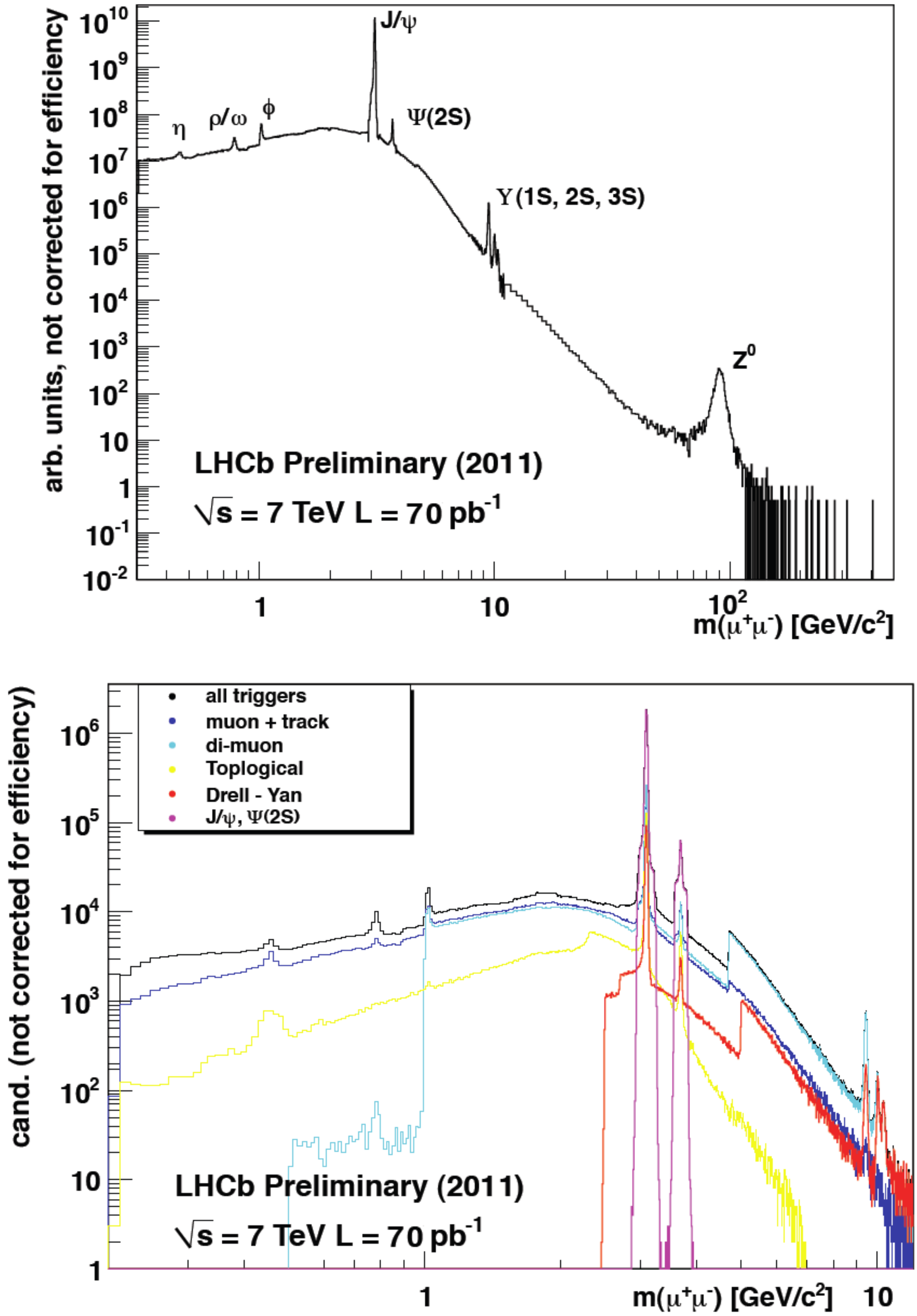

Figure 6.29: Dimuon spectrum from the ∼70 pb^{-1} recorded in the first months of 2011 (top) and contributions from the different HLT2 lines (bottom). Figures from [155].

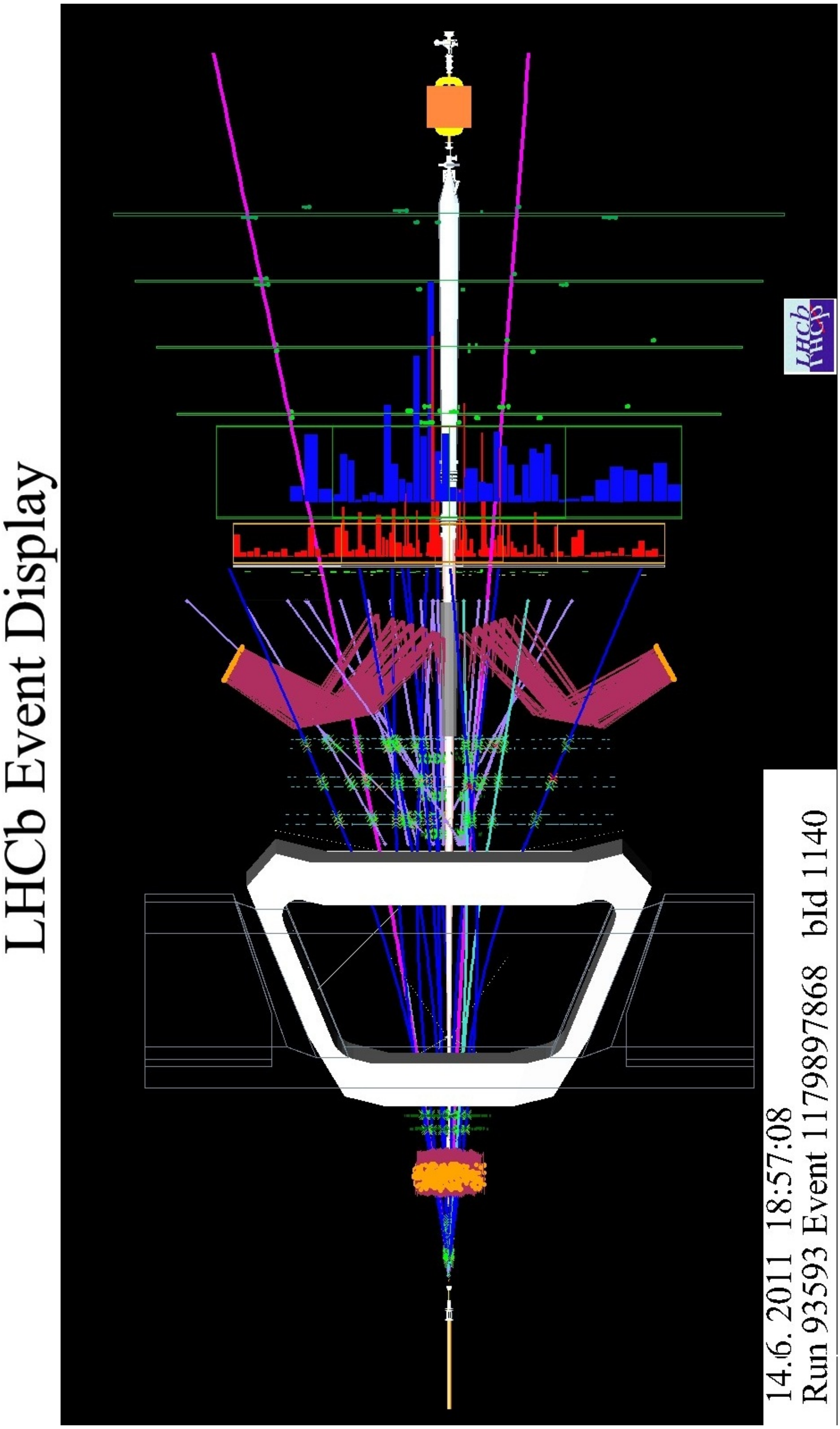

Figure 6.30: $B_s \to \mu^+\mu^-$ event candidate. Purple lines correspond to reconstructed muon tracks.

Chapter 7

Conclusions

Flavour Physics plays an important role as an indirect probe for the search for New Physics beyond the Standard Model. Muonic decays of B mesons provide a perfect benchmark for such studies.

The LHCb experiment has already started an exciting Flavour Physics program at the LHC. The first level of signal selection is applied by the trigger system. The inclusive muon+track selection, used in the two levels of the software trigger, was developed using MC simulation before the LHC start-up. The HLT1 muon+track strategy was optimized on semileptonic decays, yielding higher signal efficiencies at a fraction of the rate devoted to the single muon selection.

A muon+track selection was also implemented in HLT2 and optimized on simulated $B_d \to K^* \mu^+ \mu^-$ decays. The combination of the muon+track HLT1 alley and the muon+track HLT2 selection makes up the optimal combination of trigger selections for this key channel, resulting in high signal efficiency and negligible trigger rates.

A global optimization on MC of the HLT2 inclusive muonic triggers, single muon, dimuon and muon+track lines, in several scenarios of luminosity and bandwidth division was also performed prior to the LHC start-up. The proposed solution was a trigger strategy formed by a small number of increasingly more restrictive inclusive selections, which in each case provides high efficiency for a wide variety of muonic decays, while achieving the rate reduction power required for each scenario.

Once the first collisions were provided by the LHC, the data available was used in the commissioning of the HLT muon triggers. It was found that the performance of the HLT1 single muon line using impact parameter cuts was worse than expected, due to the measurement being affected by wrong assumptions in the algorithms used in the simplified reconstruction of the primary vertices as used in HLT1. A reasonable performance for this line was recovered once a new version of the reconstruction algorithm was implemented.

A careful study of the different reconstruction and selection stages in each of the HLT1 muon lines was carried out. The results of this work showed no significant differences between the trigger performance on data and MC expectations.

The $J/\psi \to \mu^+ \mu^-$ process provided the first source of signal decays with muons, although it lacked the separation from the primary vertices required by trigger lines developed for the selection of B meson decays. This sample was used in the commissioning of the trigger performance in terms of muon track reconstruction and the measurement of their momenta and invariant mass. The HLT1 and HLT2 lifetime-unbiased triggers provided high efficiencies for $J/\psi \to \mu^+\mu^-$ with good agreement with the performance expected from MC simulation.

The $J/\psi \to \mu^+\mu^-$ decay was also used as a benchmark for a data-driven estimation of the trigger efficiency on $B_s \to \mu^+\mu^-$, required for the normalization of the measurement of its branching ratio. The extrapolation of the measured trigger efficiencies to the harder muon momentum spectrum of this decay predicts a high L0 $\times$ HLT1 efficiency, again in good agreement with the expectation from simulated events.

The evolution of the LHC running conditions during 2010 and the expectations for the 2011 run motivated several modifications in the HLT algorithms. These modifications have allowed to run the LHCb experiment at luminosities higher than initially foreseen during the 2010 and 2011 LHC runs. An excellent performance has been achieved for the detector and both the online and offline reconstruction and selection algorithms at these demanding conditions.

Appendix A

Resumen

Este trabajo recoge el desarrollo y la optimización de las selecciones basadas en la presencia de muones para el trigger de alto nivel (HLT) del experimento LHCb, que analiza las colisiones entre protones proporcionadas por el Gran Colisionador de Hadrones (LHC).

Marco teórico

El Modelo Estándar de la Física de Partículas

El Modelo Estándar de la Física de Partículas (ME) es el modelo vigente para describir los propiedades de las partículas constituyentes de la materia, actualmente consideradas como elementales, así como las interacciones entre ellas. Este modelo se ha ido consolidando a lo largo de la segunda mitad del siglo XX, tanto por la multiplicación de sus evidencias experimentales como por la proliferación de desarrollos teóricos con gran poder de predicción.

En el ME toda la materia del Universo se compone de dos tipos de fermiones, llamados leptones y quarks, junto con sus correspondientes antipartículas. Leptones y quarks se agrupan en tres familias de propiedades idénticas, exceptuando la masa. Las interacciones descritas por el ME incluyen el electromagnetismo y las fuerzas nuclear fuerte y débil. Éstas se explican a partir del intercambio de bosones mediadores, según la teoría Electrodébil y la Cromodinámica Cuántica. La interacción electromagnética y la fuerza débil surgen a partir de la ruptura espontánea de simetría en el modelo electrodébil mediante el mecanismo de Higgs, en el cual los bosones W y Z adquieren masa y aparece un nuevo campo escalar, el bosón de Higgs. Éste es tambien el origen de las masas de los fermiones y de la mezcla entre quarks de distintas familias a través de las corrientes cargadas, descrito por la matriz de Cabibbo-Kobayashi-Maskawa (CKM). La matriz CKM constituye la única fuente de violación de la simetría combinada de conjugación de carga y paridad (CP), y describe con éxito desde su primera observación en 1964 en la desintegración de los kaones neutros hasta las medidas más recientes en factorías de mesones B. Cabe mencionar que la interacción gravitatoria no está incluida en el ME.

Física más allá del Modelo Estándar

A pesar de su éxito, a día de hoy ya son conocidas diversas razones, tanto experimentales como teóricas, por las cuales el ME no puede considerarse una teoría final, sino un modelo efectivo válido a escalas de energía inferiores al TeV. Como se ha dicho, el ME no incluye la gravedad, por lo que no proporciona ningún mecanismo de unificación de ésta con el resto de fuerzas a energías de la escala de Planck. Por otra parte, no proporciona ninguna explicación al origen de la materia oscura, sustancia que no es directamente detectable y que sin embargo es necesaria para explicar las curvas de velocidades de rotación galácticas. Además, son necesarias nuevas fuentes de violación de CP, unidas al mecanismo de la matriz CKM, para explicar la evolución desde una situación simétrica al Universo actual, dominado en su composición por materia. Por último, el fenómeno observado de las oscilaciones y mezcla de neutrinos podría ser entendido con una descripción similar a la matriz CKM para los leptones. El grado de violación de la simetría CP podria ampliarse con nuevas fases en el sector leptónico, lo cual podría contribuir a la situación asimétrica actual a través del proceso de leptogénesis. Todo ello implica que las masas de los neutrinos no podrían ser nulas, al contrario de lo asumido en el actual ME.

Desintegraciones muónicas en LHCb

El Gran Colisionador de Hadrones (LHC) y sus experimentos asociados se han construido con el objetivo de explorar la escala del TeV y determinar el rango de validez del ME. Se espera descubrir finalmente el bosón de Higgs, elemento pendiente del ME, o bien algún otro mecanismo que cumpla una función similar. El experimento LHCb busca física más allá del ME mediante el estudio procesos de física de sabor, esto es, aquellos fenómenos mediados por interacciones que distinguen el sabor de las partículas elementales. En el ME dichos procesos están asociados a las interacciones débil y de Yukawa.

El estudio de la oscilación y desintegración de los mesones B, copiosamente producidos en las colisiones protón-protón proporcionadas por el LHC, constituye una fuente de observables tales como asimetrías de CP, fracciones de desintegración parcial, distribuciones angulares y otros. Las medidas de precisión de dichos observables constituyen una herramienta para comprobar la validez de los distintos modelos teóricos propuestos para solventar los problemas del ME.

Una parte fundamental del programa de investigación de LHCb se basa en desintegraciones de mesones B que producen muones en su estado final. Los procesos $B_s \to \mu^+\mu^-$ y $B_d \to K^*\mu^+\mu^-$, con probabilidades relativas extremadamente pequeñas, pueden proporcionar límites a los nuevos modelos de física a través de la medida de su fracción de desintegración y de distintas asimetrías en las distribuciones angulares de los productos respectivamente. Así mismo, la medida de la violación de CP en el proceso de mezcla de mesones B puede ser estudiada, por ejemplo, con procesos $B_s \to J/\psi(\mu^+\mu^-)\phi$ y semileptónicos.

El detector LHCb del Gran Colisionador de Hadrones

El Gran Colisionador de Hadrones

El Gran Colisionador de Hadrones (LHC) del CERN es el mayor y más potente acelerador de partículas del mundo, situado en la region fronteriza entre Suiza y Francia, cerca de la ciudad de Ginebra (Fig. A.1). Ocupa un tunel de 27 km en forma de anillo y situado bajo tierra a una profundidad media de 100 m. Está compuesto por dos aceleradores paralelos por los que circulan haces de protones en ambos sentidos y diseñado para hacerlos chocar a una energía nominal en el centro de masas de 14 TeV. Los protones viajan agrupados en racimos separados a intervalos de 25 ns, lo que produce un ritmo de cruces de 40 MHz. Tras su puesta en marcha a finales de 2009, ha sido operado durante 2010 y 2011 a una energía de colisión de 7 TeV.

Las colisiones entre protones del LHC son analizadas por varios detectores de partículas. Los principales son: ATLAS y CMS, detectores de propósito general que buscan nuevas partículas masivas como el bosón de Higgs o las predichas por los modelos supersimétricos; ALICE, que estudia las propiedades de la materia en estados de extrema densidad producidos en las colisiones entre protones y entre iones pesados; LHCb, experimento dedicado al estudio de la Física de Sabor y al que se refiere el presente trabajo.

El experimento LHCb

El experimento LHCb del LHC consiste en un detector diseñado en forma de espetrómetro de un solo brazo y optimizado para el estudio de los procesos de desintegración de los mesones B. Esta disposición, semejante a la de un detector de blanco fijo, obedece al hecho de que estas partículas se producen a bajo ángulo respecto al haz de protones. Por otro lado, la luminosidad instantánea en el punto de interacción de LHCb (2×10^{32} $\text{cm}^{-2}\text{s}^{-1}$) es menor que la observada por el resto de detectores, lo cual permite que en cada cruce de paquetes de protones haya en general un único proceso de colisión. Esto permite al detector distinguir entre el vértice primario (PV), punto de la colisión entre protones, y el secundario, punto de desintegración de las partículas B objeto de estudio.

El detector LHCb (Fig. A.1) está compuesto de un conjunto de subsistemas, cada uno de ellos con una tarea especializada. Los detectores de trazas (VELO, TT, TS) y el imán permiten reconstruir las trazas dejadas por las partículas cargadas así como medir su momento. La identificación de la naturaleza de cada partícula se realiza a partir de la información proporcionada por el resto de sistemas: los detectores basados en el efecto Cherenkov (RICH 1 y 2) que permiten medir la masa de las particulas cargadas en un amplio rango de momentos; el sistema de calorímetros (SPD, PS, ECAL y HCAL) que mide la energía depositada por las partículas en su interacción con sucesivas placas de material denso; y el sistema de muones, formado por cinco planos de detección, estando cuatro de ellos más allá de los calorímetros y separados por material absorbente, lo cual hace que sólo sean accesibles a los penetrantes muones.

El VELO, cuyos sensores están situados a 8 mm del eje determinado por los haces de protones, permite una gran precisión en la reconstrucción de los vertices así como en la medida del parámetro de impacto (IP) de las trazas respecto de éstos. Debido a que el punto de desintegración de los mesones B tiene un desplazamiento apreciable respecto del PV ($\sim$1 cm), valores altos de IP son un rasgo particular de las trazas que provienen de esta desintegración.

Las técnicas de Monte-Carlo (MC) son empleadas para la simulación de sucesos de colisión, que permiten el estudio y la optimización del rendimiento del detector y los algoritmos de reconstrucción y selección de sucesos de señal. Con el objetivo de optimizar las selecciones del HLT descritas en este trabajo, se han empleado dos tipos de muestras simuladas. La primera está formada por sucesos de colisión genéricos con al menos dos trazas reconstruidas en el detector (*Minumum Bias*). Esta muestra se emplea para calcular la retención de sucesos no interesantes, es decir, el ritmo de trigger. El otro tipo de

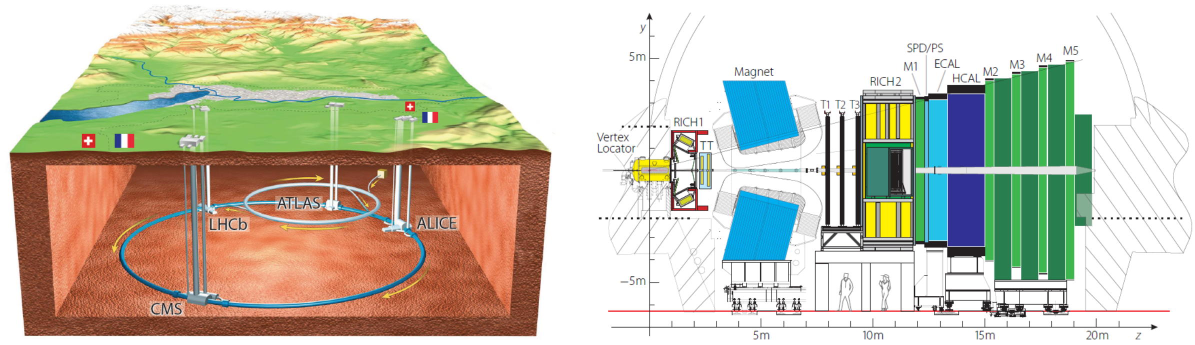

Figure A.1: Vista del túnel del LHC en la frontera franco-suiza, indicando los detectores principales (ATLAS, ALICE, CMS y LHCb) (izquierda) y esquema del detector LHCb con sus sistemas principales: detector de vertices (VELO), detectores de trazas (TT, T1, T2 y T3), iman dipolar, detectores Cherenkov (RICH 1 y 2), calorimetros (SPD, PS, ECAL, HCAL) y cámaras de muones (M1 a M5) (derecha).

sucesos (*señal*) simulan un proceso de desintegración específico y son usados para calcular la eficiencia de selección en sucesos útiles.

El sistema de trigger del experimento LHCb

El sistema de disparo (trigger) del experimento LHCb realiza el análisis de las colisiones de protones con el objetivo de descartar rápidamente aquellos sucesos sin interés. De esta forma se evita que sean registrados y hayan de ser procesados posteriormente. Las características del sistema de trigger vienen determinadas por el objetivo de analizar los procesos de física de mesones B en el entorno de colisiones hadrónicas del LHC.

Necesidad de un sistema de trigger

Los sucesos que son utiles para los objetivos de LHCb se encuentran diluidos en sucesos de colisiones de protones sin mayor interés. El cociente de la sección eficaz de producción de B respecto del total nos indica que se produce un par $b\bar{b}$ por cada 150 colisiones. En condiciones de luminosidad de diseño, esto equivale a un ritmo de producción de unos 100 kHz, de los cuales el 15% apunta en la dirección del detector. Teniendo en cuenta que las desintegraciones interesantes ocurren con una probabilidad de 10^{-4} o menor, la frecuencia de sucesos interesantes visibles por el detector es de 1 Hz o menor.

Por otro lado, el ritmo de colisiones visibles por LHCb es de ∼14 MHz, lo cual indica que los procesos interesantes estan diluidos en fondo en una proporción de uno a diez millones en el mejor de los casos. Por tanto, el trigger de LHCb debe rechazar la mayor parte de sucesos. Las relativamente elevadas masa y vida media de los mesones B proporcionan la clave para distinguir el pruducto de sus desintegraciones, al dotar a sus descendientes de alto momento transverso respecto de la direccion del haz (p_{T}) y de IP.

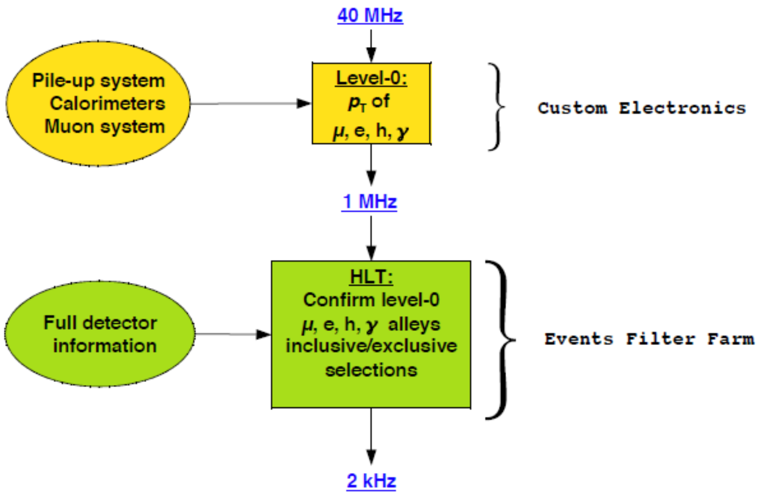

Figure A.2: Niveles de trigger de LHCb.

El trigger del experimento LHCb

La estrategia de trigger de LHCb se encuentra condicionada por dos frecuencias limitantes: la máxima frecuencia de lectura del detector, a 1 MHz y la máxima frecuencia de escritura de sucesos a disco, cuyo valor admisible a largo plazo se ha estimado en ∼2 kHz. Por ello, el trigger de LHCb ha sido diseado en dos niveles (Fig. A.2). El primero de ellos (L0) está formado por componentes electrónicos que reducen la frecuencia de sucesos desde ∼14 MHz a 1 MHz. Su decisión se basa en la presencia de objetos de alta energ´a o momento transverso en el calorímetro o en los detectores de muones.

El segundo nivel (High Level Trigger o HLT) está implementado en algoritmos informáticos, ejecutados en una granja de procesadores (EFF) sobre los sucesos que pasan el L0, y que procesan la información procedente del detector, tomando finalmente la decisión de almacenar o no cada suceso. Debido a que no es posible ejecutar la reconstrucción completa de cada suceso al ritmo de 1 MHz, este nivel se encuentra dividido a su vez en dos etapas: el HLT1, que emplea una reconstrucción parcial hasta reducir el ritmo de sucesos a 40 kHz, y el HLT2, en el que partiendo de la reconstrucción del suceso, se aplican diversas selecciones con distinto grado de inclusividad.

Selecciones de muones para el trigger de LHCb

Como se ha mencionado anteriormente, existe un variado conjunto de desintegraciones muónicas de los mesones B, entre las que se incluyen algunas de las más importantes para el programa de LHCb. Por esta razón es necesario que existan lineas de trigger encargadas de su selección, tanto en L0 como en ambos niveles del HLT.

En el caso del L0, existen dos selecciones basadas en la presencia de un muón (*single muon*) o una pareja de muones (*dimuon*) con alto p_T. Las selecciones muónicas en los dos niveles del HLT incluyen versiones de *single muon* y *dimuon lifetime-biased*, con cortes en IP, y *lifetime-unbiased* sin cortes en IP, pero con cortes más duros en p_T o en la masa invariante del dimuón. En el caso de HLT1, el primer algoritmo que se ejecuta en todas las selecciones de muones es la confirmación del objeto seleccionado en L0. Esto se realiza exigiendo que se pueda reconstruir alguna traza compatible en posición y momento con el candidato de L0.

Además, tanto en HLT1 como HLT2 existe una línea de trigger basada en la reconstrucción de un muón y otra traza que provenga de la misma desintegración (*muon+track*). La selección se basa en cortes en p_{T} e IP en ambas trazas, la menor distancia entre ellas ($DOCA$), la masa invariante de la pareja asumiendo la masa del muón para la traza sin identificar, la separación del punto de mayor proximidad entre ambas respecto del PV (DZ), y el momento transverso de la pareja respecto de la direccion determinada por este punto y el PV (*pointing*).

Desarrollo y optimización de líneas de triggers muónicas con Monte-Carlo

La selección *muon+track* en HLT1

Esta selección de trigger ha sido optimizada empleando sucesos simulados de desintegraciones semileptónicas. Además de su empleo en el estudio de la violacion de CP en la mezcla de mesones B neutros, estos sucesos son importantes para la calibración de los algoritmos de asignación de sabor, necesarios para estudiar las oscilaciones de sabor de los mesones B.

Para cada variable discriminante propuesta se realiza un barrido de eficiencia en señal frente a ritmo de salida de trigger. En cada caso se encuentra un comportamiento de *meseta*, es decir, un rango de valores de salida para el cual la eficiencia del corte es máxima y cercana al 100%. Se escoge como valor de corte para cada variable aquel que hace mínimo el ritmo de salida manteniendo la máxima eficiencia. A partir de aquí, dado que la elección de cortes más duros conlleva una pérdida de eficiencia para cada variable, se hace una variación simultánea de todos los parámetros. Dentro de cada conjunto de combinaciones de cortes que producen un ritmo de salida equivalentes entre sí (compatibles dentro de la incertidumbre estadística), se escoge aquel que proporciona mayor eficiencia.

Dicha optimización se refleja en la Fig. A.3, que muestra los resultados de eficiencia obtenidos sobre $B_s \to D_s^- \mu^+ \nu_\mu$. Para un ritmo de salida de sucesos superior a unos 10 kHz, es posible evitar el uso de variables como la masa invariante y el *pointing*, que pueden complicar el análisis posterior de la muestra seleccionada. Por debajo de este valor, añadir dichas variables supone una ventaja, y por debajo de 5 kHz la tercera estrategia, usando cortes en ambas variables, es sin duda la mejor opción en términos de eficiencia. En cualquier caso, los resultados a cualquier valor razonable de salida son mejores que los correspondientes a una selección *single muon*.

La selección *muon+track* en HLT2

La selección *muon+track* es suficientemente robusta y flexible como para poder ser utilizada en HLT2 y empleada de modo inclusivo para distintos canales de desintegración. La optimización de *muon+track* en HLT2 se ha realizado sobre sucesos de $B_d \to K^* \mu^+ \mu^-$,

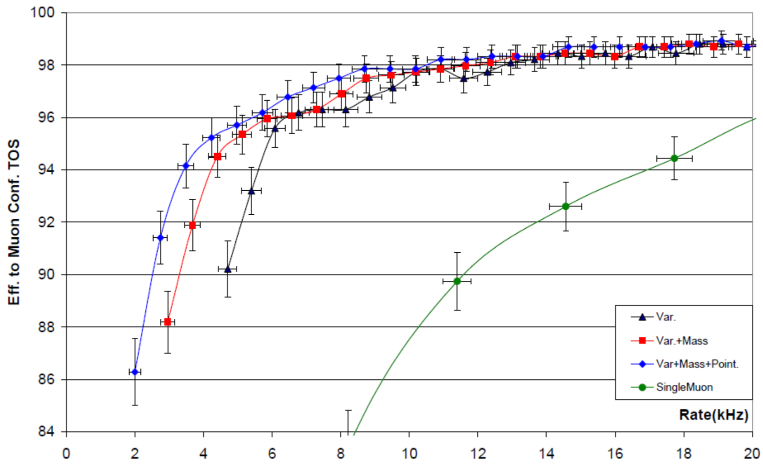

Figure A.3: Eficiencia de *muon+track* en HLT1 sobre $B_s \to D_s^- \mu^+ \nu_\mu$ para la mejor combinación de cortes en cada rango de ritmo de salida de acuerdo a las variables simples p_{T}, IP, DOCA y DZ, estas variables simples junto con la masa invariante, y las variables simples junto con la masa invariante y la medida de pointing. Se comparan con el resultado obtenido mediante una selección basada en un muón con cortes en p_{T} e IP.

de modo que además de obtener la máxima eficiencia, se han minimizado los sesgos que pueda introducir el trigger en la distribución de masa invariante de la pareja de muones.

El resultado es que la combinacin de selecciones de trigger más eficiente para este canal emplea la estrategia *muon+track* tanto en HLT1 como HLT2. Como puede observarse en la Fig. A.4, el efecto de las selecciones de trigger sobre la distribución de masa invariante de los muones procedentes de $B_d \to K^* \mu^+ \mu^-$ es inapreciable.

Optimizacion global de las selecciones de muones para HLT2

Las selecciones *single muon*, *dimuon* y *muon+track* de HLT2, cuyo objetivo común es la selección de desintegraciones muónicas, han de coordinarse, de modo que el ancho de banda total sea empleado de la forma más eficiente. El valor del ancho de banda asignado a cada grupo de selecciones inclusivas de trigger depende de las prioridades que la colaboración LHCb estrablezca respecto de los objetivos del experimento. De este modo, se propusieron diferentes escenarios en los que las selecciones de muones tenan asignado el 60% (*B leptónico* a 1.2 kHz), 30% (*Charm* a 0.6 kHz) y 20% (*B hadrónico* 0.4 kHz) del total respectivamente.

Cada selección simple fue estudiada por separado en un conjunto de muestras de señal (véase Tabla A.1), con el fin de determinar el rendimiento de cada una de ellas y obtener un conjunto de puntos de trabajo representativos del potencial de cada una. Posteriormente, se evaluó el rendimiento conjunto y se estableció el conjunto de selecciones elementales a emplear en cada escenario:

B leptónico: se emplean las selecciones *single muon* con IP, *dimuon* (con y sin IP) y *muon+track*.

Charm: para este escenario se usa la selección *muon+track*, con cortes más duros que en el escenario anterior y las versiones *lifetime-unbiased* de las selecciones de *dimuon*.

B hadrónico: en este caso extremo se emplean las selecciones *muon+track* y la variante

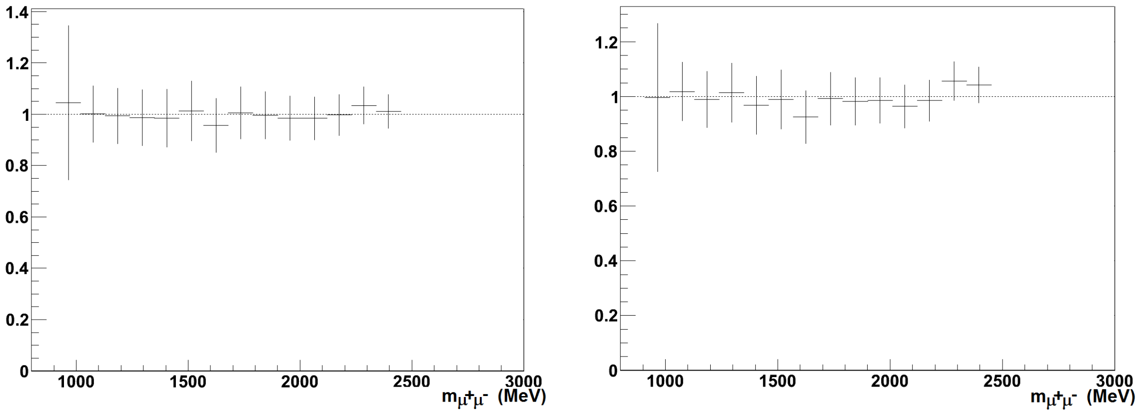

Figure A.4: Cociente de distribuciones de masa invariante, normalizadas a la unidad, para $B_d \to K^* \mu^+ \mu^-$: efecto de HLT2 *muon+track* respecto de sucesos que pasan los niveles de trigger anteriores, L0 y HLT1 (izquierda) y efecto de la cadena de trigger completa, L0, HLT1 y HLT2 *muon+track*, respecto de la muestra de partida (derecha).

lifetime-unbiased de la *dimuon* pero con cortes aún más duros.

El rendimiento conjunto de las selecciones inclusivas de muones se muestra en la Tabla A.1, que además de la eficiencia sobre señal respecto de L0 y HLT1, muestra el porcentaje de sucesos de salida del trigger que contienen un quark b. En el primer escenario encontramos altas eficiencias para todas las muestras. En los siguientes casos la eficiencia de señal, en especial de $B_d \to K^* \mu^+ \mu^-$ y $B_s \to J/\psi(\mu^+\mu^-)\phi$ decrece a consecuencia de los cortes cada vez más estrictos.

	B Leptónico	Charm	B Hadrónico
Salida	1260 ± 30 Hz	650 ± 20 Hz	420 ± 16 Hz
Pureza en B (%)	54 ± 1	49 ± 2	63 ± 2
$\epsilon(B_s \to \mu^+\mu^-)$ (%)	98	97	97
$\epsilon(B^+ \to J/\psi(\mu^+\mu^-)K^+)$ (%)	98	96	85
$\epsilon(B_s \to J/\psi(\mu^+\mu^-)\phi$ Unb.) (%)	95	95	27
$\epsilon(B_s \to J/\psi(\mu^+\mu^-)\phi$ Bias.) (%)	97	92	66
$\epsilon(B_d \to K^*\mu^+\mu^-)$ (%)	93	84	78

Table A.1: Rendimiento de la combinación de selecciones muónicas de HLT2 en cada escenario de reparto del ancho de banda total: eficiencias de señal respecto de sucesos que pasan L0 y HLT1 y fracción de contenido en B de los sucesos de salida.

Una vez se identificaron las condiciones de energía y luminosidad con las que arrancaría el funcionamiento del LHC, fue necesario evaluar de nuevo el rendimiento de las lineas de trigger de muones sobre nuevas muestras de sucesos simulados, que reflejaran dichas condiciones. Para hacer frente a las sucesivas etapas de luminosidad creciente, se propuso una estrategia de trigger basada en una sola configuración de L0 y HLT1, que proporcionara una reducción del ritmo de sucesos suficiente como para poder hacer la lectura del detector y reconstruir totalmente los sucesos. La reducción de salida final debía corresponder por tanto a las selecciones de HLT2.

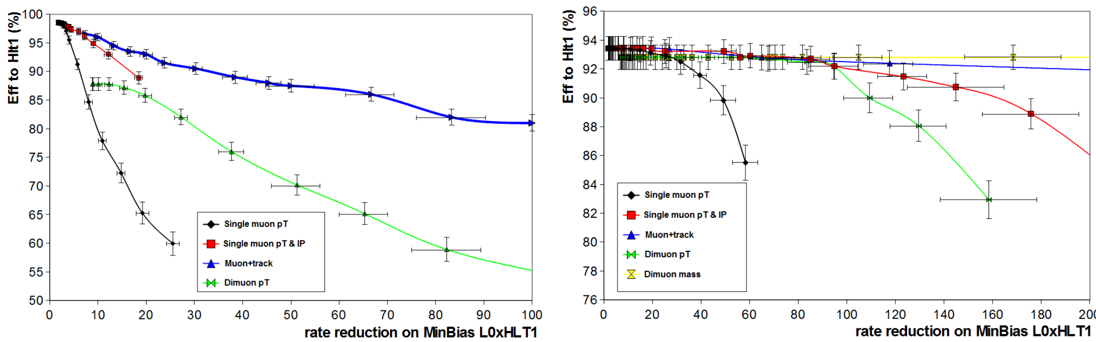

Figure A.5: Eficiencia respecto de L0 y HLT1 para diferentes selecciones de muones de HLT2 en función del factor de reducción de salida con respecto de HLT1: para $B_d \to K^* \mu\mu$ (izquierda) y $B_s \to \mu\mu$ (derecha).

Una primera inspección del rendimiento, basada en el estudio de eficiencias y retención en función de los cortes para selecciones simples, muestra que la estrategia debe evolucionar en función del factor de reducción de salida necesario. Como se puede observar en Fig. A.5, cada selección presenta un rango de utilidad, por encima del cual la eficiencia se degrada considerablemente.

La estrategia inclusiva de muones de implementó en base a conjuntos de selecciones simples, que en cada caso constituían un subconjunto del grupo anterior. El diseño de cada conjunto, en función de la reducción de salida de sucesos requerida, se puede ver en la Fig. A.6. Comenzándo con selecciones *single muon* con cortes en p_{T} e IP y *dimuon* con un corte en p_{T} mínimo, la combinación evoluciona hacia selecciones más restrictivas y con menor solapamiento entre ellas. En el escenario más extremo volvemos a encontrar las selecciones *muon+track* y *dimuon* sin cortes de IP. La Figura. A.6 nos muestra también el rendimiento de esta estrategia, en términos de eficiencia sobre señal para un conjunto de muestras de desintegraciones muónicas. De nuevo, mientras que el canal $B_s \to \mu^+\mu^-$ es eficientemente seleccionado incluso en el caso más estricto, la eficiencia sobre $B_d \to K^*\mu^+\mu^-$ disminuye debido a una mayor reducción de salida de sucesos exigida a la selección *muon+track*.

Puesta en marcha y validación de los triggers muónicos

Una vez que el LHC comenzó a funcionar produciendo las primeras colisiones a $\sqrt{s} = 7$ TeV el 30 de marzo de 2010, los datos obtenidos fueron utilizados para evaluar el funcionamiento de las líneas muónicas del HLT, desarrolladas con ayuda de simulación.

La estrategia del trigger de LHCb en la puesta en marcha del LHC

La baja luminosidad instantánea proporcionada inicialmente hizo posible que el experimento registrase todas las colisiones que presentaban una mínima actividad en los calorímetros o las cámaras de muones (*minimum bias* L0). En esta configuración, el HLT dejaba pasar todos los sucesos que superasen este L0, de modo que pudieran ser empleados tanto para estudios de producción de partículas de sabores ligeros, como para la puesta a punto del detector. En paralelo se implementó un trigger alternativo, basado en un disparo aleatorio

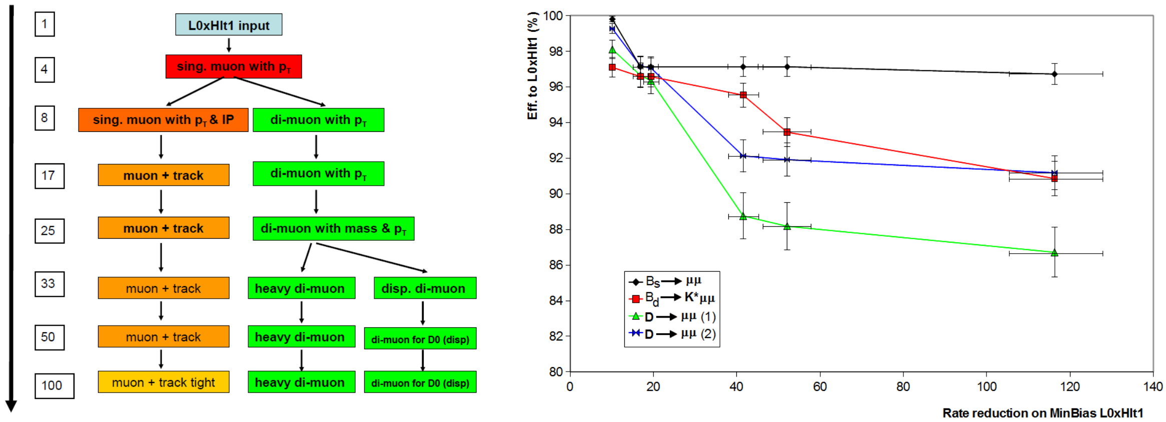

Figure A.6: Evolución de la estrategia inclusiva de muones para HLT2 en función del factor de reducción sobre la salida de L0 y HLT1 requerido (izquierda). Eficiencia de HLT2 sobre algunos canales muónicos en cada uno de estos escenarios: $B_s \to \mu^+\mu^-$, $B_d \to K^*\mu^+\mu^-$ y dos muestras distintas de $D \to \mu\mu$ (derecha).

del L0, de modo que los sucesos eran grabados a disco si los algoritmos de reconstruccion del HLT podían encontrar al menos un segmento de traza en el VELO o las cámaras de trazas (*microbias trigger*). Finalmente, las líneas de física de B del L0 y del HLT tambien eran ejecutadas, de modo que su correcto funcionamiento pudiera ser comprobado.

Validación de las lineas muónicas del HLT1

Una vez se recogió una cantidad suficiente de datos con triggers aleatorios y de minimum bias, se procedió a verificar el comportamiento de los algoritmos de reconstrucción y selección del HLT. Se pudo comprobar el correcto funcionamiento de la etapa de confirmación mediante trazas de los candidatos de muón procedentes del L0. Los resultados de retención de sucesos debida al proceso de confirmación del L0 para cada linea de muones de HLT1 se muestran en la Tabla A.2. Estos resultados, junto con las distribuciones de multiplicidad de trazas y momento transverso de los candidatos de muón, eran compatibles con lo previsto de acuerdo a la simulación.

	data (%)	MC (%)
Single muon / Muon+Track lines	81.2 ± 0.4	83.5 ± 0.4
Dimuon from L0 Dimuon lines	51.5 ± 1.2	47.6 ± 1.7
Dimuon from 2 L0 lines	81.2 ± 0.4	83.5 ± 0.4
Dimuon from L0Seg lines	42.7 ± 0.5	41.0 ± 0.6

Table A.2: Retención de sucesos en la secuencia de algoritmos que conduce a la confirmación de los candidatos de L0 para todas las líneas de muones del HLT1.

Sin embargo, se comprobó que el algoritmo de reconstrucción de vértices, en la versin simplificada tal como estaba previsto usar en el HLT1 (PV2D), no producía los resultados esperados a partir de la simulación. Esto afectaba a la medida del IP de las trazas respecto del vértice primario, lo que causaba que el poder de discriminación de esta variable se viera reducido. El algoritmo de reconstrucción simplificada fue sustituido por el empleado en HLT2 (PV3D), lo cual fue suficiente para recuperar el rendimiento deseado (Fig. A.7).

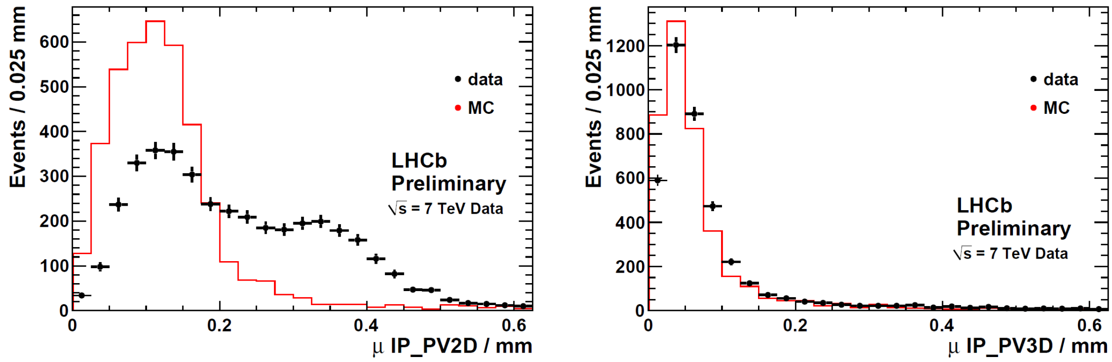

Figure A.7: Distribución del IP para trazas de muón en HLT1 respecto de los vértices reconstruidos con PV2D (izquierda) y PV3D (derecha) para datos y sucesos minimum bias de MC.

El resto de variables de selección y algoritmos de reconstrucción empleados en las líneas de muones del HLT1 fue estudiado en detalle. En ningún caso, aparte del ya mencionado IP, se encontraron discrepancias significativas respecto a la predicción a partir del MC. Los resultados de retención de sucesos para cada selección estan resumidos en la Tabla A.3, mostrando en general retenciones sobre sucesos reales ligeramente superiores a las medidas en MC, aunque en ningún caso preocupantes.

	data (%)	MC (%)
Single muon	11.3 ± 0.3	8.0 ± 0.3
Single muon No IP	17.6 ± 0.4	14.3 ± 0.4
Muon+track	3.8 ± 0.2	2.2 ± 0.2
Dimuon from L0Di	33.8 ± 1.2	29.5 ± 1.6
Dimuon from L0Di No IP	7.1 ± 0.6	4.7 ± 0.7
Dimuon from 2 L0	26.9 ± 0.4	25.1 ± 0.5
Dimuon from 2 L0 No IP	2.6 ± 0.2	1.4 ± 0.1
Dimuon from L0Seg	33.9 ± 0.4	32.1 ± 0.5
Dimuon from L0Seg No IP	9.1 ± 0.3	6.1 ± 0.3

Table A.3: Retención de sucesos por las selecciones de muones del HLT1 para datos y MC.

Evaluación de la eficiencia sobre señal y extrapolación a $B_s \to \mu^+\mu^-$

Los sucesos de desintegración $J/\psi \to \mu^+\mu^-$ proporcionaron la primera fuente abundante de muones procedentes de señal, lo cual permitió evaluar el comportamiento del HLT en términos de eficiencias. Sin embargo, la fracción mayoritaria de lasJ/ψ proceden del PV, o bien de la desintegración de estados excitados del charmonio, por lo que no cuentan con la separación respecto del PV necesaria para comprobar el correcto rendimiento de líneas de trigger diseñadas para la selecciones de mesones B. No obstante, el resultado del análisis del comportamiento del trigger sobre estas muestras sí permitió verificar la reconstrucción de las trazas de muones y la medida de su momento y masa invariante.

La muestra de sucesos seleccionados de acuerdo a la desintegración $J/\psi \to \mu^+\mu^-$ presenta la distribución de masa invariante de dimuones en Fig. A.8 (izquierda). Las regiones

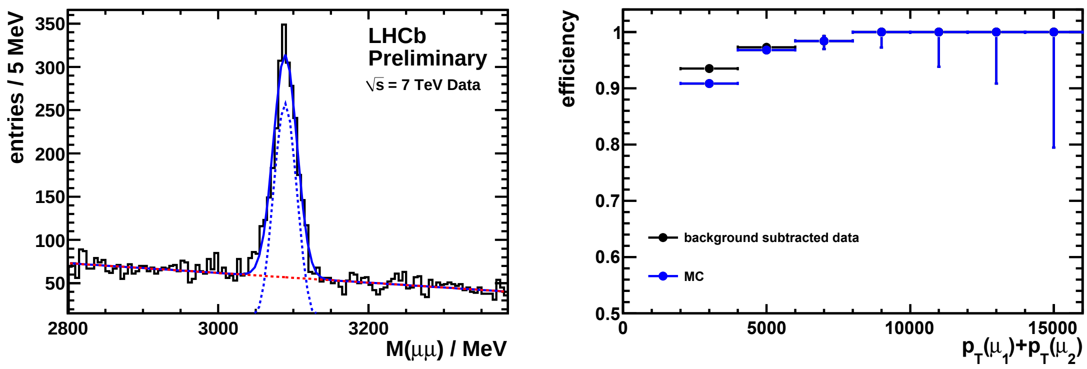

Figure A.8: Masa de dimuones en la muestra de datos seleccionados de acuerdo a la desintegración $J/\psi \to \mu^+\mu^-$ Se extrae la contribución del fondo empleando un ajuste gaussiano para el pico y un ajuste lineal para el fondo (izquierda). Eficiencia de L0×HLT1 para sucesos $J/\psi \to \mu^+\mu^-$ corregida por fondo, y comparada con la eficiencia sobre sucesos MC, para diferentes bines de la suma de p_{T} de ambos muones.

a ambos lados del pico centrado en la masa de J/ψ permiten deducir la contribución del fondo a la muestra, y eliminar su efecto sobre la medida de la eficiencia del trigger, calculada sobre los sucesos bajo el pico y en función de la suma de los p_{T} (Σp_{T}) para ambos muones (Fig. A.8, derecha). La comparación es satisfactoria, aunque hay una ligera discrepancia en el primer bin de Σp_{T}.

Esta medida de la eficiencia del trigger, obtenida a partir de procesos $J/\psi \to \mu^+\mu^-$ seleccionados de datos reales, se puede aplicar al espectro de Σp_{T} para el proceso $B_s \to \mu^+\mu^-$, obtenido a partir de simulación. Esto nos permite hacer una predicción para la eficiencia integrada sobre $B_s \to \mu^+\mu^-$, con el resultado

$$\epsilon_{trg}(B_s \to \mu^+\mu^-)_{dataJ/\psi} = 98.8 \pm 0.2(stat) \pm 1.3(syst)\%,$$

donde se ha tomado como error sistemático la diferencia entre la medida de la eficiencia integrada sobre $J/\psi \to \mu^+\mu^-$ para datos y MC.

Desarrollos posteriores en los triggers de muones

Las condiciones de luminosidad del LHC evolucionaron de forma rápida en la segunda mitad del periodo de toma de datos de 2010. La luminosidad instantánea vista por LHCb se acercó al valor nominal, aunque concentrada en una fracción de los paquetes de protones previstos. Estas condiciones se correspondían con un número medio de colisiones por cruce de hasta 2.5, cuando el valor nominal se situaba en 0.4. Además, estos sucesos debían ser filtrados por el HLT, que se ejecutaba en una granja con sólo una tercera parte de las CPUs previstas. Estas circunstancias hicieron necesarias una serie de modificaciones en los algoritmos del HLT:

- La estrategia de confirmación de candidatos del L0 mediante trazas en las líneas hadrónicas debió ser abandonada y sustituida por la reconstrucción de una única traza, a la que se exigen alto p_{T} e IP. Al ser independiente del L0, las trazas correspondientes a muones tambien son seleccionadas.

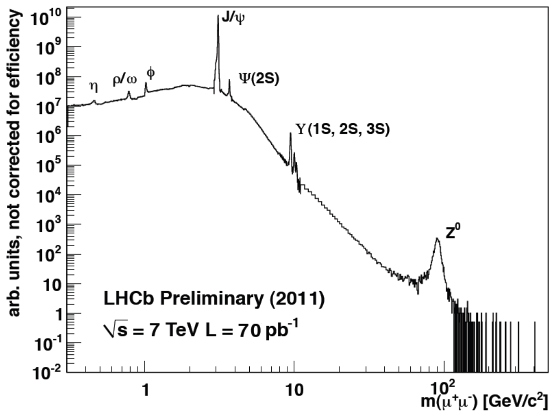

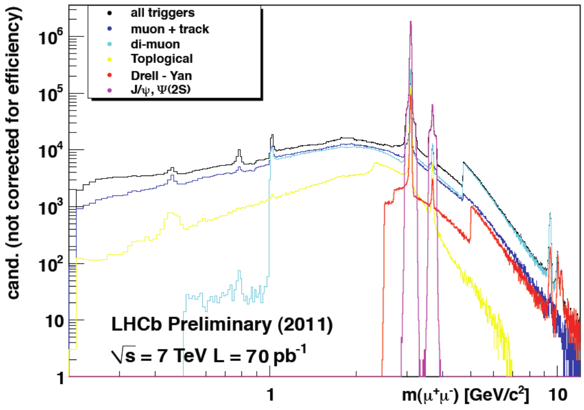

Figure A.9: Espectro de dimuones obtenido a partir de $\sim$70 pb^{-1} registrados en los primeros meses del 2011 (izquierda) y contribución de las diferentes líneas del HLT2 (derecha).

- La reconstrucción de trazas y vértices en el VELO ha sido reoptimizada, eliminando además todos los supuestos que habían conducido al fallo del algoritmo anterior sobre colisiones reales.
- Una nueva forma de reconstruir las trazas de muones en HLT1 ha sido implementada, que emplea trazas del VELO para definir regiones de interés en las cámaras de muones.
- Un nuevo conjunto de selecciones inclusivas ha sido implementado en HLT2, lo que permite la selección de procesos de desintegración con varios cuerpos, generalizando la estrategia del *muon+track*. La selección mediante cortes ha sido además sustituida por un análisis multivariable más potente.

Espectro de dimuones en LHCb

Todas las modificaciones del HLT descritas anteriormente, junto con la robustez demostrada por el detector y los algoritmos de reconstrucción y selección han permitido a LHCb tomar datos a una luminosidad superior a la anticipada. El excelente rendimiento de todos estos elementos puede ser observado en la Fig. A.9, que nos muestra el espectro de dimuones reconstruido por LHCb hasta la masa del Z^0, así como la contribución de las distintas líneas del HLT2 en la obtención de esta muestra.

Conclusiones

El experimento LHCb ha comenzado un emocionante programa de física de sabor analizando las colisiones proporcionadas por el LHC. El primer nivel de selección necesario para separar señal del fondo en que se encuentra diluida es el trigger, un conjunto de mecanismos que con un tiempo e información limitados debe decidir si registrar o no cada uno de los sucesos observados.

Dada la importancia de las desintegraciones muónicas de los mesones B para el programa de LHCb, ha sido necesario implementar algoritmos de trigger especializados en este tipo de sucesos. Estos algoritmos han sido diseñados y optimizados con éxito usando simulación

MC. El rendimiento de estos algoritmos con datos reales ha sido satisfactorio, exceptuando la reconstrución erronea de los vértices primarios, que hubo de ser modificada. Las altas eficiencias medidas en las primeras muestras de señal anticipan un excelente redimiento del trigger para procesos clave como $B_s \to \mu^+\mu^-$.

Las modificaciones introducidas en el HLT a raiz de los cambios en las condiciones de luminosidad que el experimento debió afrontar a partir de la segunda mitad de 2010 han permitido tomar datos durante 2011, con un excelente rendimiento, y con unos valores de la luminosidad instantánea mayores de los inicialmente previstos.

List of Figures

2.1 First evidence of intermediate vector bosons . . . 4
2.2 Classification of light hadrons into octets according to their electric charge and strangeness . . . 5
2.3 Generic vertex for the weak charged currents . . . 7
2.4 Unitarity condition for the CKM matrix associated to B_d system represented in the complex plane. . . . 8
2.5 Current best fit for unitarity triangle for B_d system . . . 10
2.6 Running coupling constants in the SM and MSSM . . . 12
2.7 β decay at quark level in the elementary and effective (Fermi) theories. . . 14
2.8 Feynman diagrams for FCNC transitions . . . 15
2.9 Interfering amplitudes producing CP violation . . . 16
2.10 Dominant diagrams for B_s-$\bar{B}_s$ mixing in the SM. . . . 17
2.11 Oscillation and decay of neutral B mesons . . . 19
2.12 Classification of processes inducing CP violation . . . 20
2.13 Experimental contraints to Δ_d and Δ_s mixing parameters . . . 22
2.14 Examples of diagrams contributing to $B_s \to \mu^+\mu^-$ . . . 24
2.15 Expected sensitivity for the measurement of $BR(B_s \to \mu^+\mu^-)$ at LHCb . . 25
2.16 SM diagrams for the $B_d \to K^*\mu^+\mu^-$ decay . . . 26
2.17 Angular description of the $B_d \to K^*\mu^+\mu^-$ decay . . . 27
2.18 Theoretical predictions for A_{FB} . . . 27
2.19 Expected sensitivity for the measurement of $A_{FB}(q^2)$ in $B_d \to K^*\mu^+\mu^-$ at LHCb with 1 fb^{-1} . . . 28
2.20 SM diagrams contributing to $B_s \to J/\psi\phi$ decays . . . 29
2.21 ϕ_s-$\Delta\Gamma_s$ confidence contours from CDF results . . . 30
2.22 Confidence contours in the ϕ_s-$\Delta\Gamma_s$ plane as measured by LHCb with 2010 data. The point corresponds to SM expectations. . . . 30
2.23 Mixing induced charge asymmetry in semileptonic decays as measured by D0 32
2.24 LHCb prospects for mixing induced asymmetry in semileptonic decays . . . 32

3.1 Schematic view of the LHC ring indicating its four main experiments . . . 34
3.2 LHC dipole magnet cross section . . . 34
3.3 CERN accelerator chain used as injector system to the LHC. . . . 35
3.4 Schematic view of the CMS, ATLAS and ALICE detectors. . . . 37
3.5 Main contributions to b quark production at the LHC . . . 38
3.6 Angular distribution of $b\bar{b}$ quark pair production . . . 38

3.7 Number of proton-proton interactions per bunch crossing as a function of instantaneous LHC luminosity 40
3.8 Schematic side view of the LHCb detector indicating its subsystems 41
3.9 Main component of the LHCb magnetic field as a function of the z coordinate 42
3.10 Cross section of the VELO silicon sensors in the xz plane 43
3.11 Velo modules in operating and beam injection positions 44
3.12 Velo module sketch showing the $r\phi$ geometry 45
3.13 View of TT vertical and stereo layers 45
3.14 View of IT vertical (x) and second stereo (u) layers. 46
3.15 Front view of the OT stations and cross section for one of the its modules . 46
3.16 Tracking and momentum measurement principle 47
3.17 Types of tracks in the LHCb track reconstruction 48
3.18 Radiation interaction with detector layers 50
3.19 Cherenkov light shockwave cone. 51
3.20 Cherenkov angle versus momentum for different particles and radiators . . 51
3.21 Schematic view of the RICH detectors 52
3.22 LHCb ECAL and HCAL calorimeters 54
3.23 Segmentation for the Electromagnetic and Hadronic LHCb calorimeters . . 54
3.24 Side view of the LHCb muon stations layout 56
3.25 Schematic front view of one quadrant of a muon station 56
3.26 LHCb simulation and data processing applications 58

4.1 Cross sections and event rates as a function of collision energy for hard hadron scattering 60
4.2 Measured total, elastic and inelastic cross sections for hard hadron scattering 61
4.3 LHCb trigger levels. 62
4.4 LHCb trigger and DAQ systems 63
4.5 LHCb trigger strategy compared to other experiments 64
4.6 LHCb sub-detectors used in the Level 0 trigger 65
4.7 Level 0 calorimeter architecture 66
4.8 Level 0 muon candidate reconstruction and momentum estimate 66
4.9 Level 0 muon architecture 67
4.10 View of a section of the LHCb Event Filter Farm, where the software trigger is executed. 68
4.11 L0 muon candidate confirmation with T-tracks 70
4.12 Momentum resolution of L0 muon candidates after confirmation with tracks 70
4.13 Impact parameter of muon tracks, for the example of a $B_s \to \mu^+\mu^-$ event. 71
4.14 Event selected by the single muon trigger independently of the signal particle (B), as the triggering muon is a product of the semileptonic decay of the companion $\bar{B}$. 74
4.15 Trigger decision classification according to its relation to signal 74

5.1 $B_s \to D_s^- \mu^+ \nu_\mu$ muon+track efficiency vs. rate for combinations of muon and companion track p_T cuts 80
5.2 $B_s \to D_s^- \mu^+ \nu_\mu$ muon+track efficiency vs. rate for different combinations of DZ and DOCA cuts 80

5.3 $B_s \to D_s^- \mu^+ \nu_\mu$ muon+track efficiency vs. rate for combinations of muon and track minimum IP . . . 81
5.4 $B_s \to D_s^- \mu^+ \nu_\mu$ muo+track efficiency vs. rate for combinations of cuts on muon+track vertex pointing variable and invariant mass . . . 82
5.5 $B_s \to D_s^- \mu^+ \nu_\mu$ best muon+track efficiency vs. rate for different choices of discriminating variables . . . 83
5.6 HLT2 efficiency to reconstruct two muon tracks TOS as a function of the invariant mass of the MC muon pair for offline selected $B_d \to K^* \mu^+ \mu^-$ events 86
5.7 HLT2 efficiency to reconstruct a muon and companion tracks TOS as a function of the invariant mass of the MC muon pair, for offline selected $B_d \to K^* \mu^+ \mu^-$ events . . . 87
5.8 $B_d \to K^* \mu^+ \mu^-$ muon+track efficiency vs. rate for muon p_{T} and IP cuts . . 88
5.9 $B_d \to K^* \mu^+ \mu^-$ muon+track best efficiency vs. rate for the combinations of muon p_{T} and IP cuts . . . 89
5.10 $B_d \to K^* \mu^+ \mu^-$ muon+track efficiency vs. rate for different DOCA cuts . . 89
5.11 $B_d \to K^* \mu^+ \mu^-$ best efficiency vs. rate for muon+track vertex DOCA and DZ combinations of cuts . . . 90
5.12 $B_d \to K^* \mu^+ \mu^-$ muon+track efficiency vs. rate for different cuts on the pointing variable . . . 90
5.13 $B_d \to K^* \mu^+ \mu^-$ muon+track efficiency vs. rate for cuts on invariant mass . 91
5.14 $B_d \to K^* \mu\mu$ best TOS efficiency vs. rate for LHT2 muon+track selection, calculated from combinations of cuts on p_{T} and IP for both muon and companion tracks and on the combination pointing. . . . 92
5.15 Invariant mass distributions for MC muons from the $B_d \to K^* \mu^+ \mu^-$ decay after each trigger stage . . . 93
5.16 Trigger acceptances on $B_d \to K^* \mu^+ \mu^-$ invariant mass distribution 93
5.17 B purity of minimum bias events passing HLT2 single muon selection for combinations of muon p_{T} and IP cuts . . . 96
5.18 Best efficiency for individual muon selections as a function of minimum bias reduction factor with respect to HLT1 rate for several muonic benchmark channels . . . 101
5.19 Evolution of the HLT2 inclusive muon trigger strategy in terms of selections as a function of the required rate reduction factor on minimum bias passing L0 and HLT1 . . . 105
5.20 Evolution of the HLT2 inclusive muon trigger efficiency as a function of the rate reduction factor for the samples provided by the Rare Decays working group . . . 107
5.21 Evolution of the HLT2 inclusive muon trigger efficiency as a function of the rate reduction factor for the samples provided by the CP violation working group . . . 107
5.22 Evolution of the HLT2 inclusive muon trigger efficiency as a function of the rate reduction factor for the samples provided by the Flavour Physics working group . . . 108

6.1 First 15 nb^{-1} recorded in 2010 as a function of fill number 111
6.2 Dimuon invariant mass distribution for $J/\psi \to \mu^+ \mu^-$ event sample used for L0 muon commissioning . . . 112

6.3 L0 muon efficiency comparison for $J/\psi \to \mu^+\mu^-$ events from data and MC samples . . . 112
6.4 Comparison between data and MC of the L0-muon confirmation with T stations . . . 114
6.5 Comparison of muon tracks IP with respect to PV2D and PV3D . . . 115
6.6 Comparison between data and MC of VELO reconstruction and matching between VELO segments and T stations . . . 116
6.7 Highest p_{T} amongst the muon tracks in each event and retention vs. p_{T} cut for data and MC . . . 117
6.8 Highest IP measured to PV3D amongst the muon fitted tracks and retention vs. IP cut for data and MC . . . 118
6.9 Quality of fitted muon tracks . . . 118
6.10 Number of input L0 candidates for the HLT1 dimuon lines . . . 119
6.11 Confirmation of L0 candidates with T+3D VELO tracks in the HLT1 dimuon lines . . . 119
6.12 DOCA between confirmed muon track pairs in the HLT1 dimuon lines . . . 120
6.13 Invariant mass for pairs of unfitted muon tracks in the HLT1 dimuon lines 121
6.14 Invariant mass for pairs of fitted muon tracks in the HLT1 dimuon lines . . 122
6.15 HLT1 muon+track VELO filtering . . . 123
6.16 Forward reconstruction of the companion track in the HLT1 muon+track alley . . . 124
6.17 Kinematic filtering after forward reconstruction of companion tracks in the HLT1 muon+track alley . . . 125
6.18 Quality of the track fit for companion tracks in the HLT1 muon+track alley 126
6.19 Highest IP with respect to PV3D amongst the companion fitted tracks in the HLT1 muon+track alley . . . 126
6.20 HLT1 muon efficiency with respect to L0 muon as a function of the sum of the p_{T} for both muons from $J/\psi \to \mu^+\mu^-$ sample comparing data and MC. 128
6.21 HLT2 muon efficiency with respect to HLT1 muon as a function of the sum of the p_{T} for both muons from $J/\psi \to \mu^+\mu^-$ sample comparing data and MC.129
6.22 L0+HLT1+HLT2 muon triggers efficiency with respect to all selected events as a function of the sum of the p_{T} for both muons from $J/\psi \to \mu^+\mu^-$ sample comparing data and MC. . . . 130
6.23 Invariant mass of $J/\psi \to \mu^+\mu^-$ in data and MC . . . 131
6.24 L0 $\times$ HLT1 efficiency for data $J/\psi \to \mu^+\mu^-$ events after correction for background compared to MC . . . 131
6.25 L0 $\times$ HLT1 efficiency for data $J/\psi \to \mu^+\mu^-$ events measured with the TIS and micro bias methods . . . 132
6.26 Trigger efficiency evaluation for $B_s \to \mu^+\mu^-$ from the extrapolation of the measured efficiency on selected $J/\psi \to \mu^+\mu^-$ . . . 133
6.27 Evolution of the average number of visible interactions per bunch crossing at LHCb in the second half of the 2010 run . . . 134
6.28 Dimuon spectrum for 2010 data and contributions from the different HLT2 lines . . . 138
6.29 Dimuon spectrum for initial 2011 data and contributions from the different HLT2 lines . . . 139

6.30 $B_s \to \mu^+\mu^-$ event candidate 140

A.1 Esquema del LHC y del experimento LHCb 146
A.2 Niveles de trigger de LHCb 147
A.3 Optimización de muon+track en HLT1 149
A.4 Optimización de muon+track en HLT2 150
A.5 Rendimiento de selecciones muónicas en HLT2 151
A.6 Evolución de la estrategia inclusiva de muones para HLT2 para el arranque del LHC 152
A.7 Distribución del IP para trazas de muón en HLT1 para PV2D y PV3D . . 153
A.8 Medida de la eficiencia de trigger sobre sucesos $J/\psi \to \mu^+\mu^-$ 154
A.9 Espectro de dimuones en LHCb con los datos iniciales del 2011 155

List of Tables

2.1 Fermion families in the Standard Model 4
2.2 Boson content of the Standard Model 4

4.1 Comparison of LHCb, ATLAS and CMS running parameters and trigger requirements 64

5.1 Selection criteria for the semileptonic decays used to optimize HLT1 muon+track 78
5.2 L0 and muon confirmation efficiencies for semileptonic decays 79
5.3 Semileptonic decay retention for HLT1 muon+track cuts 84
5.4 Signal and minimum bias retention per HLT1 muon+track algorithm . . . 84
5.5 Timing results for muon+track algorithms 85
5.6 L0 and HLT1 muon alleys efficiencies for $B_d \to K^* \mu^+ \mu^-$ 87
5.7 L0 and HLT1 efficiencies for HLT2 benchmark signal channels MC06 . . . 95
5.8 Proposal for HLT2 bandwidth division scenarios 95
5.9 HLT2 muon+track selection in the three bandwidth division scenarios . . . 97
5.10 Performance of HLT2 muon+track on MC06 samples 97
5.11 Performance of HLT2 lifetime-biased dimuon on MC06 samples 97
5.12 Performance of HLT2 lifetime-biased dimuon on MC06 samples 98
5.13 Performance of the HLT2 inclusive muon selections on MC06 samples . . . 99
5.14 Reduction factors from global HLT2 rate reduction and bandwidth division scenarios 102
5.15 Inclusive HLT2 single muon for LHC start-up 102
5.16 Inclusive HLT2 muon+track for LHC start-up 102
5.17 Inclusive HLT2 dimuon for LHC start-up 103
5.18 Performance of HLT2 muon selections on minimum bias MC09 104
5.19 Performance of combined HLT2 muon selections on minimum bias MC09 . 106

6.1 L0 settings under TCK 0x1309 110
6.2 L0 settings under TCK 0x1810 - Minimum bias triggers 111
6.3 L0 settings under TCK 0x1810 - L0 trigger for the LHCb core physics program 113
6.4 Event retention and number of candidates in the HLT1 single muon confirmation sequence 116
6.5 Event retention of muon confirmation sequences for data and MC classified according to the L0 seed types 117
6.6 Retention of HLT1 muon lines for data and MC 124
6.7 Selection criteria for $J/\psi \to \mu^+ \mu^-$ sample used in the initial estimation of trigger performance on signal 127

6.8 Summary of L0 muon confirmation performance on data and MC $J/\psi \rightarrow \mu^+\mu^-$ samples 128
6.9 Selection criteria for the $J/\psi \rightarrow \mu^+\mu^-$ sample used for the evaluation of trigger efficiencies and its extrapolation to $B_s \rightarrow \mu^+\mu^-$ 130
6.10 Signal and background fractions in the $J/\psi \rightarrow \mu^+\mu^-$ sample in bins of Σp_T 131

A.1 Rendimiento de la combinación de selecciones muónicas de HLT2 150
A.2 Retención de sucesos en la secuencia de algoritmos que conduce a la confirmación de los candidatos de L0 para todas las líneas de muones del HLT1. 152
A.3 Retención de sucesos por las selecciones de muones del HLT1 para datos y MC 153

Bibliography

[1] S.L. Glashow. *Partial-symmetries of weak interactions*. Nucl. Phys. 22 , pp. 579-587 (1961).

[2] A. Salam and J. C. Ward. *Electromagnetic and weak interactions*. Phys. Lett. 13, pp. 168-171 (1964).

[3] S. Weinberg. *A Model of Leptons*. Phys. Rev. Lett. 19, pp. 1264-1266 (1967).

[4] P. W. Higgs. *Broken Symmetries and the Masses of Gauge Bosons*. Phys. Rev. Lett. 13, pp. 508-509 (1964).

[5] F. Englert and R. Brout. *Broken Symmetry and the Mass of Gauge Vector Mesons*. Phys. Rev. Lett 13, pp. 321-323 (1964).

[6] Y. Ne'eman. *Derivation of strong interactions from a gauge invariance*. Nucl. Phys. 26, pp. 222-229 (1961).

[7] G. Zweig. *An SU(3) model for strong interaction symmetry and its breaking, I and II*, 1964. Developments in the Quark Theory of Hadrons, vol. 1, pp 22-101, Hadronic Press (1980).

[8] K. Nakamura et al. (Particle Data Group). *The Review of Particle Physics*. J. Phys. G 37, 075021 (2010).

[9] Ch. Berger et al. (the PLUTO Collaboration). *Evidence for gluon bremsstrahlung in e+e- annihilations at high energies*. Phys. Lett. 86 B pp.418-425 (1979).

[10] G. Arnison et al. (the UA1 Collaboration). *Experimental Observation of Lepton Pairs of Invariant Mass Around 95 GeV at the CERN SPS Collider*. Phys. Lett. B 126, 5. pp. 398-410 (1983). Image of first Z event recorded: CERN document service CERN-EX-8704168.

[11] H. Fritzsch, M. Gell-Mann and H. Leutwyler. *Advantages of the Colour Octet Gluon Picture*. Phys. Lett. B47, 365 (1973).

[12] D. J. Gross and F. Wilczek. *Ultraviolet Behavior of Non-Abelian Gauge Theories*. Phys. Rev. Lett. 30, 1343 (1973).

[13] H. D. Politzer. *Reliable Perturbative Results for Strong Interactions?*. Phys. Rev. Lett. 30, 1346 (1973).

[14] M. Gell-Mann. *A Schematic Model of Baryons and Mesons*. Phys. Lett. 8, pp. 214-215 (1964).

[15] M. Gell-Mann. *Quarks: Developments in the Quark Theory of Hadrons.* Acta Phys. Austriaca Suppl. 9, 733 (1972).

[16] S.L. Glashow, J. Iliopoulos and L. Maiani. *Weak Interactions with Lepton-Hadron Symmetry.* Phys. Rev. D 2, pp. 1285-1292 (1970).

[17] M. Kobayashi and T. Maskawa. *CP-Violation in the Renormalizable Theory of Weak Interaction.* Prog. Th. Phys. 2, pp. 652-657 (1973).

[18] K. Nakamura et al. (Particle Data Group). *The Review of Particle Physics: The CKM quark mixing matrix.* J. Phys. G 37, 075021 (2010).

[19] N. Cabibbo. *Unitary Symmetry and Leptonic Decays.* Phys. Rev. Lett. 10 pp. 531-533 (1963).

[20] L. Wolfenstein. *Parametrization of the Kobayashi-Maskawa Matrix.* Phys. Rev. Lett. 51, 1945 (1983).

[21] A. Pich. *The Standard Model of Electroweak Interactions.* arXiv:0705.4264v1 [hep-ph] (2007).

[22] C. Jarlskog. *Commutator of the Quark Mass Matrices in the Standard Electroweak Model and a Measure of Maximal CP Nonconservation.* Phys. Rev. Lett. 55, pp. 1039-1042 (1985).

[23] K. Nakamura et al. (Particle Data Group). *The Review of Particle Physics: CP Violation in Meson Decays.* J. Phys. G 37, 075021 (2010).

[24] J. Charles et al. (CKMfitter Group) *CP violation and the CKM matrix: assessing the impact of the asymmetric B factories.* Eur. Phys. J. C41, 1-131, arXiv:0406184v3 [hep-ph] (2005). Updated results at `http://ckmfitter.in2p3.fr`.

[25] T. D. Lee and C. N. Yang. *Question of Parity Conservation in Weak Interactions.* Phys. Rev. 104, pp. 254258 (1956).

[26] C. S. Wu et al. *Experimental Test of Parity Conservation in Beta Decay.* Phys. Rev. 105, pp. 14131415 (1957).

[27] J. H. Christenson, J. W. Cronin, V. L. Fitch and R. Turlay. *Evidence for the 2π Decay of the K_2^0 Meson.* Phys. Rev. Lett. 13, pp. 138140 (1964).

[28] B. Aubert et al. (the BaBar Collaboration). *Observation of CP Violation in the B^0 Meson System.* Phys. Rev. Lett. 87, 091801 (2001).

[29] K. Abe et al. (the Belle Collaboration). *Observation of Large CP Violation in the Neutral B Meson System.* Phys. Rev. Lett. 87, 091802 (2001).

[30] Y. Chao et al. (the Belle Collaboration). *Evidence for Direct CP Violation in $B^0 \to K^+\pi^-$ Decays.* Phys. Rev. Lett. 93, 191802 (2004).

[31] B. Aubert et al. (the BaBar Collaboration). *Observation of CP Violation in $B^0 \to K^+\pi^-$ and $B^0 \to \pi^+\pi^-$.* Phys. Rev. Lett. 99, 021603 (2007).

[32] M. Morello, for the CDF Collaboration. *CP and charge asymmetries at CDF*. J. Phys. Conf. Ser. 110:052040, arXiv:0711.0693v1 [hep-ex] (2007).

[33] G. W. S. Hou. *Search for TeV Scale Physics in Heavy Flavour Decays*. arXiv:0710.5424v2 [hep-ex] (2007).

[34] T. Nakada. *Flavour Physics Experiments: LHCb and flavour physics at the LHC*. Lectures at the Taller de Altas Energias 2010, Universitat de Barcelona. Slides at `http://benasque.org/2010tae/talks_contr/083_nakada_lecture.pdf`.

[35] K. Nakamura et al. (Particle Data Group). *The Review of Particle Physics: Production and Decay of b-Flavored Hadrons*. J. Phys. G 37, 075021 (2010).

[36] R. Lambert. *LHCb Hybrid Photon Detectors and Sensitivity to Flavour Specific Asymmetry in Neutral B-Meson Mixing* Thesis University of Edimburgh, CERN-THESIS-2009-001 (2009).

[37] A. Lenz and U. Nierste. *Theoretical update of $B_s - \bar{B}_s$ mixing*. arXiv:0612167v3 [hep-ph] (2007).

[38] K. Nakamura et al. (Particle Data Group). *The Review of Particle Physics: Higgs Boson, Theory and Searches*. J. Phys. G 37, 075021 (2010).

[39] D. I. Kazakov. *Beyond the Standard Model (In Search of SuperSymmetry)*. arXiv:0012288v2 [hep-ph] (2001).

[40] K. Nakamura et al. (Particle Data Group). *The Review of Particle Physics: Grand Unified Theories*. J. Phys. G 37, 075021 (2010).

[41] G. Bertone, D. Hooper and J. Silk. *Particle Dark Matter: Evidence, Candidates and Constraints*. arXiv:0404175v2 [hep-ph] (2004).

[42] P. J. Peebles and B. Ratra. *The Cosmological Constant and Dark Energy*. arXiv:0207347v2 [astro-ph] (2002).

[43] A.D. Sakharov. *Violation of CP invariance, C asymmetry and Baryon asymmetry of the Universe*. Pisma Zh. Eksp. Teor. Fiz. 5, p. 32-35 (1967).

[44] P. Huet and E. Sather. *Electroweak baryogenesis and standard model CP violation*. Physical Review D 51, p. 379 (1995).

[45] A. Riotto. *Theories of Baryogenesis*. arXiv:9807454v2 [hep-ph] (1998).

[46] M. Maltoni et al. *Status of global fits to neutrino oscillations*. arXiv:0405172v6 [hep-ph] (2007).

[47] M. Fukugita and T. Yanagida. *Baryogenesis without Grand Unification*. Phys. Lett. B 174, 45 (1986).

[48] T. Ibrahim and P. Nath. *CP Violation From Standard Model to Strings*. arXiv:0705.2008v2 [hep-ph] (2008).

[49] G. D. Rochester and C. C. Butler. *The Penetrating Particles in Cosmic-ray Showers: II. The Lightly-ionizing Penetrating Particles in Penetrating Showers*. Proc. Phys. Soc. 61 535 (1948).

[50] M. Gell-Mann. *Isotopic Spin and New Unstable Particles*. Phys. Rev. 92 833 (1953).

[51] J. E. Augustin et al. *Discovery of a Narrow Resonance in e^+e^- Annihilation*. Phys. Rev. Lett. 33, 14061408 (1974).

[52] J. J. Aubert et al. *Experimental Observation of a Heavy Particle J*. Phys. Rev. Lett. 33, 14041406 (1974).

[53] F. J. Hasert et al. *Observation of neutrino-like interactions without muon or electron in the Gargamelle neutrino experiment*. Nucl. Phys B 73, 1-22 (1974).

[54] S. W. Herb et al. *Observation of a Dimuon Resonance at 9.5 GeV in 400-GeV Proton-Nucleus Collisions*. Phys. Rev. Lett. 39, 252255 (1977).

[55] F. Abe et al (the CDF Collaboration).*Observation of Top Quark Production in $\bar{p}p$ Collisions with the Collider Detector at Fermilab*. Phys. Rev. Lett. 74, 26262631 (1995).

[56] H. Albrecht et al (the ARGUS Collaboration). *Observation of $B^0 - \bar{B}^0$ Mixing*. Phys. Lett. B 192, 245-252 (1987).

[57] A. Buras. *Operator Product Expansion, Renormalization Group and Weak Decays*. Lect. Notes Phys. 558, pp. 65-85, arXiv:9901409 [hep-ph] (2000).

[58] E. Fermi. *An attempt of a theory of beta radiation*. Nuovo Cimento 11, 119 (1934).

[59] B. Adeva et al (the LHCb Collaboration). *Roadmap for selected key measurements of LHCb*. arXiv:0912.4179v2 [hep-ex] (2009).

[60] M. Artuso et al. Report of working group 2 of the CERN Workshop *Flavour in the era of the LHC: B, D and K decays*. arXiv:0801.1833v1 [hep-ph] (2008).

[61] A. Buras et al. *Higgs-mediated FCNCs: Natural Flavour Conservation vs. Minimal Flavour Violation*. arXiv:1005.5310v3 [hep-ph] (2010).

[62] The CDF Collaboration. *Search for $B^0_s \to \mu^+\mu^-$ and $B^0_d \to \mu^+\mu^-$ decays in $3.7fb^{-1}$ of $p\bar{p}$ Collisions with CDF II*. CDF Public Note 9892 (2009).

[63] R. Fleischer, N. Serra, N. Tuning. *New Strategy for B_s Branching Ratio Measurements and the Search for New Physics in $B^0_s \to \mu^+\mu^-$*. Phys. Rev. D 82, 034038, arXiv:1004.3982v3 (2010).

[64] R. Aaij et al (the LHCb Collaboration). *Search for the rare decays $B^0_s \to \mu^+\mu^-$ and $B^0_d \to \mu^+\mu^-$*. CERN-PH-EP-2011-029, arXiv:1103.2465v2 [hep-ex] (2011).

[65] U. Egede et al. *New observables in the decay mode $\bar{B}_d \to \bar{K}^0 l^+ l^-$*. JHEP 11 (2008) 032, arXiv:0807.2589v3 [hep-ph] (2009).

[66] W. Reece. *Exploiting angular correlations in the rare decay $B_d \to K^0\mu^+\mu^-$ at LHCb*. Thesis Imperial College London, CERN-THESIS-2010-095 (2010).

[67] M. Beneke et al. *Systematic approach to exclusive $B \to Vl^+l^-$, $V\gamma$ decays*. Nucl. Phys. B 612, 25-58, arXiv:0106067v2 [hep-ph] (2001).

[68] M. Beneke et al. *Exclusive radiative and electroweak $b \to d$ and $b \to s$ penguin decays at NLO*. Eur. Phys. J. C 41 (2005) 173-188, arXiv:0412400v1 [hep-ph] (2004).

[69] H. Skottowe. *Studies of RICH detectors and the $B_d \to K^* \mu^+ \mu^-$ decay at the LHCb experiment*. Thesis University of Cambridge, CERN-THESIS-2010-102 (2010).

[70] The CDF Collaboration. *An Updated Measurement of the CP Violating Phase $\beta_s^{J/\psi\phi}$ in $B_s^0 \to J/\psi\phi$ Decays using $5.2 fb^{-1}$ of Integrated Luminosity.* CDF/ANAL/BOTTOM/PUBLIC/10206 (2010).

[71] The LHCb Collaboration. *Tagged time-dependent angular analysis of $B_s^0 \to J/\psi\phi$ decays with the 2010 LHCb data* LHCb-Conf-2011-006 (2011).

[72] V. M. Abazov et al (The D0 Collaboration). *Evidence for an anomalous like-sign dimuon charge asymmetry.* Fermilab-Pub-10/114-E, arXiv:1005.2757v1 [hep-ex] (2010).

[73] R. Fleischer. *Highlights of the B-Physics Landscape*. J. Phys. G 32, 71-125 (2006). arXiv:0512253v1 [hep-ph], CERN-PH-TH/2005-263 (2005).

[74] R. Aaij et al (the LHCb Collaboration). *Measurement of $\sigma(pp- > b\bar{b}X)$ at $\sqrt{s} = 7TeV$ in the forward region*. Phys. Lett. B 694 209. arXiv:1009.2731v2 [hep-ex] (2010).

[75] R. W. Lambert. *Heavy Flavour in a Nutshell*. arXiv:1105.1061v2 [hep-ex] (2011).

[76] L. Evans and P. Bryant (editors). *The LHC Machine*. JINST 3 S08001 (2008).

[77] *CERN releases analysis of LHC incident*. CERN press release (16 October 2008), `http://public.web.cern.ch/press/pressreleases/Releases2008/PR14.08E.html`.

[78] G. Aad et al (the ATLAS Collaboration). *The ATLAS Experiment at the CERN Large Hadron Collider*. JINST 3 S08003 (2008).

[79] P.A. Aarnio et al (the CMS Collaboration). *The CMS experiment at the CERN LHC*. JINST 3 S08004 (2008).

[80] K. Aamodt et al (the ALICE Collaboration). *The ALICE experiment at the CERN LHC*. JINST 3 S08002 (2008).

[81] G. Anelli et al (the TETOM Collaboration). *The TOTEM Experiment at the CERN Large Hadron Collider*. JINST 3 S08007 (2008).

[82] O. Adriani et al (the LHCf Collaboration). *The LHCf detector at the CERN Large Hadron Collider*. JINST 3 S08006 (2008).

[83] S. Cecchini et al (the MoEDAL Collaboration). *Technical Design Report of the MoEDAL Experiment*. CERN-LHC-2009-006 (2009).

[84] B. Adeva et al (the LHCb Collaboration). *The LHCb Detector at the LHC*. JINST 3 S08005 (2008).

[85] B. Adeva et al (the LHCb Collaboration). *A dedicated LHC Collider Beauty Experiment for Precise Measurements of CP Violation*. LHCb Letter of Intent, CERN-LHCC-95-5 (1995).

[86] R. Aaij et al (the LHCb Collaboration). *Measurement of b-hadron production fractions in 7 TeV centre-of-mass energy pp collisions*. LHCb-PAPER-2011-018 (2011).

[87] J. Nardulli. *Reconstruction of two-body B decays in LHCb*. Thesis Vrije Universiteit Amsterdam, CERN-THESIS-2007-063 (2007).

[88] B. Adeva et al (the LHCb Collaboration). *LHCb Magnet Technical Design Report*. CERN-LHCC-2000-007 (2000).

[89] B. Adeva et al (the LHCb Collaboration). *LHCb Vertex Locator Technical Design Report*. CERN-LHCC-2001-011 (2001).

[90] D. Petrie, C. Parkes and S. Viret. *Study of the impact of VELO misalignments on the LHCb tracking and L1 trigger performance*. LHCb-2005-56 (2005).

[91] B. Adeva et al (the LHCb Collaboration). *LHCb Inner Tracker Technical Design Report*. CERN-LHCC-2002-029 (2002).

[92] B. Adeva et al (the LHCb Collaboration). *LHCb Outer Tracker Technical Design Report*. CERN-LHCC-2001-024 (2001).

[93] J. Albrecht. *Fast Track Reconstruction for the High Level Trigger of the LHCb Experiment*. Thesis University of Heidelberg, CERN-THESIS-2009-120 (2009).

[94] R. Frhwirth. *Application of Kalman filtering to track and vertex fitting*. Nucl. Instrum. Meth. A 262 p. 444-450 (1987).

[95] R. v. d. Eijk, R. Hierck, M. Merk and M. Needham. *Performance of the LHCb OO Track Fitting Software*. LHCb-2000-086 (2000).

[96] G. Conti. *LHCb detector momentum calibration with the first year data and a performance study of CP violation measurement with the $B_s^0 \to J/\psi\phi$ decays*. Thesis École Polytechnique Fédérale de Lausanne, CERN-THESIS-2010-128.

[97] B. Adeva et al (the LHCb Collaboration). *LHCb RICH Technical Design Report*. CERN-LHCC-2000-037 (2000).

[98] P. Cherenkov. *Visible emission of clean liquids by action of γ radiation*. Proceedings of the USSR Academy of Sciences, 2 p. 451 (1934).

[99] B. Adeva et al (the LHCb Collaboration). *LHCb Calorimeters Technical Design Report*. CERN-LHCC-2000-036 (2000).

[100] B. Adeva et al (the LHCb Collaboration). *LHCb Muon system Technical Design Report*. CERN-LHCC-2001-010 (2001).

[101] N. Metropolis and S. Ulam. *The Monte Carlo Method*. Journal of the American Statistical Association 44 (247), p. 335-341 (1949).

[102] T. Sjöstrand et al. *PYTHIA*. `http://home.thep.lu.se/~torbjorn/Pythia.html`.

[103] A. Ryd et al. *EvtGen, a Monte Carlo Generator for B Physcis*. BAD 522 V6 (2004). `http://www.slac.stanford.edu/~lange/EvtGen/`.

[104] J. Allison et al (the GEANT4 Collaboration). *GEANT4*. `http://geant4.cern.ch/`.

[105] B. Adeva et al (the LHCb Collaboration). *LHCb Computing Technical Design Report*. CERN-LHCC-2005-019 (2005).

[106] G. Barrand et al. *GAUDI - A software architecture and framework for building LHCb data processing applications*. Proc. of CHEP 2000 (2001).

[107] G. Altarelli and M. Mangano (editors). *Proceedings of the Workshop on Standard Model Physics (and more) at the LHC: QCD*. CERN 2000-004 (2000).

[108] G. Antchev et al (the TOTEM Collaboration). *First measurement of the total proton-proton cross section at the LHC energy of* $\sqrt{s} = 7$ *TeV*. CERN-PH-EP-2011-158, TOTEM-2011-02 (2011).

[109] B. Adeva et al (the LHCb Collaboration). *LHCb Trigger System Technical Design Report*. CERN-LHCC-2003-031 (2003).

[110] B. Adeva et al (the LHCb Collaboration). *LHCb Online system, Data Acquisition and Experiment Control Technical Design Report*. CERN-LHCC-2001-40 (2001).

[111] J. A. Hernando, D. Martinez, X. Cid, G. Guerrer, A. Gomes and J. Albrecht. *The Hadron Alley of the LHCb High Level Trigger*. LHCb-2009-034 (2010).

[112] K. Senderowska, M. Witek and A. Zuranski. *HLT1 Electromagnetic Alley*. LHCb-PUB-2009-001 (2010).

[113] S. Amato, A. Satta, B. Souza de Paula and L. de Paula. *HLT1 Muon Alley description*. LHCb-2008-058 (2008).

[114] A. Perez-Calero and H. Ruiz. *The muon+track alley of the LHCb High Level Trigger*. LHCb-2008-075 (2009).

[115] V. Gligorov. *A single track HLT1 trigger*. LHCb-PUB-2011-003 (2011).

[116] J. Albrecht, M. Needham and H. Terrier. *L0 confirmation with fast, Tsa based tracking in the T-stations*. LHCb-2007-118 (2007).

[117] J. Albrecht. *L0 Muon Confirmation settings for 2010*. `https://indico.cern.ch/getFile.py/access?contribId=3&resId=0&materialId=slides&confId=82194` (2010).

[118] B. Souza de Paula. *Studies on Systematic effects of the Trigger on Flavour Tagging on the Generator Level*. LHCb-2006-046 (2006).

[119] M. Calvi, O. Leroy and M. Musy. *Flavour Tagging Algorithms and Performances in LHCb*. LHCb-2007-058 (2007).

[120] M. Calvi. *M. Selection of* $B_d \to D^* \mu\nu$ *events and flavour tagging in LHCb*. LHCB 2007-036 (2007).

[121] O. Leroy, F. Muheim, S. Poss and Y. Xie. *Selection of $B_s \to D_s\mu\nu$ events in LHCb.* LHCB 2007-029 (2007).

[122] M. Calvi. *DC06 selection for $B_d \to D^*\mu\nu$, Rate on Minimum Bias events.* http://indico.cern.ch/getFile.py/access?contribId=7&resId=1&materialId=slides&confId=26053.

[123] M. Patel and H. Skottowe. *A Fisher discriminant selection for $B_d \to K^*\mu^+\mu^-$ at LHCb.* LHCb-2009-09 (2009).

[124] M. Patel and H. Skottowe. *A cut-based selection for $B_d \to K^*\mu^+\mu^-$ at LHCb.* LHCb-2009-08 (2009).

[125] J. Albrecht Inclusive HLT2 τ-unbiased Dimuon Selection. https://indico.cern.ch/getFile.py/access?contribId=10&sessionId=0&resId=0&materialId=slides&confId=44441 (2008).

[126] M. Gandelman. *Bandwidth division for L0 and HLT1.* https://indico.cern.ch/getFile.py/access?contribId=6&resId=0&materialId=slides&confId=58528 (2009).

[127] T. Blake and M. Patel. *Trigger Acceptance Biases on $B_d \to K^*\mu^+\mu^-$.* LHCb-PUB-2010-013 (2010).

[128] U. Egede. *Progress plans for HLT2 implementation.* https://indico.cern.ch/getFile.py/access?contribId=0&resId=2&materialId=slides&confId=61292 (2009).

[129] L. De Paula. *Progress on HLT2 for biased dimuon line.* https://indico.cern.ch/getFile.py/access?contribId=1&resId=0&materialId=slides&confId=57251 (2009).

[130] J. Albrecht. *HLT2 inclusive dimuon triggers.* https://indico.cern.ch/getFile.py/access?contribId=13&sessionId=1&resId=0&materialId=slides&confId=57687 (2009).

[131] M. Patel. *HLT2 Leptons: Performance in different rate scenarios.* https://indico.cern.ch/getFile.py/access?contribId=7&sessionId=0&resId=1&materialId=slides&confId=62651 (2009).

[132] H. Dijkstra. *Preparation for the LHCb week Physics/Trigger session.* https://indico.cern.ch/getFile.py/access?contribId=4&resId=0&materialId=slides&confId=47403 (2009).

[133] M. Gandelman. *L0-HLT1 optimisation with prompt charm in mind.* https://indico.cern.ch/getFile.py/access?contribId=1&resId=0&materialId=slides&confId=64031 (2009).

[134] U. Egede. *HLT/physics issues to be addressed with MC09 data* https://indico.cern.ch/getFile.py/access?contribId=9&resId=0&materialId=slides&confId=65848 (2009).

[135] H. Dijkstra.*L0/HLT1 tunning, CPU and tools*. https://indico.cern.ch/getFile.py/access?contribId=2&resId=0&materialId=slides&confId=71650 (2009).

[136] LHCb Rare Decays Working Group. *MC09 samples for trigger training*. https://twiki.cern.ch/twiki/bin/view/LHCb/RareDecaysTriggerTrainingMC09.

[137] LHCb CP Violation Working Group. *MC09 samples for trigger training*. https://twiki.cern.ch/twiki/bin/view/LHCb/NewCpOfflineSelected.

[138] LHCb Flavour Physics Working Group. *MC09 samples for trigger training*. https://twiki.cern.ch/twiki/bin/viewauth/LHCbPhysics/FWGMCSamples2009#MC09_samples_of_offline_selected.

[139] *LHCb Trigger Configuration Keys and scripts*. https://twiki.cern.ch/twiki/bin/view/LHCb/TCK.

[140] J. Cogan and J. Serrano. https://twiki.cern.ch/twiki/bin/view/LHCbPhysics/MicroDST_DiMuonIncLoose_20100601?redirectedfrom=LHCb.MicroDST_DiMuonIncLoose_20100601 (2010).

[141] J. Albrecht. *Track reconstruction in the HLT: early data tunings*. https://indico.cern.ch/getFile.py/access?contribId=4&resId=0&materialId=slides&confId=82202 (2010).

[142] R. Aaij et al (the LHCb Collaboration). *Measurement of Charged Particle Multiplicities in proton-proton collisions at a centre-of-mass energy of $\sqrt{s} = 7$ TeV in the forward region*. LHCb-PAPER-2011-011 (2011).

[143] A. Perez-Calero. *Muon (+track) alleys VELO confirmation*. https://indico.cern.ch/getFile.py/access?contribId=2&resId=0&materialId=slides&confId=82192 (2010).

[144] A. Perez-Calero. *Validation of HLT1 muon triggers*. https://indico.cern.ch/getFile.py/access?contribId=2&resId=0&materialId=slides&confId=86609 (2010).

[145] A. Perez-Calero. *HLT1 muon performance*. https://indico.cern.ch/getFile.py/access?contribId=3&resId=0&materialId=slides&confId=82202 (2010).

[146] A. Perez-Calero. *HLT1 muon performance update*. https://indico.cern.ch/getFile.py/access?contribId=3&resId=0&materialId=slides&confId=82208 (2010).

[147] J. Albrecht, L. de Paula, A. Perez-Calero and F. Teubert. *Commissioning and Performance of the LHCb HLT1 muon trigger*. LHCb-PUB-2011-006 (2011).

[148] J. A. Hernando, E. Lopez, D. Martinez, H. Ruiz and F. Teubert. *Measurement of trigger efficiencies and biases*. LHCb-2008-073 (2008).

[149] F. Alessio. *Operation and Performance of the LHCb experiment*. LHCb-PROC-2011-016 (2011).

[150] P. de Simone. *Operation and Performances of the LHCb experiment*. LHCb-PROC-2011-039 (2011).

[151] X. Cid and J. A. Hernando. *What triggers the hlt1 hadron alley?*. LHCb-INT-2009-020 (2009).

[152] O. Callot. *FastVelo, a fast and efficient pattern recognition package for the Velo*. LHCb-PUB-2011-001 (2011).

[153] R. Aaij and J. Albrecht *Muon triggers in the High Level Trigger of LHCb* LHCb-PUB-2011-017 (2011).

[154] V. Gligorov, C. Thomas and M. Williams. *The HLT inclusive B triggers*. LHCb-PUB-2011-016 (2011).

[155] U. Kerzel. *The $\mu\mu$ invariant mass spectrum*. https://indico.cern.ch/getFile.py/access?contribId=5&resId=0&materialId=slides&confId=105675 (2011).

that which does not kill us makes us stronger